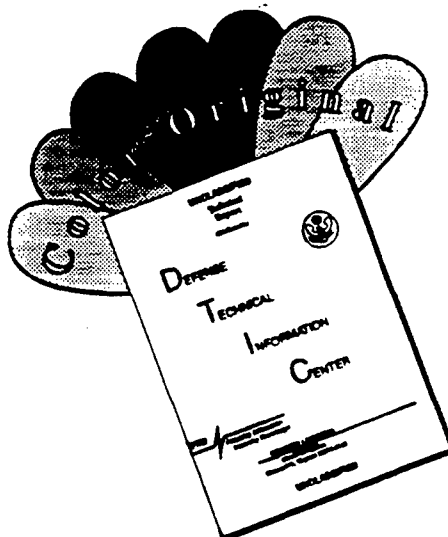


REPORT DOCUMENTATION PAGE			Form Approved OMB No. 0704-0188	
Public reporting burden for this collection of information is estimated to average 1 hour per response, including the time for reviewing instructions, searching existing data sources, gathering and maintaining the data needed, and completing and reviewing the collection of information. Send comments regarding this burden estimate or any other aspect of this collection of information, including suggestions for reducing this burden, to Washington Headquarters Services, Directorate for Information Operations and Reports, 1215 Jefferson Davis Highway, Suite 1204, Arlington, VA 22202-4302, and to the Office of Management and Budget, Paperwork Reduction Project (0704-0188), Washington, DC 20503.				
1. AGENCY USE ONLY (Leave blank)		2. REPORT DATE 9 Jan 97		3. REPORT TYPE AND DATES COVERED
4. TITLE AND SUBTITLE Terrain-Induced Midtropospheric Frontogenesis and Jet Streak Development During Storm-Fest IOP-17, 8 & 9 March 1992			5. FUNDING NUMBERS	
6. AUTHOR(S) Michael E. Adams				
7. PERFORMING ORGANIZATION NAME(S) AND ADDRESS(ES) North Carolina State University			8. PERFORMING ORGANIZATION REPORT NUMBER 96-48D	
9. SPONSORING/MONITORING AGENCY NAME(S) AND ADDRESS(ES) DEPARTMENT OF THE AIR FORCE AFIT/CIA 2950 P STREET WPAFB OH 45433-7765			10. SPONSORING/MONITORING AGENCY REPORT NUMBER	
11. SUPPLEMENTARY NOTES				
12a. DISTRIBUTION AVAILABILITY STATEMENT Unlimited			12b. DISTRIBUTION CODE	
13. ABSTRACT (Maximum 200 words)				
19970117 120				
14. SUBJECT TERMS			15. NUMBER OF PAGES 214	
			16. PRICE CODE	
17. SECURITY CLASSIFICATION OF REPORT		18. SECURITY CLASSIFICATION OF THIS PAGE		19. SECURITY CLASSIFICATION OF ABSTRACT
				20. LIMITATION OF ABSTRACT

DISCLAIMER NOTICE



THIS DOCUMENT IS BEST QUALITY AVAILABLE. THE COPY FURNISHED TO DTIC CONTAINED A SIGNIFICANT NUMBER OF COLOR PAGES WHICH DO NOT REPRODUCE LEGIBLY ON BLACK AND WHITE MICROFICHE.

**TERRAIN-INDUCED
MIDTROPOSPHERIC FRONTOGENESIS
AND JET STREAK DEVELOPMENT
DURING STORM-FEST IOP-17, 8 & 9 MARCH 1992**

by

MICHAEL E. ADAMS

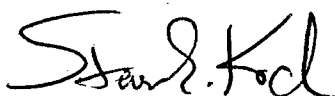
A dissertation submitted to the Graduate Faculty of
North Carolina State University
in partial fulfillment of the
requirements for the Degree of
Doctor of Philosophy

DEPARTMENT OF MARINE, EARTH, AND ATMOSPHERIC SCIENCES

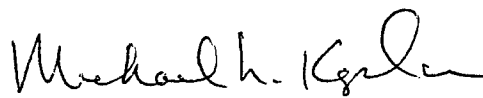
Raleigh

1996

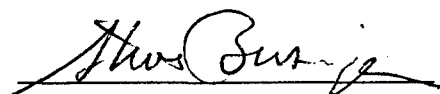
APPROVED BY:



Steven E. Koch



Michael L. Kaplan



Steven Businger
Co-chair of Advisory Committee



Gerald F. Watson
Co-chair of Advisory Committee

ABSTRACT

ADAMS, MICHAEL E. Terrain-Induced Midtropospheric Frontogenesis and Jet Streak Development During STORM-FEST IOP-17, 8 & 9 March 1992. (Under the direction of Steven Businger and Michael L. Kaplan)

Diagnostic analysis and numerical modeling studies of STORM-FEST IOP-17 data from 8-9 March 1992 reveal that terrain forced mesoscale secondary circulations play a prominent role in cold front aloft (CFA) formation and in the bifurcation of the polar jet downwind of a barrier. Terrain enhanced adiabatic and diabatic forcing, associated with focused leeside warming to the south and an equatorward surge of cold air from the north, generate mass perturbations that lie within the Rossby radius of deformation. The perturbation results in an imbalance between the mass and momentum field as an increased separation develops between the observed and geostrophic jet max. In order to regain a balance, the divergent part of the wind responds by establishing a thermally-direct circulation within the jet exit region. In response, the 'classical jet streak' configuration is distorted as the exit region accelerates downstream. The positive velocity divergence tendency produces a net mass flux divergence throughout the column. In turn, ascent and midtropospheric cooling is observed within the right exit region of the accelerating jet streak. The baroclinic zone associated with the primary trough over the inner-mountain region weakens as cold air is generated downstream of the mountain. The CFA formation is initially dominated by tilting of the vertical temperature gradient and then enhanced by confluence and shear contributions as a 'balanced' thermally-indirect circulation is regained. The resulting cooling acts to retard height rises in a region which typically experiences a build up of mass induced by subsiding air. This destabilization acts to promote an environment conducive to severe weather downstream of the mountains.

PERSONAL BIOGRAPHY

Major Michael E. Adams is a Officer in the United States Air Force. He was born in New Haven, Connecticut on September 24, 1950. He received a Bachelor of Science degree in Meteorology from Lyndon State College, Vermont in 1981. Upon graduation, Major Adams was commissioned a Second Lieutenant through the Air Force Reserve Officer Training Corps program at Saint Michael's College in Burlington, Vermont. His active military career began at Air Force Global Weather Central, Offutt Air Force Base, Nebraska. His assignment began as Officer-In-Charge (OIC) of the Asian Forecast Section then OIC of the Upper-Air Analysis Section, and then finally Assistant Operations Officer.

In 1984, Major Adams was assigned as Wing Weather Officer to Detachment 3, 28th Weather Squadron, Royal Air Force Base, Lakenheath, England. Specialized Electro-Optic weather support was provided to four squadrons of F-111 aircraft. He was promoted to the rank of Captain in August 1985.

He entered North Carolina State University in 1987 through the Air Force Institute of Technology program earning a Master of Science in Meteorology. His thesis topic dealt with the processes associated with "Explosive Cyclogenesis".

In 1989, he was assigned to Patrick AFB, Florida. He was initially assigned as staff meteorologist to the Department of Defense Managers for Space Shuttle Contingency Support office responsible for establishing and managing weather support at overseas abort landing sites and shuttle ferry flight operations. In 1990, he served as the NASA Staff Meteorologist to the Kennedy Space Center. He was directly responsible for the

planning, coordinating, and directing the full range of environmental support to the Space Shuttle program. In September 1992 his responsibility was increased and was made the OIC of the Cape Canaveral Forecast Facility. He was responsible for all aspects of operational weather support to NASA's Kennedy Space Center and the Cape Canaveral Air Force Station. He managed a team of eighteen meteorologists located within the Range Weather Operations Flight. The team's responsibilities included direct launch weather support for the operational testing and launching of Trident submarine ballistic missiles and unmanned space launches of Titan, Atlas, and Delta rockets. He also supervised the Launch Weather Team supporting manned Space Shuttle launches, landings, and cross country ferry flights atop a modified B-747 Shuttle Carrier Aircraft. Major Adams served as the Staff Weather Officer to the Eastern Range providing meteorological consultation to both government and commercial launch programs. He is also was responsible for the operation and implementation of state-of-the-art meteorological equipment. He was selected for promotion to Major in December 1992.

In 1993, he was selected by the Air Force Institute of Technology program to attend North Carolina State University to work towards his Ph.D.

Major Adams has earned the Senior Meteorologist Badge. His military decorations include the Air Force Commendation Medal with one oak leaf cluster and the Air Force Achievement Medal. He is married to the former Susan Jayne Goblen and has two children, a daughter, Katelyn Christine, and a son, Jonathan Michael.

ACKNOWLEDGMENTS

This research was supported by the United States Air Force through the Air Force Institute of Technology (AFIT) program. This program has provided me the opportunity to return to the academic environment to continue my education in pursuit of an advanced degree. I would like to express my heartfelt appreciation to Col.'s John Madura and John Upchurch (USAF Ret) for their assistance in making this assignment possible.

I would like to take this opportunity to express my appreciation to committee members Mike Kaplan and Steve Koch for opening my eyes to the amazing world beyond Q.G. theory. Also, to Steven Businger and Gerry Watson for providing me the opportunity to conduct this exciting research.

Special appreciation is extended to Dr. Jennifer M. Cram, NOAA/ERL/FSL, for graciously providing the basic code used to retrieve the mass and thermal structure from the observed momentum fields of the STORM-FEST data set. Her assistance was invaluable in applying this technique to improve the mesoscale analysis of the data set.

I would like to thank John Zack and Ken Waight of MESO Inc. for making the MASS model available for this research and assistance in technical issues that arose. Also, to Arnold Hori of the University of Hawaii for the time and effort he provided so that I could run the MASS model on their computer system.

I must recognize my colleagues Bob Rozumalski, Tom Graziano, Bill Bauman, and Steve Chiswell for their invaluable assistance in guiding me in computer operations, data processing, intellectual enlightenment, and most of all moral support. Bob's generosity of

time and programs were invaluable as he instructed me on the MASS model operations and making his trajectory package available to me. Tom's support and help in preparing for the written and oral exams and use of various GEMPAK scripts were extremely important in successfully completing this program. Bill's encouragement to enter this program and ever present support were greatly appreciated. His unselfish efforts in assuring my use of the Kubota workstation was critical in my successful completion within the allotted time. And of course -- Chiz. His assistance, in what must have been a seemingly endless request for help, was invaluable in acquiring and processing data. His patience was truly appreciated in dealing with what must have seemed like some of the most basic questions while I worked to overcome that learning curve. These individuals have provided many hours of laughter, wit, and friendship which has made this experience that much more bearable over the past three years and for that I am most grateful.

DEDICATION

To my parents John and Regina. The love and guidance you provided through my childhood has prepared me well in facing the many challenges into adulthood. The opportunities and experiences you provided has allowed me to realize the importance in working hard and doing your best.

Finally, my deepest love and appreciation to my wife Susan and my children Katelyn and Jonathan. Your encouragement, patience and love throughout has allowed me to achieve my goals.

TABLE OF CONTENTS

	Page
LIST OF TABLES	ix
LIST OF FIGURES	x
1. INTRODUCTION	
1.1 Background.....	1
1.2 Overview	16
2. DATA AND ANALYSIS METHODOLOGY	
2.1 Overview	20
2.2 Introduction	21
2.3 Data and Methodology	25
2.4 Results of The Divergence Method Using All Available Winds	32
2.5 Results of the Divergence Method Solely Using Profiler Winds.....	40
2.6 Summary.....	42
3. GEOSTROPHIC ADJUSTMENT AND CFA FORMATION IN RESPONSE TO LEESIDE WARMING ALONG THE SOUTHERN FRONT RANGE	
3.1 Overview	45
3.2 Objectives	45
3.3 Observational and Modeling Data Sets	46
3.3.1 Observational Data Sets and Analysis Scheme.....	46
3.3.2 Mesoscale Model and Experimental Design.....	47
3.4 Observed Evidence of Cold Front Aloft and Downstream Impact	53
3.5 Regional Overview	62
3.5.1 Evolution of the Low-Level Features	62
3.5.2 Evolution of the Midtropospheric Atmosphere	70
3.6. Terrain-Induced Leeside Warming and Associated Mass Perturbation.....	74
3.6.1 Downslope Adiabatic Warming	74
3.6.2 Focused Boundary Layer Sensible Heating	79
3.6.3 Mountain Wave Activity	81
3.6.4 Terrain Induced Mass Perturbation	87
3.7 Geostrophic Adjustments and Genesis of the Cold Front Aloft.....	89
3.7.1 Modified Secondary Circulation	89
3.7.2 Cold Front Aloft Structure	102

	Page
3.8 Numerical Modeling Studies	112
3.8.1 Evolution of Background Synoptic Scale Flow.....	112
3.8.2 Mesoscale Environment	119
3.8.3 Adiabatic Sensitivity Study.....	131
 4. GEOSTROPHIC ADJUSTMENT AND CFA FORMATION IN RESPONSE TO A DEVELOPING COLD SURGE ALONG NORTHERN FRONT RANGE	
4.1 Overview	140
4.2 Objectives	141
4.3 Observational Perspective.....	141
4.3.1 Evolution of the Low-Level Features	141
4.3.2 Evolution of the Midtropospheric Atmosphere	146
4.4 Cold Surge Structure.....	148
4.4.1 Flow Blockage Requirements.....	149
4.4.2 Application of Theory of Flow Blockage to Observations.....	150
4.5 Development of CFA and Bifurcated Jetstream.....	160
4.5.1 Cold Front Aloft Structure	162
4.5.2 Cold Front Aloft Destabilization and Convective Initiation	167
4.5.3 Observed CFA Generation and Geostrophic Adjustments.....	171
4.5.4 MASS Model Trajectory Analysis.....	184
4.5.5 MASS Model Derived fields	188
4.6 Terrain Impact in CFA Formation and Jetstream Bifurcation.....	192
 5. SUMMARY AND CONCLUSIONS	199
6. LIST OF REFERENCES	207

LIST OF TABLES

	Page
Table 1.0 Significant Weather Events of 8-9 March 1992	18
Table 2.0 Standard Deviation (σ) of the difference between the retrieved	36
Table 3.0 Specification for MASS Model version 5.8	50
Table 4.0 Summary of MASS model experiments conducted.....	53
Table 5.0 Backward trajectory initiated at 2300 UTC 8 March 1992	159
Table 6.0 Forward trajectory initiated at 2100 UTC 8 March 1992.....	186

LIST OF FIGURES

		Page
Figure 1.1	Conceptual model depicting structure of Cold Front Aloft.	3
Figure 1.2	Conceptual model detailing the development of a Cold Front Aloft in response to orographic modifications to the atmosphere.....	5
Figure 1.3	(a) Depiction of an upper-level jet streak in which cold advection modifies the ageostrophic motion. (b) Cross section through entrance region of jet streak.....	9
Figure 1.4	Idealized upper-level jet streak and associated ageostrophic flow.....	10
Figure 2.1	Domain of STORM-FEST upper air observations used in objective analysis scheme..	28
Figure 2.2	Retrieved 500 mb geopotential height field for (a) 2100 UTC 8 March 1992 and (b) 0300 UTC 9 March 1992.....	34
Figure 2.3	Difference between the retrieved height field and observed height field at 500 mb level for 0300 UTC 9 March 1992..	35
Figure 2.4	Distribution of the difference between the 500 mb retrieved and the observed heights.....	37
Figure 2.5	Skew-T plot of derived and observed temperature profiles for Geymon, Oklahoma.....	39
Figure 2.6	Retrieved 500 mb height field for (a) 2100 UTC 8 March 1992 and (b) 0300 UTC 9 March 1992.....	41
Figure 3.1	850 mb height field comparison between observed conditions and 18 hour MASS model forecast valid at 1800 UTC 8 March 1992.....	48
Figure 3.2	A 14 km MASS model run was constructed with a 240x210 grid domain	52
Figure 3.3a	GOES-7 infrared satellite imagery valid at 1301 UTC 8 March 1992.....	55

	Page
Figure 3.3b	GOES-7 infrared satellite imagery valid at 1731 UTC 8 March 1992..... 57
Figure 3.3c	GOES-7 infrared satellite imagery valid at 2101 UTC 8 March 1992..... 58
Figure 3.3d	GOES-7 infrared satellite imagery valid at 2331 UTC 8 March 1992..... 60
Figure 3.4	Amarillo, Texas sounding profile for 2100 UTC 8 March 1992 and 0000 UTC 9 March 1992..... 61
Figure 3.5	1200 UTC 08 March 1992 (a) surface and (b) 500 mb analysis 63
Figure 3.6	1800 UTC 08 March 1992 (a) surface and (b) 500 mb analysis 65
Figure 3.7	2100 UTC 08 March 1992 (a) surface and (b) 500 mb analysis 66
Figure 3.8	(a) 2100 UTC 8 March 1992 surface streamline analysis, and position of surface low and dryline. (b) Surface equivalent potential temperature analysis and surface moisture convergence 68
Figure 3.9	Midland, Texas sounding profile for 8 March 1992, 1500 UTC, 1800 UTC, and 2100 UTC 69
Figure 3.10	0000 UTC 09 March 1992 (a) surface and (b) 500 mb analysis 71
Figure 3.11	Back trajectory constructed from 14 km full physics MASS model output. Trajectory initialized at 2100 UTC 8 March 1992 and ran to 1500 UTC 8 March 1992..... 78
Figure 3.12	(a) Topography over New Mexico/Texas and (b) 1200 UTC 8 March 1992 objectively analyzed 700 mb streamline analysis and kinematic omega..... 82
Figure 3.13	(a) 1200 UTC 8 March 1992 sounding from El Paso, Texas and (b) corresponding vertical profile of Scorer parameter..... 84

	Page
Figure 3.14	14 km MASS model-generated fields valid at 1800 UTC 8 March 1992. (a) 600 mb wind barbs, isotachs, isotherms (b) kinematic omega, and (c) Cross section of kinematic omega, theta, and RH..... 86
Figure 3.15	Six hour change in 500 mb height and surface theta fields between 1200 UTC and 1800 UTC 8 March 1992..... 88
Figure 3.16	1800 UTC 8 March 1992 objectively analyzed (a) total wind and geostrophic wind (b) inertial Rossby number and thermal wind 91
Figure 3.17	1800 UTC 08 March 1992 500 mb ageostrophic wind analysis derived from gridded data set. 94
Figure 3.18	2100 UTC 08 March 1992 500 mb ageostrophic wind analysis derived from gridded data set. 96
Figure 3.19	1800 UTC 08 March 1992 500 mb summation of four terms of the non-linear balance equation and 2100 UTC isotachs 98
Figure 3.20	Back trajectory constructed from 14 km full physics MASS model output. Trajectory initialized at 2100 UTC 8 March 1992 and ran back to 1500 UTC 8 March 1992 100
Figure 3.21	(a) 2100 UTC 8 March 1992 three hour temperature advection by the observed wind and observed three hour temperature change between 2100 UTC 8 March and 0000 UTC 9 March 1992. (b) 0000 UTC 9 March 1992 gridded fields of: ageostrophic streamline, heights, isotachs and equivalent potential temperature 103
Figure 3.22	0000 UTC 9 March 1992 vertical cross section through the nose of an accelerating jet exit region..... 105
Figure 3.23	Hourly profiler display from Vici, Oklahoma from 2100 UTC 8 March to 0600 UTC 9 March 1992 106
Figure 3.24	Observed 2100 UTC 8 March 1992 500 mb frontogenesis calculations based on Miller Frontogenetic function. (a) Total frontogenesis, (b) tilting term, (c) horizontal shear term, and (d) confluence term 109

	Page
Figure 3.25	Observed 0000 UTC 9 March 1992 500 mb frontogenesis calculations based on Miller Frontogenetic function. (a) Total frontogenesis, (b) tilting term, (c) horizontal shear term, and (d) confluence term 111
Figure 3.26	160 km full physics 500 mb MASS model output of heights, isotachs, wind barbs, and theta valid at (a) 1200 UTC 8 March 1992, (b) 1800 UTC 8 March 1992, (c) 2100 UTC 8 March 1992, and (d) 0000 UTC 9 March 1992..... 113
Figure 3.27	160 km full physics 500 mb MASS model output of heights, isotachs, ageostrophic streamlines valid at (a) 1200 UTC 8 March 1992, (b) 1800 UTC 8 March 1992, (c) 2100 UTC 8 March 1992, and (d) 0000 UTC 9 March 1992..... 115
Figure 3.28	Back trajectory constructed from 160 km full physics MASS model output. Trajectory initialized at 0000 UTC 9 March 1992 and ran to 1500 UTC 8 March 1992..... 116
Figure 3.29	0000 UTC 9 March 1992 160 km MASS model diagnostics. (a) 500 mb mass divergence calculations and (b) total 500 mb frontogenesis calculations based on Miller frontogenetic function..... 118
Figure 3.30	60 km full physics 500 mb MASS model output of heights, total wind isotachs/barbs, and theta valid at (a) 1500 UTC 8 March 1992, (b) 1800 UTC 8 March 1992 120
Figure 3.31	60 km full physics 500 mb MASS model output of heights, total wind isotachs, vertical motion, and ageostrophic flow valid at 1500 UTC 8 March 1992. 121
Figure 3.32	1800 UTC 8 March 1992 60 km full physics 500 mb MASS model output of (a) Total and geostrophic wind isotachs, graphical subtraction of both fields, and theta. (b) heights, ageostrophic streamlines, and inertial Rossby number 123
Figure 3.33	60 km full physics 500 mb MASS model output of heights, total wind isotachs/barbs, and theta valid at (a) 2100 UTC 8 March 1992, (b) 0000 UTC 9 March 1992 125

	Page
Figure 3.34	2100 UTC 8 March 1992 500 mb frontogenesis calculations based on Miller Frontogenetic function derived from the 60 km MASS model simulation with high resolution terrain data base. (a) Total frontogenesis, (b) tilting term, (c) horizontal shear term, and (d) confluence term 126
Figure 3.35	0000 UTC 9 March 1992 500 mb frontogenesis calculations derived from the 60 km full physics MASS model simulation with high resolution terrain data base. (a) Total frontogenesis, (b) tilting term, (c) horizontal shear term, and (d) confluence term 127
Figure 3.36a	60 km full physics MASS model cross section valid at 1500 UTC 8 March 1992 extending from 35°N, 105°W to 35°N 95°W 129
Figure 3.36b	60 km full physics MASS model cross section valid at 2100 UTC 8 March 1992 extending from 35°N, 105°W to 35°N 95°W 130
Figure 3.37	2100 UTC 8 March 1992 60 km 500 mb MASS modeling study of (a) full physics output and (b) adiabatic model run. Fields of heights, theta, and winds are displayed 133
Figure 3.38	Graphical subtraction of the 2100 UTC 8 March 1992 60 km 500 mb full physics model output from the adiabatic model output files. Displayed fields are difference in (a) theta, (b) geopotential height, (c) <i>u</i> -wind component, (d) <i>v</i> -wind component 134
Figure 3.39	2100 UTC 8 March 1992 60 km 700 mb MASS modeling study of (a) full physics output and (b) adiabatic model run. Fields of heights, theta, and winds are displayed 136
Figure 3.40	Graphical subtraction of the 2100 UTC 8 March 1992 60 km 700 mb full physics model output from the adiabatic model output files. Displayed fields are difference in (a) theta, (b) geopotential height, (c) <i>u</i> -wind component, (d) <i>v</i> -wind component 137
Figure 3.41	2100 UTC 8 March 1992 500 mb frontogenesis calculations derived from the 60 km Adiabatic MASS model simulation with high resolution terrain data base. (a) Total frontogenesis, (b) tilting term, (c) horizontal shear term, and (d) confluence term 139

	Page
Figure 4.1	0300 UTC 09 March 1992 (a) surface and (b) 500 mb analysis 144
Figure 4.2	0600 UTC 09 March 1992 (a) surface and (b) 500 mb analysis 145
Figure 4.3	850 mb analysis for (a) 0000 UTC 9 March 1992 and (b) 0600 UTC 9 March 1992)..... 151
Figure 4.4	Observed weather conditions at Denver, Colorado for the 24 hour period 1200 UTC 8 March to 1200 UTC 9 March 1992 154
Figure 4.5	Denver, Colorado sounding profile for 9 March 1992 at 0000 UTC and 0600 UTC..... 155
Figure 4.6	9 March 1992 0300 UTC objectively analyzed cross section derived from observed STORM-FEST data sets..... 157
Figure 4.7	Forward trajectories based on 14 km resolution MASS full physics model simulation initialized at 1200 UTC 8 March 1992. Each of the four parcel positions are plotted every hour beginning at 2300 UTC 8 March 1992 and ending at 0600 UTC 9 March 1992..... 158
Figure 4.8	Observed hourly consensus averaged winds from the Granada, Colorado NOAA 403-MHz Profiler. Data displayed from 2100 UTC 8 March 1992 to 1200 UTC 9 March 1992 161
Figure 4.9	Guymon, Oklahoma sounding profile for 2100 UTC 8 March 1992 and 0000 UTC 9 March 1992 163
Figure 4.10	0300 UTC 9 March 1992 500 mb observed frontogenesis calculations based on Miller Frontogenetic function for horizontal confluence, shear, and tilting term contributions..... 164
Figure 4.11	0300 UTC 9 March 1992 vertical cross section through the nose of an accelerating jet exit region..... 166
Figure 4.12	Depiction of the relationship between dryline, CFA, and convection at (a) 0000 UTC 9 March 1992 and (b) 0300 UTC 9 March 1992..... 169

	Page
Figure 4.13	0000-0600 UTC 9 March 1992 500 mb height fall pattern and isallobaric wind vector 174
Figure 4.14a	Vertical cross section valid at 0000 UTC 9 March 1992 extending from 37°N, 104°W to 34°N 94°W 176
Figure 4.14b	Vertical cross section valid at 0300 UTC 9 March 1992 extending from 37°N, 104°W to 34°N 94°W 177
Figure 4.14c	Vertical cross section valid at 0600 UTC 9 March 1992 extending from 37°N, 104°W to 34°N 94°W 179
Figure 4.15	600 mb objective analysis for (a) 0000 UTC and (b) 0300 UTC 9 March 1992 180
Figure 4.16	500 mb objective analysis for (a) 0600 UTC and (b) 0900 UTC 9 March 1992 182
Figure 4.17	500 mb objective analysis of the summation of four terms that make up the non-linear balance for (a) 0000 UTC and (b) 0600 UTC 9 March 1992 183
Figure 4.18	Forward trajectory constructed from 60 km full physics MASS model output. Trajectory started at 2100 UTC 8 March 1992 and ran to 0900 UTC 9 March 1992 185
Figure 4.19	MASS model 60 km output from (a) 0300 UTC 9 March 1992 and (b) 0600 UTC 9 March 1992 189
Figure 4.20	MASS model 60 km output displaying (a) 0600 UTC 9 March 1992 inertial Rossby number and the 500 mb temperature advection by the 09/03 UTC total wind. (b) 0300 UTC 9 March 1992 600 to 400 mb layer averaged mass divergence and the derived $\Delta\theta$ between 09/03 and 09/0600 UTC 191
Figure 4.21	(a) 60 km MASS model output with high resolution surface terrain data base. (b) 60 km MASS model output with flat 1200 m surface elevation. Model generated fields are from the 15 hour forecast valid at 0300 UTC 9 March 1992 194

	Page
Figure 4.22	0300 UTC 9 March 1992 500 mb frontogenesis calculations based on Miller Frontogenetic function derived from the 60 km MASS model simulation with high resolution terrain data base 196
Figure 4.23	0300 UTC 9 March 1992 500 mb frontogenesis calculations based on Miller Frontogenetic function derived from the 60 km MASS model simulation with flat terrain data base..... 197
Figure 5.1	Conceptual model depicting structure of terrain induced Cold Front Aloft and developing midtropospheric jet streak over the central Plains in response to terrain induced secondary circulation downstream of the mountains 206

1. INTRODUCTION

1.1 Background

Orography provides an important mechanism in altering the atmospheric structure as the mean flow is intercepted by a barrier. Significant mountain ranges such as the Alps, Pyrenees, Tibetan Plateau, and the Rockies all influence the environment on their downwind side. Nearly 60 years ago, Bergeron (1937) provided early insight into the topographical influence in altering observed weather conditions over northern Europe. His keen observation of terrain impact in altering the precipitation structure of transient waves and restructuring of the frontal zones revealed the complex interactions between the observed flow and orography. Field programs such as the 1981 Cooperative Convective Precipitation Experiment (CCOPE) over Montana, the 1982 Alpine Experiment (ALPEX) over southern Europe, and the Pyrenees Experiment (PYREX) along the border of France and Spain conducted during the fall of 1990 have provided researchers with the types of data required to investigate the interactions more completely.

An important consequence of the terrain influence on the atmosphere is the formation of a cold front aloft (CFA). The CFA is a midtropospheric feature that is characterized by an elevated pool of cool-dry air positioned out ahead of the surface frontal zone (Hobbs *et al.* 1990). Though this feature is not unique to the United States, the CFA provides an effective mechanism for generating some of the most severe weather conditions over a concentrated area encountered on the face of the earth. The unique geographical environment over the Great Plains results in differential temperature and

moisture advection patterns that encourage the generation of potential instability downstream of the Front Range (Carlson and Ludlam 1968). Studies have indicated that the destabilization brought on by an advancing CFA is especially effective in generating severe weather east of the Rockies. Lichtblau (1936) attributed the generation of heavy winter precipitation to an advancing CFA. A follow-on investigation by Lloyd (1942) recognized the CFA importance in destabilizing the atmosphere to generate strong thunderstorm and tornado activity over the central Plains. More recently, Hobbs *et al.* (1990) and Locatelli *et al.* (1995) point out that the CFA acts as an effective lifting mechanism in the triggering of severe convection as the capping inversion breaks down.

The CFA is characterized by an elevated region of cool-dry air with a significant thermal gradient between this advancing cold pool and the warm air ahead. The transition zone is typically characterized by a length scale on the order of ~1000 km and a width of ~100 km (Keyser and Shapiro 1986). A conceptual model of a cold front aloft developed by Hobbs *et al.* (1990) is depicted in Fig. 1.1. An increase in the convective instability is realized as cool-dry (low θ_e) air overrides the warm moist (high θ_e) low-level air. A maximum of convective instability is observed from the surface trough to the base of the CFA. Some of the signatures developed by Hobbs *et al.* for meteorologists to use in identifying a CFA consists of:

- i) Main precipitation band located ahead of surface boundary
 - Organized band of convection ~ 200-300 km ahead of surface boundary
- ii) Satellite photographs reveal cloud band located ahead of surface boundary
 - Cloud band orthogonal to surface boundary
 - Rapid decrease in cloud top temperature behind CFA position

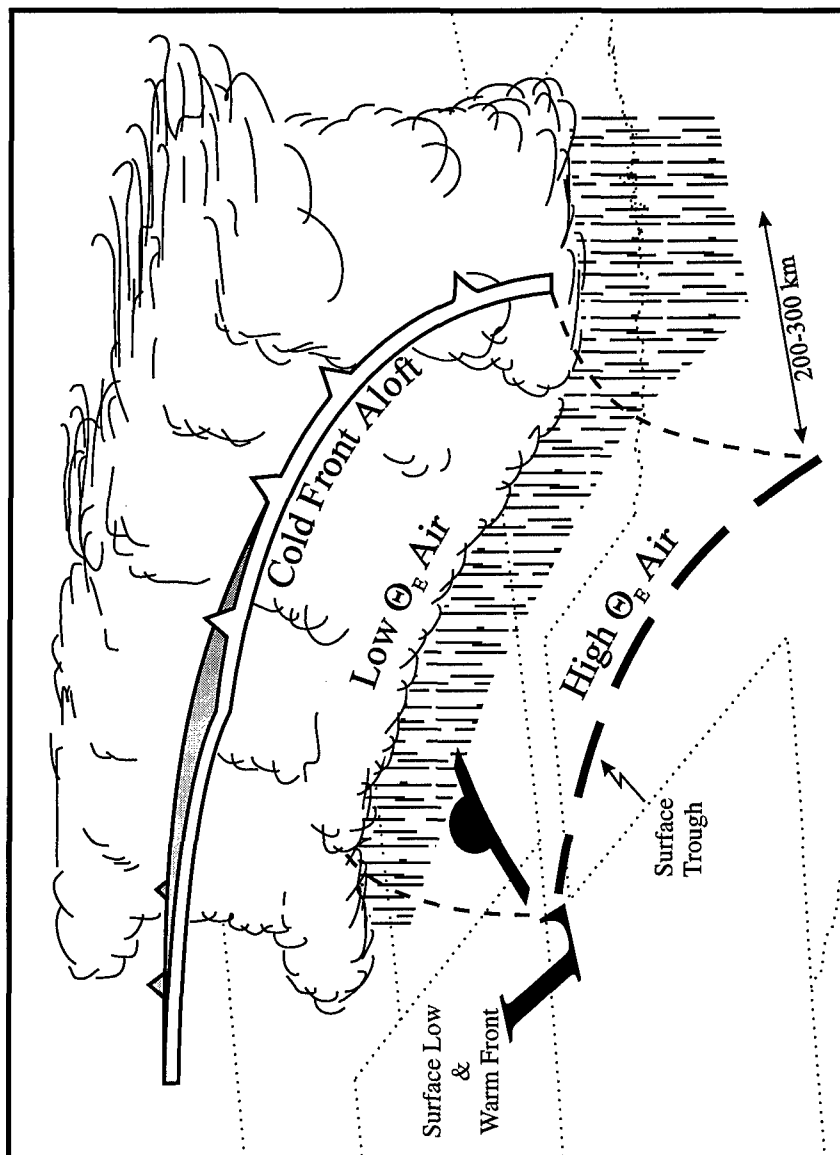


Figure 1.1. Conceptual model depicting structure of Cold Front Aloft. Adapted from Hobbs (1990).

- iii) Juxtaposition of 1000-500 mb thickness ridge and the surface pressure trough
- iv) Mid-level thermal gradient stronger than large scale thermal structure
 - Observed in vicinity of precipitation field
- v) 700 mb cold advection ahead of surface boundary
 - NEXRAD radial velocity signature of cold advection aloft
- vi) Cross section of θ_e indicates elevated gradient ahead of surface boundary
 - Moisture discontinuity provides good tracer of CFA position
- vii) Concentration of absolute momentum within the frontal zone
 - In response to increased vertical and horizontal geostrophic wind shear
- viii) Ascent in vertical velocity field found ~ 200-300 km ahead of surface boundary

Most studies relate CFA formation with the process by which the lower tropospheric cold air is modified by the mountains while the mid-level cold pool moves out of the inner mountain region unimpeded (Martin *et al.* 1990, Locatelli *et. al.* 1995). A three-dimensional depiction of the evolution of the CFA is displayed in Fig. 1.2 (Hobbs *et al.* 1994). The source of cold air for the CFA is associated with an upper-level trough and associated cold pool over the inner-mountain region (Fig. 1.2a). As the low-level cold air crosses the mountain barrier, the strong adiabatic descent warms the air parcels in the lower troposphere (Fig. 1.2b). In response, the surface based cold front is eroded while the mid-level cold air continues its eastward propagation into the central Plains as mid-level cold advection extends out into the central Plains (Fig. 1.2c). As this elevated pool of cold air overrides the low-level warm moist air over the central Plains a rapid destabilization generates convective clouds along the CFA (Fig. 1.2d).

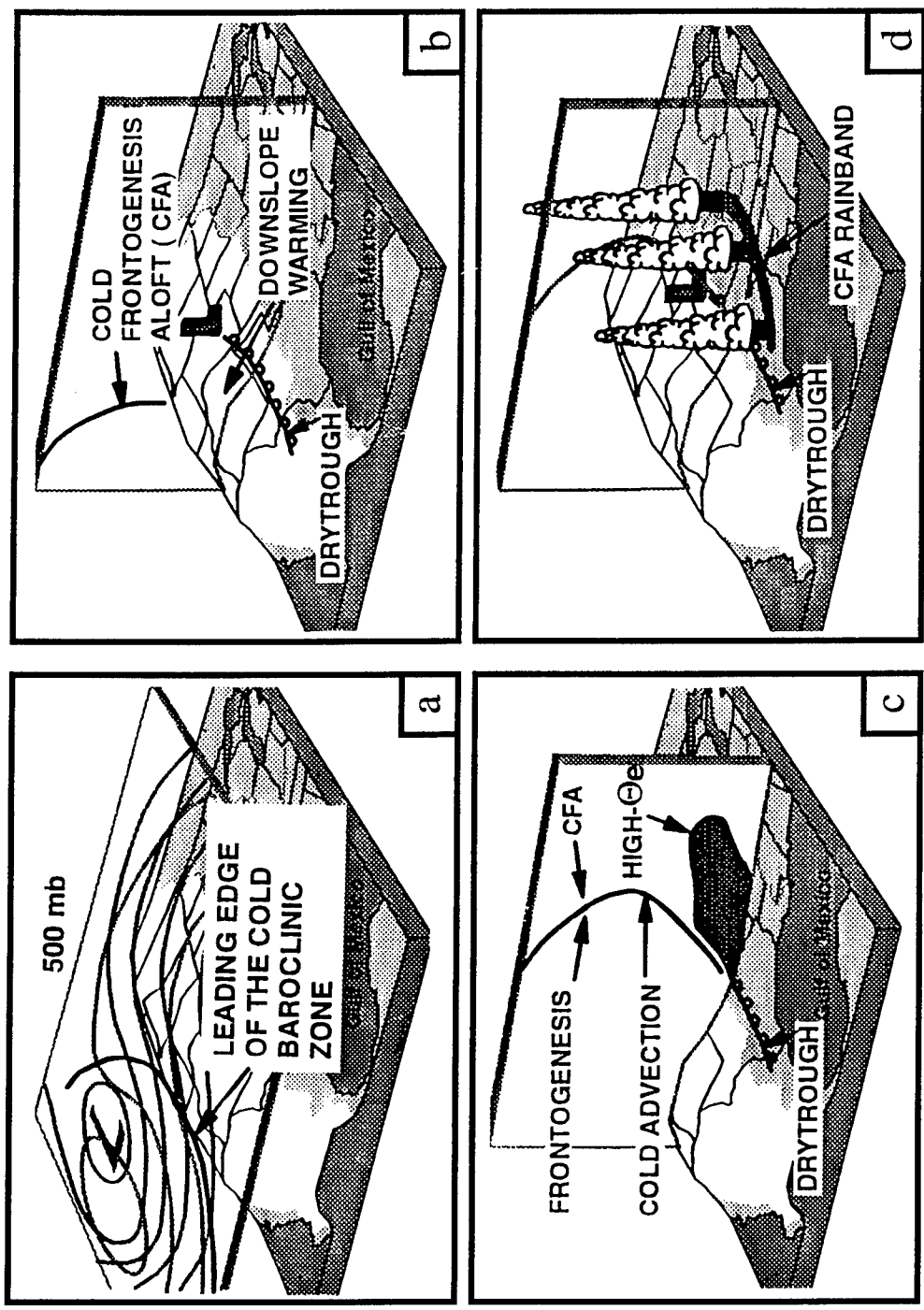


Figure 1.2. Conceptual model detailing the development of a Cold Front Aloft (CFA) in response to orographic modifications to the atmosphere. (a) Representation of horizontal mid-tropospheric structure. (b) Vertical structure of developing CFA. (c) Mechanisms responsible for CFA development and resultant destabilization. (d) Depiction of resulting surface features and CFA squall line development. (Hobbs *et al.* 1994).

Based upon semi-geostrophic principles, the formation and maintenance of upper-level frontal zones have been investigated through the use of the Sawyer-Eliassen equation (Sawyer, 1956). In a vertical plane normal to the front (y,-p)

$$\begin{aligned}
 \text{Circulation Intensity} \quad & \frac{\partial^2 \psi}{\partial y^2} \left[-\frac{\partial \theta}{\partial p} \frac{R}{f_o p} \left(\frac{p}{p_o} \right)^{\kappa} \right] + \frac{\partial^2 \psi}{\partial y \partial p} \left(2 \frac{\partial u_g}{\partial p} \right) + \frac{\partial^2 \psi}{\partial p^2} \left(f_o - \frac{\partial u_g}{\partial y} \right) = \\
 & \qquad \qquad \qquad A \qquad \qquad \qquad B \qquad \qquad \qquad C \\
 & \qquad \qquad \qquad \qquad \qquad \qquad \qquad \qquad \qquad \qquad \qquad \qquad \qquad (1) \\
 \text{Frontogenetic Forcing} \quad & 2 \frac{R}{f_o p} \left(\frac{p}{p_o} \right)^{\kappa} \left(\frac{\partial \theta}{\partial y} \frac{\partial v_g}{\partial y} + \frac{\partial \theta}{\partial x} \frac{\partial u_g}{\partial y} \right) - \frac{R}{C_p f_o p} \frac{\partial}{\partial y} \left(\frac{dQ}{dt} \right) \\
 & \qquad \qquad \qquad D \qquad \qquad \qquad E \qquad \qquad \qquad F
 \end{aligned}$$

This semi-geostrophic formulation defines a stream function (ψ) which describes the secondary circulation of the cross-stream ageostrophic flow (v_a) and the vertical motion distribution (ω). In this formulation $v_a = -\partial\psi/\partial p$ and $\omega = \partial\psi/\partial y$. The x-axis is orientated along the frontal zone, positive to the right, and the y-axis lies across the front, positive towards the cold air. This frontogenetic equation assumes:

- i) The thermal gradient is strongest perpendicular to the x-axis, though an along-front temperature gradient is allowed
 - Therefore $\partial\theta / \partial x \neq 0$
- ii) Accelerations occur only across the front ($dv/dt \neq 0$)
 - The along front ageostrophic flow is zero ($u_{ag} = 0$)
- iii) Flow is considered to be nearly zonal for simplicity
 - Pure shear vorticity ($\partial u/\partial x \neq 0$)
 - No vorticity due to curvature ($\partial v/\partial x = 0$)

The left hand side of the equation describes the intensity of the circulation. Term A provides the static stability contribution, term B the horizontal temperature gradient/vertical shear contribution, and term C is related to inertial stability. Terms A and C describe the intensity of the circulation, while term B describes the tilt of the circulation. The right hand side of Eq. 1 describes the frontogenetic forcing. Terms D and E are the contributions associated with stretching and shear deformation, respectively, and term F accounts for the effects of differential diabatic heating.

Investigation of the intensity of the secondary circulation and its role on frontogenesis can be assessed by looking at the distribution of the stream function. Frontogenesis and strengthening of a jet streak are found where the forcing is acting positively in the y - p plane. Ignoring the tilting contribution Eq. (1) reduces to

$$(A) \frac{\partial^2 \psi}{\partial y^2} + (C) \frac{\partial^2 \psi}{\partial p^2} > 0 \quad (2)$$

Substituting ω for $\partial\psi/\partial y$ and v_a for $-\partial\psi/\partial p$, then it is apparent that if the inertial forcing is stronger than the static stability, the circulation is dominated by the cross-stream ageostrophic branch ($-\partial v_a/\partial p$) inducing a broad circulation. The circulation will have a greater vertical structure when the static stability term ($\partial\omega/\partial y$) dominates.

In evaluating the forcing function, the angle between the gradient of the geostrophic wind and that of the thermal field determines the relative role of the deformation processes. If the angle is less than 45° , then deformation due to stretching dominates; if the angle is greater than 45° shear deformation dominates (Shapiro 1981, 1982). Consequently, in the case of cold advection into a trough the secondary

circulations are shifted such that the maximum descent is observed along the jet axis (Fig. 1.3). In the left entrance region, the shear term ($\partial u_g / \partial y \partial \theta / \partial x$) is negative, while the stretching term ($\partial v_g / \partial y \partial \theta / \partial y$) is positive. In the right entrance region, both the shear and stretching terms are positive. The shear term dominates in this example since the advection angle is in excess of 45° resulting in the shift of the vertical motion distribution. This process is consistent with work by Danielsen (1968), Bosart (1970), Uccellini *et al.* (1985), and Adams (1989) in which the role of a tropopause fold is identified as an important means of transporting high values of stratospheric potential vorticity to lower levels and the resultant generation of cyclonic vorticity (Reed, 1955). The influence of the terrain in impeding the surface based cold front, and the role of deformation processes, as described by the Sawyer-Eliassen equation, in the maintenance of the mid-level thermal gradients combine in the development of a CFA structure as depicted in Fig. 1.1 and 1.2.

As the flow intercepts a barrier, the downstream thermal and moisture structure is dramatically modified, resulting in the development of complex secondary circulations. When superimposed upon the background synoptic scale flow, these circulations act to disrupt the ageostrophic circulation normally associated with a propagating jet streak as an adjustment process is initiated to regain a balance between the mass and momentum fields. For a simplified straight-line jet streak, as depicted in Fig. 1.4, the entrance region is typically characterized by a thermally-direct circulation while a thermally-indirect circulation is found in the exit region (Murray and Daniels 1953; Newton 1958; Reiter 1969; Uccellini 1976). These secondary circulations develop in order for the atmosphere

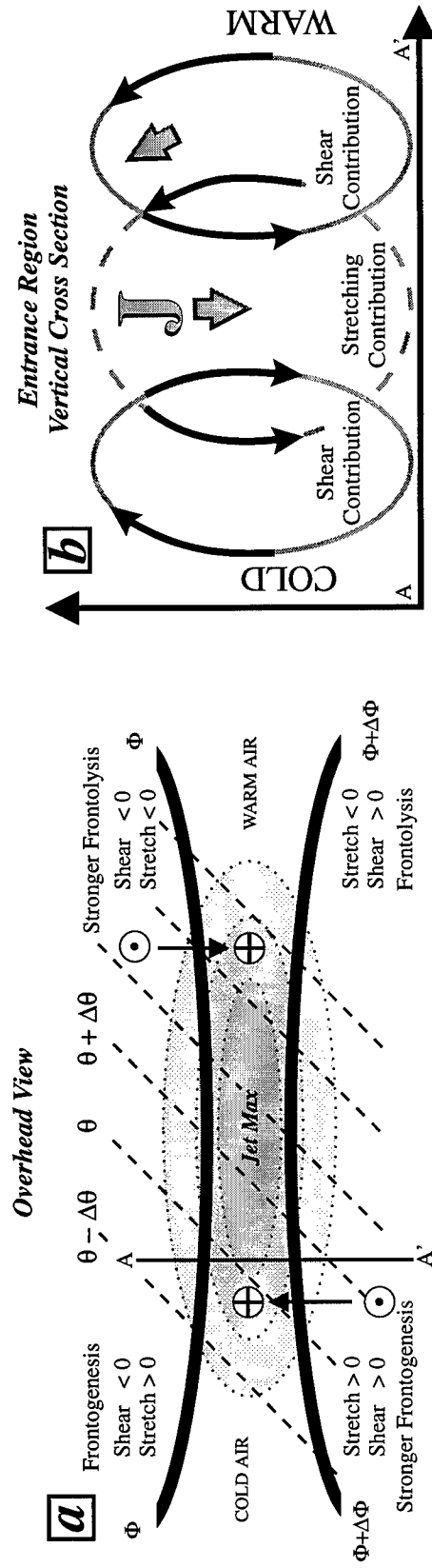


Figure 1.3. (a) Depiction of an upper-level jet streak in which cold advection modifies the ageostrophic motion. Sawyer-Eliassen equation evaluation of geostrophic deformation contributions are depicted along with the relative magnitude. Positive geostrophic forcing related to frontogenesis. Shear deformation dominates when the angle between the wind field and the thermal field is greater than 45° . Heavy solid lines depict geopotential height field, dotted lines depict isotherms, shaded region depicts isotach, and arrows depict ageostrophic flow. (b) Cross section through entrance region of jet streak. Ellipses and depicted arrows give general sense of ageostrophic flow generated in response to geostrophic deformation fields. Jet axis depicted by "J". Strongest decent is found along the jet axis and upward vertical motion shifted southward of the axis.

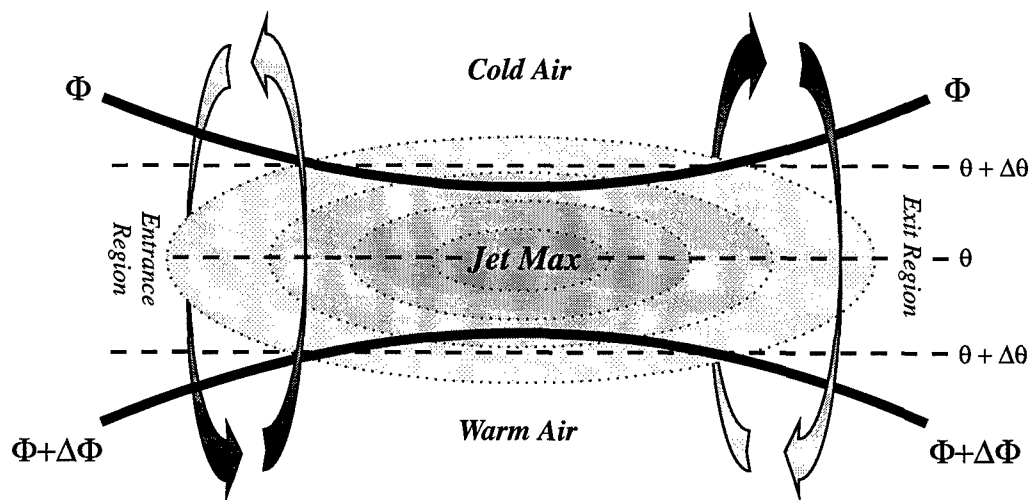


Figure 1.4. Idealized upper-level jet streak and associated ageostrophic flow. Dashed lines are isotherms, thick solid lines are geopotential height field, and dotted/shaded region are isotachs. Arrows depict ageostrophic circulation (Adapted from Shapiro, 1983).

to maintain a balance between the mass and momentum fields and are fully consistent with quasi-geostrophic dynamics.

The momentum field of the jet streak generally moves slower than the air parcels themselves. Consequently, the flow in the forward portion of the jet streak is typically characterized as supergeostrophic. For an idealized straight jet streak model, air parcels with high momentum exiting the jet streak experience an environment supportive of a weaker wind field. In order to regain a balance between the mass and momentum field, air parcels must decelerate so they tend towards the right of the flow, reducing the parcels kinetic energy. This tendency results in the development of a divergent field in the left front quadrant of the jet streak. As the flow veers to the right, low-level convergence and upward vertical motion result in adiabatic cooling of the atmospheric column within the left exit region. Meanwhile, net mass flux convergence and descent are found on the right front quadrant of the jet resulting in an adiabatic warming of the column. The resulting thermally-indirect circulation acts to increase the horizontal temperature gradient reestablishing the balance between the mass and momentum fields.

The introduction of a perturbation upon the flow can act to disrupt the balance between the mass and momentum fields. According to classical adjustment theory, the critical parameter controlling the geostrophic adjustment process is related to the Rossby radius of deformation (L_R) which is defined as

$$L_R = NH / f_0 \quad (3)$$

where 'N' is the Brunt-Väisälä frequency, H is the vertical length scale of the perturbation, and f_0 is the Coriolis parameter (Rossby 1938, Blumen 1972, Gill 1982). This defines the

distance within which ageostrophic adjustments dominate in regaining a balance between the mass and momentum fields. For scales smaller than L_R , the mass field adjusts to the wind field while for scales larger than L_R , the winds adjust to the mass field. For typical atmospheric conditions in midlatitudes $L_R \approx 1000$ km, where $f_0 = 10^{-4} \text{ s}^{-1}$, $N = .01 \text{ s}^{-1}$ and $H = 10$ km. In response to mass perturbations that lie within L_R , the ageostrophic adjustment process dominates in regaining thermal wind balance.

The thermal wind relates the vertical shear of the geostrophic wind to the horizontal temperature gradient (Holton 1979). For a given thermal gradient directed towards the south, the associated pressure surface slope producing vertical wind shear. If the thermal gradient is impulsively increased by some mechanism, i.e. terrain, convection, or deformation, a rapid change in the slope of the pressure surfaces develops. This in turn results in an imbalance between the mass and momentum field resulting in an adjustment process. Aloft, the increased pressure gradient force is directed towards the north. In turn, a northerly directed cross stream flow is generated resulting in divergence, ascent and adiabatic cooling to the right of the westerly flow while convergence and descent generate a warming to the left (Bluestein 1993). This response decreases the temperature gradient as a return to balance is achieved.

The orographic disruption of flow often results in the formation of mass perturbations downwind of the barrier which initiate complex secondary circulations that are contrary to those expected about a straight-line jet streak. Such mass perturbations are manifested through areas of localized heating that develop in response to prolonged downslope adiabatic warming, convectively induced diabatic heating, and even through

localized sensible heating in the boundary layer. The generation of such circulations have been documented to influence a wide range of weather phenomena downstream of major mountain ranges. Kaplan and Karyampudi (1992a, b) point out that the introduction of diabatic heat sources along the flow will accelerate air parcels making quasi- and semi-geostrophic approximations inappropriate. This acceleration causes the divergent wind field rather than the rotational part of the wind to dominate in adjusting to the heat source. The accelerating flow is dominated by isallobaric accelerations rather than by the Coriolis force alone. Such conditions alter the structure of the jet streak through mass and momentum adjustments dominated by ageostrophic rather than geostrophic flow.

Efforts by Mattocks and Bleck (1986) related the dynamics associated with flow blockage to rapid cyclogenesis in the lee of the Alps. On the windward side, the lower tropospheric cold air is retarded by the mountains while descending air warms on the leeward side. Thus a warm/cold dipole generates across the barrier. As the propagating jet streak advances across the mountains, a strong thermally-direct circulation develops within the exit region. The vertical motion is increased as the atmosphere attempts to cool the atmospheric column to compensate for the lack of cold air that is typically found in the lower troposphere. This results in a secondary circulation associated with an approaching jet streak that is quite different from the thermally-indirect circulation discussed by Uccellini and Johnson (1979). Such conditions can result in a prolonged period of rapid cyclone spin-up in the lee of a significant mountain barrier.

The terrain impact has also been identified to influence the formation of along-stream frontogenesis (Kaplan and Karyampudi 1992a, b). This process is in response to

terrain imposed adiabatic heating which results in a non-linear interaction between the along-stream acceleration and the along-stream pressure gradient force resulting in mesoscale along-stream frontogenesis.

Downstream of Australia's Great Dividing Range, evidence of unbalanced flow has been cited as a contributing factor in rapid cyclogenesis off the northern coast of New South Wales (Feren 1995). The development of a distinctive banded 'delta shaped' cloud element provides a signature of the associated mass flux divergence and cooling associated with the accelerating jet exit region. In response to the enhanced vertical motion and evacuation of mass, substantial surface pressure falls are observed.

Efforts by Kaplan *et al.* (1996) have identified a multi-stage process of geostrophic adjustments in response to terrain/flow interaction that result in the generation of inertia-gravity waves. Their numerical model simulations show that a thermally-indirect circulation associated with the background jet resulted in the generation of a secondary jet streak. This jet streak became superimposed upon a region in which the mountains generated an elevated area of warm-dry air. The developing secondary circulation of the new jet streak tilted the vertical gradient of potential temperature into the horizontal resulting in a downstream shift in the mass field. This resulted in an unbalanced formation of a third jet streak as air parcels accelerated within the exit region of the original jet. A low-level jet developed in response to the mass perturbation established by ascent and cooling associated with the accelerating jet exit region. Finally, this enhanced the development of hydrostatic mountain waves that were of similar wavelength to the gravity wave activity observed (Koch and Dorian 1988).

These investigations of the problem of mass and momentum adjustments, have focused on the generation of terrain induced warming as the perturbation source that eventually leads to the development of complex secondary circulations downwind of the barrier. Similarly, the confinement of an intense wedge of cold lower tropospheric air along a mountain barrier can similarly act to disrupt the mutual balance between these fields resulting in a geostrophic adjustment. During the winter months, cold continental air masses are redirected or blocked by large topographical barriers. In response, a build up of mass is typically observed in the lee of the mountains. In time, an equatorward transport of cold-dry air, termed a 'cold surge' (Williams 1981), is observed. These cold surges are routinely observed along the Andes, Tibetan plateau, and the Front Range of the Rockies (Chang *et al.* 1983, Fortune and Kousky 1983, Mecikalski and Tilley 1992). The dynamical process controlling the development of this feature is not uniformly accepted across the meteorological community. The characteristics of such cold surges have been related to edge wave theory in which the structure and propagation are governed by the slope of the terrain and rotational effects (Tilley 1990). Colle and Mass (1995) have studied cold surges east of the Rockies and concluded that these features are not the result of rotational trapped waves but rather due to the interaction of the large scale flow with the mountains and the sloping terrain of the Great Plains.

Despite the questions of the physical processes governing development, there is no question that these features bring about rapid changes in the environment. Cold surges have been observed to extend over 4500 km in the terrain-parallel direction while limited to ~1500 km normal to the terrain (Orlanski 1975). These surges often are accompanied

by a 24-hour temperature drop of 20°-30° C, pressure increase of 15-30 mb, and surface winds gusting in excess of 20 ms⁻¹ (Bluestein 1993).

1.2 Overview

The motivation for this research is to investigate the dynamics associated with the development of a cold front aloft (CFA) and midtropospheric jet streak in relation to terrain-induced secondary circulations. The development of these features play a prominent role in the initiation and severity of convection effecting weather conditions nearly 2000 km downstream of the barrier. Unlike the view taken by Hobbs *et al.* (1996), the development is not considered simply the result of a quasi-geostrophic process of cold air advecting out of the inner-mountain region. Rather, the development is attributed to terrain enhanced adiabatic and diabatic processes that induce perturbations in the mass field. These perturbations bring about an imbalance between the mass and momentum fields which lead to an acceleration in the jet exit region. In order to restore thermal wind balance, a thermally-direct circulation develops in the exit region to convert the potential energy of the horizontal temperature gradients directly into kinetic energy of the horizontal wind. In time, a balance is regained as the vertical momentum flux penetrates lower levels of the atmosphere increasing the vertical shear. The accelerating flow results in enhanced divergence, upward vertical motion, and cooling of the atmosphere. In response, the formation of the CFA and a bifurcation of the jet stream develop.

The STORM-Fronts Experiment System Test (STORM-FEST) field program conducted over the midwest U.S. during February/March 1992 provided a unique opportunity to investigate the complex interactions taking place over the region. This research supports a key component of the STORM-FEST program by providing a *“sharply focused investigation of the structures and evolution of fronts and associated mesoscale phenomena in the central United States, with emphasis on precipitation and severe weather”* (STORM-FEST Operations Summary 1993). During intensive operating period-17 (IOP-17), 8-9 March 1992, the synoptic pattern consisted of an upper-level low situated over the desert southwest with a well-established southern branch of the polar jet cutting across northern Mexico. The STORM-FEST Operations Summary described the weather scenario on 8 March as one in which: *“A 100 kt jet moving around the cutoff low was expected to move over southeast Texas, putting the Texas/Oklahoma Panhandle region under the left exit region of the jet ... severe thunderstorms and tornadoes were possible.”* Indeed, during the 24-hour period beginning 1200 UTC 8 March 1992, the Great Plains experienced a wide variety of severe weather conditions (Table 1.0). Portions of the northern Plains were brought to a standstill as blizzard conditions raged across the region. Heavy thunder snowstorms pounded the region from northeastern Colorado into Nebraska with winds in excess of 30 ms^{-1} and 2 foot snowfalls. In contrast, warm temperatures and widespread severe weather was encountered over the southern Plains. Numerous hail-producing thunderstorms, up to 4.5” diameter hail in Carter county in Oklahoma, were reported along with several weak tornadoes. Though the Operations Summary correctly anticipated the severe weather, the commencement of the outbreak

occurred in relation to the right exit region of the jet streak rather than the anticipated left exit region. This scenario is indicative of the unbalanced state of the propagating jet streak, i.e., the normally (semi-geostrophic) decelerating exit region was accelerating as described by Koch and Dorian (1988). The varied weather conditions experienced, though not uncommon to the region, provides some of the most diverse weather conditions observed as a result of the unique geography and its impact on a propagating jet streak.

Table 1.0 Significant Weather Events of 8-9 March 1992

Date / Time	Location	Weather Event
08/1300 UTC →	Nebraska	Heavy Snows (14") & Gust 31 ms ⁻¹
08/2200 UTC →	West & Southern Ok.	Numerous Hail Reports
08/2301 UTC	Washington Cnty, Co.	2 Tornadoes (F-0)
08/2345 UTC	Custer Cnty, Ok.	1.75" Hail & Tornado (F-0)
09/0020 UTC	Archer Cnty, Tx.	3" Hail & 23 ms ⁻¹ Wind Gust
09/0100 UTC →	Colorado	Blizzard Conditions
09/0120 UTC	Woods Cnty, Co.	1.75" Hail
09/0308 UTC	Kiowa Cnty, Ks.	Tornado (F-1)
09/0315 UTC	Sumner Cnty, Ks.	1.75" Hail
09/0403 UTC	Carter Cnty, Ok.	4.5" Hail & Tornado (F-0)
09/0440 UTC	Butler Cnty, Ks.	Tornado (F-0)

During the course of IOP-17, the terrain interaction with the flow generates two distinct sub-Rossby radius of deformation mass perturbations downwind of the mountains. The development is observed in association with a concentrated region of leeside warming to the south and an intense narrow surge of cold air along the lee of the northern Rockies. In response, two distinct episodes of geostrophic adjustments develop within a sub-inertial time-scale of ~6 hours as the divergent part of the wind responds to the mesoscale perturbation imposed upon the flow. The interaction between the terrain-induced mass perturbations and the atmospheric adjustments provide a key mechanism in CFA and jet

streak formation downstream of the mountains. The formation of these features are remarkable in that the forcing is not dominated by the upper-level synoptic scale dynamics. Rather, lower tropospheric processes act to control the observed geostrophic adjustment processes. This results in increased ageostrophic motion leading to frontogenesis and jet streak formation. It is these adjustments which will be analyzed in an indepth manner.

In order to fully exploit all available STORM-FEST observational data sources a technique of extracting the mass field from the wind field is employed. This technique makes use of the combined data sets of wind observations from the enhanced rawinsonde network and NOAA 403-MHz profilers sites. Consequently, a mesoscale network of data is available to detail the development of the CFA. Section 2 provides a complete description of this technique along with observational comparisons between the retrieved height field and those observed. Sections 3 and 4 will document, with the aid of observed STORM-FEST observations and mesoscale modeling studies, key dynamical processes involving two distinct episodes of geostrophic adjustment which were observed to alter the polar jet stream producing a midtropospheric jet streak and generation of cold pool leading to CFA formation. Section 3 will highlight the impact on the jet stream of a mass perturbation generated in response to a localized region of leeside warming induced by downslope adiabatic warming and intense boundary layer sensible heating. Section 4 will focus on the impact on the jet stream of a mass perturbation generated in response to an advancing cold surge along the lee slope of the northern Rockies. Finally, section 5 will summarize the findings from the analysis of the 8-9 March 1992 STORM-FEST data sets in relation to the development of the midtropospheric jet streak and cold front aloft.

2. DATA AND ANALYSIS METHODOLOGY

2.1 Overview

The temporal resolution of wind profiles from the NOAA Profiler network can document mesoscale structures of weather systems affecting the network. Conventional observations of the height and temperature structure of the atmosphere at a comparable temporal resolution are currently unavailable. However, by making use of the full divergence equation, the mesoscale height field can be extracted from the observed wind field. Mass changes associated with irrotational ageostrophic motions are retained for a nearly complete description of the height field. Once the height field is determined, the temperature field can be derived by assuming hydrostatic balance and applying the hypsometric equation. In this section we refine previous applications of this divergence method by adapting it to a large (synoptic) domain containing asynoptic rawinsonde observations taken during the STORM-Fronts Experiment System Test (STORM-FEST). This allows direct comparison between the retrieved height and temperature fields with in situ rawinsonde observations.

The application of the divergence method to the combined wind data from profiler and rawinsonde sites provides a retrieved fields capable of resolving mesoscale features not fully captured by the rawinsonde data alone. The results also show excellent agreement between the retrieved heights and temperatures and the observed values at rawinsonde sites. Standard deviations of the difference between the retrieved and observed

data lie well within the precision of the rawinsonde instruments. The divergence method was also applied to hourly profiler data at asynoptic times. The results indicate that valuable information on the evolution of atmospheric height and temperature fields can be retrieved between conventional rawinsonde release times. The implications of these results for application in case study analysis and for data assimilation in numerical weather prediction are discussed.

2.2. Introduction

The modernization of the National Weather Service (NWS) and subsequent routine availability of data from a number of new atmospheric observation systems (WSR-88D Doppler radar, Automated Surface Observation System, and GOES-8 and 9 satellite imagery), has significantly increased our ability to identify the structure and dynamics of mesoscale features that underlie observed weather conditions. The installation of the NOAA Profiler Network over the central plains provides meteorologists the opportunity to detect physical signatures down to the meso-alpha and meso-beta scale. Six-minute samples and hourly consensus averaging of wind profiles constitute a valuable data set with which to identify and understand phenomena such as gravity waves, convective systems, frontal structure, and jet streak evolution.

Due to the prohibitive cost of asynoptic radiosonde releases, there remains a lack of observational data with which to resolve the temperature and mass fields needed for a complete thermodynamic description of mesoscale systems. To circumvent this deficiency,

the mass and thermal structure for a region of the atmosphere can be retrieved through knowledge of the wind field and application of the divergence equation (Fankhauser 1974; Kuo and Anthes 1985; Kuo *et al.* 1987a, b; Modica and Warner 1987; and Cram *et al.* 1991).

Inspection of the full divergence equation reveals that it is made up of terms composed of the horizontal components of the wind and a Laplacian of the geopotential height field. An approximate solution to the Laplacian term can be obtained by employing the Liebmann over-relaxation method (Haltiner and Williams 1980), allowing the mass structure to be obtained from knowledge of the momentum field. The thermal structure is then derived making use of hydrostatic approximation. An advantage of this *divergence method* is that it uses the total wind field comprising its rotational and irrotational components. Limiting assumptions concerning a balance between the mass and momentum fields through either semi- or quasi-geostrophic assumptions are not necessary since the total derivative of the divergence field is retained. Consequently, mass changes induced by ageostrophic motions are preserved in the retrieved mass field.

Past researchers have derived the height field from the wind field using select terms of the divergence equation in concert with either model-generated wind profiles or a limited mesoscale network of rawinsondes. A number of studies have made use of model-generated fields to verify their results. Making use of limited rawinsonde observations and no profiler data, Fankhauser (1974) employed the full divergence equation to generate a mass field. Bleck *et al.* (1984) were the first to examine the potential for using wind profiler data to retrieve the height and temperature field, but they chose to use the

nonlinear balance equation since their interest was in large-scale phenomena. Kuo and Anthes (1985) and Modica and Warner (1987) applied various forms of the divergence equation to determine model sensitivity in retrieving the mass structure (Observing System Simulation Experiment). Both studies used model-generated wind profiles in constructing the mass field and verified the extracted mass field against the model. Their efforts showed errors were reduced when the divergence and vertical motion terms were included with the balance equation to form the complete divergence equation. Using model generated data sets, Kuo *et al.* (1987 a, b) applied the full divergence equation in a terrain-following σ -coordinate system. The retrieval procedure gave similar results whether using σ or p as the vertical coordinate, but the results were quite sensitive to applied boundary conditions. The use of Dirichlet boundary conditions provided the least error in the retrieved fields.

Cram *et al.* (1991) were the first to apply the divergence method to wind profiler observations from a small mesoscale network of profilers located in northeast Colorado. The resulting height field was able to resolve a terrain-induced meso-scale trough that had gone undetected by the standard synoptic network. However, direct verification of the accuracy of the generated fields was not possible, and model output and other data sources were used to infer the accuracy of the results. Karyampudi *et al.* (1995) extended the work of Cram *et al.* (1991) in computing various kinematic diagnostics to identify a variety of mesoscale features. The fields were generated using the same approach employed by the latter authors except the vertical motion fields were derived kinematically using an O'Brien (1970) adjustment scheme. The derived fields were then verified against

the linear vector point function method of Zamora *et al.* (1987). Their efforts were successful in identifying the signature of a mountain wave, unbalanced upper-level alongstream frontogenesis, and a mesoscale tropopause fold coupled to the developing frontogenesis at mid levels.

This paper is the first in a series of papers that will investigate the physical/dynamical mechanisms important in the generation and propagation of a cold front aloft (Hobbs *et al.* 1990) and jet streak, and their implications for severe weather downstream of the Rocky Mountains. The divergence method is applied over the central Plains IOP-17 of STORM-FEST for the period 8-9 March 1992. The STORM-FEST project was conducted in an effort to increase knowledge of the structure and evolution of fronts and precipitation in response to mesoscale processes associated with winter storms over the central United States. The field phase of the project was conducted over a ~40 day period during the months of February and March 1992 and detailed information was collected by operational and research observation systems deployed over the central plains during this time. The availability of asynoptic rawinsonde observations from a mesoscale network provides a special opportunity to make direct comparisons between the mass and temperature fields sampled by the rawinsondes with those derived from profiler observations.

2.3 Data and Methodology

The NOAA 403-MHz profilers installed over the central plains consist of a ground-based Doppler radar with a three beam antenna field (Strauch *et al.* 1987). The geometry of the system consists of a vertically oriented antenna and two other antennas directed in the north-south and east-west plane, respectively, and offset from the zenith by an angle of 16.3° , thus providing *in situ* measurements of the u , v , and w components of the momentum field. The vertical beam detects the vertical motion field in the absence of precipitation, while the north and east pointing beams measure off-zenith radial velocities. Based upon Doppler principles, each antenna successively emits a pulse and then detects the reflected energy returned to the sensor. This process allows the system to retrieve a sample every six minutes. These samples are averaged over an hour period to provide a consensus averaged wind observation.

Despite differences in measurement techniques, an extended comparison between profiler and rawinsonde winds show a standard deviation of 2.5 ms^{-1} (Weber and Wuertz 1990). More detailed analyses have shown the horizontal wind components over all levels to be within $\pm 1 \text{ ms}^{-1}$ (May and Strauch 1989, Strauch *et al.* 1987). Depending on the availability of atmospheric scatterers and weather conditions, the profilers have the ability to sample the atmosphere from 0.5 to 16 km at a vertical resolution of 250 m (below 9 km) and 1 km (at higher levels).

The mass and thermal structure of the atmosphere can be extracted from hourly profiler data through application of the full divergence equation. The divergence equation in pressure coordinates can be written as follows:

$$\frac{d(D)}{dt} = (D)^2 - \nabla \omega \bullet \frac{\partial V}{\partial P} + f\zeta + 2J(u, v) - \nabla^2 \phi - \beta u + \gamma v + \frac{\partial F_u}{\partial x} + \frac{\partial F_v}{\partial y} \quad (4)$$

$\begin{matrix} 1 & 2 & 3 & 4 & 5 & 6 & 7 & 8 & 9 & 10 \end{matrix}$

where D is the horizontal two dimensional velocity divergence, u , v , and ω are the components of the total wind, f is the Coriolis parameter, γ and β are the longitudinal and meridional variation respectively of f , ζ is the relative vorticity, J is the Jacobian operator ($\partial u / \partial x \bullet \partial v / \partial y - \partial u / \partial y \bullet \partial v / \partial x$), ϕ is the geopotential height, and F represents the frictional contribution. Kuo and Anthes (1985) demonstrated that deriving the mass field from the “balance equation”, which neglects the divergence and vertical motion terms in Eq. 4, provides inferior results when compared to that of the full divergence equation, since the total rate of change of the divergence field and vertical motion distribution are not considered in the reconstruction of the mass field. In the full divergence equation, if frictional effects are considered to be minimal above the boundary layer, Eq. 4 is reduced to the horizontal components of the wind and the Laplacian of the geopotential height field. By obtaining the horizontal winds on a pressure surface, the geopotential height field can be generated through use of the Liebmann over-relaxation method (Haltiner and Williams 1980).

Two applications of the divergence method were undertaken in this study: (i) The 3-hourly STORM-FEST rawinsonde wind observations and supplemental CLASS winds are used in combination with the profiler wind data to retrieve the mass and thermal fields for application in case-study analyses. (ii) The heights derived only from profiler winds are compared with rawinsonde observations in a test of the potential of the divergence method to provide supplemental data from the profiler network on a routine basis.

In order to accommodate the distribution of the combined rawinsonde/profiler sites (mean spacing of 128 km) and the rawinsonde sites alone (mean spacing of 210 km), a grid spacing of 85 km was selected (Fig. 2.1). This grid spacing preserves the minimal resolvable waves without contaminating the field with noisy derivatives generated as a result of an inappropriate grid size. In the vertical, the objective analysis was constructed at nine levels (850, 800, 700, 600, 500, 400, 300, 200, and 100 mb).

The divergence method used to generate the mass field in this research is based on efforts by Cram *et al.* (1991) and Karyampudi *et al.* (1995). Their approach was modified in several ways: (i) the data domain was expanded to include new data sites, including 3-hourly rawinsonde observations from the STORM-FEST domain, (ii) interpolation of observed data to grid points was improved by adding a bilinear interpolation scheme, and (iii) a means of accounting for profiler elevation variability was supplied. The individual terms of the divergence equation were separated in a fashion similar to that presented by Kuo and Anthes (1985).

A two-pass objective analysis scheme (Barnes 1964) was employed to obtain a gridded wind field from the combined data sets of soundings and profilers. A gridded

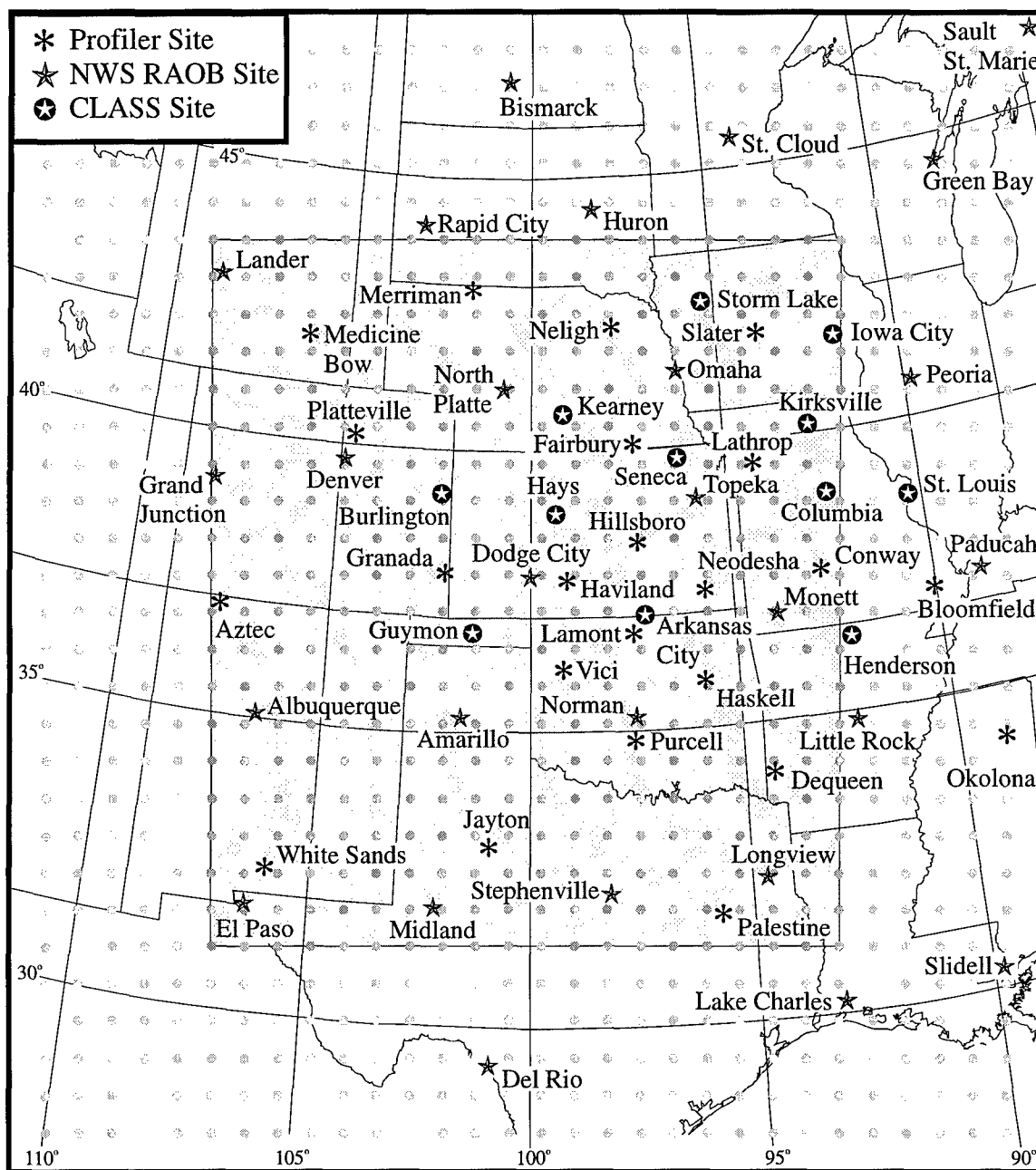


Figure 2.1. Domain of STORM-FEST upper air observations used in objective analysis scheme. Data set includes 23 profiler sites (asterisks), 26 NWS rawinsonde sites (stars), and 12 NCAR CLASS sites (circled stars). Objective analysis scheme is based upon a grid spacing of 85 km. Shaded region depicts primary 20x20 data grid domain. The outer 30x30 grid depicts data used to assist in the analysis along the boundary.

analysis of the mass field for two time periods is required to derive this field, which is then used to correctly convert the altitude of the profiler winds to the corresponding pressure level. Rawinsonde mass fields that correspond in time and space to the observed profiler data are then generated by applying linear time-interpolation. Operationally, twelve-hourly synoptic rawinsonde observations must be used for this purpose. However, the temporal resolution was greatly increased with the release of three-hourly balloons during the STORM-FEST field project. The increased temporal resolution of the mass field reduces errors that result from the longer interpolation time associated with standard synoptic sounding releases. This provides superior Dirichlet boundary conditions used in obtaining a solution to the Laplacian term of the divergence equation (Kuo *et al.* 1987a). The more accurate height field also minimizes potential errors in matching observed profiler winds to their appropriate pressure level.

A bilinear interpolation from the four surrounding grid point height values for a specific pressure level provided a consistent height estimate at the profiler sites. Wind profilers provide winds at 250-m increments. Consequently, a vertical linear interpolation of the wind data was performed to extract the appropriate horizontal wind components for the given pressure level. The combined set of profiler and rawinsonde observed winds was then objectively analyzed at each pressure level.

The first step in retrieving the mass field from the full divergence equation was to generate fields of two-dimensional horizontal divergence and kinematic vertical motion from the horizontal wind field for a given pressure level. The horizontal divergence calculations were determined through second-order centered finite difference calculations.

This simplifies the computation of the divergence field, but is susceptible to error. Care was taken to ensure that the wind profile did not contain erroneous wind speeds or directions. Normally precipitation will have a large effect only on the vertical beam measurements, due to Rayleigh scattering effects, since the profiler is measuring fall speeds rather than air velocity. However, when precipitation is highly inhomogeneous as in convective rain events, then the horizontal winds can become unreliable (Ralph *et al.* 1995).

The kinematic vertical motion field was determined by vertically integrating the horizontal divergence, under the assumption that the vertical motion of the lowest layer is zero. An O'Brien (1970) adjustment technique was employed to minimize the accumulation of errors as divergence is vertically integrated to the top of the domain at the 100 mb level. Although profiles provide direct measurements of vertical hydrometer velocities, these data were not used due to problems of sampling, variability, and representativeness.

The individual terms of the divergence equation were separated in a similar fashion as presented by Kuo and Anthes (1985). The frictional terms were ignored under the assumption that such effects are minimal in the free atmosphere. This assumption could have its greatest impact in the lowest levels as divergence calculations are not influenced by the momentum fluxes experienced in the convective boundary layer (Karyampudi *et al.* 1995). Equation 4 can then be expressed

$$\begin{aligned}
-m^2 \nabla^2 \phi = & \frac{\partial D'}{\partial t} + m^2 \left(u \frac{\partial D}{\partial x} + v \frac{\partial D}{\partial y} \right) + m^2 (D)^2 + 2m^2 \left(\frac{\partial v}{\partial x} \frac{\partial u}{\partial y} - \frac{\partial u}{\partial x} \frac{\partial v}{\partial y} \right) \\
& + \omega \frac{\partial D'}{\partial P} + m \left(\frac{\partial \omega}{\partial x} \frac{\partial u}{\partial P} + \frac{\partial \omega}{\partial y} \frac{\partial v}{\partial P} \right) - m\gamma v + m\beta u - f\zeta \equiv F
\end{aligned} \tag{5}$$

where 'm' is the map factor, and $D' = m^2 \nabla \cdot \mathbf{V}/m$.

The sum of the forcing terms is denoted by F. The forcing function on the right hand side of Eq. 5 can be expressed in terms of the three components of the wind field. The individual terms of the forcing function can be evaluated from the analyzed wind field based on the rawinsonde and profiler data. Then, by employing the Liebmann over-relaxation method, an approximate numerical solution to the Laplacian function can be obtained subject to known boundary conditions, yielding the geopotential height field. The rawinsonde-generated height fields are used as the first guess and provide the necessary Dirichlet boundary conditions for the grid, while the calculated forcing function values make up the interior portion of the domain. Each interior grid point is evaluated through the relation,

$$(\Phi_1 + \Phi_2 + \Phi_3 + \Phi_4 - 4\Phi_0) - F = \hat{R} \tag{6}$$

where \hat{R} is the residual. At a particular grid point, if the computed residual is less than a predetermined tolerance value, the grid value is retained, and the neighboring grid point is evaluated. When the residual is greater than the assigned tolerance value, the grid point

value is multiplied by a relaxation factor and assigned a new value before moving to the next grid point. On the subsequent sweep of the domain, the grid point is recalculated once all other grid point residuals have been evaluated. An appropriate relaxation factor lies between 0.25 and 0.5. A tolerance value of 1.0 m and a relaxation factor of 0.375 were used over the entire domain to control the number of iterations required to converge to a unique solution.

Once the height field is generated, the thermal structure is computed by assuming hydrostatic balance and making use of the hypsometric equation,

$$\phi(z_u) - \phi(z_l) = R \int_{P_u}^{P_l} T d \ln P = R \bar{T} \ln \frac{P_l}{P_u} \quad (7)$$

Here, \bar{T} is the mean temperature over the 500 m thick layer centered on the pressure surface of interest.

2.4. Results of the Divergence Method Using All Available Winds

The application of the divergence method using all available wind data in the STORM-FEST data set provides a compelling test of the overall robustness of the approach. Additionally, the increase in resolution of the retrieved fields afforded by the inclusion of the profiler data is of benefit in case study analysis and mesoscale numerical model simulations.

The 500-mb height fields (Fig. 2.2), derived using all available wind data, document the evolution of an approaching upper-level low over the Front Range of the Rocky Mountains. A developing trough over the inner-mountain region at 2100 UTC 8 March 1992 is captured (Fig. 2.2a), and a building ridge over the central plains is consistent with the anticyclonic flow over this region. By 0300 UTC 9 March 1992, the trough has deepened significantly over the New Mexico/Colorado border, where six-hour height falls exceed 60 m (Fig. 2.2b).

Within the broad pattern of low heights, subtle mesoscale structures are resolved. For example, the height field at 09/03 UTC shows a tendency for ridging over southwestern Oklahoma, with height falls of only 25-30 meters over the region. To the east an elongated trough extending from northwest Kansas to southeast Oklahoma is detected. This trough aligns well with a rainband that has propagated ahead of a developing low pressure system in the lee of the Rocky Mountains. This rainband is documented in Martin *et al.* (1995) as a pre-drytrough rainband. Figure 2.3 quantifies the mesoscale signals resolved through the addition of the profiler data. The developing low over the Front Range is much deeper than objectively analyzed with rawinsonde data alone. Moreover, the mesoscale ridge over southwestern Oklahoma and the eastern panhandle of Texas is more pronounced than in the rawinsonde analysis.

The extracted heights compare well with observed rawinsonde heights (Fig. 2.2). The differences between the retrieved and observed heights at the rawinsonde sites are well within the measurement errors associated with the sounding systems (± 24 m

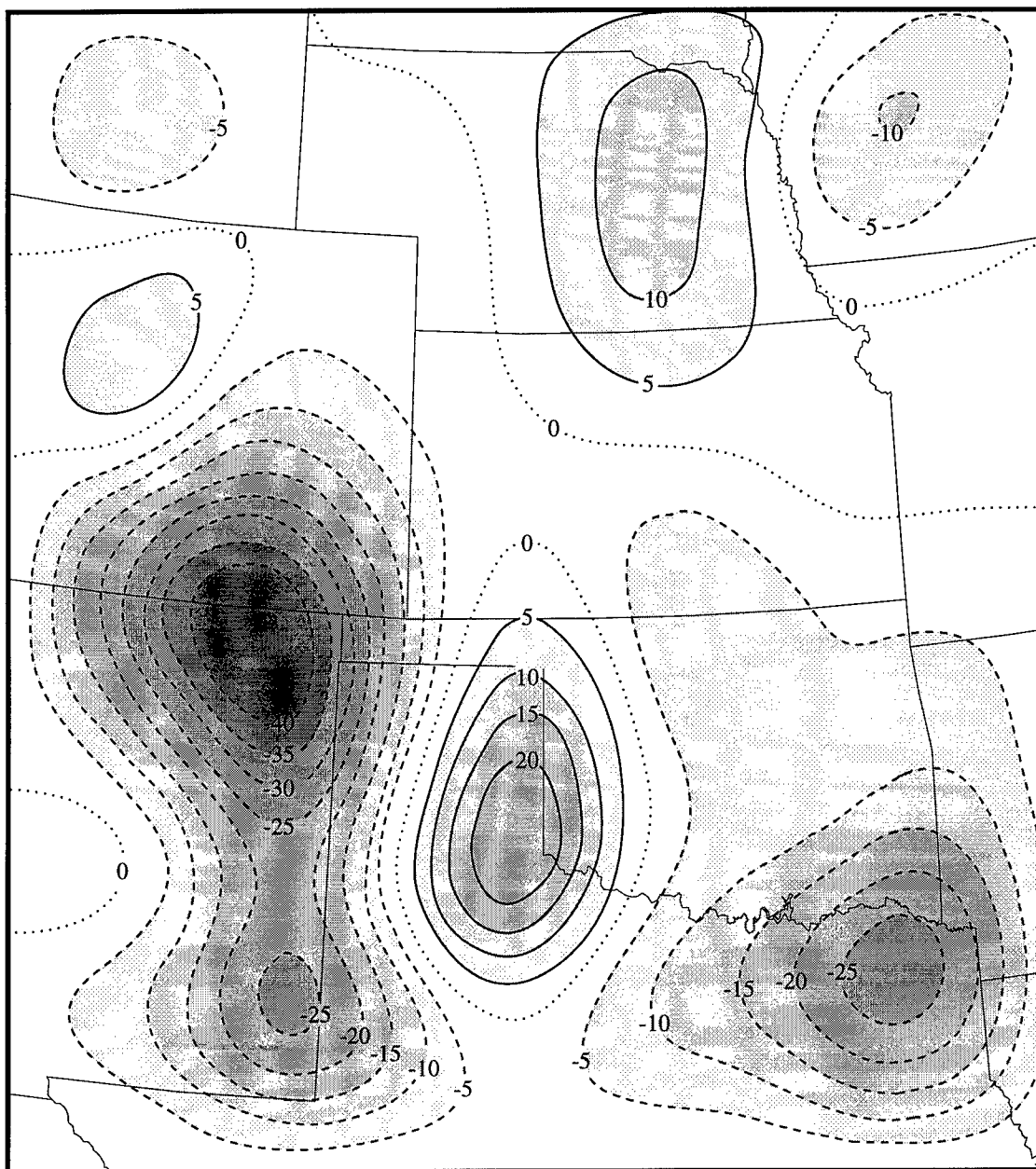


Figure 2.3. Difference between the retrieved height field and observed height filed at 500 mb level for 0300 UTC 9 March 1992. Negative values are indicated by dashed lines and positive values are indicated by solid lines. Successively greater differences between the fields are shaded accordingly.

according to Hoehne 1980). Examination of the distribution and standard deviation of the difference data provides a convenient way to survey the accuracy of the method (Fig. 2.4). At 2100 UTC the height differences have a standard deviation of 7 m, with the retrieved heights showing a slight bias towards lower values than those observed. At 0300 UTC, the standard deviation is 5 m.

Further analysis of the method's accuracy shows that the standard deviations of the height differences for 5 times and at 4 levels all fall within the accuracy of the rawinsonde observations (Table 2.0). The best results (smallest deviations) are seen at lower atmospheric levels and the deviations increase at higher levels, consistent with findings of previous studies using model-generated data sets. Kuo and Anthes (1985), using data from the Observing Systems Simulation Experiment (OSSE), conducted a number of experiments to test the usefulness of the retrieved fields. Using model-generated wind profiles on a regularly spaced 50-km horizontal grid and model-generated boundary conditions resulted in a 4-m root-mean-square (RMS) height error. However, this error increased to over 18 m when a random 1 ms^{-1} error in the wind field was introduced and boundary conditions were exposed to height errors typical of a 12-hour model forecast.

Table 2.0 Standard Deviation (σ) of the difference between the retrieved height (m)/temperature ($^{\circ}\text{C}$) field and the observed height/temperature field from rawinsondes over a twelve-hour period centered at 0000 UTC 9 March 1992.

<i>Time/Level</i>	<i>1800 UTC</i>	<i>2100 UTC</i>	<i>0000 UTC</i>	<i>0300 UTC</i>	<i>0600 UTC</i>	<i>Mean σ</i>
<i>700 mb</i>	7m/1.5 $^{\circ}$	5m/1.3 $^{\circ}$	7m/1.3 $^{\circ}$	13m/1.9 $^{\circ}$	14m/1.5 $^{\circ}$	9m/1.5 $^{\circ}$
<i>500 mb</i>	8m/1.2 $^{\circ}$	7m/0.9 $^{\circ}$	10m/1.1 $^{\circ}$	5m/1.4 $^{\circ}$	10m/1.2 $^{\circ}$	8m/1.1 $^{\circ}$
<i>400 mb</i>	9m/1.0 $^{\circ}$	13m/1.3 $^{\circ}$	10m/1.1 $^{\circ}$	7m/1.3 $^{\circ}$	11m/1.2 $^{\circ}$	10m/1.2 $^{\circ}$
<i>300 mb</i>	13m/1.9 $^{\circ}$	12m/2.3 $^{\circ}$	16m/2.4 $^{\circ}$	13m/1.9 $^{\circ}$	17m/1.5 $^{\circ}$	14m/2.0 $^{\circ}$

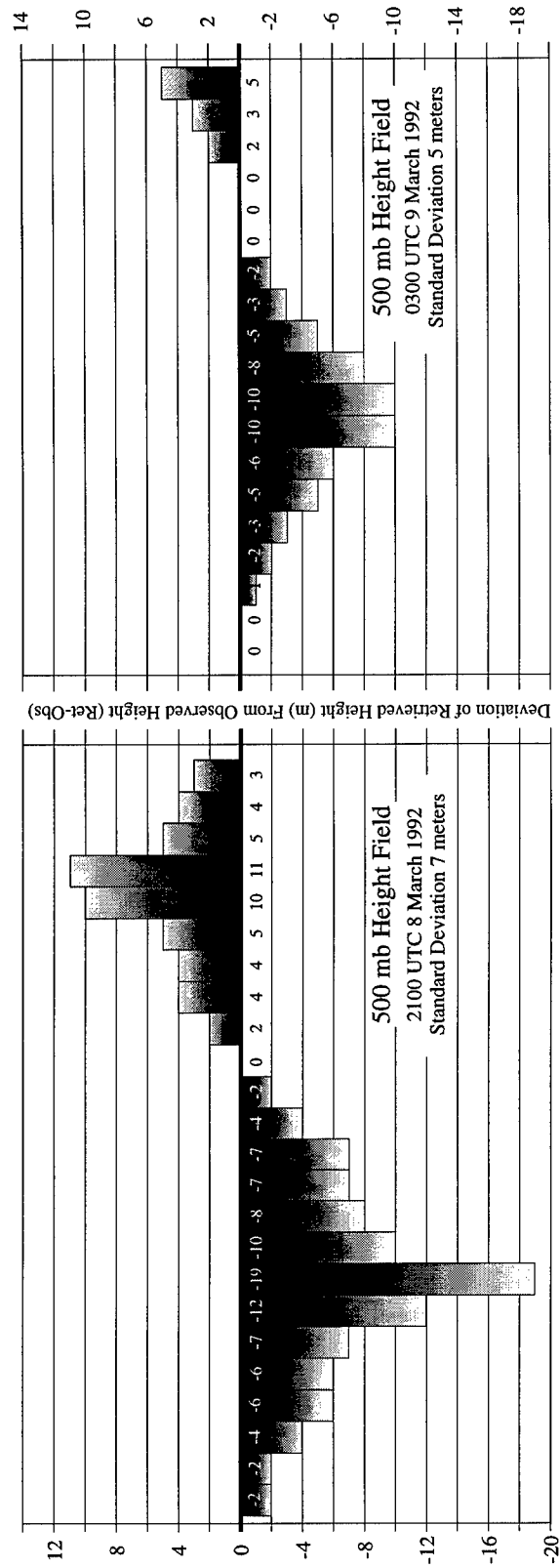


Figure 2.4. Distribution of the difference between the 500 mb retrieved and the observed heights. The left graph depicts the deviation for 2100 UTC 8 March 1992 and the right graph shows the deviation for 0300 UTC 9 March 1992. Each column represents the deviation from an individual site (Retrieved - Observed Sounding). The vertical axis is the deviation (m). The dashed line identifies one standard deviation.

Investigation of the corresponding temperature differences reveals similar results to those obtained for the height data (Table 2.0). The retrieved temperatures are within 1°-2° C of the observed values. This result compares well with the results by Kuo and Anthes (1985) who found RMS errors of 1.55° for model-generated fields subjected to random errors representative of observed conditions. The temperature deviations shown in Table 2.0 again indicate the errors increase with elevation. At the 200-mb level, the mean standard deviation for the 12-hour period is 2.9°. The decreased accuracy of the thermal structure at higher levels of the troposphere can be attributed to several factors: (i) the loss in representativeness of the upper-level rawinsonde observation as the balloon travels downwind, (ii) the smaller number of observations available at higher altitudes, and (iii) the influence of stratospheric intrusions on the thermal structure in relation to the vertical resolution of the retrieval process. These results are similar to findings by Kuo *et al.* (1987a) where RMS errors up to 8.75 degrees were obtained in the upper levels in a study using model generated profiles.

Figure 2.5 compares a retrieved thermal profile with the corresponding observed STORM-FEST CLASS sounding at Guymon, Oklahoma. Since the vertical resolution of the extracted temperature field is rather coarse (100-mb intervals above 800 mb), a reproduction of the detailed structure of the observed temperature profile should not be expected. This comparison was selected for the rapid changes occurring over this region during the time interval. Of particular interest is the signature of a cold front aloft, observed between 700 and 400 mb, whose evolution is correctly captured by the derived

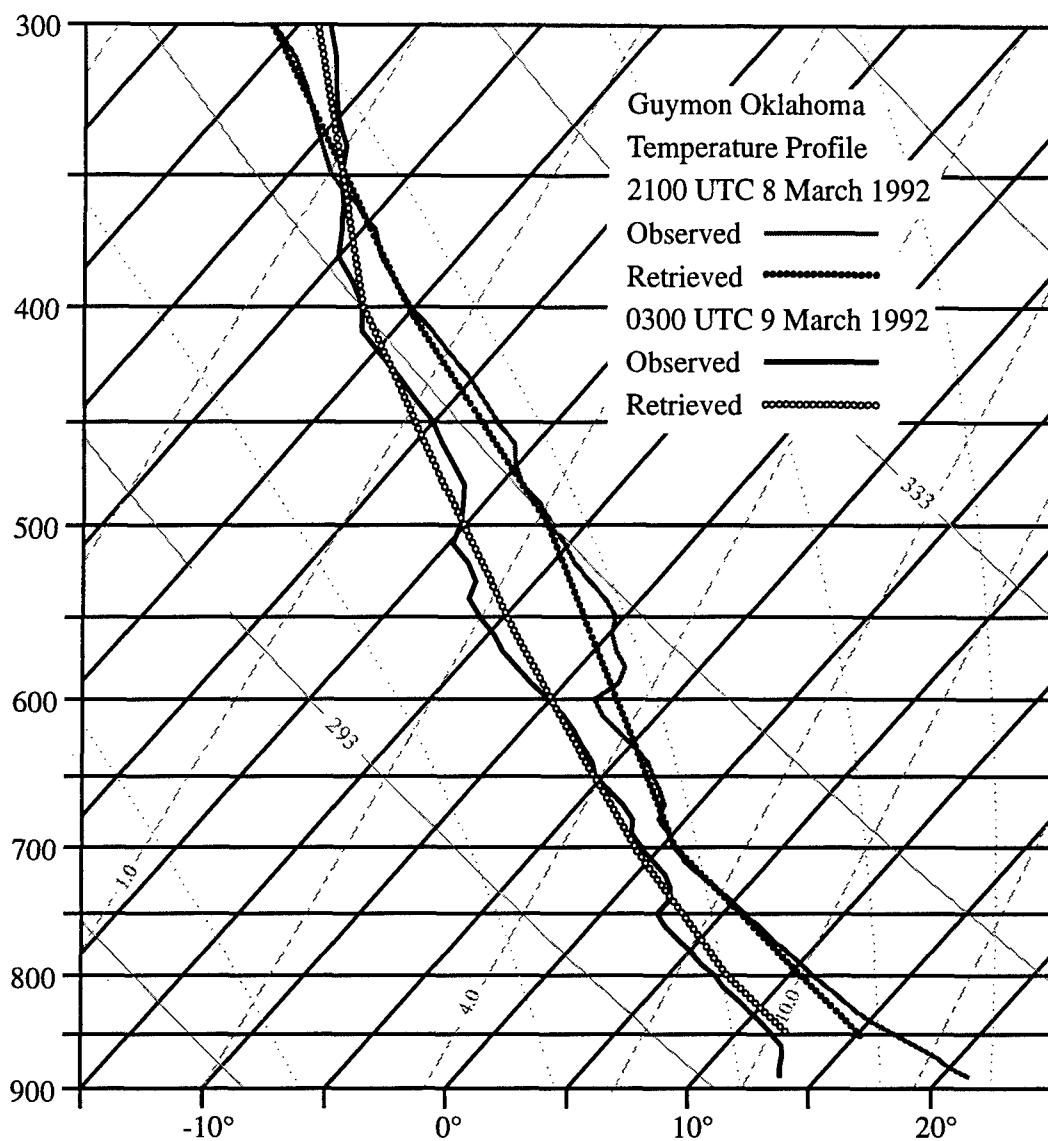


Figure 2.5. Skew-T plot of derived and observed temperature profiles for Guymon, Oklahoma. Temperature profile for 2100 UTC 8 March 1992 is depicted in gray and temperature profile for 0300 UTC 9 March 1992 is depicted in black. Solid lines represent the observed CLASS sounding temperature profile and the linked circles show the retrieved temperature profile. Isotherms - dark solid lines running from lower left to upper right, dry adiabats - light solid lines running from lower right to upper left, moist adiabats - light dotted lines running from lower right to upper left, mixing ratio - dashed lines running from lower left to upper right.

temperature profiles. The standard deviation between the derived and observed temperature profiles is 0.79°C at 2100 UTC and 0.42°C at 0300 UTC.

2.5. Results of the Divergence Method Solely Using Profiler Winds

Since the profiler network provides a robust source of wind data at hourly intervals, it is useful to investigate the potential of the divergence method to derive mass and thermal fields from the profiler network on a routine basis. As the standard for comparison, the height field constructed using all available wind data will be used.

Dirichlet boundary conditions used to invert the profiler wind data were obtained from the standard 12-hourly synoptic sounding data through linear interpolation in time. When the weather pattern is slowly changing, the height field extracted from the profiler winds is comparable to the standard height field generated using all wind data (Fig 2.6a). However, by 0300 UTC, the widely scattered profiler observations are unable to fully detect the strong divergence signal. Consequently, the heights in the vicinity of the upper-level low center are more than 20 meters too high when compared with those constructed using the full data set. In summary, the application of the divergence method to the profiler winds provides useful height information at times when rawinsonde observations are unavailable.

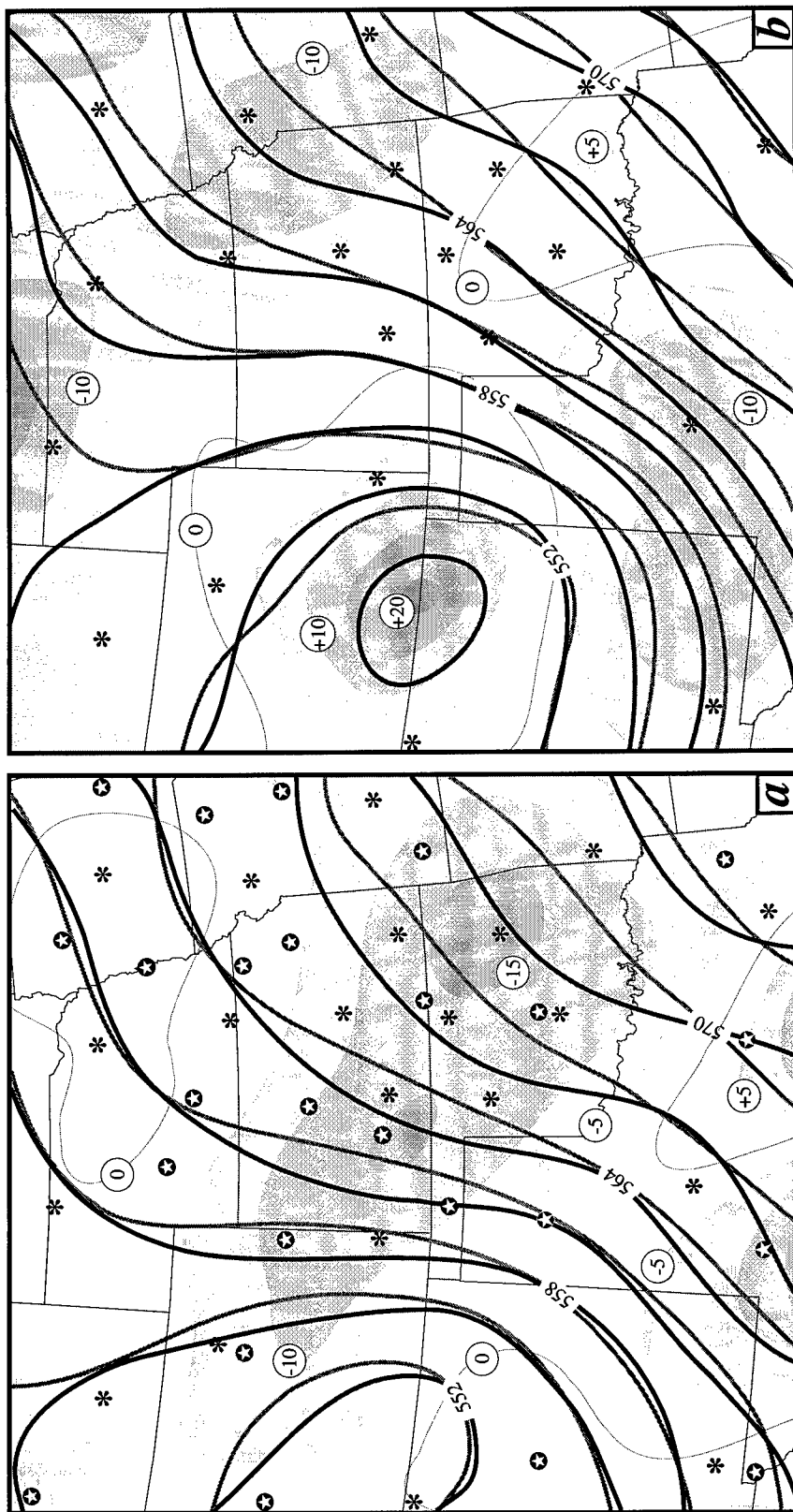


Figure 2.6. Retrieved 500 mb height field (dm) for (a) 2100 UTC 8 March 1992 and (b) 0300 UTC 9 March 1992. Solid gray lines depict heights derived from profiler winds alone and solid black lines depict height field obtained from combined rawinsonde and profiler wind observations. Shaded region depict the areas of successively greater difference between the height fields (Profile minus rawinsonde /Profiler derived heights). The location of rawinsonde sites are indicated by stars and the location of profiler sites are indicated by asterisks. The distribution of all rawinsonde and profiler sites is shown in (a), whereas the location of the profiler sites alone are indicated in (b).

2.6. Summary

The STORM-FEST field experiment provides an excellent context in which to review and refine a method, based on application of the divergence equation, to extract geopotential height and thermal structure from observed wind data. Above the boundary layer, in the absence of friction, the divergence equation is composed of horizontal components of the wind field and a Laplacian term of the geopotential height field. Application of the Liebmann over-relaxation method provides an approximate solution to the Laplacian term. Once the mass field is determined, the thermal structure is obtained through assumption of hydrostatic balance.

Although this method has been successfully employed in the past (Fankhauser 1974; Kuo and Anthes 1985; Cram *et al.* 1991), the work described in this paper is the first time the *divergence method* has been applied over a large regional network and in the context of a field experiment rich in upper-air data. The divergence method was applied during STORM-FEST IOP-17 (8-9 March 1992). This IOP is characterized by a deepening midtropospheric low center in the vicinity of the Oklahoma panhandle.

Based only on the momentum field, the divergence method was able to correctly capture a 12-hour, 500-mb height fall of 110 m over the region. Moreover, the retrieved height field captured mesoscale features not resolved by the rawinsonde observations alone. Similarly, retrieved temperature fields detected the formation and propagation of a cold front aloft (CFA) (e.g., Hobbs *et al.* 1990, Businger *et al.* 1991) between 700 and 400 mb over the Texas panhandle region .

At rawinsonde sites, the retrieved heights compared very well with observed heights (Table 2.0). When comparisons were made at a number of times and at various levels in the troposphere, the average standard deviation was only ~10 m, well within the accuracy of the rawinsonde instrumentation (± 24 meters). Results of the comparison of retrieved and observed temperatures show comparable accuracy to that of the heights, with an average standard deviation of $\sim 1.5^{\circ}\text{C}$. The retrieved temperature profile was within 1°C of the observed temperature sounding over Guymon Oklahoma, as the CFA passed over the area. For both retrieved fields (temperature and height) the greatest accuracy was obtained at lower atmospheric levels (700 and 500 mb) and the accuracy decreased at higher levels.

The application of the divergence method, using hourly profiler data, provided encouraging results at asynoptic times. The results indicate that valuable information on the evolution of atmospheric height and temperature fields can be retrieved between rawinsonde releases.

The success of the divergence method described in this paper provides meteorologists with a tool to improve the resolution of height and temperature fields for use in case-study analysis and for comparison with mesoscale numerical model output. The derived fields can be applied in defining the initial state of or in nudging mesoscale numerical models in research mode. Moreover, the divergence method can be applied to wind data regardless of their source, including wind data derived from satellite (e.g., Nieman *et al.* 1993) and Doppler radar (e.g., Campistron *et al.* 1991). Applications to

NWP initialization require significant additional research to dynamically assimilate the time continuous data.

The fact that useful information can be retrieved from wind data at asynoptic times suggests that an application of this technique to a combination of profiler, WSR-88D, and satellite-derived wind data could provide valuable mass and thermal constraints for the update cycle of operational numerical models at the National Center for Environmental Prediction, as well as to regional mesoscale models run locally in a quasi-operational mode. Such constraints may be especially valuable when extracted from satellite-derived winds over the open ocean.

3. GEOSTROPHIC ADJUSTMENT AND CFA FORMATION IN RESPONSE TO LEESIDE WARMING ALONG THE SOUTHERN FRONT RANGE

3.1 Overview

The generation and propagation of a cold front aloft (CFA) can significantly impact weather conditions from the Front Range eastward to the coastal plains. (Hobbs *et al.* 1990, Businger *et al.* 1991). The Rocky mountains act as an important source region for CFA generation as both adiabatic and diabatic processes produce an environment favorable for development. In order to gain insight into the dynamical processes at work, a detailed analysis was conducted of the STORM-FEST IOP-17 data sets for 8-9 March 1992 in conjunction with high resolution numerical modeling studies.

3.2 Objectives

The focus of this portion of the research will investigate the geostrophic adjustment process in response to the interaction between the wind field and a mesoscale warm pool in the lee of the southern Rockies. The following sections will document the orographic impact in altering the secondary circulations downstream of the mountains which influence CFA and midtropospheric jet streak development. Section 3.3 will overview the analysis scheme and modeling aspects of this research. Section 3.4 will provide observational evidence of the existence of a CFA and developing jet. Section 3.5 will define the environment in which the CFA develops. Section 3.6 will employ observed

data elements to define the physical processes at work in generating these feature. Section 3.7 will address the issue of terrain-induced mass perturbations and associated geostrophic adjustments. In section 3.8, numerical modeling studies, ranging from a large scale background flow down to the meso- β scale, will be presented to highlight specific physical processes influencing development.

3.3 Observational and Modeling Data Sets

3.3.1 Observational Data Sets and Analysis Scheme

The observational analysis takes advantage of the increased resolution provided by the RAOB and profilers by making use of the extract height fields as described in section 2. The objective analysis of the combined sets of wind observation also provide a higher resolution of data for this analysis. The retrieval of the height field provides the opportunity to extract the thermal structure by making use of the hypsometric equation (Eq. 7) as discussed in section 2. The results provided useful information and agreed quit well with the individual observation sites. However, a consistent set of data at all levels and for all time periods were not generated making its use less desirable than the objective analysis performed on the rich number of RAOB observed temperatures. Consequently, the observed gridded fields are from the retrieved heights, objective analysis of the combined profiler and RAOB winds, and the objective analysis of the RAOB observed temperature data.

3.3.2 Mesoscale Model and Experimental Design

Numerical modeling studies were conducted to provide a high temporal and spatial resolution data set with which to evaluate the atmospheric response to low-level forcing. The modeling experiments were run using the Mesoscale Atmospheric Simulation System (MASS) model version 5.8 (MESO 1995). Over the years, a number of studies have been successfully conducted using various forms of this model (e. g. Zack and Kaplan 1987; Cram *et al.* 1991; Manibianco *et al.* 1991; Kaplan and Karyampudi 1992 a, b; Karyampudi *et al.* 1995; Kaplan *et al.* 1996). A similar version of this model is currently providing real-time meso-scale forecast output for analysis by the North Carolina State University Department of Marine, Earth, and Atmospheric Sciences and the Raleigh National Weather Service Forecast Office. Additionally, a real-time model is currently in use at the Kennedy Space Center and Cape Canaveral AFS in support of launch/recovery and daily ground processing operations (Bauman 1996).

The simulation of the evolving weather conditions over the central Plains was a considerable challenge. Original attempts to initialize the run at 08/00 UTC were unsuccessful. This effort resulted in the development of a low pressure center over southeast New Mexico that rapidly deepened as it raced into southeast Colorado by 08/12 UTC. The 18-hour forecast had anchored a low center over the eastern slopes of Colorado resulting in the model-generated 850 mb height field that was over 80 meters lower than that observed (Fig. 3.1) This result was not unique to the MASS model but

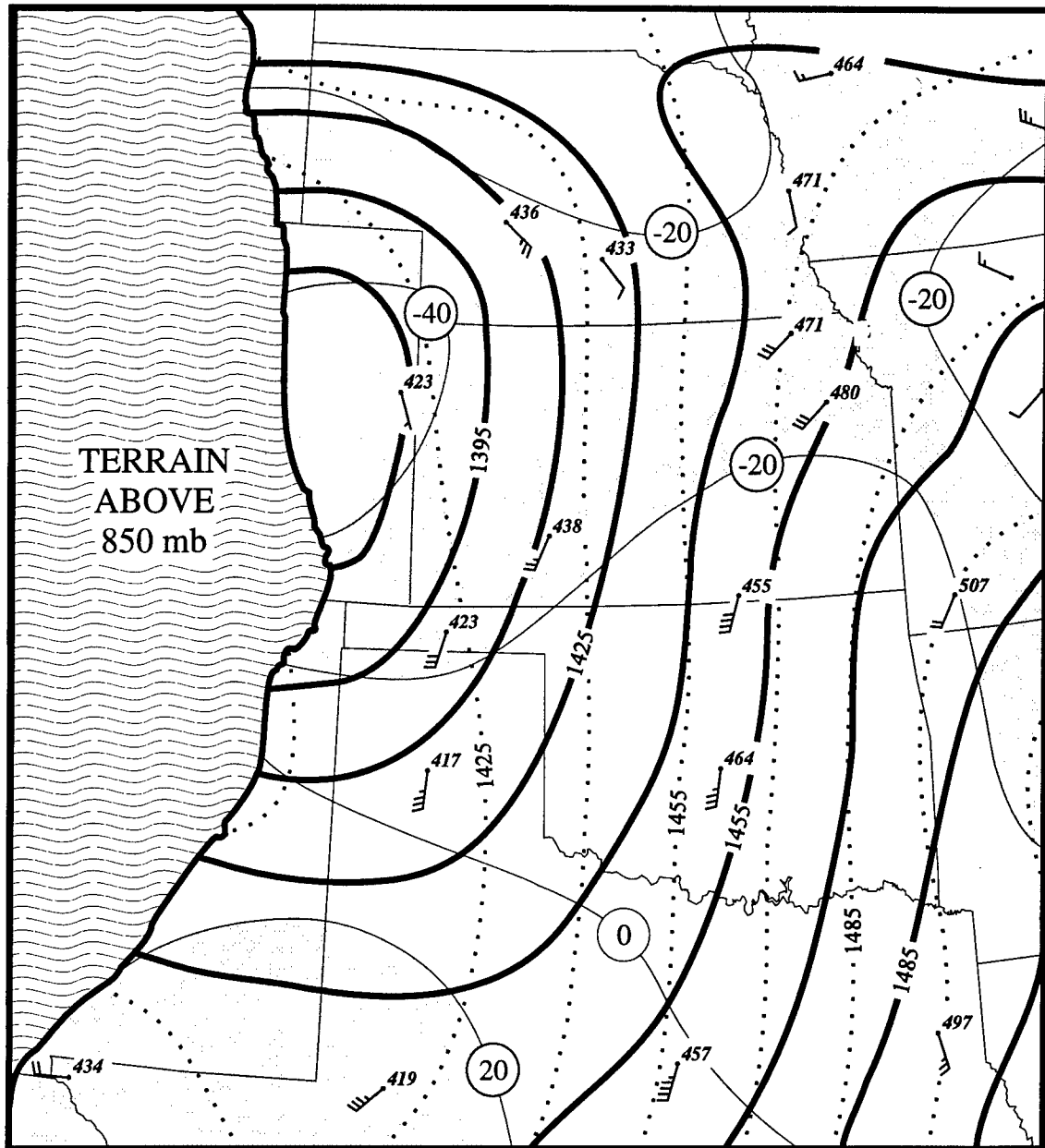


Figure 3.1. 850 mb height field comparison between observed conditions at 1800 UTC 8 March 1992 (Dotted line -- 30 m interval) and the MASS Model 18 hour 850 mb forecast (Solid line -- 30 m interval). Height difference is contoured at a 20 m interval. Observed heights (m -- preceding one omitted) and winds (full staff -- 5 ms⁻¹ and half staff -- 2.5 ms⁻¹).

also found in the real-time model run produced by the STORM-FEST MM-4 model output. The initial state over the inner-mountain region contained an extensive adiabatic layer that may have acted in focusing internal wave energy over eastern Colorado resulting in the unrealistic simulation results. Consequently, initializing the model at 08/00 UTC was abandoned in favor of the 08/12 UTC time period.

The model was initialized from the 1200 UTC 8 March 1992 data base using first guess fields provided by the NMC/NCAR ReAnalysis Project (Kalnay *et al.* 1996). This field consists of a $2.5^{\circ} \times 2.5^{\circ}$ lat/lon global grid domain with a vertical resolution of 17 pressure levels. A high resolution terrain field was generated consistent with the grid spacing for the particular run. The terrain grid was subjected to one pass of a 9-point smoother to minimize terrain-induced instabilities. The gridded domain was initialized using a 3D-Optimal Interpolation scheme (Daley 1991). The vertical resolution consisted of 28 sigma surfaces from the surface to the 100 mb level. The vertical separation was selected to ensure hydrostatic consistency in which the horizontal grid spacing (Δx) and the vertical separation of the sigma surfaces ($\Delta \sigma$) satisfied the relation $\Delta \sigma / \Delta x < \Delta h / \Delta x$, where Δh is the maximum terrain height. The moisture analysis was enhanced by the use of a synthetic RH retrieval scheme which incorporates surface cloud observations and Manually Digitized Radar data to provide a better representation of the moisture field. Boundary conditions were available every six hours from the NMC/NCAR ReAnalysis grids. The available climatological soil moisture file was subjectively modified based on the observed Palmer Drought Index for the period of interest. The specifics of the schemes used to conduct the runs are detailed in Table 3.0.

Table 3.0 Specification for MASS Model version 5.8

Numerics

- Hydrostatic primitive equation model
- 3-D primitive equations for u , v , T , q , and p
- Vertical resolution consist of 28 sigma levels
- Energy absorbing upper domain sponge layer
- High resolution run: 14 km grid on a 240x210 grid matrix
- Medium resolution run: 60 km grid on a 80x65 grid matrix
- Course resolution run: 160 km grid on a 40x30 grid matrix
- Terrain following sigma-p coordinate system
- Fourth-order accurate horizontal spatial differencing
- 20 sec. short time step gravity wave mode
 - Forward-backward scheme
- 40 sec. long time step slow advective mode
 - Split-explicit time marching integration employing Adams-Bashforth scheme

Initialization Scheme

- First Guess provided by NMC/NCAR ReAnlaysis gridded data set
 - $2.5^\circ \times 2.5^\circ$ lat/lon global grid
 - 17 vertical pressure levels
- ReAnalysis using 3-D OI scheme (Daley 1991)
- High resolution average terrain using one pass 9-point smoother
- Enhanced moisture analysis through synthetic RH retrieval scheme
- Weekly averaged $1^\circ \times 1^\circ$ lat/lon SST data
- Anderson Level II land use classification scheme (Anderson *et al.* 1976)
- Climatological subsoil moisture database
- Normalized Difference Vegetation Index (NDVI)

PBL Specification

- Modified Blackadar high resolution PBL scheme (Zang and Anthes 1982)
- Surface energy budget based upon Noilhan and Planton scheme (1989)
- Soil hydrology based upon Mahrt and Pan scheme (1984)

Moisture Physics

- Grid scale prognostic equations for cloud water and ice, rain water, and snow
- Sub-grid scale Kuo-MESO convective parameterization scheme

The grid domain for various runs, regardless of the grid spacing, were constructed over an area where the southwest corner is located at 20° N, 120° W and the northeast corner is located at 48.8° N, 86.1° W in which the grid spacing is true at 36° N, 100° W (Fig. 3.2). A coarse grid of 160 km over a 40x30 grid domain defined the large scale quasi-geostrophic background flow. A 60 km run on a 80 x 65 grid was generated to capture the sub-synoptic scale non-linear interactions while attempting to filter out some of the effects induced by terrain. In order to capture dynamical processes on the order of meso- β to meso- α scale, a high resolution 14 km model run was constructed over a 240x210 grid domain. The various model runs were performed to identify the role of specific physical processes in perturbing the large scale background flow resulting in a geostrophic adjustment between the mass and momentum fields. In order to address the impact of daytime sensible heating in amplifying the mass perturbation an adiabatic simulation was conducted. This run was performed by eliminating the vertical heat flux from the lowest sigma level and eliminating the generation of any latent heat flux. Any moisture captured in the initial state acts as a tracer as it is simply advected about the model domain. Additionally, a sensitivity study was conducted whereby the surface file was replaced with a uniform terrain of an elevation of 1200 m. This study was conducted in order to evaluate the topographical impact in altering the secondary circulations downstream of the mountains. A listing of the various experiments conducted are provided in Table 4.0. A number of experiments were ran with various combinations of nudging options employed. These efforts provided mixed results. In order to maintain the integrity of the data sets, the final simulations were ran without nudging the model.

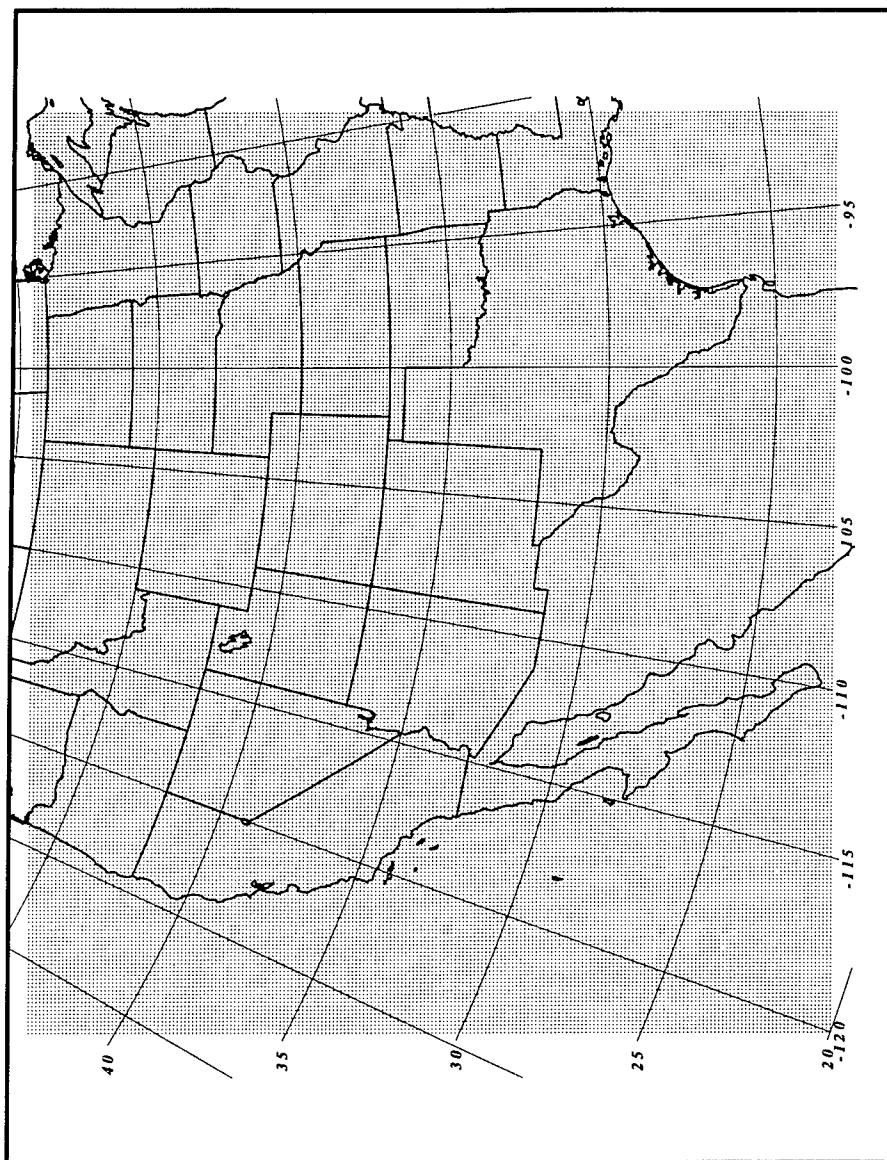


Figure 3.2. A 14 km MASS model run was constructed with a 240x210 grid domain. The domain was constructed over an area in which the southwest corner is located at 20° N, 120° W and the northeast corner is located at 48.8° N, 86.1° W and the grid spacing is true at 36° N, 100° W. A 160 km course grid over a 40x30 grid domain and a finer 60 km grid with a 80 x 65 grid domain were constructed over the same region.

Table 4.0

Listing of various MASS modeling experiments conducted.

Resolution	Initialized	Model Experiments / First Guess Field			Nudging		
		Full Physics	Adiabatic	Flat Moist	RAOB	Sfc Obs	MDR
160 km	08/12 UTC	ReAnal	—	—	None	None	None
60 km	07/12 UTC	GOI	—	—	None	None	None
	08/00 UTC	GOI	—	—	None	None/ 36 hrs	None/ 36 hrs
		ETA Model	—	—	None	None	None
		ReAnal	—	—	None	None	None
	08/12 UTC	GOI	—	—	None/ 6 /24 hrs	None/ 24 hrs	None/ 24 hrs
		ReAnal	ReAnal	ReAnal	None	None	None
14 km	08/00 UTC	GOI	—	—	None	None/ 36 hrs	None/ 36 hrs
		ETA Model	—	—	None	None	None
		ReAnal	—	—	None	None/ 36 hrs	None/ 36 hrs
	08/12 UTC	GOI	—	—	None/ 6 /24 hrs	None/ 24 hrs	None/ 24 hrs
		ReAnal	ReAnal	ReAnal	None	None	None

3.4. Observed Evidence of Cold Front Aloft and Downstream Impact

IOP-17 was initiated on 5 March 1992 in anticipation of a major winter storm forecast to develop over the STORM-FEST domain over the next 72 hours. A strong zonal Pacific jet stream approached the west coast of North America at the start of this period. The main branch of the polar jet traversed the southern tier of the Canadian

Provinces while a secondary branch was diverted down along the California coast. During the next 48 hours, cold air associated with the southern jet settled over the desert southwest producing a quasi-stationary upper-level low while a broad ridge was building over the Great Plains (Martin *et al.* 1995).

The 1301 UTC imagery for 8 March 1992 clearly depicts the large scale cloud shield associated with the circulation of the upper-level low over the desert southwest (labeled "A") (Fig. 3.3a). A band of clouds extend northward through western New Mexico parallel to the existing 500 mb jet streak. The influx of a limited amount of Pacific moisture combined with the destabilizing cold air associated with the upper low allow the generation of cold core convective cells producing heavy rains over southeast Arizona. The irregularity of the terrain interacts with the flow to generate a variety of complex cloud features. Of note, as the moisture axis slowly advances into central New Mexico, the vertical motion forced by the mountains is revealed by the cap cloud induced by the Sacramento and Guadalupe mountains of south central New Mexico (labeled "B"). Over eastern New Mexico into west Texas, the pre-dawn radiational cooling is evident in the infrared imagery as clear dry conditions maximize cooling throughout this area. Meanwhile, the warm moisture laden air (darker region) over central Texas defines the emerging dryline over west Texas. The entrenched pool of cold air over the inner-mountain region acts to suppress the subtropical jet further south. This axis is evident from the tip of Baja northeastward into eastern Texas as a series of wave packets of moisture advance eastward with the flow.

1301 08MR92 19E-287 01463 20851 RB35N105W-Z

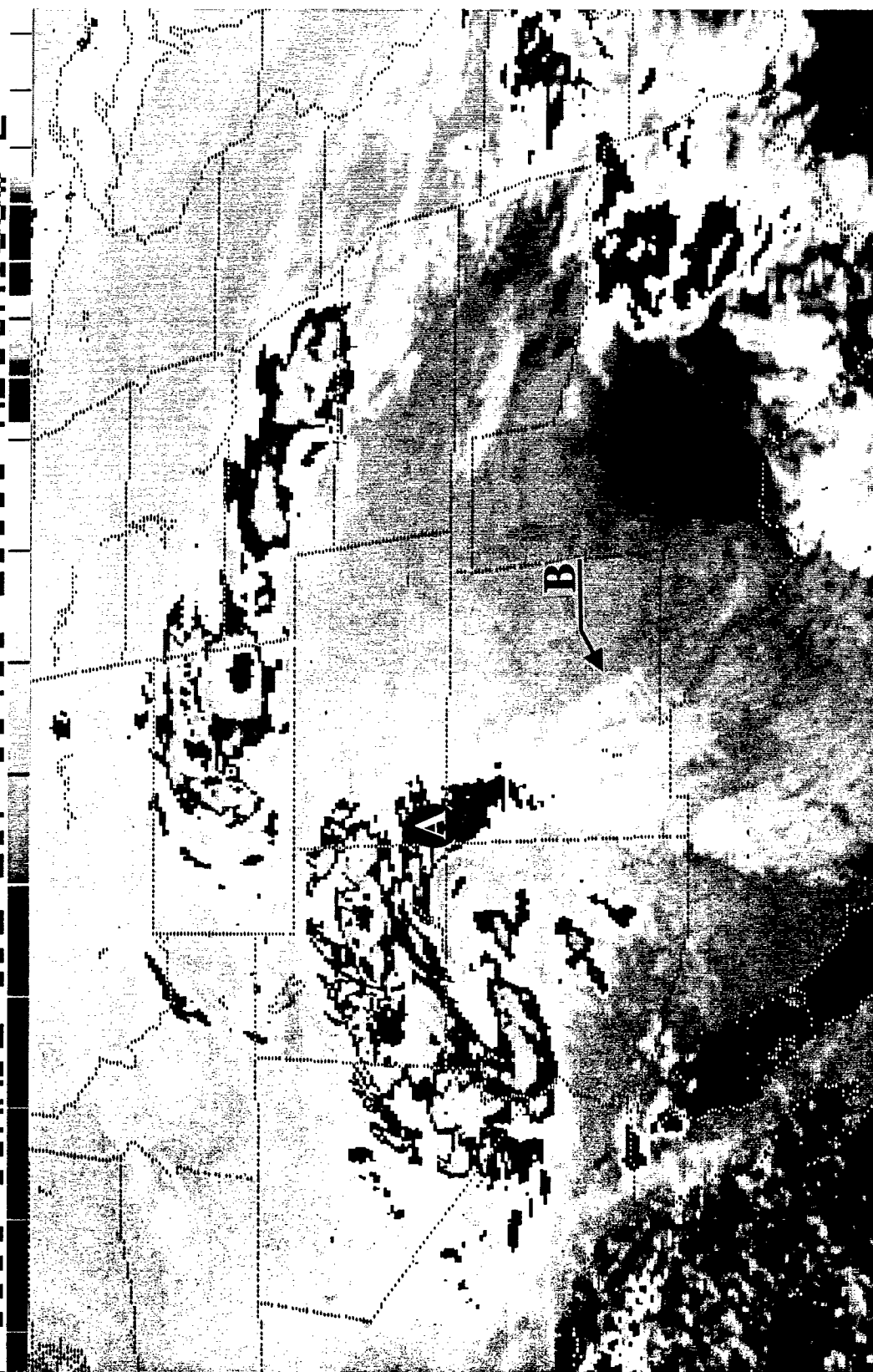


Figure 3.3a. GOES-7 infrared satellite imagery valid at 1301 UTC 8 March 1992. Refer to text for explanation of letter designators.

As the morning progressed, the 1731 UTC satellite image clearly details the wedge of clear air resulting in intense boundary layer warming focused over the southwestern Plains (Fig. 3.3b). The combined effects of downslope adiabatic warming and strong surface sensible heating increase the boundary layer thickness enhancing the wedge of warm air to the lee of the southern Rockies. In sharp contrast, convective elements are expanding over the inner-mountain region in response to the destabilization. The cloud band associated with the upper low (element "A") is enhanced over central New Mexico as forced ascent is imposed by the Rockies. Meanwhile, a hard edge is found on the advancing side of the cloud shield due to the downslope motion in the lee of the mountains. Interestingly enough, a cloud element has formed within the wedge of warm-dry air over eastern New Mexico (element "C"). A review of satellite imagery indicates that this feature becomes evident as moisture from cloud element "A" advances sufficiently eastward to supply an influx of moisture into the vertical motion pattern set off by observed standing mountain wave activity first revealed by cloud element "B".

During the course of the day, cloud element "A" progressed eastward at a rate of approximately 45 km hr^{-1} which would put this band of clouds into eastern New Mexico by 08/21 UTC. However, at this time, satellite imagery indicates an enhanced cumuliform cloud formation that has developed 300 km downstream of this synoptic scale feature. Despite the very dry conditions, the vertical motion is of sufficient strength to produce some cloud elements over the Texas panhandle.

The enhanced cumuliform cloud mass is observed to enter the Amarillo, Texas (AMA) area by 2101 UTC (Fig. 3.3c). Inspection of the AMA sounding reveals the signal

1731 08MR92 19E-287 01442 20851 RB35N105W-Z

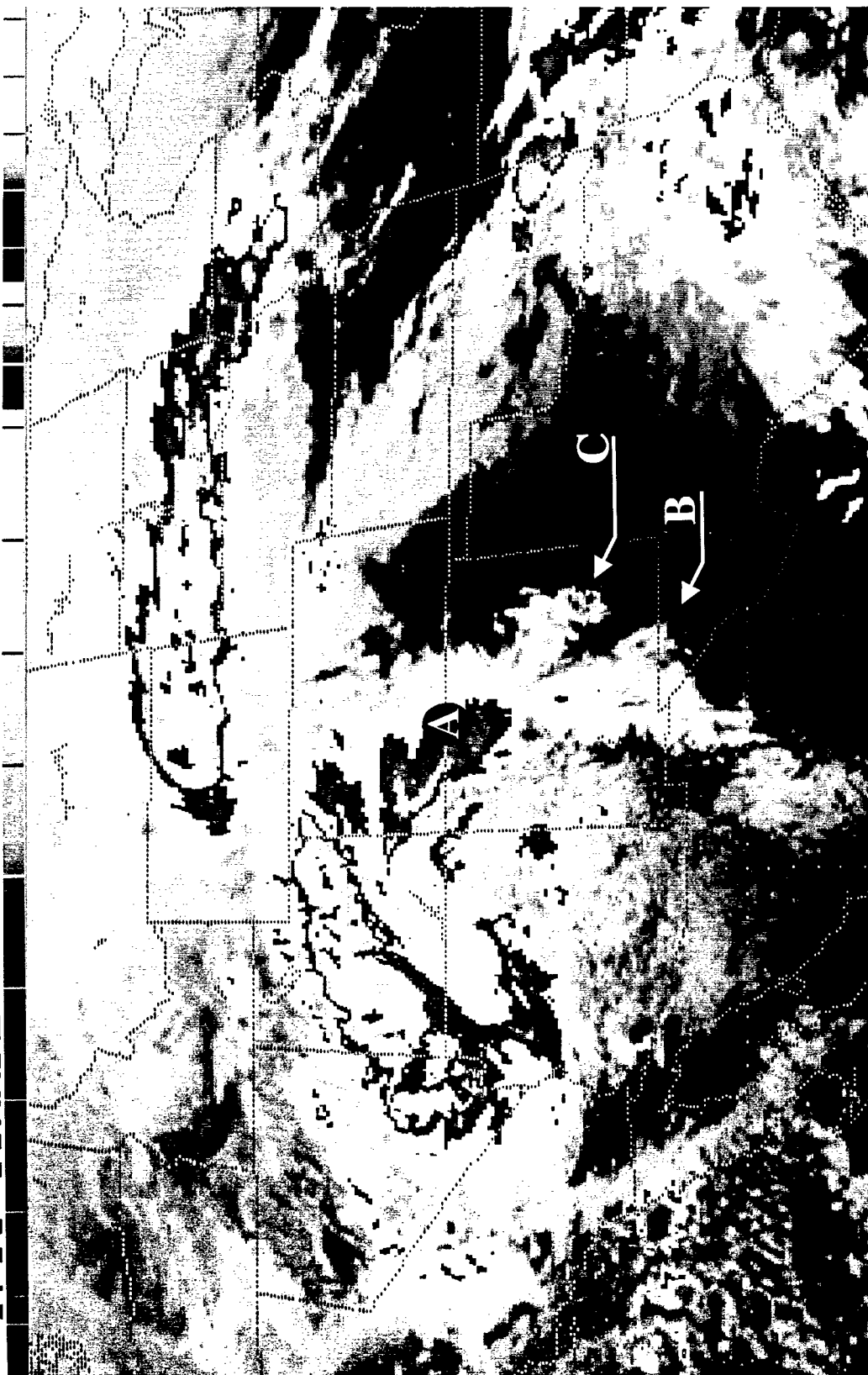


Figure 3.3b. GOES-7 infrared satellite imagery valid at 1731 UTC 8 March 1992. Refer to text for explanation of letter designators.

2101 08MR92 19E-287 01442 20842 RB35N105W-Z

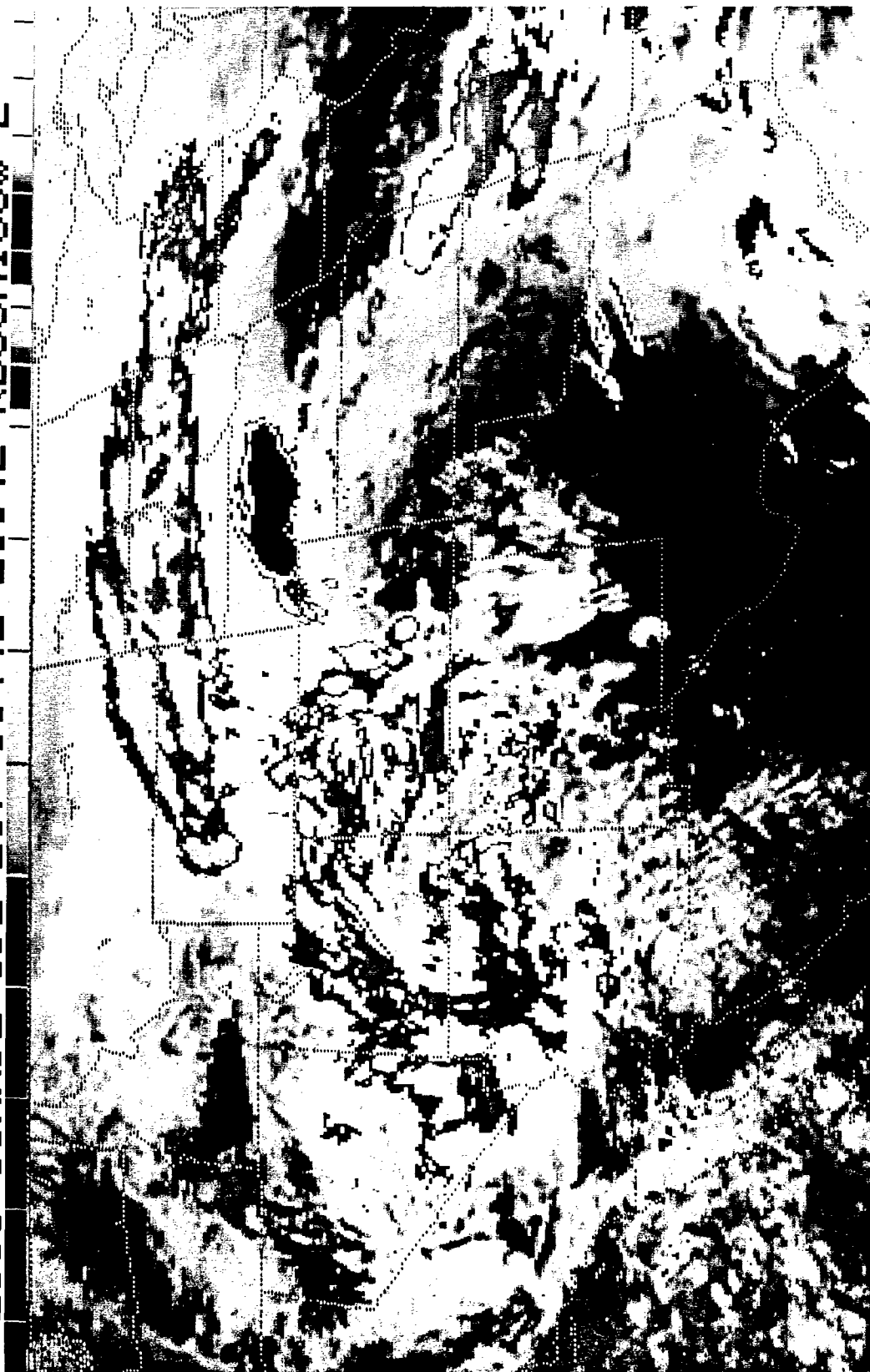


Figure 3.3c. GOES-7 infrared satellite imagery valid at 2101 UTC 8 March 1992.

of the CFA passing over the site between 08/21 and 09/00 UTC (Fig. 3.4). At 08/21 UTC, the profile possesses characteristics of a post dryline structure with a well-mixed dry layer below 650 mb. Three hours later, dramatic cooling is observed between 400 and 660 mb in response to the elevated influx of cold air. Maximum cooling occurs at 550 mb where a 5°C drop in temperature was observed. This cooling is not solely the result of horizontal advective processes. Inspection of the vertical wind profile reveals a wind field that weakly backs with height. Winds at 08/21 UTC at 650 mb are from 210° and back to 200° at the top of the cooled layer. This slight backing of the wind profile is considered insufficient to fully account for the observed 5°C cooling due to thermal wind arguments and is a likely signal of other processes at work. Above 500 mb, the increase vertical shear is consistent with the appearance of enhanced baroclinicity. The magnitude of the momentum field undergoes rapid increase as the jet exit region expands towards the Texas panhandle. In a three-hour period, the AMA wind profile depicts winds over 35 ms⁻¹ descending over 100 mb to the 500 mb level by 09/00 UTC.

In response to the cooling and destabilization associated with the CFA, 2331 UTC satellite imagery in Fig. 3.3d depicts an area of isolated showers trying to develop in the post dryline air mass over the Texas/Oklahoma panhandle. Despite the lack of appreciable moisture, the developing cold air is sufficiently able to destabilize the air mass enough to generate the limited convective activity observed over the region. Inspection of the AMA sounding reveals that the formation of the CFA had destabilized the environment as evident in the reduction of the Lifted Index to 1.5°C and an increase in the Total Totals

2331 08MR92 19E-287 01451 20842 RB35N105W-Z

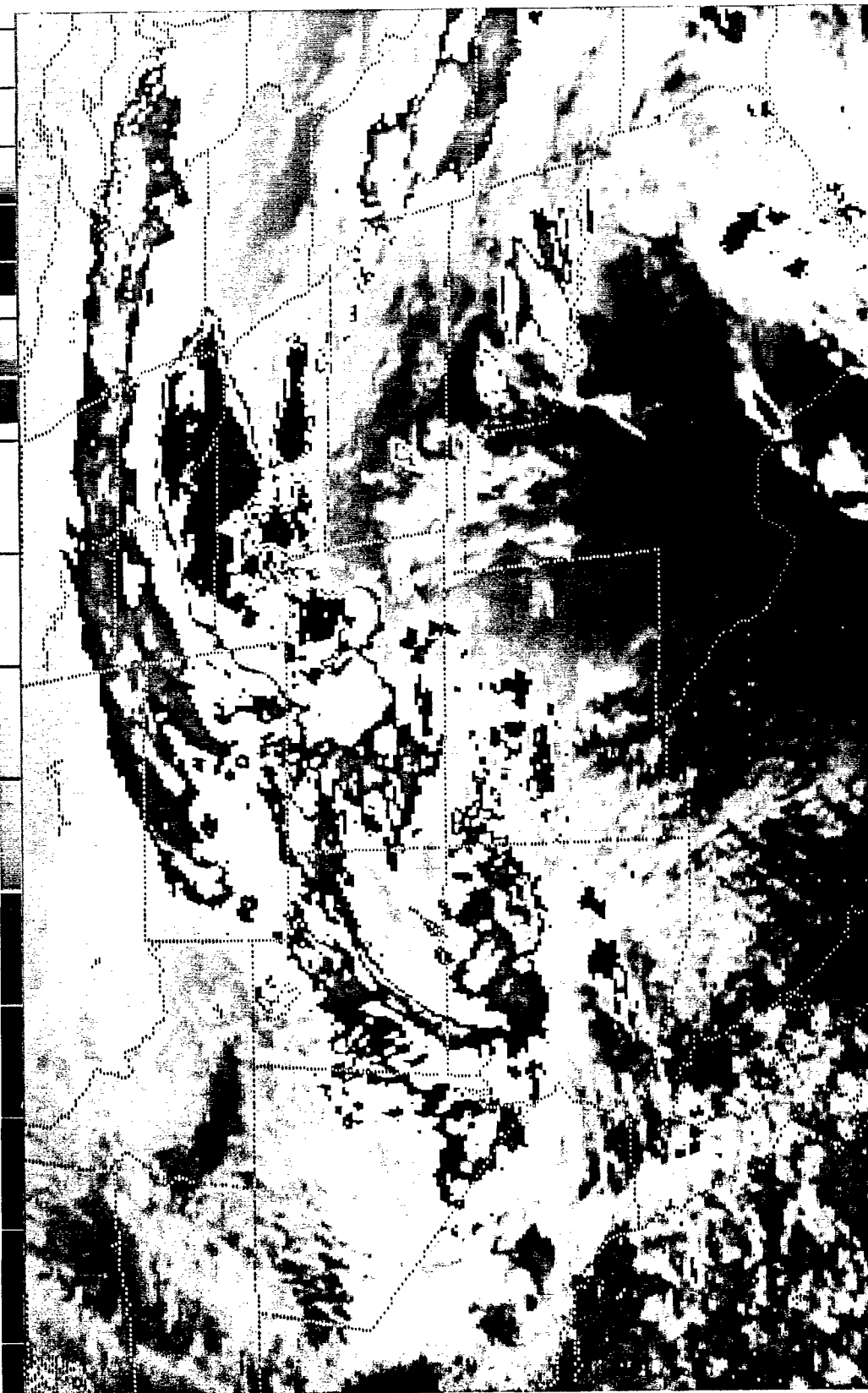


Figure 3.3d. GOES-7 infrared satellite imagery valid at 2331 UTC 8 March 1992.

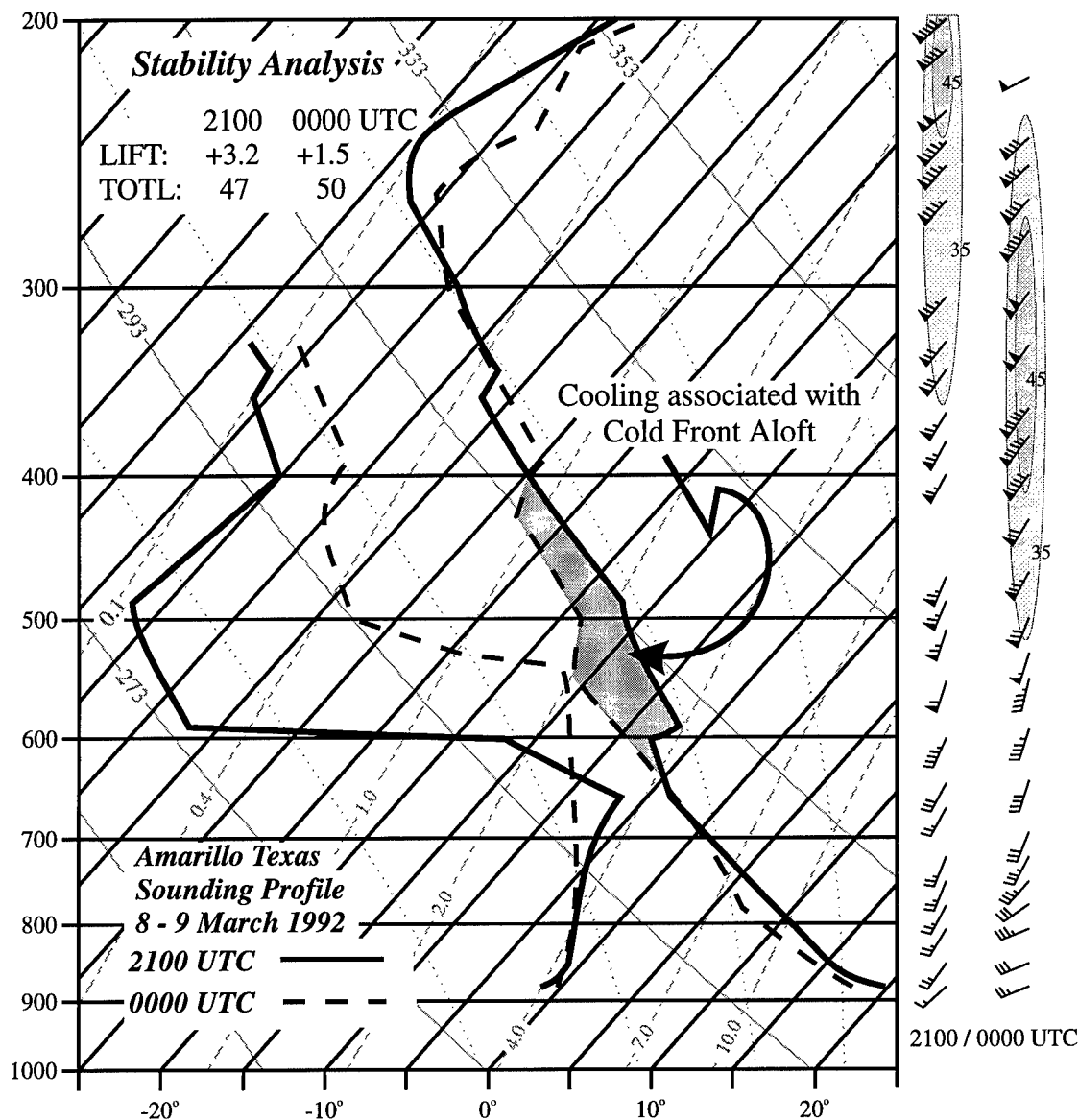


Figure 3.4. Amarillo, Texas sounding profile for 8 March 1992, 2100 UTC (solid line) and 9 March 1992, 0000 UTC (dashed line). Isotherms - dark solid lines running from lower left to upper right, dry adiabats - light solid lines running from lower right to upper left, moist adiabats - light dotted lines running from lower right to upper left, mixing ratio - dashed lines running from lower left to upper right. Wind profile depicted to right (flag is 25 ms^{-1} , full staff - 5 ms^{-1} , half staff - 2.5 ms^{-1}).

Index from 47 to 50 (Fig. 3.4). Along the dryline itself, sufficient low-level moisture and potential instability exist to initiate severe convection as the CFA over-spreads the region.

3.5. Regional Overview

3.5.1 Evolution of the Low-Level Features

The 1200 UTC 8 March 1992 surface pattern over the central Plains is depicted in Fig. 3.5a. The surface winds over New Mexico southward into El Paso, Texas (ELP) provide a weak signal of the cross-mountain flow occurring over the region. In the lee of the mountains, a trough is observed coincident with the area of strongest downslope warming. The northern portion of this trough extends back towards Utah in relation to the upper-level low. In the lee of the Rockies, a well-defined dryline has developed along the New Mexico/Texas border. This feature separates warm-moist air from the Gulf region from the warm-dry air descending down the Front Range. The dryline is found within the thermal ridge axis and along the strongest moisture gradient. Across the boundary a 25K change in equivalent potential temperature (θ_e) is observed. During the pre-dawn hours, the lack of moisture west of the dryline allows strong radiational cooling to take place. This results in cool dry conditions behind the boundary. Ahead of the dryline, precipitation and cloud cover are widely scattered with the exception of an area of showers organizing along the leading edge of warm air extending from southwest Nebraska to eastern

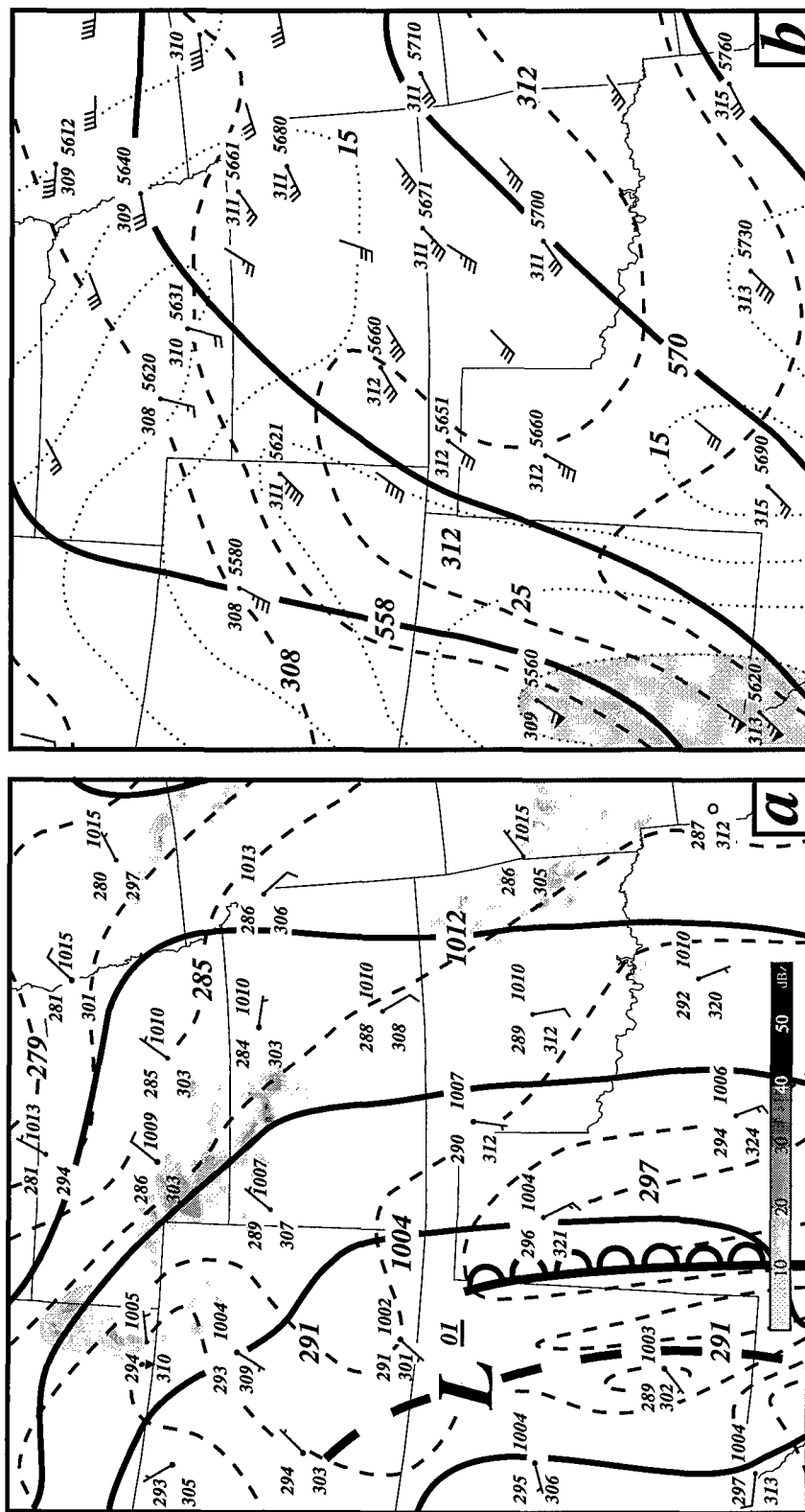


Figure 3.5. (a) 1200 UTC 08 March 1992 surface analysis: isobars (solid - mb), theta (dashed - $^{\circ}\text{K}$), radar echo's (shading - interval of 10 dBz). Station plot: theta, theta-e, PMSL, observed weather, wind barb (full staff - 5 ms^{-1} , half staff - 2.5 ms^{-1}). Surface dry line depicted by line of open semicircles. (b) 1200 UTC 08 March 1992 500 mb analysis: heights (solid - dm), isotachs (dotted / shading - ms^{-1}), theta (dashed - $^{\circ}\text{K}$). Station plot: theta, height, wind barb (flag - 25 ms^{-1} , full staff - 5 ms^{-1} , half staff - 2.5 ms^{-1}). Upper level cold front depicted by line of open triangles.

Oklahoma. According to the work of Martin *et al.* (1995), these showers were the result of geostrophic deformation processes associated with the leading edge of the warm sector.

During the course of the morning, a persistent cross-mountain flow provides clear skies and a low humidity profile allowing maximum sensible heating to be focused over the southern portion of the western Plains. By 08/18 UTC, a strong thermal ridge develops within eastern New Mexico into Colorado (Fig. 3.6a). This pocket of warm dry air is bounded by the mountains to the west and to the east by a region of suppressed diabatic heating due to low clouds and scattered showers. Shortly after 08/15 UTC, the rather benign leeside trough begins to intensify as an organized area of low pressure develops at the apex of the thermal ridge over southeastern Colorado. Coincident with this development, the dryline propagates eastward and the strong wedge of warm dry air infiltrates the central Plains. Over the northern Plains a weakening frontal boundary is observed in response to a departing short-wave trough along the northern branch of the polar jetstream. In its wake, a ridge of high pressure over central Alberta Canada provides a source of cold air over the high Plains. A developing frontal zone is observed over southern Nebraska as low pressure develops over southeast Colorado. The associated circulation rapidly advects warm moist air northward enhancing the convergence and baroclinicity over this region.

By 08/21 UTC the surface low had nearly reached its lowest pressure of 993 mb (Fig. 3.7a). During the previous six hours the low experiences a rapid deepening in excess of 1 mb hr^{-1} . The increased isallobaric forcing acts to accelerate warm moist air northward into the central Plains. The streamline analysis in Fig. 3.8a reflects the strengthening

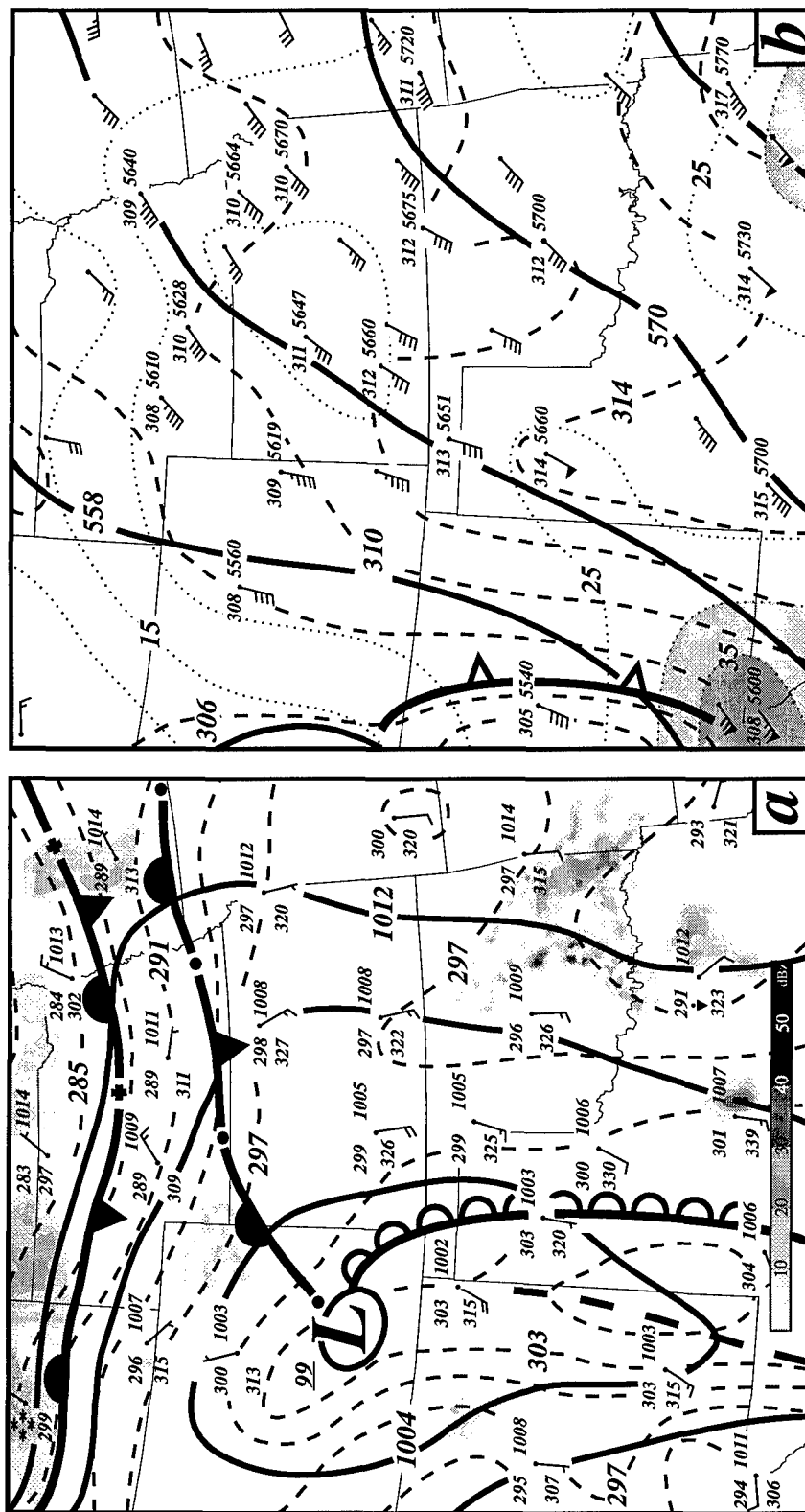


Figure 3.6. (a) 1800 UTC 08 March 1992 surface analysis: isobars (solid - mb), theta (dashed - °K), radar echo's (shading - interval of 10 dBz). Station plot: theta, theta-e, PMSL, observed weather, wind barb (full staff - 5 ms⁻¹, half staff - 2.5 ms⁻¹). Surface dry line depicted by line of open semicircles. Frontogenesis depicted by broken line separated by a closed circle. Frontolysis depicted by broken line separated by a cross. (b) 1800 UTC 08 March 1992 500 mb analysis: heights (solid - dm), isotachs (dotted / shading - ms⁻¹), theta (dashed - °K). Station plot: theta, height, wind barb (flag - 25 ms⁻¹, full staff - 5 ms⁻¹, half staff - 2.5 ms⁻¹). Upper level cold front depicted by line of open triangles.

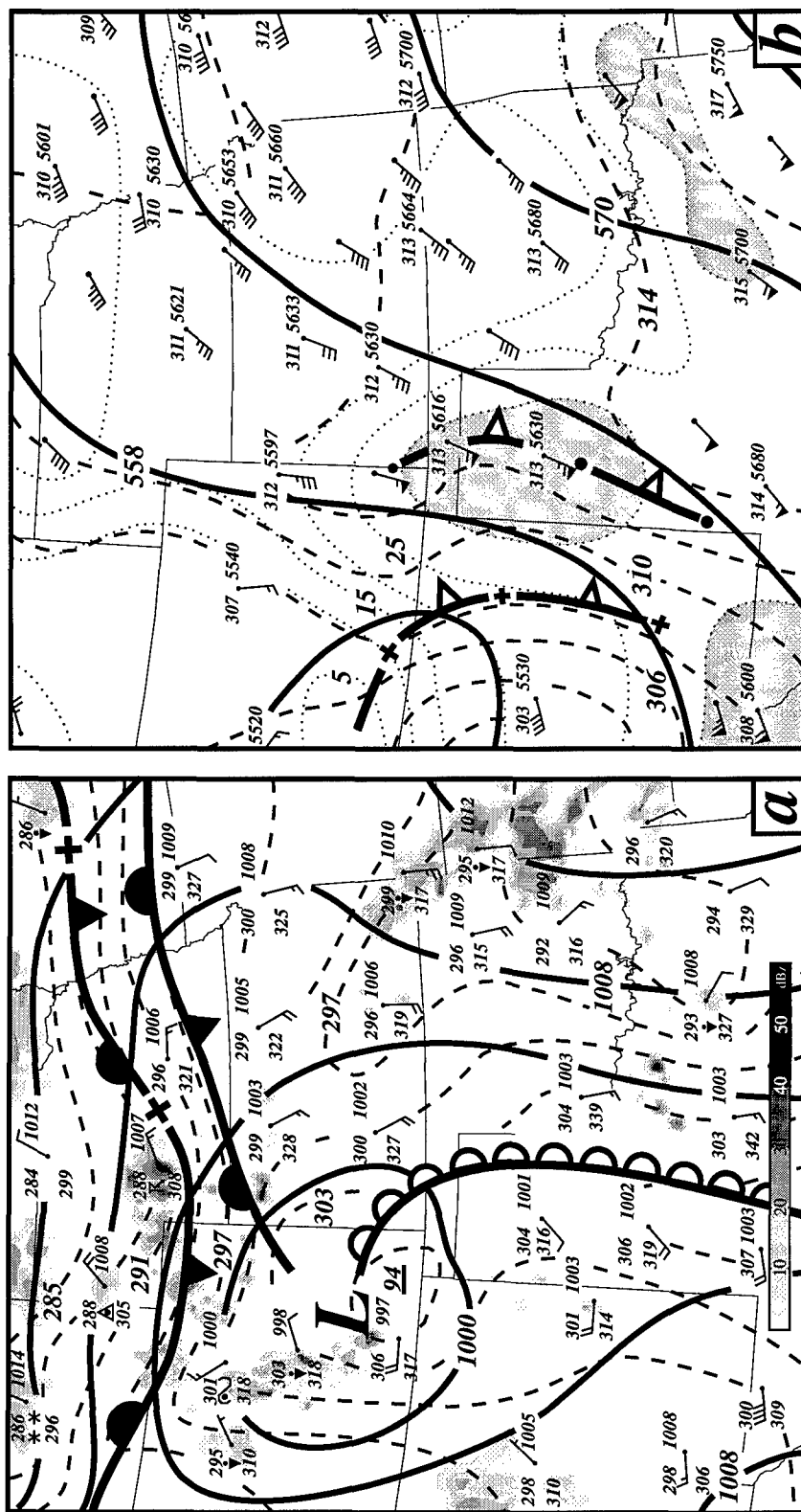


Figure 3.7. (a) 2100 UTC 08 March 1992 surface analysis: isobars (solid - mb), theta (dashed - °K), radar echo's (shading - interval of 10 dBz). Station plot: theta, theta-e, PMSL, observed weather, wind barb (full staff - 5 ms⁻¹, half staff - 2.5 ms⁻¹). Surface dry line depicted by line of open semicircles. Frontolysis depicted by broken line separated by a cross. (b) 2100 UTC 08 March 1992 500 mb analysis: heights (solid - dm), isobars (dotted / shading - ms⁻¹), theta (dashed - °K). Station plot: theta, height, wind barb (flag - 25 ms⁻¹, full staff - 5 ms⁻¹, half staff - 2.5 ms⁻¹). Upper level cold front depicted by line of open triangles.

convergent zone as the eastward propagating dryline encounters the intensifying southerly flow of the eastern Plains. In response, the moisture flux convergent zone becomes much stronger over central Texas (Fig. 3.8b). The dryline is analyzed along the leading edge of the tight gradient where the maximum moisture flux convergence has increased to $6.3 \times 10^{-7} \text{ gm kg}^{-1} \text{ s}^{-1}$ over northcentral Texas. Meanwhile, a convergent asymptote over southern Nebraska intensifies supporting frontogenesis as surface moisture flux convergence exceeds $2.0 \times 10^{-7} \text{ gm kg}^{-1} \text{ s}^{-1}$.

The area bound by the dryline to the west and the stationary boundary to the north is characterized by cool overcast conditions with persistent scattered rainshowers. In marked contrast, boundary layer heating continues to focus over the southwestern Plains. The availability of 3-hourly sounding profiles for Midland, Texas (MAF) depicted in Fig. 3.9 show the rapid evolution of the boundary layer. The soundings provide a signal of an expanding convective boundary layer as daytime heating rapidly modifies the structure. During the course of the day, the inversion base rises from 785 mb at 08/15 UTC to 640 mb at 08/21 UTC. The associated turbulent mixing acts to transport strong westerly momentum and dry air towards the surface. In response, the moisture profile experiences a rapid drying between 08/15 and 08/18 UTC. During this 3-hour period, low-level dew point depression values dramatically increase from 1.5°C to 16°C allowing strong sensible heating to take place. The wind profiles indicate that winds in excess of 20 ms^{-1} descend nearly a kilometer from 811 mb at 08/15 UTC to the surface at 08/21 UTC. By 08/21 UTC, an expansive area of downslope low-level winds in excess of 10 ms^{-1} are observed throughout west Texas (Fig. 3.8a). This influx of warm dry westerly flow aids in the

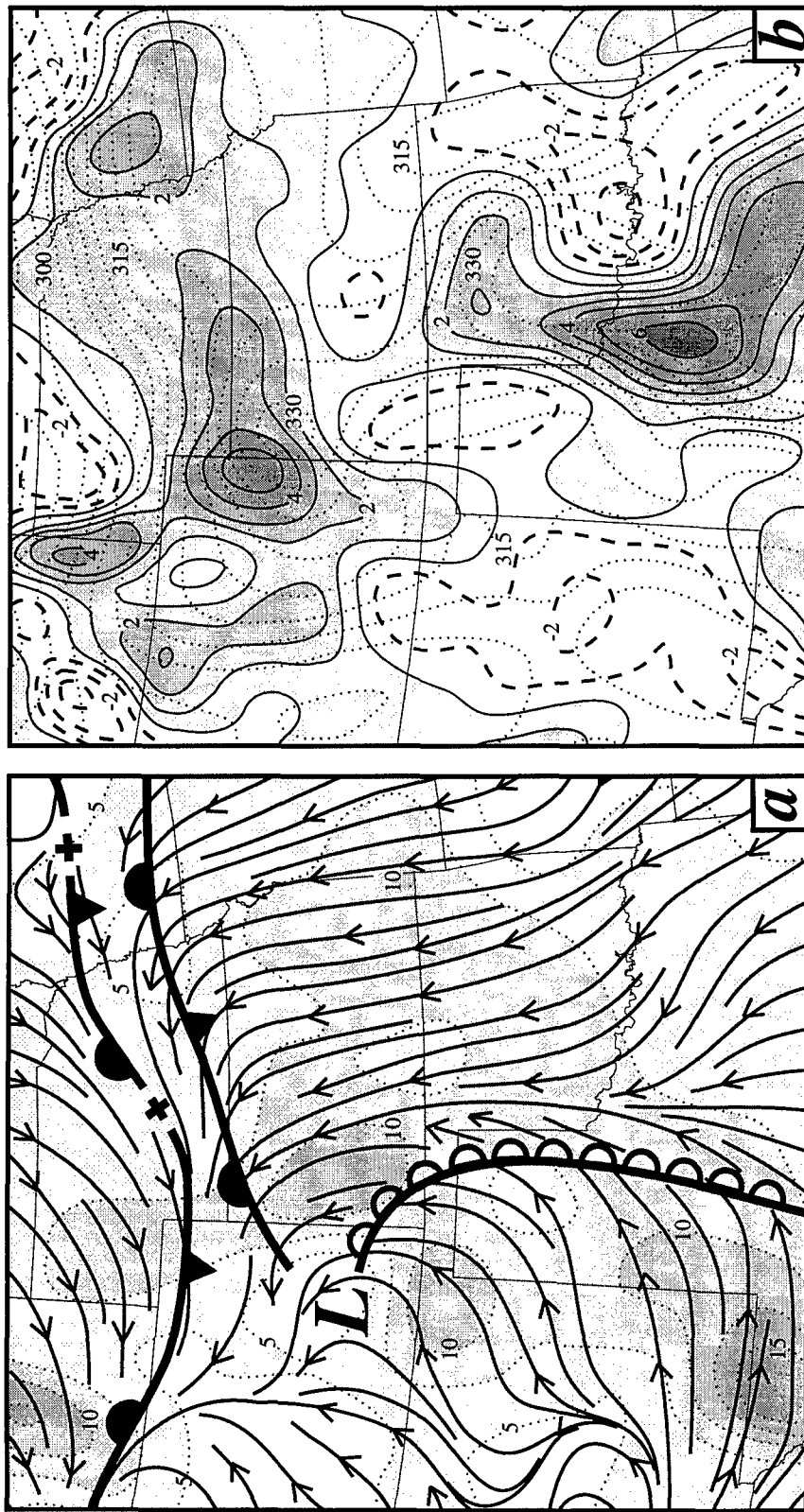


Figure 3.8. (a) 2100 UTC 8 March 1992 surface streamline analysis (thin arrows), isotachs (dotted lines - ms^{-1}) and position of surface low and dryline. (b) Surface equivalent potential temperature analysis (dotted line - $^{\circ}\text{K}$) and surface moisture convergence (thin solid line), divergence (dashed line), $\text{gm kg}^{-1} \text{sec}^{-1} \times 10^{-7}$.

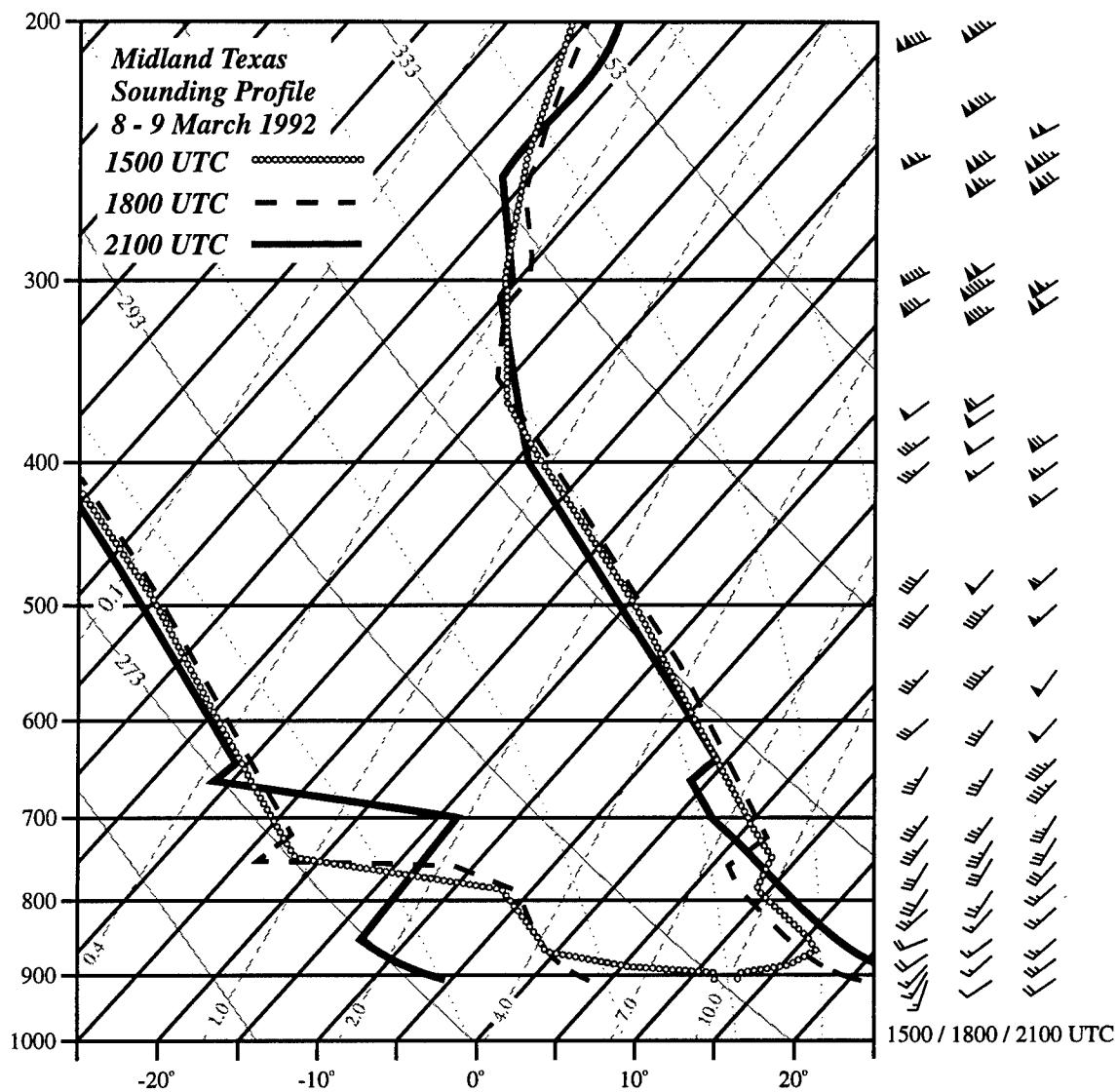


Figure 3.9. Midland, Texas sounding profile for 8 March 1992, 1500 UTC (thin solid), 1800 UTC (dashed line), 2100 UTC (thick solid line). Isotherms - dark solid lines running from lower left to upper right, dry adiabats - light solid lines running from lower right to upper left, moist adiabats - light dotted lines running from lower right to upper left, mixing ratio - dashed lines running from lower left to upper right. Wind profile depicted to right (flag is 25 ms^{-1} , full staff - 5 ms^{-1} , half staff - 2.5 ms^{-1}).

propagation of the dryline and expansion of the wedge of warm-dry air into central Texas (Koch and McCarthy 1982).

By 09/00 UTC, a broad cyclonic circulation covers the Great Plains with blizzard conditions experienced over the northern Plains while severe thunderstorms activity is initiated to the south (Fig. 3.10a). The dryline has advanced into west-central Oklahoma as the broadening thermal ridge of warm air expands across the Plains. Ahead, warm-moist air with θ_e exceeding 330K extends well into northern Oklahoma, while dry air infiltrating from the west results in a 20-30K drop in θ_e behind the boundary. Along this boundary, a corridor of potential instability is established from central Texas northward into Kansas. Strong sensible heating over the plateau region of the southern Rockies acts as an elevated source of warm arid air. As the boundary layer expands during the course of the day, the stronger winds aloft advect the dry air mass eastward. The superposition of dry air over the low-level high θ_e air establishes a region of increased potential instability.

3.5.2 Evolution of the Midtropospheric Atmosphere

The evolving low-level circulation is accompanied by the mid-level development of a CFA and bifurcation of the polar jetstream over the central Plains. The availability of asynoptic rawinsonde data provides a unique opportunity to observe the midtropospheric evolution of these features. The 500 mb analysis at 08/12 UTC depicts a low situated over the four corners region with a building ridge over the central Plains (Fig. 3.5b). A 30 ms^{-1} jet streak is detected over central New Mexico indicative of the vertical extent of the cross

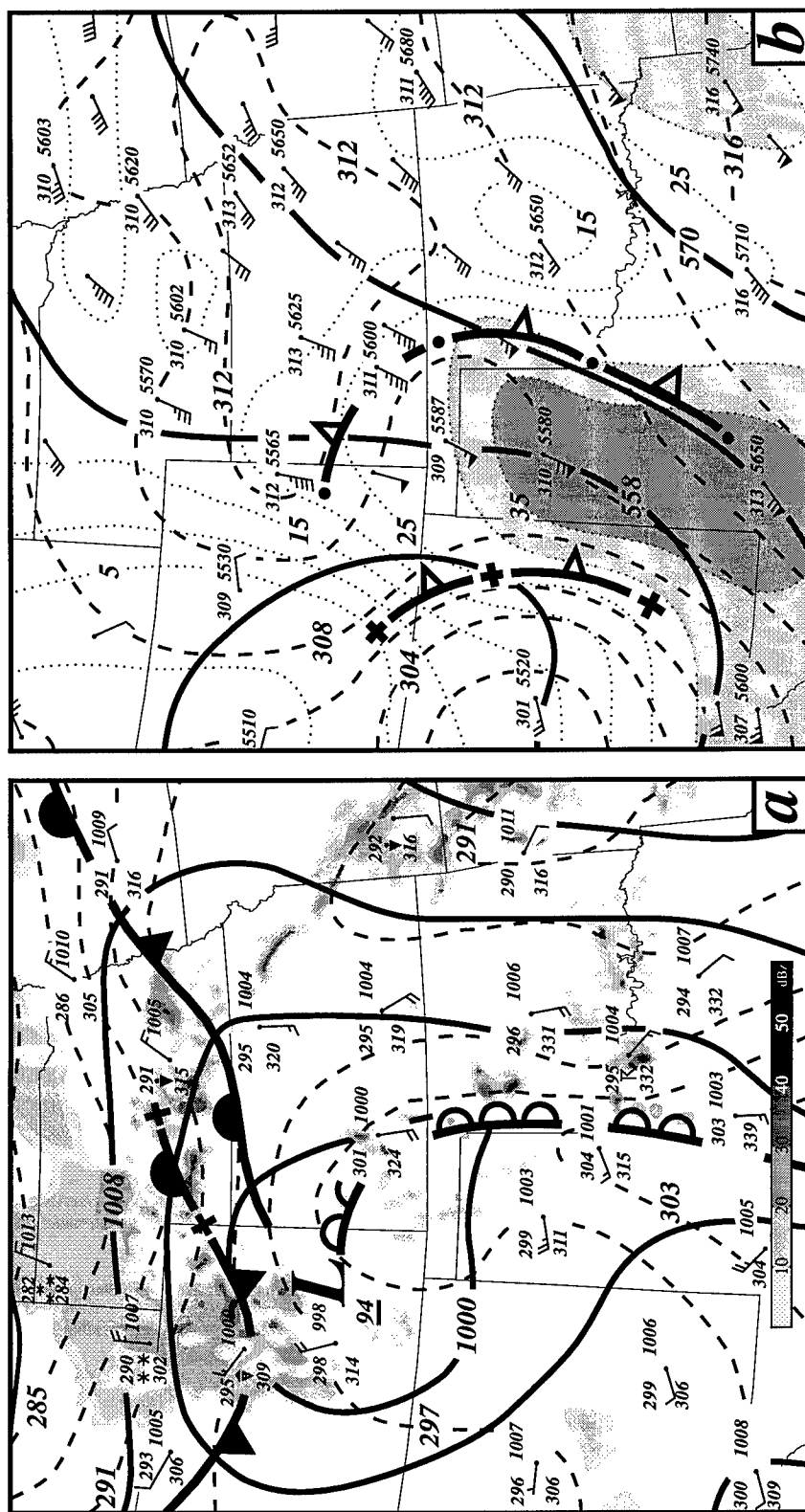


Figure 3.10. (a) 0000 UTC 09 March 1992 surface analysis: isobars (solid - mb), theta (dashed - $^{\circ}\text{K}$), radar echo's (shading - interval of 10 dBz). Station plot: theta, theta-e, PMSL, observed weather, wind barb (full staff - 5 ms^{-1} , half staff - 2.5 ms^{-1}). Surface dry line depicted by line of open semicircles. Frontolysis depicted by broken line separated by a cross. (b) 0000 UTC 09 March 1992 500 mb analysis: heights (solid - dm), isotachs (dotted / shading - ms^{-1}), theta (dashed - $^{\circ}\text{K}$). Station plot: theta, height, and wind barb (flag - 25 ms^{-1} , full staff - 5 ms^{-1} , half staff - 2.5 ms^{-1}). Upper level cold front depicted by line of open triangles. Frontogenesis depicted by broken line separated by a closed circle. Frontolysis depicted by broken line separated by a cross.

mountain flow over west Texas. This feature represents the forward extent of the southern branch of the polar jet that extends westward across the northern portion of the Baja peninsula. Inspection of the thermal field over the central Plains reveals a distinct disruption of the temperature pattern. A pool of cold air is poised over the inner-mountain region with an upper-level cold front situated over western New Mexico. Meanwhile, a narrow ridge of warm air is tied to the Front Range of the Rockies as potential temperature in excess of 312K extend well into east-central Colorado. The strong warming induces a cold pool over Oklahoma as temperatures remain near 311K well into southern Oklahoma.

By 08/18 UTC the 500 mb pattern appears to have changed little over the past six hours (Fig. 3.6b). However, the cold dome over the inner-mountain region has shifted slowly eastward enhancing the baroclinicity over eastern New Mexico. Passage of the upper-level cold front over ELP has resulted in a 5°C drop while temperatures fell 4°C at Albuquerque, New Mexico (ABQ). Despite the eastward propagation of the cold dome, height falls are confined to the inner-mountain region as leeside warming acts to retard the propagation of the cold air. Modest six-hour height falls of 20 m are observed over New Mexico while the height field is kept in check in the lee of the mountains. Observations from AMA; Guymon, Oklahoma (GUY); and Burlington, Colorado (3V1) all report negligible change in the reported 500 mb heights. The amplified height gradient produces an increase in the geostrophic wind field over eastern New Mexico. Meanwhile, the main portion of the observed jet streak, previously located over New Mexico, is suppressed southward. The juxtaposing of the observed and the geostrophic jet max provides a signal

of the developing imbalance between the mass and momentum fields. In response, a finger of momentum is observed to be racing out ahead into the Texas panhandle indicative of the accelerations taking place as the observed winds strive to regain a balance with the geostrophic winds. These signals will be addressed indepth in section 3.7.

By 08/21 UTC a distinct disruption in the thermal field is observed coincident with the developing jet streak as a cold pool forms downstream of the mountain barrier (Fig. 3.7b). Sounding data from AMA (Fig. 3.4) captures the onset of cooling as it over spreads the area extending from northeastern New Mexico into the Texas panhandle. The corresponding infrared satellite image reveals an enhanced mid-level cloud formation over this region developing out ahead of the main cloud mass poised over the inner-mountain region (Fig. 3.3c). This downstream cloud mass forms (in an area that was previously devoid of any moisture) in response to the destabilization brought on by the mid-level cooling. At this time, a distinct bifurcation in the southern jet has developed over the Texas panhandle. The wind direction has become more southerly while the wind speed increased in excess of 30 ms^{-1} .

A significant increase in cold air over the Texas panhandle is observed by 09/00 UTC and is evidence of the formation of a CFA just east of the Texas panhandle (Fig. 3.10b). This midtropospheric feature is superimposed over a low-level thermal ridge with the cold front located well to the northwest of the region. This feature has formed 300-500 km downstream of the leading edge of cold air associated with the primary upper-level low. In response, the upper-level front over New Mexico begins to dissipate as the baroclinicity between the Front Range and the inner-mountain region is diminished.

Meanwhile, a significant jet streak has emerged over west-central Texas with 35 ms^{-1} winds extending from AMA to MAF.

3.6. Terrain-Induced Leaside Warming and Associated Mass Perturbation

3.6.1 Downslope Adiabatic Warming

The cross-mountain flow provides an important mechanism in perturbing the mass structure in the lee of the mountains. By 1200 UTC 8 March 1992, the STORM-FEST observations depict a midtropospheric jet exit region situated over eastern New Mexico. This jet streak represents the forward quadrant of the southern branch of the polar jet stream which extends well west of the Baja peninsula. The 500 mb flow in Fig. 3.5 depicts a persistent southwesterly flow across the southern Rockies. This cross-mountain flow intercepts the barrier within 30° of perpendicular to the ridge line supporting moderate downslope conditions. In response, a wedge of warm air forms along the southern Front Range of the Rockies. This zone of localized warming acts to disrupt the thermal pattern over the central Plains separating a pool of cold air over the inner-mountain region from cooler conditions over eastern Oklahoma (Fig 3.5a and b).

Between 08/12 and 08/21 UTC, the 500 mb temperatures warm to -16°C as far north as the panhandle of Oklahoma. Calculations of thermal advection in the lower troposphere don't account for the strong warming observed over this area. One of the primary mechanism for this warming is generated by adiabatic compression as air parcels

descend down the Front Range of the southern Rockies. A signal of this warming is observed in the sounding data located along the southern foothills. A series of sounding profiles from MAF reflect the existence of a building dry adiabatic layer during the course of the day (Fig. 3.9). As the air flows down the mountain side, the vertical temperature profile tends towards an adiabatic lapse rate. At 08/15 UTC the adiabatic layer extends from 865 mb to 790 mb. By 08/21 UTC, the terrain enhanced warming builds the adiabatic layer up to the 700 mb level. An additional signal of the observed warming is obtained by vertical cross sections constructed over southeast New Mexico. These plots reveal a signal of descending motion in the lower troposphere as the flow crosses the barrier. A strong signal of a downfolding of the isentropic surfaces, in relation to the descending motion, is observed in the immediate lee of the Rockies indicative of the developing adiabatic layer in the lower atmosphere (Fig. not shown).

Parcel trajectories provide further insight into the impact of the downslope flow. In order to accurately follow the positions of parcels as they move through the simulated environment, the Mesoscale Atmospheric Simulation System Trajectory package (MASSTRAJ) was developed and tested by Rozumalski (1996). MASSTRAJ is a trajectory package which utilizes the MASS model's simulated mass and momentum fields to retrace the path of a parcel. Trajectory calculations are performed within the same σ_p coordinate system (u, v, σ) as the simulation in which parcels are advected by a time dependent iterative scheme

$$X^{(n+1)\delta t} = X^{n\delta t} + \bar{u}_i^{n\delta t} m \delta t \quad (8)$$

$$y^{(n+1)\delta t} = y^{n\delta t} + \bar{v}_i^{n\delta t} m \delta t \quad (9)$$

$$\sigma^{(n+1)\delta t} = \sigma^{n\delta t} + \bar{\sigma}_i^{n\delta t} \delta t \quad (10)$$

where 'm' is the map scale factor on the polar stereographic grid, Δx and Δy is the model horizontal grid spacing, 'n' is a timestep number ranging from $1 \rightarrow N$ where N is a user specified value, and δt is the small time step used between dataset updates for the advection of parcels as determined by $\delta t = \Delta t/N$. Here Δt is the time between model simulation datasets. For all the trajectory computations in this study, $\Delta t = 30$ min, $N=20$, and $\delta t = 90$ sec.

The individual components of the advective velocities (\bar{u} , \bar{v} , $\bar{\sigma}$) are determined by the following

$$\bar{v}_i^{n\delta t} = \bar{v}_i^{t_0} + \left[\frac{(\bar{v}_i^{t_0+\Delta t} - \bar{v}_i^{t_0})}{\Delta t} \right] n\delta t, \quad (11)$$

$$\bar{u}_i^{n\delta t} = \bar{u}_i^{t_0} + \left[\frac{(\bar{u}_i^{t_0+\Delta t} - \bar{u}_i^{t_0})}{\Delta t} \right] n\delta t, \quad (12)$$

$$\bar{\sigma}_i^{n\delta t} = \bar{\sigma}_i^{t_0} + \left[\frac{(\bar{\sigma}_i^{t_0+\Delta t} - \bar{\sigma}_i^{t_0})}{\Delta t} \right] n\delta t, \quad (13)$$

The subscript i denotes the number of iterations done to determine the final mean advection velocity. The mean velocities between datasets are determined by first temporally interpolating between model data sets to obtain an initial velocity at time t_0 . The parcel is then advected forward (backward) by δt to a new location in time and space ($t_0 + \delta t$). The new parcel velocity is determined and the parcel is returned to its original position at t_0 . At this point the two parcel velocities at t_0 and $t_0 + \delta t$ are averaged and the new mean velocity is used to advect the parcel again. This iterative process occurs three times before the final mean velocity vector is $(\bar{u}, \bar{v}, \bar{\sigma})$ at which time the final advection of the parcel occurs.

Parcel characteristics are taken to be the same as those of its surrounding environment. Changes in the potential temperature of a parcel are assumed to be due to diabatic processes, although some small errors from interpolation may occur. Horizontal gridded data are interpolated to the parcel position by a bi-cubic interpolation method. This method is an improvement over traditional bi-linear schemes in regions of large horizontal gradients often simulated by high resolution atmospheric models. Backward trajectories are computed in the same manner as forward trajectories with $\delta t = -\delta t$.

In order to determine the source of the low-level air, trajectories were initiated at a near surface pressure level of 850 mb at 08/21 UTC and run back in time to 08/15 UTC. Back trajectories for two parcels depicted in Fig. 3.11 reveal the strong downslope signal as the flow passes over the mountain barrier. The topography in this region is unique in that its concave orientation to the flow provides a focused region of warming downwind of the barrier. The western parcel over New Mexico originates at the 818 mb level at

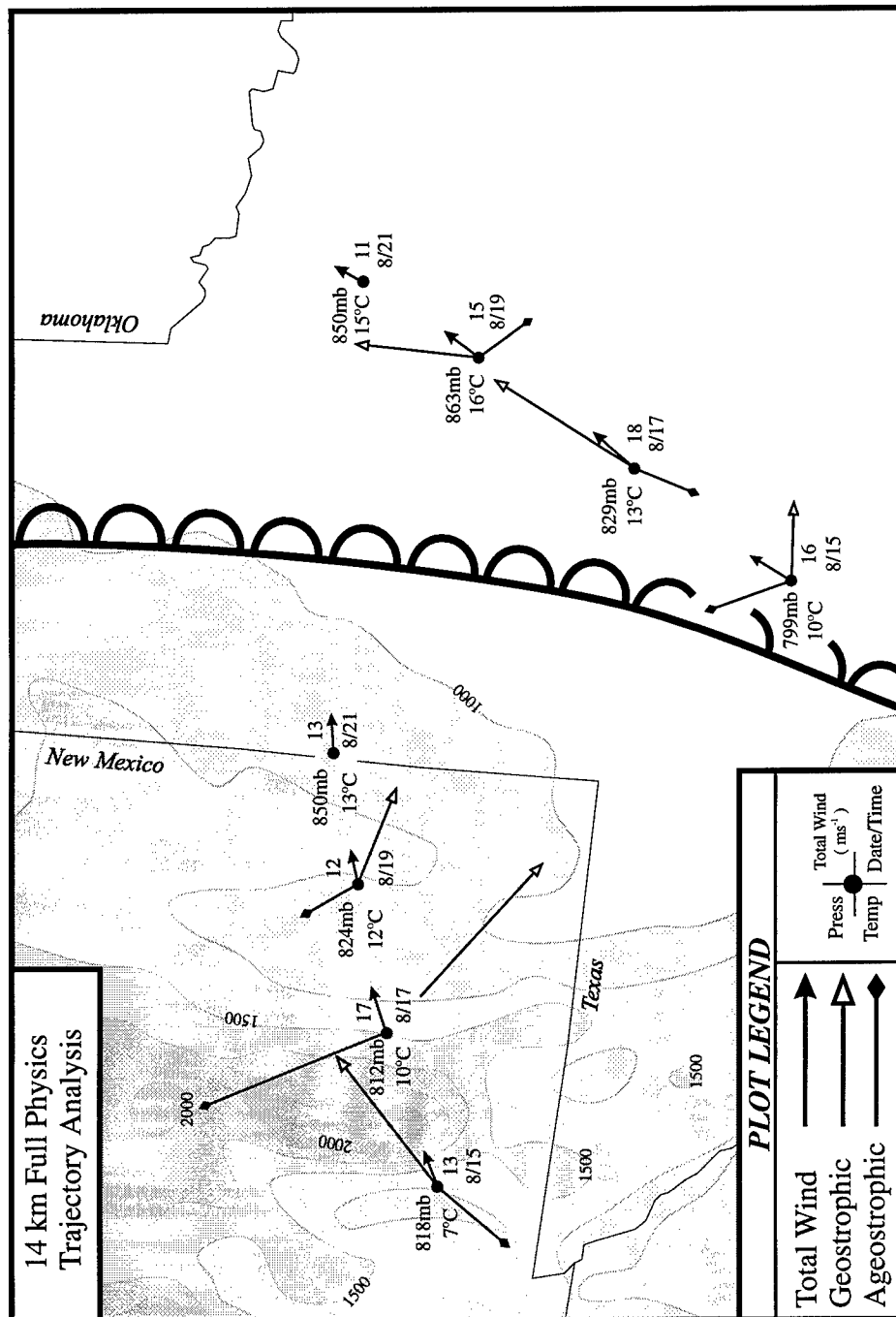


Figure 3.11. Back trajectory constructed from 14 km full physics MASS model output. Trajectory initialized at 2100 UTC 8 March 1992 and ran to 1500 UTC 8 March 1992. Station plot contains parcel pressure level (mb), temperature (°C), total wind speed (ms⁻¹) and time of parcel location. Displayed wind vectors depict total wind vector (solid head), geostrophic component (open head), ageostrophic component (diamond head). The 1800 UTC dryline position is depicted by the thick solid line with half circles. Topography shaded/contours at 250 m interval above 1000 m.

08/15 UTC and rapidly descends to 850 mb by 08/21 UTC. During the course of this descent, the parcel passes over the Sacramento mountains at over a 75° angle to the barrier. In response, the parcel undergoes significant warming as initial temperatures of 7°C warm to 13°C by 08/21 UTC. The strong topographical impact on the parcel motion is evident in the disruption in the geostrophic and ageostrophic components of the wind field as the parcel interacts with the terrain. This results in a pattern that is too convoluted to provide meaningful insight.

The parcel trajectory over central Texas indicates the presence of an elevated subsiding flow that extends well out over the low-level moisture field ahead of the dryline. This parcel intercepts the mountains in the Big Bend region at nearly a right angle. In a span of six hours, the parcel begins its descent from the 799 mb level down to the 850 mb level at 08/21 UTC. During the descent a 5°C increase in temperature is observed while the moisture content is reduced nearly 50% from 6.79 gm kg^{-1} to 3.53 gm kg^{-1} . This region of subsiding air acts as a source of warm dry air that limits the vertical extent of moisture while increasing the convective instability.

3.6.2 Focused Boundary Layer Sensible Heating

The downslope flow not only induces an adiabatic warming but also acts to dry the atmosphere as evident by the series of soundings from MAF (Fig. 3.9). The vertical moisture distribution reveals an extremely dry profile that extends to the surface shortly after 08/15 UTC. These conditions persist from the New Mexico/Texas border northward

into eastern Colorado. This signal is evident by the cloud free zone over the south-central Plains observed in the 1301 UTC satellite imagery (Fig. 3.3a). Shortly after sunrise, the extensive dry layer limits the amount of absorption and scattering of short-wave radiation penetrating this region. This allows maximum sensible heating of the boundary layer over a confined region along the southwest Plains. In response to the increased solar heating, the 1731 UTC infrared satellite imagery shows a narrow wedge of hot air (dark region) forming in the lee of the southern (Fig. 3.3b).

In response to the maximized surface sensible heating, the boundary layer rapidly deepens. This results in an increase of the vertical temperature gradient and thickness field over western Texas as sensible heating is maximized over the region. Typical of the sounding structure along the southwestern Plains, the series of soundings out of MAF provides a signal of the expanding boundary layer (Fig. 3.9). The evolution of the sounding structure reveals the transformation from an early morning stable (nocturnal) boundary layer to that of an expanding convective boundary layer (Stull 1993). During a span of six hours, the near-surface temperature warms from 13°C to 26°C as an unstable surface layer develops. In response, buoyancy provides an effective mechanism in driving turbulent mixing. This mixing acts to transport heat and moisture aloft resulting in a nearly uniform vertical profile as the convective boundary layer deepens. By 08/21 UTC, the expansion of the boundary layer is evident as the inversion base lifts from the 870 mb all the way to the 650 mb level.

3.6.3. Mountain Wave Activity

Downslope adiabatic flow and enhanced low-level solar heating modify the atmosphere. This restructuring often leads to the formation of a number of complex circulations of varying length scales downstream of the mountains. Large amplitude mountain waves generated by terrain can perturb the mass field and result in severe downslope winds, clear air turbulence.

During IOP-17, the interaction between the terrain and the flow results in the formation of standing mountain waves. This activity is evident from satellite imagery displayed in Figs. 3.3a and b. Cloud elements "B" and "C" reveal the formation of orographically-forced clouds that are developing on the crest of the mountain. A review of satellite imagery reveal these waves to be of a stationary nature with a wavelength of a ~160 km. The terrain over central New Mexico into western Texas is oriented nearly perpendicular to the low-level flow observed in this region (Fig. 3.12a). The terrain averages nearly 1800 meters with isolated ridges extending to 2400 meters. The southwesterly flow observed at 700 mb with 10 ms^{-1} winds provide sufficient low-level forcing to initiate wave activity. Assessment of the structure of the vertical motion pattern was obtained by taking the gridded observational data sets and computing kinematic omega using the General Meteorological Package (GEMPAK) (DesJardens *et al.* 1992). Despite the sparse data resolution over this region, the vertical motion distribution indicates a terrain-induced wave pattern consistent with that observed by satellite (Fig. 3.12b). The wind field was based upon a composite of RAOB and wind profiler data as

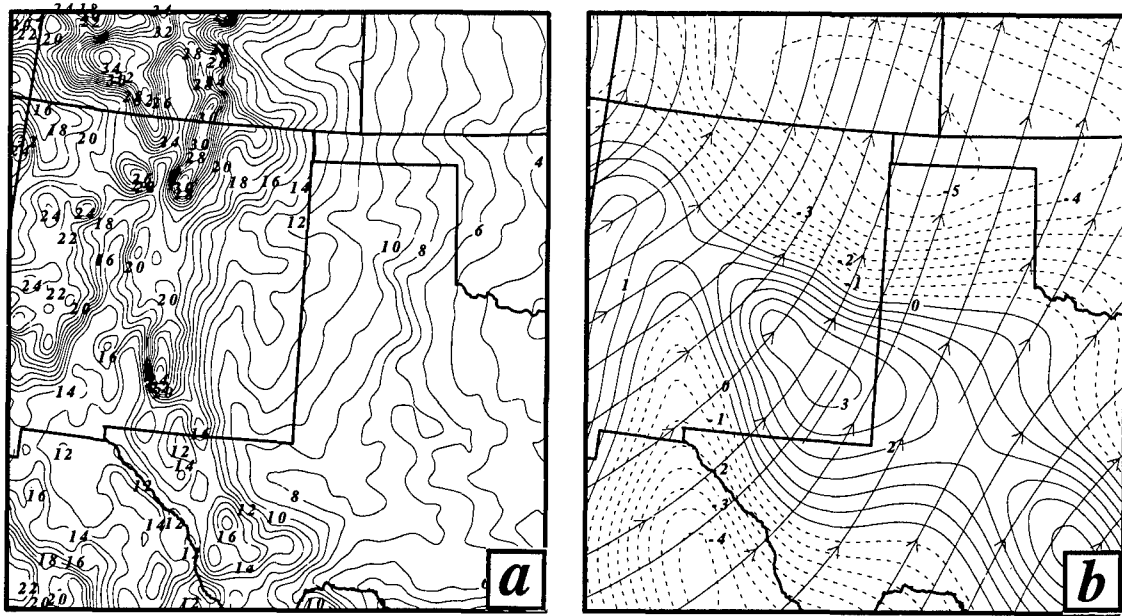


Figure 3.12. (a) Topography over New Mexico/ Texas. Solid lines depict elevation at a 100 m interval. (b) 1200 UTC 8 March 1992 objectively analyzed 700 mb streamline analysis (thin arrows) and kinematic omega at an interval of $0.5 \mu\text{bar s}^{-1}$. Thin solid line depicted region of decent and dashed lines depict ascent.

described in section 2. Due to the coarse nature of the grid and observations, the gradients and wavelength of the features are imprecise. However, a distinct wave pattern is observed in relation to the large scale terrain features. Inspection of the sounding profile over El Paso, Texas at 08/12 UTC clearly reflects an atmosphere capable of trapping energy in the low levels (Fig. 3.13a). An elevated adiabatic layer extends from 600-280 mb with stable layers above and below.

The use of linear theory to describe small amplitude gravity wave activity is not applicable to the large amplitude mountain wave activity often experienced in the lee of the Rockies (Durrán 1986). Efforts by Klemp and Lilly (1975) suggest wave formation is controlled by the vertical stability profile of the atmosphere and the magnitude of the low-level flow across the barrier. Such waves are ideally generated when the atmosphere consists of a three-layer mode in which a mid-level adiabatic layer is bounded by strong stable layers below and aloft. This profile allows a portion of the vertically propagating wave energy to be reflected back towards the surface.

Evaluation of the vertical distribution of the Scorer parameter provides an effective means of assessing the ability of the atmosphere to trap wave energy. The computation of the Scorer parameter (l^2) is determined from the vertical and horizontal wave numbers through the relation

$$l^2 = \frac{N^2}{U^2} - \frac{1}{U} \frac{d^2U}{dz^2} \quad (14)$$

where 'N' is the Brunt-Väisälä frequency and 'U' is the mean wind. Waves tend to propagate vertically in regions where the Scorer parameter is greater than the horizontal

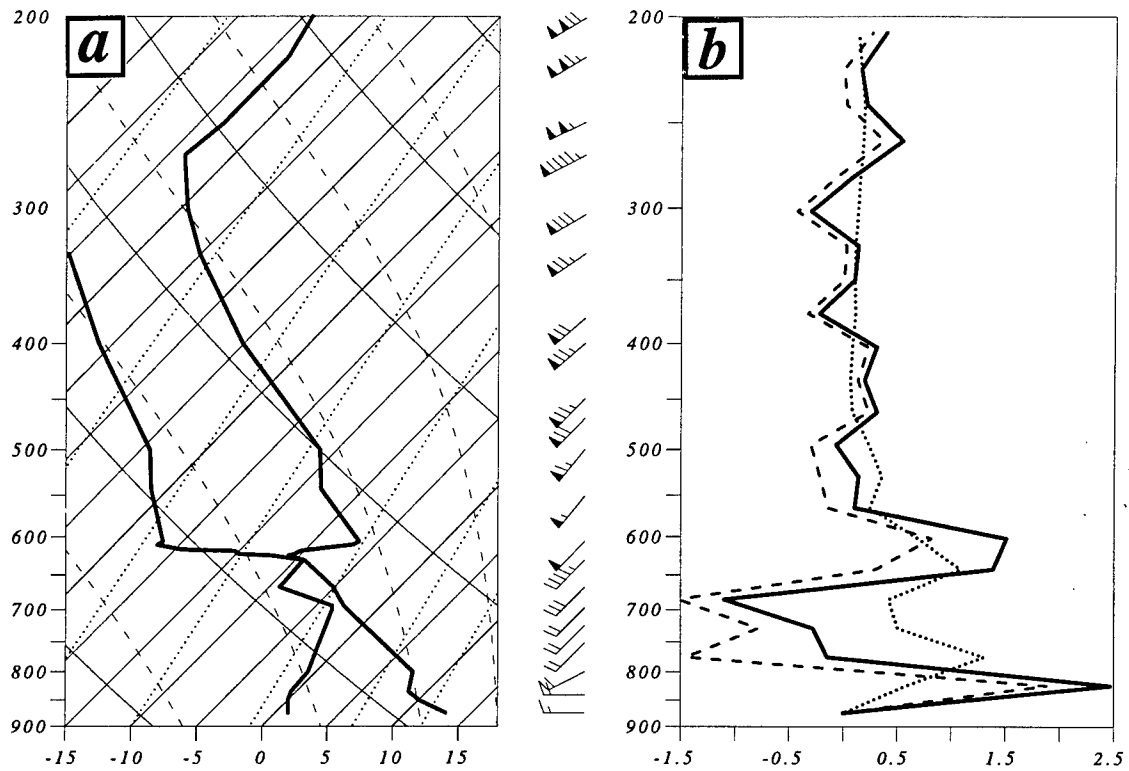


Figure 3.13. (a) 1200 UTC 8 March 1992 sounding from El Paso, Texas. Thick solid line depicts observed temperature and dew point ($^{\circ}\text{C}$). Isotherms - thin solid lines running from lower left to upper right, dry adiabats - thin solid lines running from lower right to upper left, moist adiabats - dashed lines running from lower right to upper left, mixing ratio - dotted lines running from lower left to upper right. Wind profile depicted at right (full staff - 5 ms^{-1} , half staff - 2.5 ms^{-1}). (b) The corresponding vertical profile of Scorer parameter ($\times 10^{-6} \text{ m}^{-2}$ -- solid line). First term of Scorer parameter $\{ N^2/(U-C)^2 \}$ depicted by dotted line and second term $\{ (U-C)^{-1} d^2U/dz^2 \}$ is depicted by dashed line.

wave number and where the Scorer parameter is less than the horizontal wave number the waves are evanescent. To obtain significant trapped lee wave energy in the lower levels, l^2 must decrease with height and change sign. The first term of the Scorer parameter, which controls the vertical wave number, will assist in decreasing the parameter with height if the static stability decreases with height or the ambient wind relative to the wave propagation increases. The second term, which controls the horizontal wave number, contributes to a decrease with height as the curvature of the vertical wind profile increases with height. The Scorer profile in Fig. 3.13b is derived from the ELP sounding at 08/12 UTC and is representative of the environment capable of supporting mountain wave activity. The profile is consistent with an atmosphere capable of reflecting vertically propagating wave energy where the Scorer parameter decreases rapidly with height and changes sign at the 780 mb level. The second term of the calculation dominates in reversing the sign of the profile in response to the vertical wind shear observed below 680 mb. Additionally, a decrease in the Brunt-Väisälä frequency between 680 - 840 mb contributes to the negatively-tilted profile.

Evaluation of high resolution 14 km numerical model data over the region indicates the presence of standing mountain waves. Over the period from 1200-1900 UTC 8 March 92, a strong stationary signal of mountain wave activity is found in the vicinity of the cloud elements observed in the satellite imagery (Fig. 3.3b). The six-hour forecast, valid at 08/18 UTC, shows the 600 mb flow over southwest Texas intercepting the terrain within 30° from perpendicular of the ridge line (Fig. 3.14a). The vertical motion pattern set up by this regime generates stationary waves that are aligned orthogonal to the mean

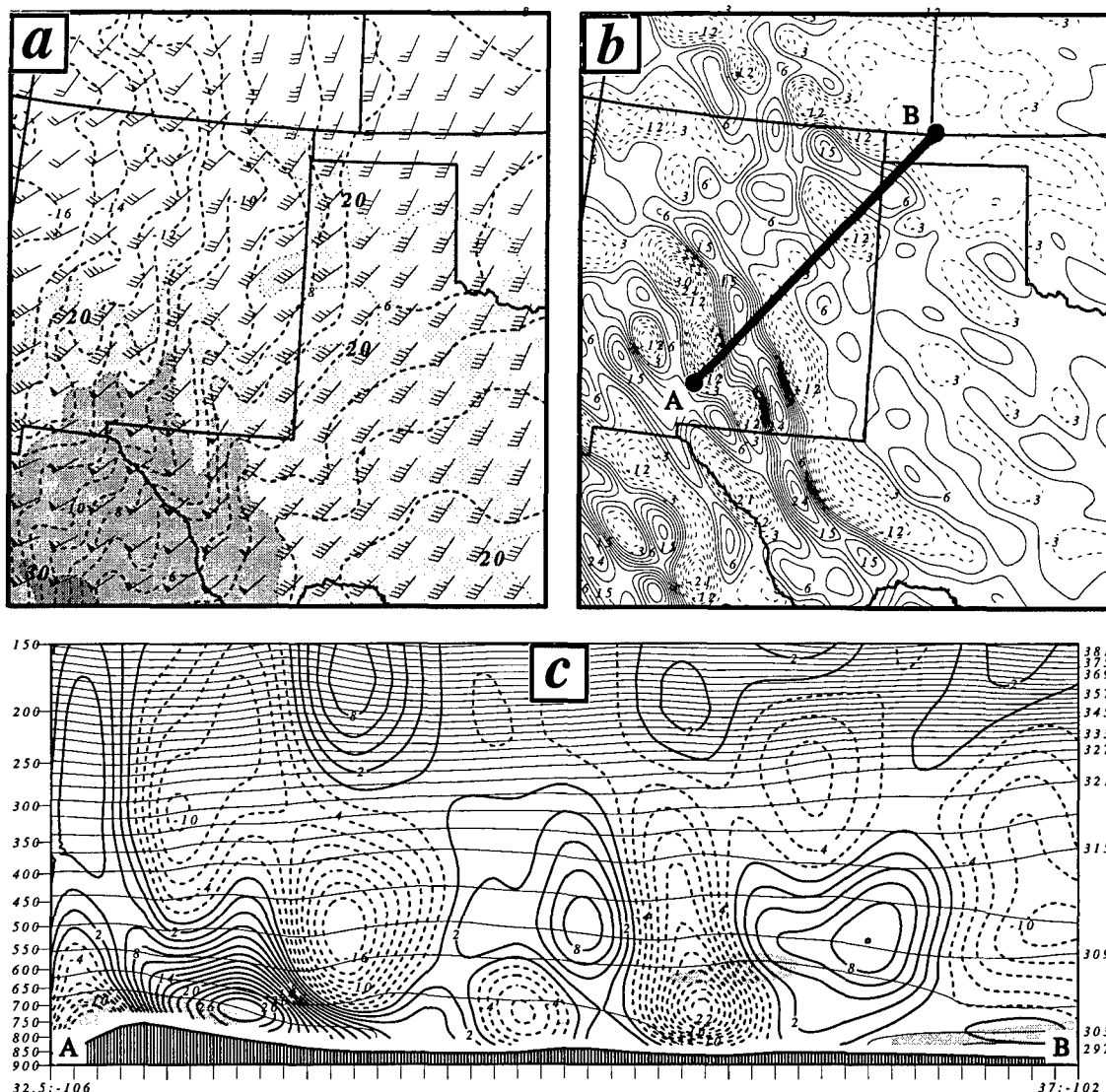


Figure 3.14. 14 km MASS model generated fields valid at 1800 UTC 8 March 1992. (a) 600 mb wind barbs (full staff - 5 ms⁻¹, half staff - 2.5 ms⁻¹), isotachs above 20 ms⁻¹ shaded at an interval of 5 ms⁻¹, and isotherms. displayed as dashed lines at an interval of 1°C. (b) 600 mb horizontal depiction of model generated values of kinematic omega depicted by dark solid lines (descent) and dashed lines (ascent) at an interval of 2 μbar s⁻¹ and (c) Vertical cross section displays kinematic omega by dark solid lines (descent) and dashed lines (ascent) at an interval of 2 μbar s⁻¹, thin solid lines depict theta surface at an interval of 3°C, and relative humidity shaded above 70%. Location of cross section 'A-B' displayed in Fig. (b).

flow (Fig. 3.14b). These waves have a horizontal wavelength of ~170 km in which wave activity extends well downstream into the Texas panhandle. A cross section, taken parallel to the flow, shows the vertical motion pattern has little phase tilt in the lower troposphere (Fig. 3.14c). This pattern is indicative of waves trapped in the lower troposphere. Meanwhile, energy that has penetrated the upper levels exhibits an upstream phase tilt characteristic of a vertically propagating wave (Lin and Wang 1996, Lindzen and Tung 1976). The generation of the mountain wave activity provides an indication of the complex interaction between the terrain and flow as complex secondary circulations are generated downstream of the barrier.

3.6.4 Terrain Induced Mass Perturbation

The combined influence of clear skies, which allow significant surface sensible heating, downslope adiabatic warming, and the formation of mountain wave activity all support the development of a narrow corridor of strong low-level warming confined to the western Plains. The impact of these processes are evident as rapid warming of the low-level temperature field is confined to the lee of the southern Rockies (Fig 3.15). Within a six-hour period, an increase in excess of 12°C in the surface temperature is observed over eastern Colorado/New Mexico. Meanwhile, persistent clouds and showers over the eastern Plains maintain a region of minimal warming despite strong warm advection from the Gulf of Mexico. The non-uniform surface heating results in intense heating focused over a localized area that induces an uneven height fall distribution over the central Plains.

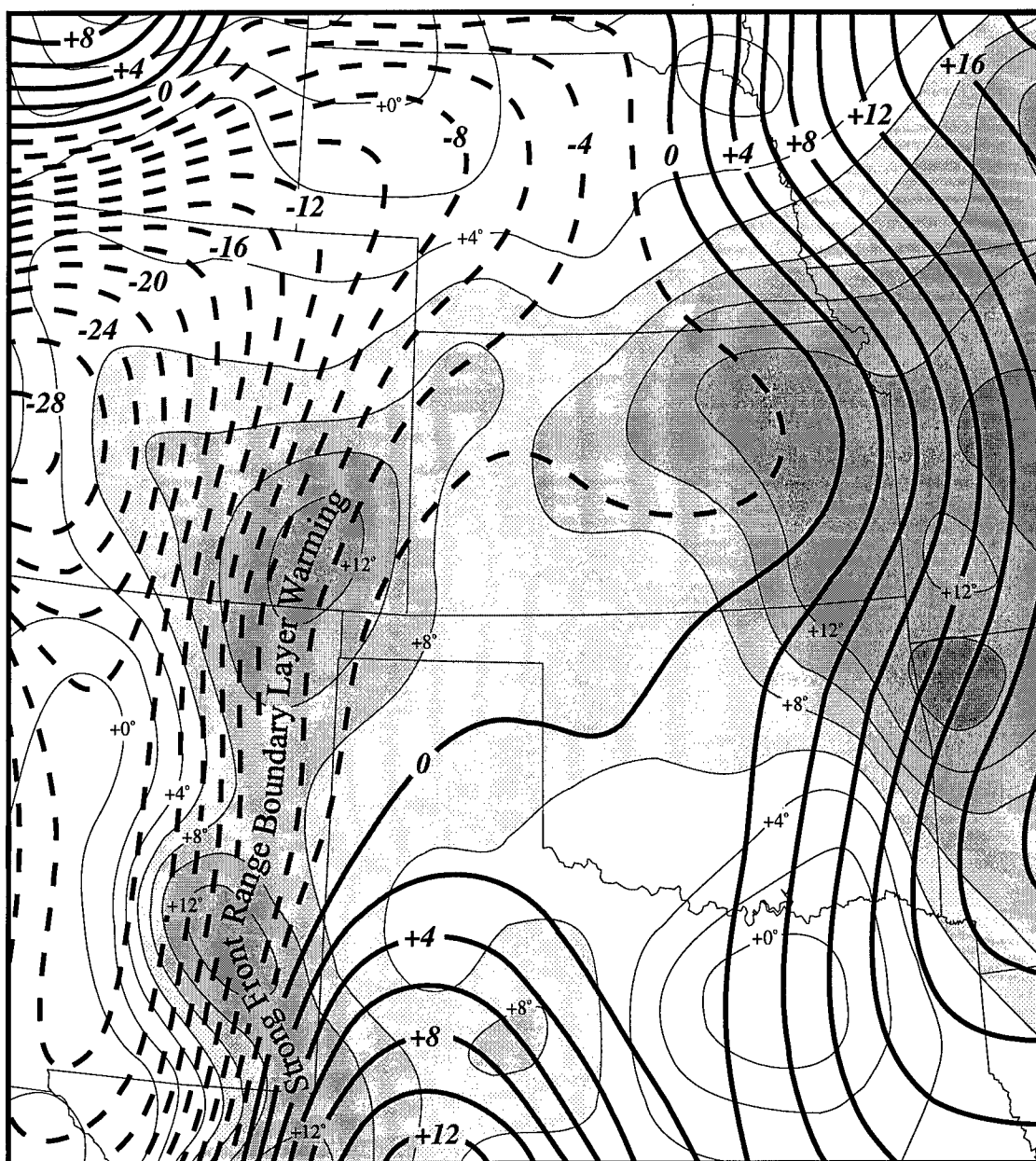


Figure 3.15. Six hour change in 500 mb height (m) and surface theta (K) fields between 1200 UTC and 1800 UTC 8 March 1992. 500 mb height falls depicted by thick dashed lines and height rises depicted by thick solid lines. Change in surface theta field depicted by thin lines/shaded region.

Inspection of the synoptic scale height change pattern reflects the quasi-geostrophic signal of the slow approaching 500 mb low over the inner-mountain region and the building ridge associated with warm advection over the Mississippi Valley (Fig. 3.15). However, in response to the wedge of low-level warming focused along the Front Range, height rises over western Texas splits the height fall pattern observed over the Great Plains.

3.7 Geostrophic Adjustments and Genesis of the Cold Front Aloft

3.7.1 Modified Secondary Circulation

During the 08/12-08/15 UTC period, the 500 mb jet streak located over central New Mexico begins to pull out of the inner-mountain region. Meanwhile, the strong warming in the lee of the Rockies acts to block the cold air from entering into the western Plains. As the jet streak extends across the Front Range the jet encounters an environment that is no longer in thermal wind balance in a manner similar to that described by Mattocks and Bleck (1986). The cold air previously associated with the jet streak is blocked by the mass perturbation in the lee of the mountains. As the jet exit extends across the mountain barrier the jet becomes superimposed with the wedge of warm air in the lee of the mountains. An atmospheric response in the form of a thermally-direct circulation develops within the jet exit region in order to compensate for the lack of lower tropospheric cold air. The role of the developing ageostrophic motion is to regain thermal wind balance.

This circulation acts to alter the vertical variation in the ageostrophic horizontal velocity which changes the vertical shear, while the vertical motion distribution modifies the temperature structure. In response, a cooling of the mid-levels is observed downstream and to the right of the flow as the atmosphere works to regain a balanced state.

The mass perturbation observed over western Texas has a horizontal length scale of ~525 km. The perturbation has a vertical length scale of ~5 km while the area of west Texas is characterized by a Brunt-Väisälä frequency of 0.01. These parameters result in a Rossby radius of deformation of ~650 km. Consequently, as the jet exit region intercepts the mass perturbation over west Texas, the slow mode of the rotational part of the wind does not have sufficient time to respond. This leads to an increase in a divergent response to the flow that produces a thermally-direct circulation within the exit region of the jet. This leftward-directed flow is not consistent with quasi- or semi-geostrophic jet streak dynamics and is indicative of an accelerating flow in the exit region. This results in the conversion of excess potential energy, generated by the mass perturbation, into kinetic energy in the form of accelerating air parcels.

The developing imbalance is evident upon comparing the observed winds and the geostrophic winds (Fig. 3.16a). Inspection of the 500 mb height field reveals a mesoscale ridge building over west Texas (as seen in Fig. 3.15). This ridge develops in response to the focused warming over the region. This ridge causes an increase in the geostrophic wind along the eastern slopes of New Mexico. By 08/18 UTC the observed jet of 35 ms^{-1} is positioned over ELP while a geostrophic wind max of 45 ms^{-1} is located 300-400 km downstream in the vicinity of Clovis, New Mexico (CVN). The disparity of the two

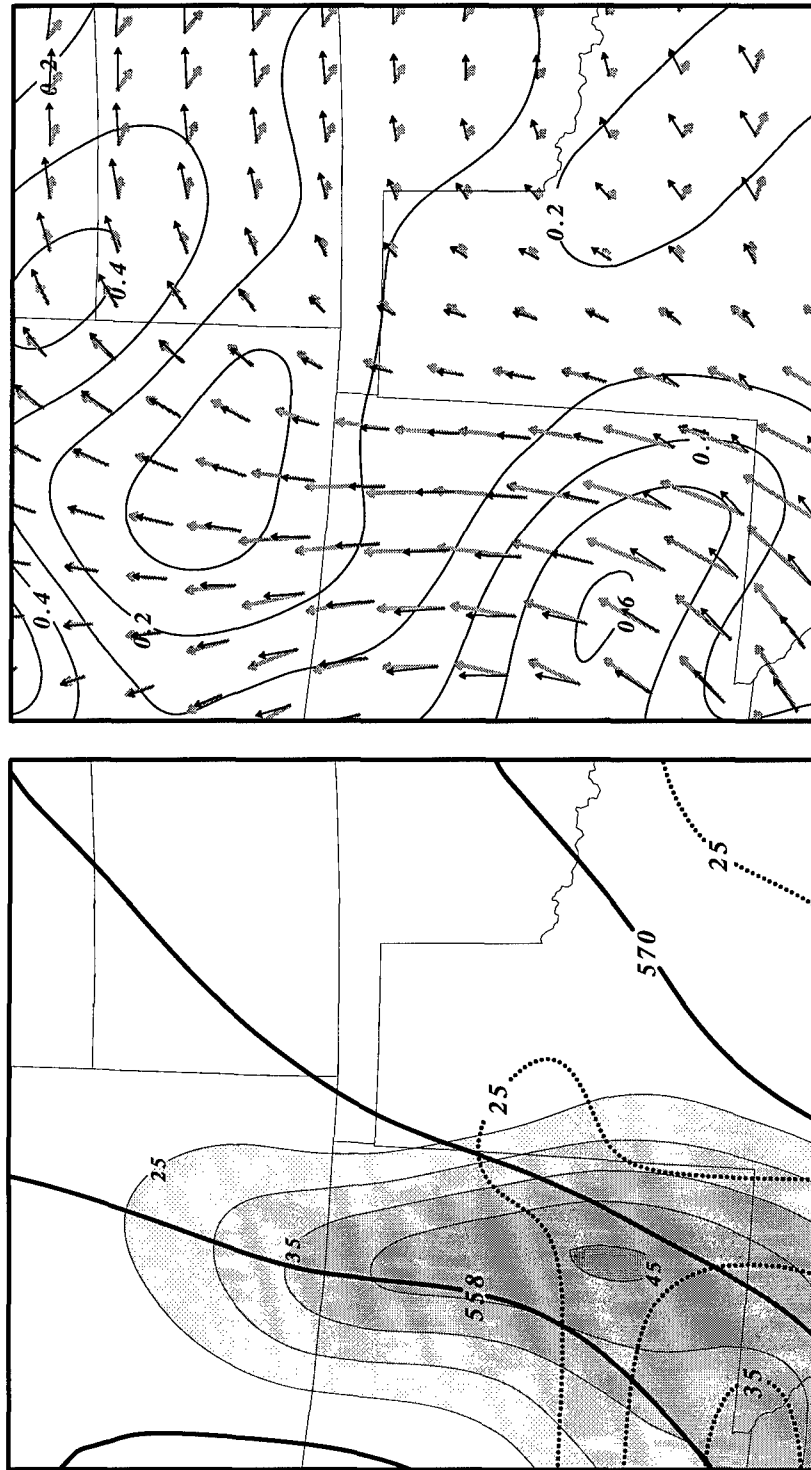


Figure 3.16. Objectively analyzed data for 1800 UTC 8 March 1992. (a) Observed height field (solid line - dm), total wind speed (dotted line - ms^{-1}), and the geostrophic wind speed (shaded - ms^{-1}). (b) Computed inertial Rossby number (solid line), vertical 700-500 mb shear vector (black arrow) and the 700-500 mb thermal wind (gray arrow).

centers results in the observed jet exit region lying within the geostrophic jet entrance region. This configuration is an indication of an accelerating jet exit which is inconsistent with balanced jet concepts. The jet exit region extends to the northeast as inertial advective forcing overwhelms the large scale rotational flow. A measure of the requirement for an adjustment between the mass and momentum field is obtained by evaluating the inertial Rossby number (R_o) which takes the form:

$$R_o \approx \frac{|\mathbf{V} \cdot \nabla \mathbf{V}|}{f|\mathbf{V}|} \quad (15)$$

Uccellini (1984) demonstrated the use of this form of R_o is effective in evaluating regions suspected of unbalanced flow. Regions where the inertial advective forcing is significantly greater than the Coriolis acceleration are an indication of imbalance. In response to the mass perturbation over eastern New Mexico at 08/18 UTC a pocket of high R_o values (in excess of 0.5) are observed (Fig. 3.16b).

Inspection of the disparity between the total and geostrophic 700-500 mb wind shear vectors indicates the thermal wind imbalance over the region wind (Fig. 3.16b). Over southeast New Mexico, the vector difference indicates the development of a thermally-direct ageostrophic flow within the exit region of the observed jet exit region. Meanwhile, over eastern New Mexico the alignment of the vectors indicates the increased along-stream inertial advective forcing acting to achieve a balance. This accelerating flow acts to increase the vertical shear while cooling the atmosphere as the acceleration

produce a net mass divergence which promotes ascent and cooling. In turn, this cooling reduces the thermal gradient thus tending towards a more balanced state.

The 08/18 UTC ageostrophic flow details the acceleration of the forward quadrant of the jet streak in the vicinity of the developing low center over northeast New Mexico (Fig. 3.17a). The streamline analysis reveals a leftward-directed and a subgeostrophic flow over eastern New Mexico indicative of the acceleration taking place. The axis of the jet exit region is influenced by both an along-stream subgeostrophic flow $>10 \text{ ms}^{-1}$ and an extensive region where the cross-stream flow is leftward directed (Fig. 3.17b). The acceleration produces a positive velocity divergence tendency in the exit region. This results in a net mass flux divergence throughout the column, upward vertical motion, and adiabatic expansion in the right-forward quadrant. These adjustments are consistent with an adjustment of the wind to the height field as the wind field strives to be in geostrophic balance through the thermally-direct secondary circulation established by the mass perturbation set up by the terrain.

By 08/21 UTC, the 500 mb analysis indicates a significant increase in the wind field over the Texas panhandle (Fig. 3.7b). However, the majority of the cold air remains tied to the inner-mountain region. In order to regain a balance between the mass and momentum field, the vertical motion over southeast Colorado is accentuated as evident by the rapid deepening of the surface low in which pressure falls exceed 1 mb hr^{-1} (Fig. 3.7a). By 08/21 UTC, the accelerating jet exit region rapidly expands into the Texas-Oklahoma panhandle as the terrain induced secondary circulation acts to further accelerate the exit

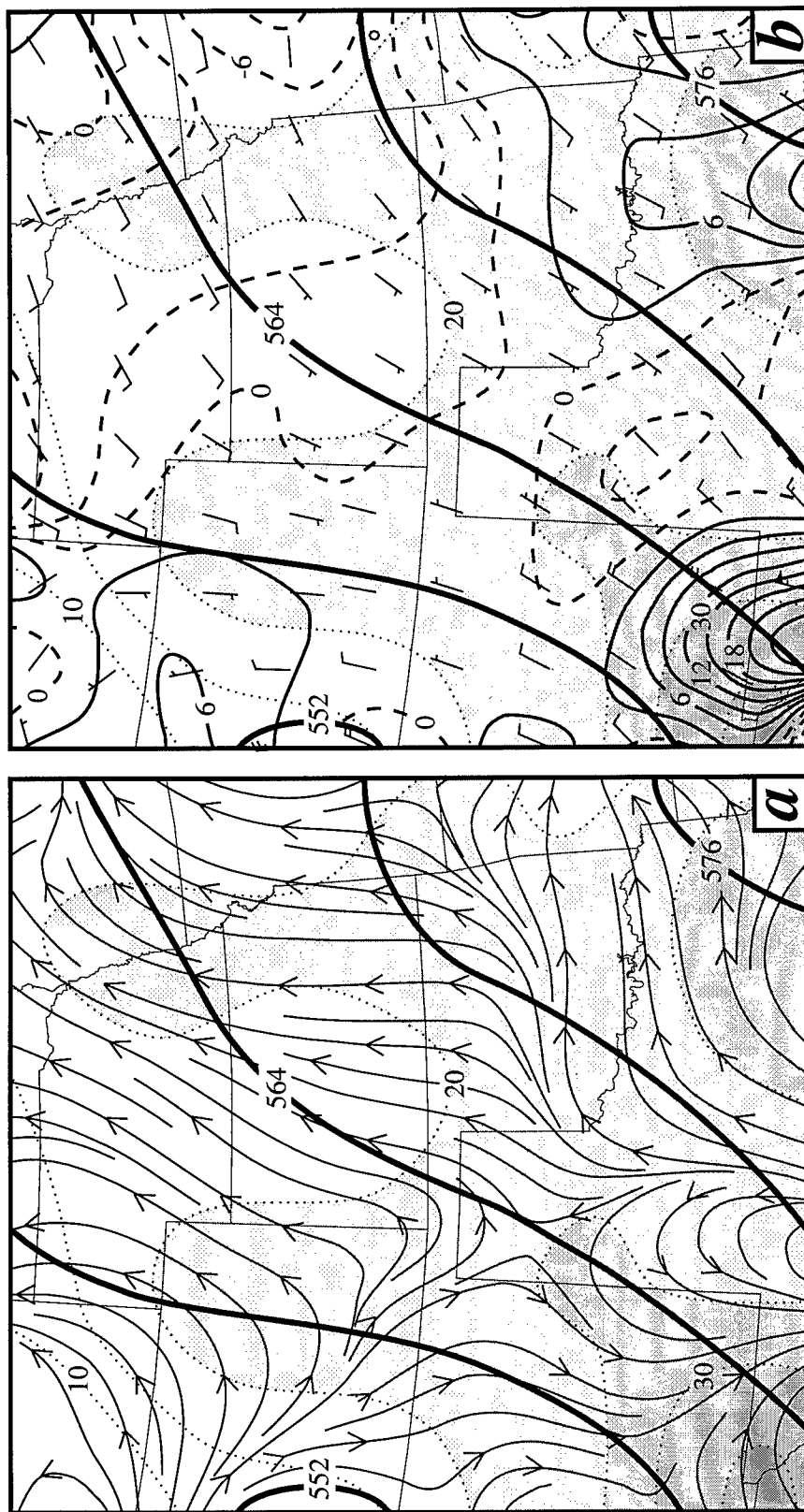


Figure 3.17. 1800 UTC 08 March 1992 500 mb ageostrophic wind analysis derived from gridded data set. (a) Ageostrophic streamline analysis: heights (solid lines - dm), isotachs (dotted/shading - ms^{-1}), streamlines (thin solid lines). (b) Ageostrophic wind components: heights (solid lines - dm), isotachs (dotted/shading - ms^{-1}), ageostrophic component directed left of the stream (thin dashed lines - ms^{-1}), ageostrophic component directed right of the stream (thin solid lines - ms^{-1}), alongstream ageostrophic wind (wind barbs - full staff - 5 ms^{-1} , half staff - 2.5 ms^{-1}).

region downstream (Fig. 3.18). From the quasi-geostrophic momentum equation, the relation between accelerations and the ageostrophic flow is represented by

$$V_a = f^{-1}k \times \frac{dV_g}{dt} \quad (16)$$

where V_a is the ageostrophic wind component, f is the Coriolis parameter, and V_g is the geostrophic wind. Consequently, an acceleration directed downstream of the exit region will result in a ageostrophic flow directed to the left. The ageostrophic streamline analysis indicates a transition period as a “balanced” thermally-indirect circulation is forming in the jet exit region at this time (Fig. 3.18a). The flow is still highly accelerative between MAF and ELP in response to the leftward-directed flow $>6 \text{ ms}^{-1}$ and a subgeostrophic flow $>20 \text{ ms}^{-1}$ (Fig. 3.18b). The inferred ascent acts to further cool the atmosphere over northeast New Mexico that was preconditioned by the earlier mountain wave activity. The partial dry ascent and midtropospheric cooling is reflected in an alongstream temperature gradient evident over the western panhandle of Texas.

Physical evidence of the cooling process is observed by the expanding area of cumuliform cloud mass observed in the satellite data over the region. Satellite imagery at 1301 UTC on 8 March 1992 depicts a north-south orientated band of clouds over western New Mexico (element ‘A’) in association with the large scale baroclinic wave over the inner-mountain region (Fig. 3.3a). Review of time-lapsed GOES-7 imagery indicates the formation of a cloud mass in the immediate lee of the New Mexican Rockies shortly after 08/15 UTC. This area takes on the form of an enhanced mesoscale area of shallow convection that has a total aerial extent covering nearly $18,000 \text{ km}^2$. The 08/1731 UTC

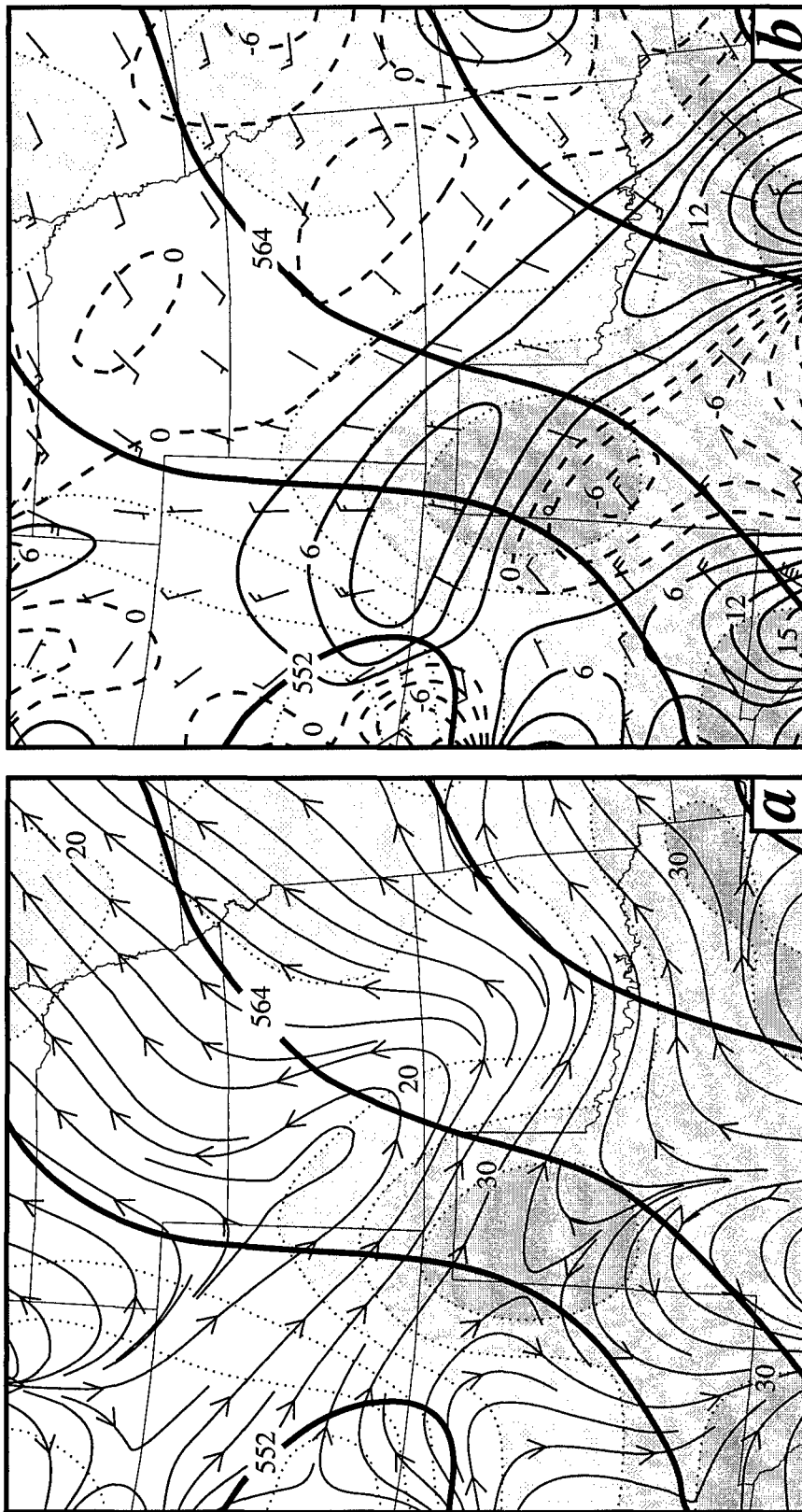


Figure 3.18. Observed 500 mb analysis valid at 2100 UTC 8 March 1992. (a) Heights displayed at an interval of 6 dm (thick solid line), ageostrophic streamline analysis (thin arrows) and isotachs at a 5 ms⁻¹ interval above 20 ms⁻¹ (shaded). (b) Heights displayed at an interval of 6 dm (thick solid line), ageostrophic streamline analysis (thin arrows) and isotachs at a 5 ms⁻¹ interval above 20 ms⁻¹ (shaded).

satellite image clearly shows the developing area extending from Roswell, New Mexico (ROW) northward through CVN and up into Las Vegas, New Mexico (LVS) (Fig. 3.3b). In time, this area rapidly expands towards the northeast leaving the baroclinic wave well behind. Despite the dry conditions, the 08/21 UTC satellite image indicates the area of shallow convection rapidly expands towards the northeast in relation to the expanding jet exit region (Fig 3.3c). By 08/2331 UTC, the enhanced cumuliform cloud mass extends well into the Texas/Oklahoma panhandle with an aerial coverage expanding to over 77,000 km² (Fig. 3.3d). The convective nature of the cloud signature provides a mesoscale signal of the vertical motion and cooling taking place.

The divergent growth over the Texas panhandle can be evaluated by application of the two-dimensional divergence equation (Eq. 4). Scale analysis of Eq. 4 indicates that terms 2, 3, 8, 9, and 10 are relatively small compared to the remaining terms 4-7 (Kaplan and Paine 1977). The first term, total rate of change of the divergent field, is assumed to be near zero while a balance exists between terms 4 through 7. These remaining terms account for the balanced relationship between the mass and momentum fields and is referred to as non-linear balance (NLB) equation. Areas in which these terms sum up to be significantly greater than zero indicate an imbalance between the mass and momentum field as the divergent component of the wind field acts to restore a balance (Moore and Abeling 1988). Application of the NLB equation over the STORM-FEST domain reveals the development of divergent growth over inner-mountain region of central New Mexico northward into Wyoming (Fig. 3.19). This region is characterized by an increasing cyclonic circulation with relatively weak flow. Over the Texas panhandle, a subtle increase

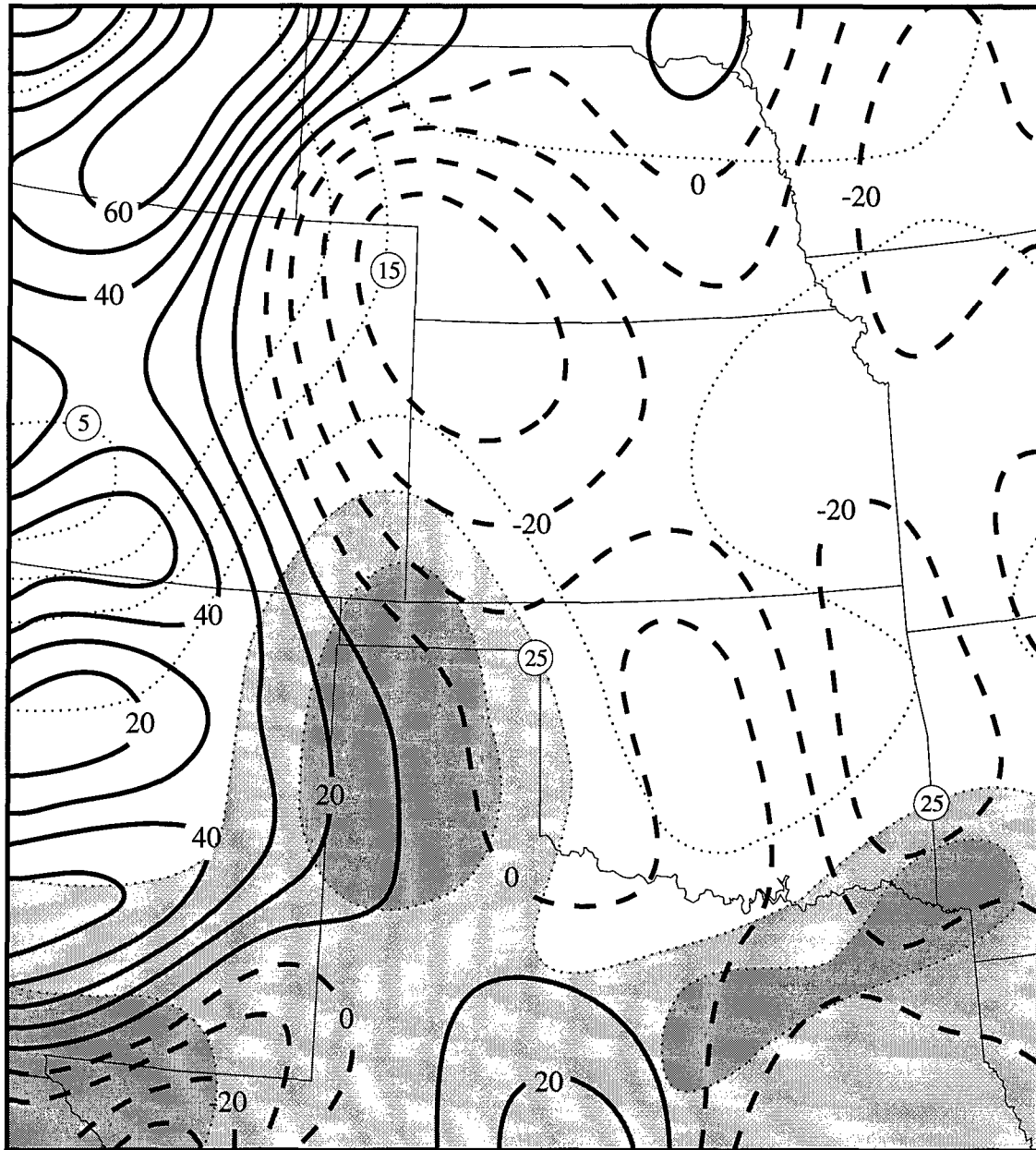


Figure 3.19. 1800 UTC 8 March 1992 500 mb summation of four terms of the non-linear balance equation ($f\zeta$, $+2J(u,v)$, $-\nabla^2\phi$, $-\beta u$). Solid lines are positive divergence values and the dashed values denote negative divergence values ($\times 10^{-10} \text{ s}^{-2}$) and 2100 UTC 08 March 1992 isotachs (dotted / shading - ms^{-1}).

in the divergent field is observed as the jet exit region encounters the mass perturbation (thermal ridge) over west Texas. The location of this feature in relation to the advancing jet streak is of more relevance than areas over the inner-mountain region. Values are not as strong as those observed over the inner-mountain region. However, this may be attributed to either the rather sparse data resolution over the area or the neglect of the advective contribution of divergence. In response to the wedge of warm air, the irrotational component of the ageostrophic flow responds to the perturbation that lies within R_L . This increase in the divergent signal is coincident with the area in which the jet exit region extends towards the Texas panhandle. The large magnitude of the summed inertial terms, $+f \zeta$ and $+2J(u,v)$, in relation to the mass term $(-\nabla^2 \phi)$ accounts for the generation of the mass divergent growth. The divergent tendency is generated as the flow responds to the mass perturbation, whereas the Laplacian of the mass field is not consistent with the flow. Thus, the terrain-induced mass perturbation manifests itself in the form of enhanced divergent field in relation to an accelerating jet exit region. By 08/21 UTC, the accelerating jet streak extends into the Texas panhandle in the region of increased divergent tendencies inferred from the summed four terms just northwest of the region.

Trajectory calculations for parcels passing through the Texas panhandle region between 08/15 and 08/21 UTC provide insight into the nature of the evolving structure of the jet exit region (Fig 3.20). The trajectories were constructed from a 14 km full-physics MASS model run initialized at 1200 UTC 8 March 1992. The parcel trajectories reflect a secondary circulation complicated by the developing mass perturbation. The trajectories

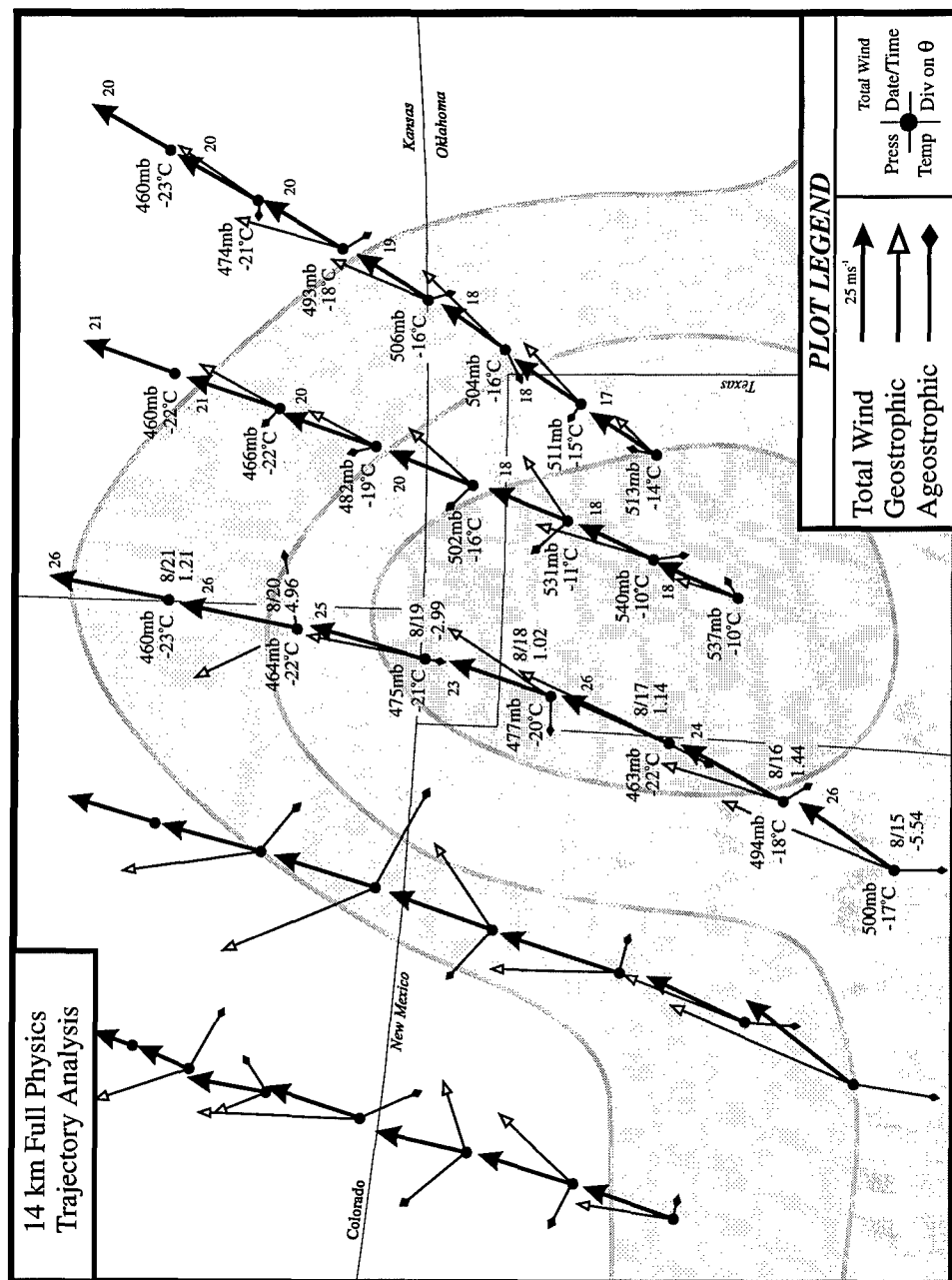


Figure 3.20. Back trajectory constructed from 14 km full physics MASS model output. Trajectory initialized at 2100 UTC 8 March 1992 and ran out to 1500 UTC 8 March 1992. Station plot contains parcel pressure level (mb), temperature ($^{\circ}\text{C}$), time of parcel location, total wind speed (ms^{-1}) and divergence on theta surface ($\times 10^{-5} \text{ s}^{-1}$). Displayed wind vectors depict total wind vector (solid head), geostrophic component (open head), ageostrophic component (diamond head). 2100 UTC 500 mb isotachs depicted above 25 ms^{-1} at a 5 ms^{-1} interval.

show a fairly straight path which indicates that centripetal acceleration does not play a significant role in the acceleration of the parcel. Consequently, the generation of subgeostrophic tendencies can be attributed to the along-stream accelerations caused by horizontal variations in the pressure gradient force taking place rather than the effects of curvature. The three eastern most parcels reflect the environment associated with the developing jet exit region. The center parcel indicates the development of a thermally-direct circulation. An increasingly subgeostrophic flow develops during the first two hours, followed by a 3-hour period in which the total wind is directed left of the geostrophic flow. By 08/20 UTC a thermally-indirect circulation develops. The transformation of the secondary circulation is occurring on a sub-inertial time scale of ~6 hours and reflects the response of the divergent part of the wind as the flow encounters the wedge of warm air. An acceleration in the wind field is observed in a region that should be decelerating according to Q-G theory. Associated with the accelerating flow is a growth in the divergent field promoting ascent and cooling. The generation of cold air as the parcels ascend acts to modify the warm air in order to regain thermal wind balance. The second parcel from the right experiences the most dramatic cooling with temperatures dropping 12°C during the period. This cooling is the result of the strong adiabatic lifting experienced by the parcel in the right exit region of the jet.

3.7.2 Cold Front Aloft Structure

The 08/21 UTC 500 mb thermal advection pattern, established by the observed wind field on a constant pressure surface is depicted in (Fig. 3.21a). The axis of the advection pattern, with values in excess of $6^{\circ}\text{C } 3 \text{ hrs}^{-1}$, lies along the lee of the Rockies. A slight warming is taking place over the Texas panhandle. The observed 3-hour temperature change reveals an area of maximum cooling located over the Texas panhandle where a 3°C drop in temperature was observed. Streamline analysis of the observed wind field from 08/21 to 09/00 UTC indicates a persistent warm southwesterly flow over this region. However, inspection of the ageostrophic wind field indicates the development of a thermal-indirect cross-stream flow. The 08/18 UTC ageostrophic streamline analysis shows an accelerating jet exit region and upward vertical motion and cooling of the atmosphere. By 09/00 UTC, a strong jet streak signal has emerged out of the southern Rockies (Fig. 3.21b). A thermally-indirect circulation is found in the emerging jet streak over the Texas panhandle while an accelerative thermally-direct circulation persists in what was formerly the jet exit region. Coincident with the thermally-indirect flow of the exit region, cold air is driven across the stream into the Texas panhandle. An east-west thermal trough of cold air is observed darting across the northern panhandle of Texas. This signal is consistent with cooling associated with the accelerating jet exit region and the cross-stream advection of cold air. Both signals act to enhance the baroclinicity aloft over the panhandle region.

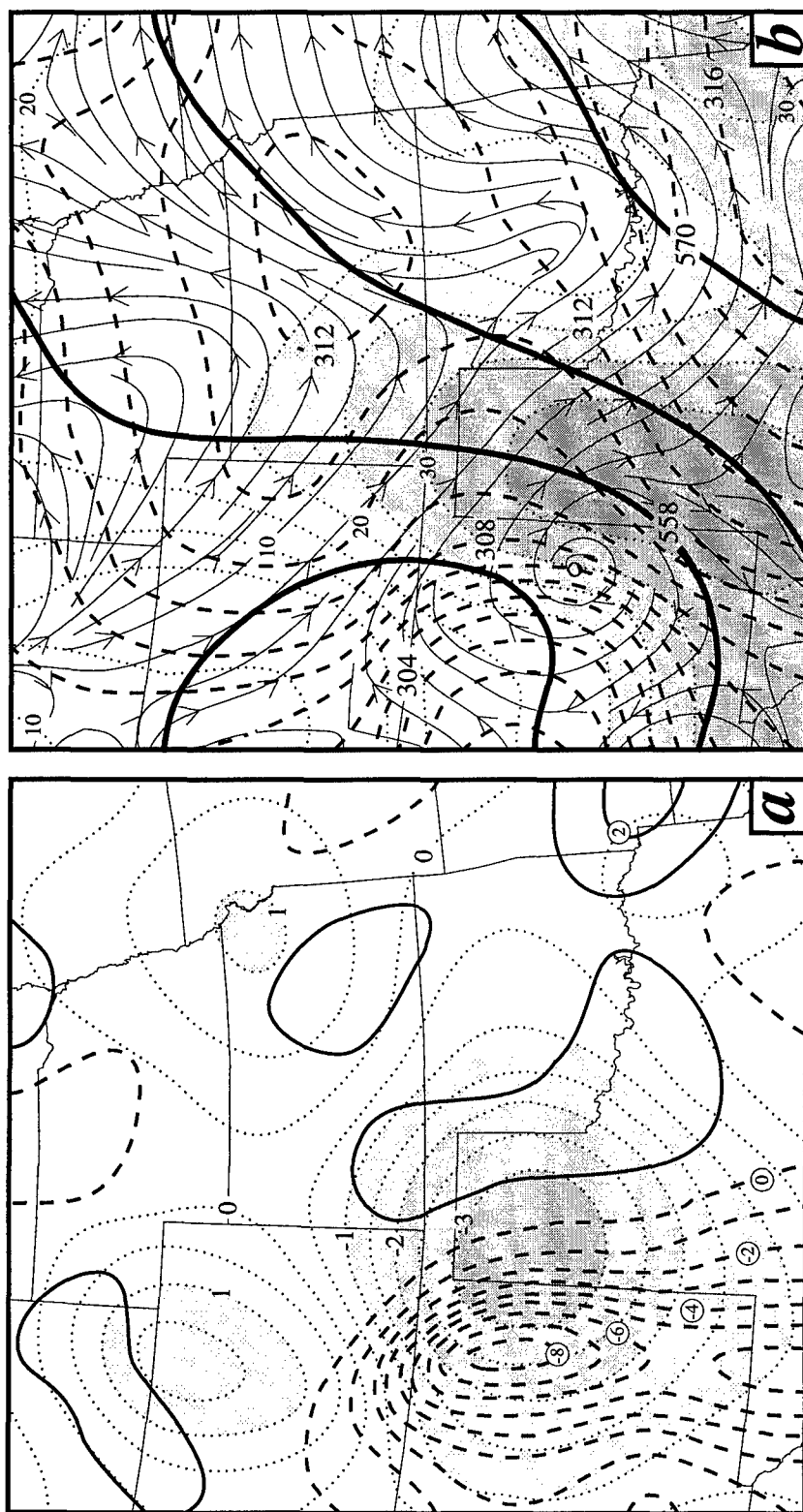


Figure 3.21. (a) Three hour temperature advection pattern driven by the observed wind from 2100 UTC 8 March 1992 (cooling depicted by dashed line - $^{\circ}\text{C } 3\text{hrs}^{-1}$, and warming depicted by solid line - $^{\circ}\text{C } 3\text{hrs}^{-1}$). Observed three hour temperature change between 2100 UTC 8 March and 0000 UTC 9 March 1992 depicted by shading / dotted line ($^{\circ}\text{C } 3\text{hrs}^{-1}$). (b) 0000 UTC 9 March 1992 gridded fields of: ageostrophic streamline analysis (thin solid line), heights (thick solid lines - dm), isotachs (dotted/shading - ms^{-1}) and equivalent potential temperature (dashed line - $^{\circ}\text{K}$).

The structure of the developing CFA and jet exit region at 09/00 UTC is displayed in Fig. 3.22. A split in the concentration of the elevated pool of low θ_e air is observed. The upper-level cold front over New Mexico begins to weaken as the thermal discontinuity breaks down in response to the cooling out ahead. Meanwhile, the generation of the CFA is evident as the observed data indicates the formation of an elevated pool of low θ_e forming over the warm-moist air ahead of the dryline. By 0000 UTC 9 March 1992, the exit region has rapidly accelerated towards the Texas/Oklahoma panhandle. The developing midtropospheric jet is evident near the 400 mb level with winds increasing to 45 ms^{-1} . The strong inertial advective forcing generates an expansive tongue of high R_o in excess of 0.5 with a maximum value of 0.75 over the Texas panhandle. The location of this maximum in the right exit region is indicative of the strong acceleration which acts to extend the exit region further downstream and to the right of the flow.

The axis of the cold surge over the Texas panhandle is aligned with the apex of the CFA and the development of thunderstorm activity forming near Vici, Oklahoma (VCI). Direct measurements of vertical motion at the VCI profiler site detects two regions of enhanced ascent that are key dynamical signals associated with the developing CFA and jet streak (Fig. 3.23). At 09/00 UTC, as the CFA approaches the station, a signal of upward vertical motion is observed from 3.1 - 4.7 km AGL. Comparison of RAOB data in the area indicates this region of upward vertical motion lies within 630 mb and 500 mb -- the same region of significant cooling as observed in the AMA soundings. Consequently, this vertical motion is tied to the advancing CFA as it passes over the station. Meanwhile, shortly after 09/00 UTC, a second area of ascent is detected above 6 km AGL. This area

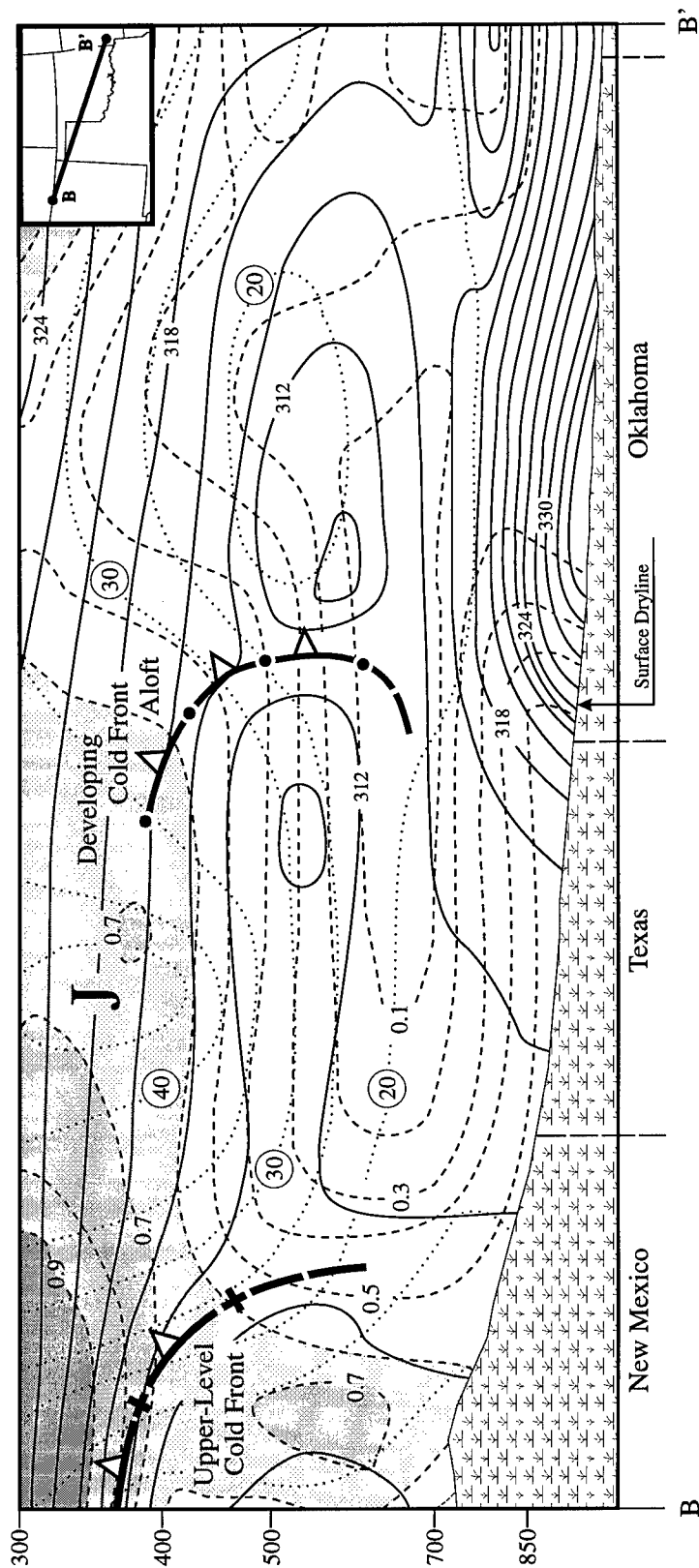


Figure 3.22. 0000 UTC 9 March 1992 vertical cross section through the nose of an accelerating jet exit region. Thin dashed lines depict inertial Rossby number (shaded area >0.6), derived isotachs (dotted lines - ms^{-1}). Thin solid lines depict equivalent potential temperature ($^{\circ}\text{K}$). Upper-level cold front and cold front aloft (CFA) depicted by heavy solid line with open triangles. Jet streak core denoted by "J". Dashed portion of front depicts where front becomes diffuse. Insert depicts orientation of cross section.

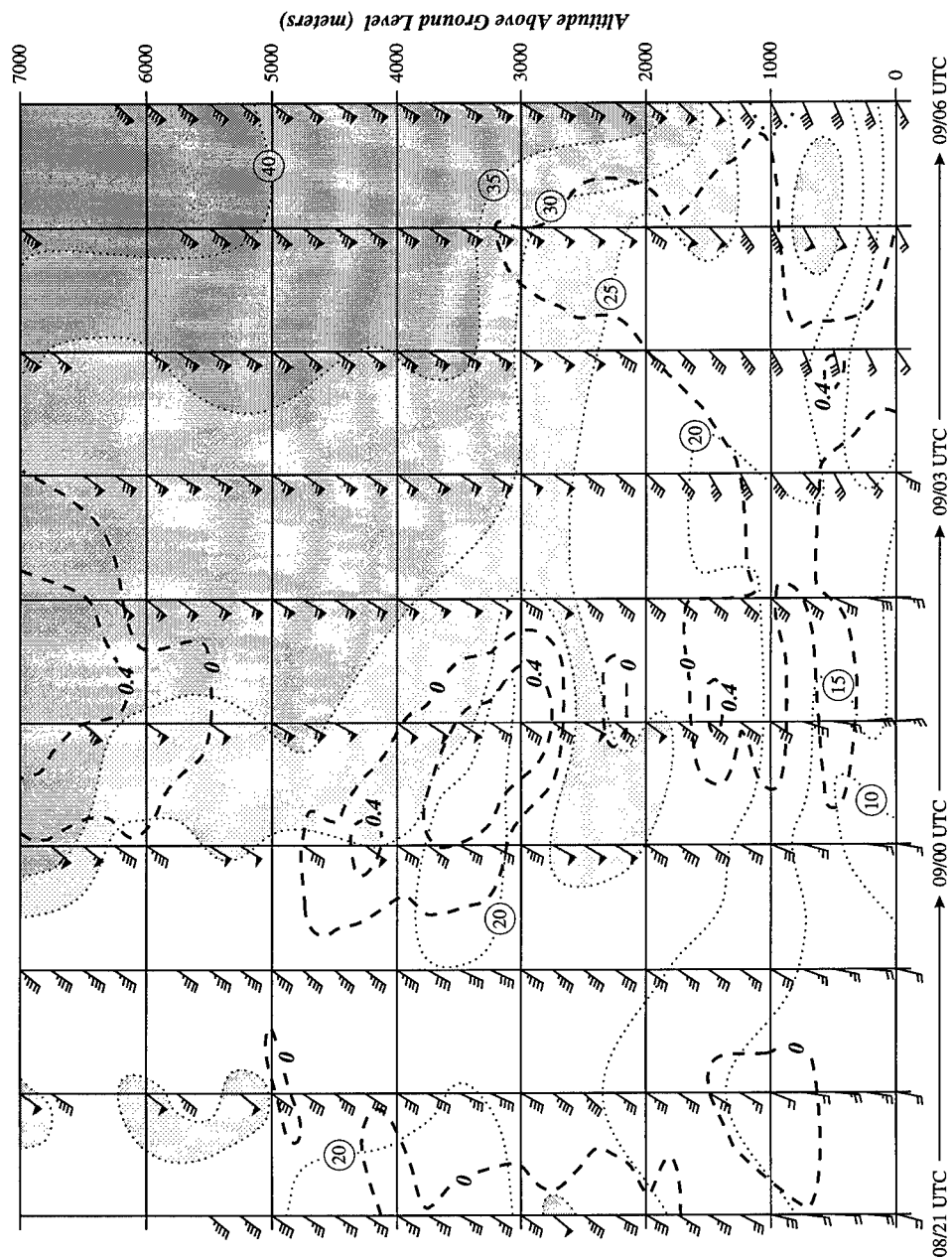


Figure 3.23. Hourly profiler display from Vici, Oklahoma from 2100 UTC 8 March to 0600 UTC 9 March 1992. Wind barbs: flag - 2.5 ms^{-1} , full staff - 5 ms^{-1} , half staff - 2.5 ms^{-1} . Isotachs depicted by dotted line and shading at 5 ms^{-1} interval above 25 ms^{-1} , upward vertical velocity depicted by dashed lines in units of ms^{-1} . Vici, Oklahoma has an elevation of 648 m and data is displayed above ground level (AGL).

of ascent is located in the vicinity of 350 mb level. When compared to the cross section in Fig. 3.22, we observe the axis of the developing jet streak is at the same altitude and that the ascent is located in the forward right quadrant of the intensifying jet streak. This reversal in the “classical” vertical motion pattern one would expect to find in the jet exit region, is evidence of the dynamic adjustment taking place between the mass and momentum fields. As the exit region moves over the site, the upward vertical motion increases to over 0.6 ms^{-1} . This region of ascending air continues for several hours as the CFA passes over the site. The ascent provides a positive feedback in cooling the atmosphere and reinforcing the formation of the CFA. Additionally, the ascending motion acts to enhance the localized evacuation of mass, enhancing low-level convergence and provides a powerful mechanism to ignite convective development.

A form of the three-dimensional frontogenesis equation developed by Miller (1948) is used to investigate the generation of the cold front aloft in response to the geostrophic adjustments taking place. The full three-dimensional frontogenesis function is defined by Eq 17. Terms 1, 5, and 9 are associated with differential diabatic forcing; terms 10 and 11 are the vertical deformation contribution; term 12 is the vertical divergence contribution; terms 2, 3, 6, and 7 are the horizontal deformation contribution; and terms 4 and 8 are the vertical tilting contribution. Terms 9-12 are neglected since we are interested in horizontal frontogenesis rather than the vertical temperature gradient structure. Additionally, the diabatic contributions were ignored for the scope of this analysis. This can be justified for the times prior to the development of strong convection.

$$\begin{aligned}
F &= \frac{D}{Dt} |\nabla \theta| \\
&= \frac{1}{\nabla \theta} \left\{ \underbrace{\frac{\partial \theta}{\partial x} \left[\frac{1}{C_p} \left(\frac{p_o}{p} \right)^k \right] \frac{\partial}{\partial x} \left(\frac{dQ}{dt} \right)}_1 - \underbrace{\frac{\partial u}{\partial x} \frac{\partial \theta}{\partial x}}_2 - \underbrace{\frac{\partial v}{\partial x} \frac{\partial \theta}{\partial y}}_3 - \underbrace{\frac{\partial \omega}{\partial x} \frac{\partial \theta}{\partial z}}_4 \right. \\
&\quad + \underbrace{\frac{\partial \theta}{\partial y} \left[\frac{1}{C_p} \left(\frac{p_o}{p} \right)^k \right] \frac{\partial}{\partial y} \left(\frac{dQ}{dt} \right)}_5 - \underbrace{\frac{\partial u}{\partial y} \frac{\partial \theta}{\partial x}}_6 - \underbrace{\frac{\partial v}{\partial y} \frac{\partial \theta}{\partial y}}_7 - \underbrace{\frac{\partial \omega}{\partial y} \frac{\partial \theta}{\partial z}}_8 \\
&\quad \left. + \underbrace{\frac{\partial \theta}{\partial z} \left[\frac{p_o^k}{C_p} \frac{\partial}{\partial z} \left(p^{-k} \frac{dQ}{dt} \right) \right]}_9 - \underbrace{\frac{\partial u}{\partial z} \frac{\partial \theta}{\partial x}}_{10} - \underbrace{\frac{\partial v}{\partial z} \frac{\partial \theta}{\partial y}}_{11} - \underbrace{\frac{\partial \omega}{\partial z} \frac{\partial \theta}{\partial z}}_{12} \right\} \quad (17)
\end{aligned}$$

The observed 08/21 UTC total frontogenetic forcing is depicted in Fig. 3.24. Prior to 08/21 UTC, a well-defined frontogenetic zone, associated with the baroclinic wave, is established over New Mexico in response to both geostrophic deformation and tilting processes. By 08/21 UTC, a split signal of frontogenesis is detected over the southern Plains (Fig. 3.24a). A strong meridional oriented zone of frontogenesis is observed over eastern New Mexico associated with the baroclinic wave over the inner-mountain region. Second area of frontogenesis, though weaker, is seen over the Texas panhandle ~300 km downstream of the initial frontal zone. This baroclinic zone is predominately due to contributions associated with tilting effects of the vertical potential temperature gradient into the horizontal plane. This signal coincides well with enhanced convective cloud cover observed on satellite over the panhandle at this time. A third region of frontogenesis is detected over eastcentral Oklahoma. This zone is associated with the leading edge of the warm sector and is responsible for the formation of a 'pre-drytrough' rainband (Martin *et*

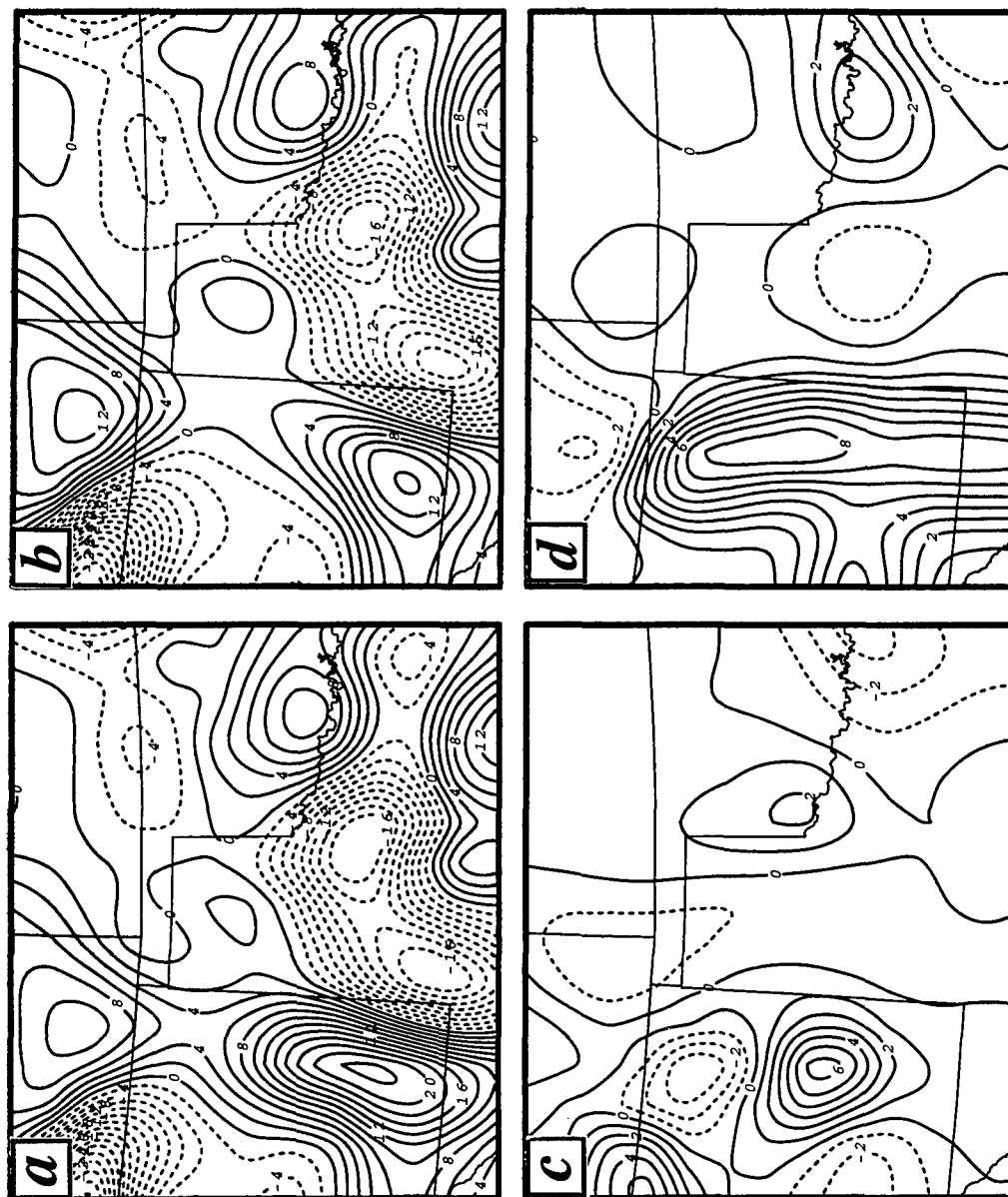


Figure 3.24. 2100 UTC 8 March 1992 observed 500 mb frontogenesis calculations based on Miller Frontogenetic function. (a) Total frontogenesis, (b) tilting term, (c) horizontal shear term, and (d) confluence term. Solid lines depict frontogenesis, dashed lines frontolysis ($\times 10^{-1} \text{ }^{\circ}\text{K } 100 \text{ km}^{-1} \text{ 3 hrs}^{-1}$).

al. 1995). Three hours later, the baroclinic zone over New Mexico begins to weaken as the thermal contrast breaks down in the lee of the mountains. Further intensification of the developing CFA is observed over central Oklahoma at 09/00 UTC (Fig. 3.25). The frontogenetic forcing has increased to over $1\text{K } 100 \text{ km}^{-1} \text{ } 3 \text{ hrs}^{-1}$ in response to strong contributions associated with the tilting term (Fig. 3.25b) while horizontal shear (Fig. 3.25c) and confluence processes (Fig. 3.25d) provide a negative impact to frontogenesis. The impact of the vertical motion distribution on the temperature field is to tilt the thermal gradient into the horizontal strengthening the frontogenetic process downstream.

The signal of frontogenesis over Oklahoma is consistent with the AMA sounding profile (Fig. 3.4). As suspected earlier, the formation of the CFA was not simply the result of geostrophic deformation processes. Rather, the formation of the CFA is strongly influenced by the secondary circulation associated with an atmosphere going through an adjustment process. These processes act to extend the jet further downstream and allow cold air to be thrust cross-stream over the convergent right exit region. This region is typically associated with descending air and compressional warming. A process which acts to stabilize the air mass and build the height field. However, the strong cross-stream cold advection acts to destabilize the atmosphere triggering a convective outbreaks.

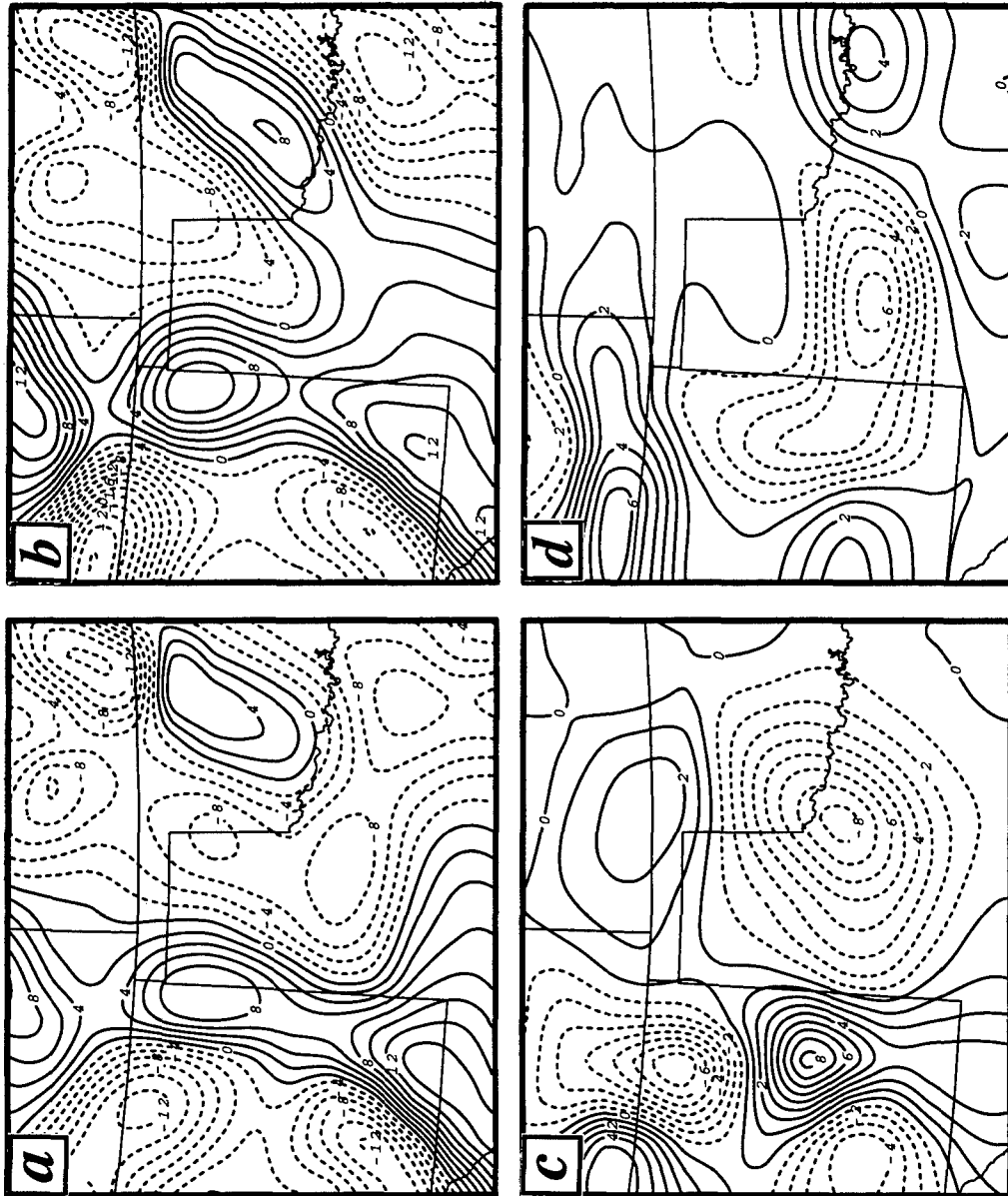


Figure 3.25. 0000 UTC 9 March 1992 observed 500 mb frontogenesis calculations based on Miller Frontogenetic function. (a) Total frontogenesis, (b) tilting term, (c) horizontal shear term, and (d) confluence term. Solid lines depict frontogenesis, dashed lines frontolysis ($\times 10^{-1} \text{ }^{\circ}\text{K } 100 \text{ km}^{-1} \text{ 3 hrs}^{-1}$).

3.8 Numerical Modeling Studies

The dynamics associated with the development of the CFA is evaluated using a series of numerical modeling studies. The model runs had grid resolutions ranging from a large scale 160 km, which resolves the large scale background forcing, down to a 60 km run that reveals the mesoscale structure. A sensitivity study was conducted to investigate the contribution of sensible heating in the CFA development.

3.8.1 Evolution of Background Synoptic Scale Flow

A 160 km full physics model run (coarse run) was conducted in order to simulate the large scale synoptic environment. The initial state of the 500 mb level (Fig. 3.26a) compares favorably with the observed data (Fig 3.5) as a broad low encompasses the desert southwest with a building ridge over the Plains. A well established wedge of warm air is observed along the Front Range of the Rockies with a pool of cold air situated over southern California. A split in the momentum field is observed over western Texas as a portion of the southern branch of the polar jet is directed northward over New Mexico and a portion of the westerly momentum of the subtropical jet is carried towards the Gulf region. This configuration leads to an expanded region of ascent (not shown) in response to the diffluent flow over eastern Texas. By 08/21, UTC the low center moves towards the four corners region while a 35 ms^{-1} jet streak develops over western Texas (Fig. 3.26c). The evolution of the associated ageostrophic pattern is indicative of a decelerating

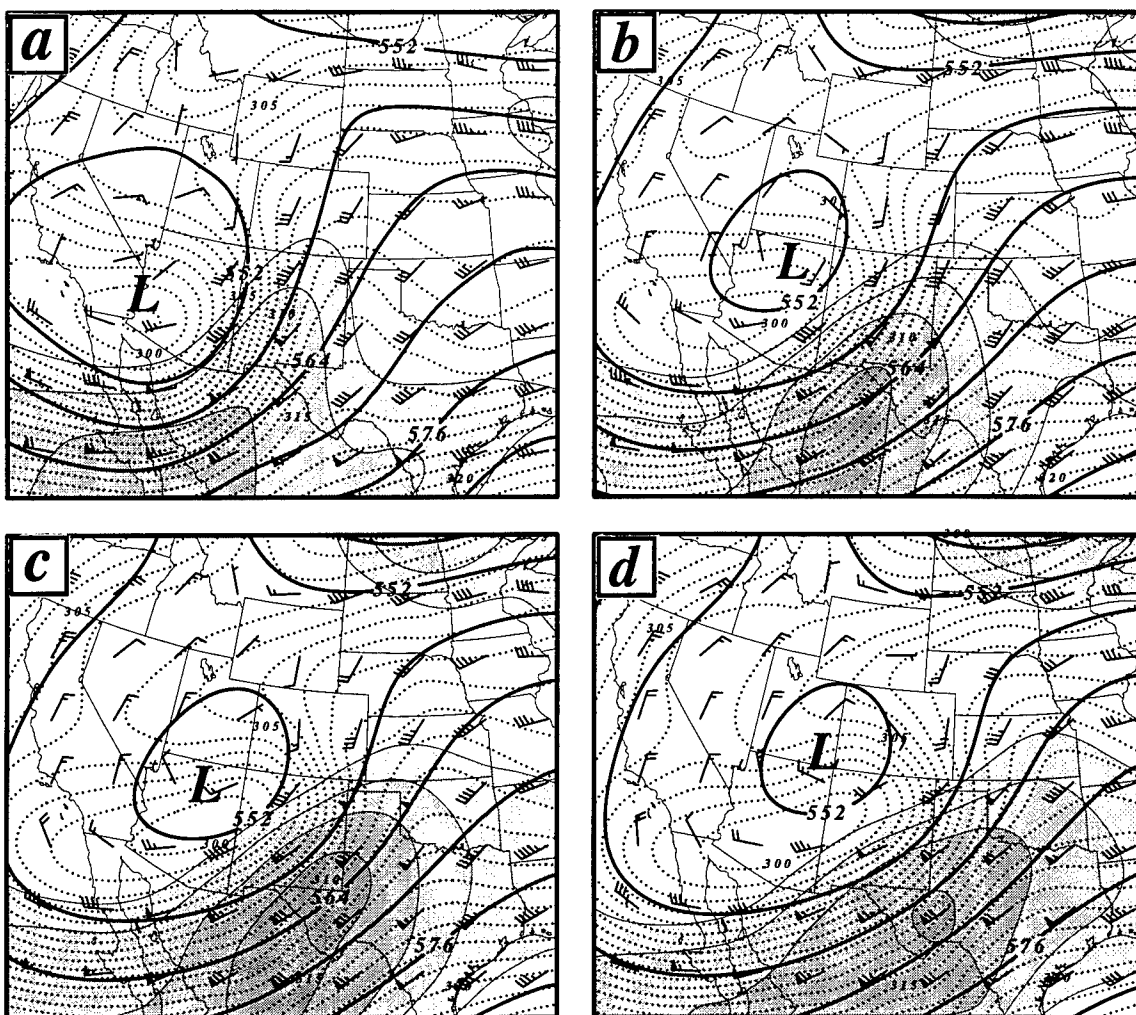


Figure 3.26. 160 km full physics 500 mb MASS model output valid at (a) 1200 UTC 8 March 1992, (b) 1800 UTC 8 March 1992, (c) 2100 UTC 8 March 1992, and (d) 0000 UTC 9 March 1992. Parameters depicted: heights (solid - 6 dm interval), isotachs above 20 ms^{-1} (shading at a 5 ms^{-1} interval), theta (dotted - 1°K interval), and wind barbs (flag - 25 ms^{-1} , full staff - 5 ms^{-1} , half staff - 2.5 ms^{-1}).

flow of the jet exit region (Fig. 3.27). The initial state indicates a thermally-indirect circulation about the forward flank of the southern and subtropical jet stream (Fig. 3.27a). The six-hour forecast indicates the jet streak associated with the subtropical jet stream moving through Louisiana (Fig. 3.27b). This allows the thermally-direct circulation of the entrance region to overspread eastern Texas. The accelerative flow allows the developing jet streak over Texas to expand eastward into Oklahoma by 08/21 UTC (Fig. 3.27c). This results in a broad region of momentum over spreading the southern Plains. As the transient subtropical jet streak moves away from the southern polar jet streak a thermally-indirect circulation redevelops by 09/00 UTC (Fig. 3.27d). The ageostrophic flow over New Mexico provides a supergeostrophic thermally-indirect circulation indicative of decelerating flow.

The thermal field details the development of a push of cold air moving out from the mountains into the Texas panhandle in a similar manner as proposed by Hobbs *et al.* (1990, 1996) in which geostrophic deformation processes act to advance the cold air out into the Plains (Fig. 3.26). The 9-hour forecast indicates a push of cold air into the Texas panhandle by 08/21 UTC (Fig. 3.26c). Despite significant warm advection over eastern Texas, the thermal ridge does not build significantly over this region.

Trajectories were constructed in order to better understand the structure governing the evolving pattern. The parcel trajectories were constructed for an east-west line passing through AMA at 09/00 UTC from the 500 mb level (Fig. 3.28). A comparison of this coarse run trajectory to the 14 km trajectory depicted in Fig. 3.20 reveals marked differences highlighting the importance of the mesoscale structure established by terrain

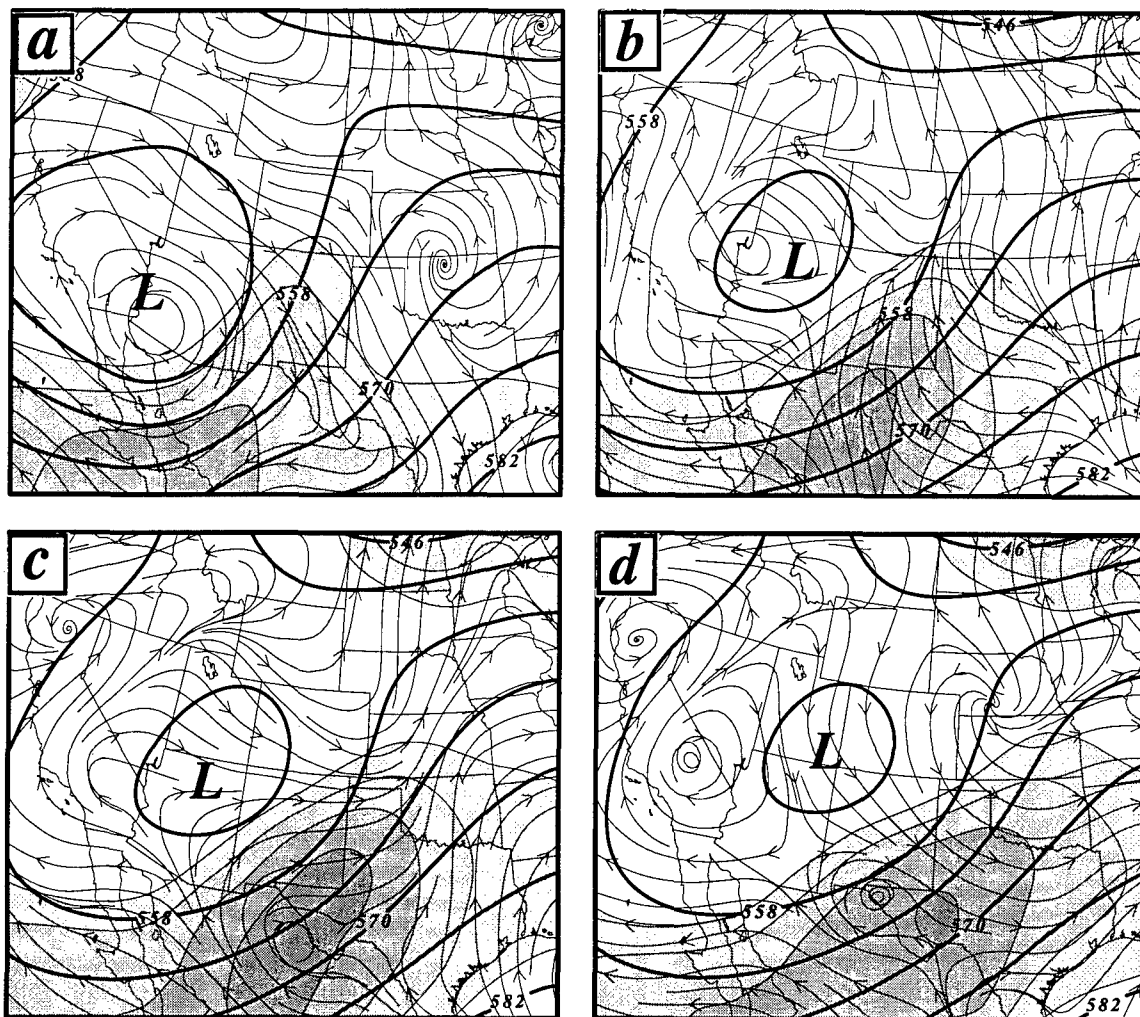


Figure 3.27. 160 km full physics 500 mb MASS model output valid at (a) 1200 UTC 8 March 1992, (b) 1800 UTC 8 March 1992, (c) 2100 UTC 8 March 1992, and (d) 0000 UTC 9 March 1992. Parameters depicted: heights (solid - 6 dm interval), isotachs above 20 ms^{-1} (shading at a 5 ms^{-1} interval), and ageostrophic streamline analysis (thin solid arrows).

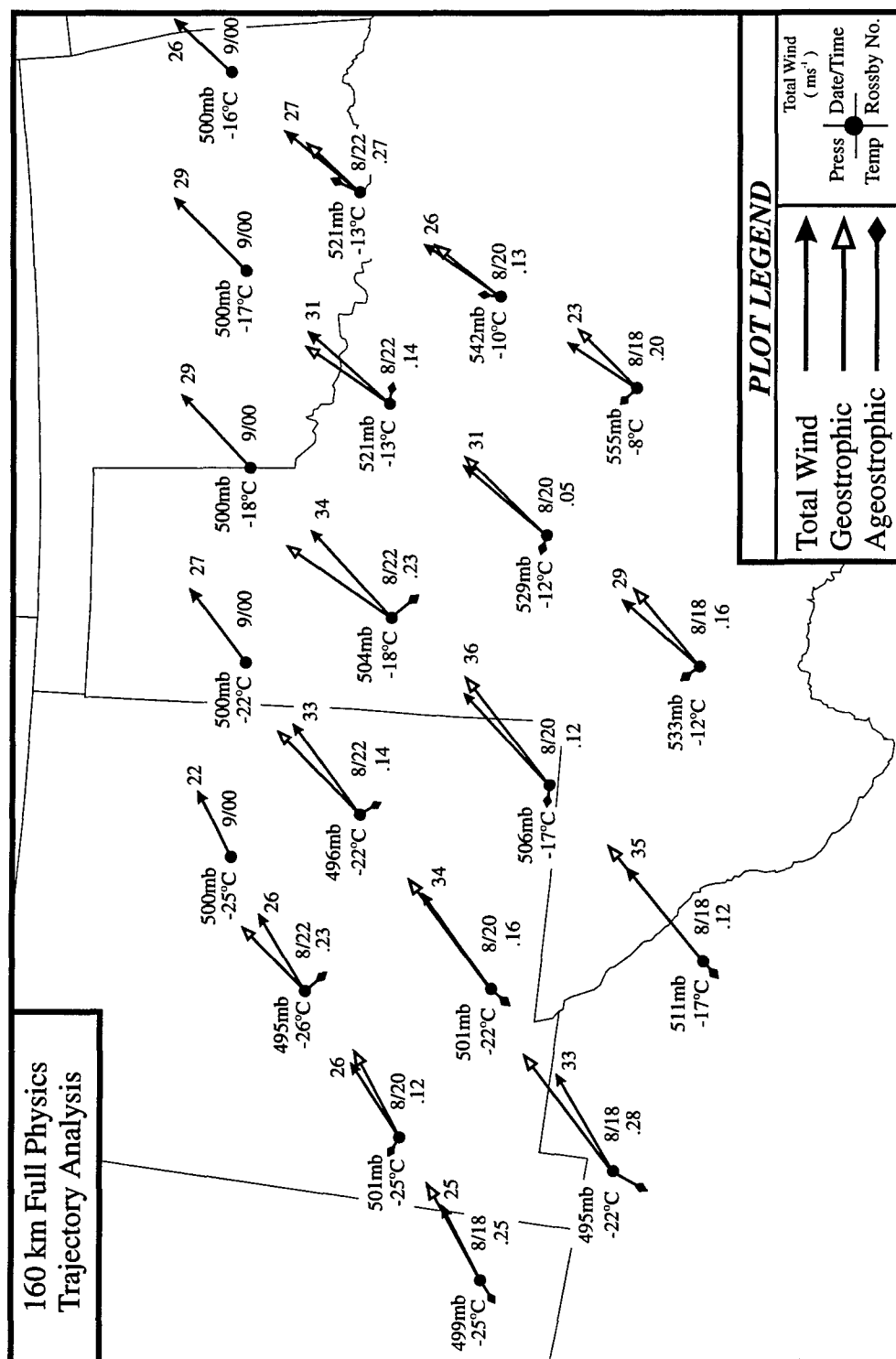


Figure 3.28. Back trajectory constructed from 160 km full physics MASS model output. Trajectory initialized at 0000 UTC 9 March 1992 and ran to 1500 UTC 8 March 1992. Station plot contains parcel pressure level (mb), temperature ($^{\circ}\text{C}$), time of parcel location, total wind speed (ms^{-1}) and inertial Rossby number. Displayed wind vectors depict total wind vector (solid head), geostrophic component (open head), ageostrophic component (diamond head).

interaction with the flow. The structure of the coarse run trajectories indicates a uniform southwesterly flow throughout the region. The total wind is within ~10% of the geostrophic wind indicative of the balanced nature of the large scale background flow. A measure of this balanced state was obtained by calculating the Lagrangian Rossby number of the parcel. The total 'instantaneous' acceleration vector of the parcel was computed by calculating the parcel location over a period of $2\delta t$, where $t = 1/20$ the time step. The ratio of this nearly instantaneous acceleration to the Coriolis acceleration provides the Lagrangian Rossby number. Inspection of the computed Rossby numbers reveal a balanced signature with values < 0.28 throughout the domain.

The calculations indicate the source of cold air, for the three western most parcels, originated over northern Mexico. The trajectory data reveals that the parcels experienced little vertical motion as cold air was simply advected into the region. In fact these parcels underwent slight descent as they passed through a region marked by considerable deceleration and mass convergence. By 09/00 UTC, the jet exit region over west-central Texas is marked by mass convergence in excess of $0.4 \times 10^{-5} \text{ kg m}^{-3} \text{ s}^{-1}$ (Fig. 3.29a). Meanwhile, over Oklahoma parcels experience significant ascent (55 mb) as temperatures cooled 8°C (Fig. 3.28). The advection of cold air to the west and adiabatic cooling of air parcels to the east result in a break down in the generation of frontogenesis observed over the Texas panhandle. Frontogenetic calculations based on Eq. 17 indicated significant frontolysis over the Texas panhandle (Fig. 3.29b). This is evident in the 12-hour forecast where tilting and shear terms act to reduce the frontogenetic properties of the surge of cold air while confluence contributes weakly.

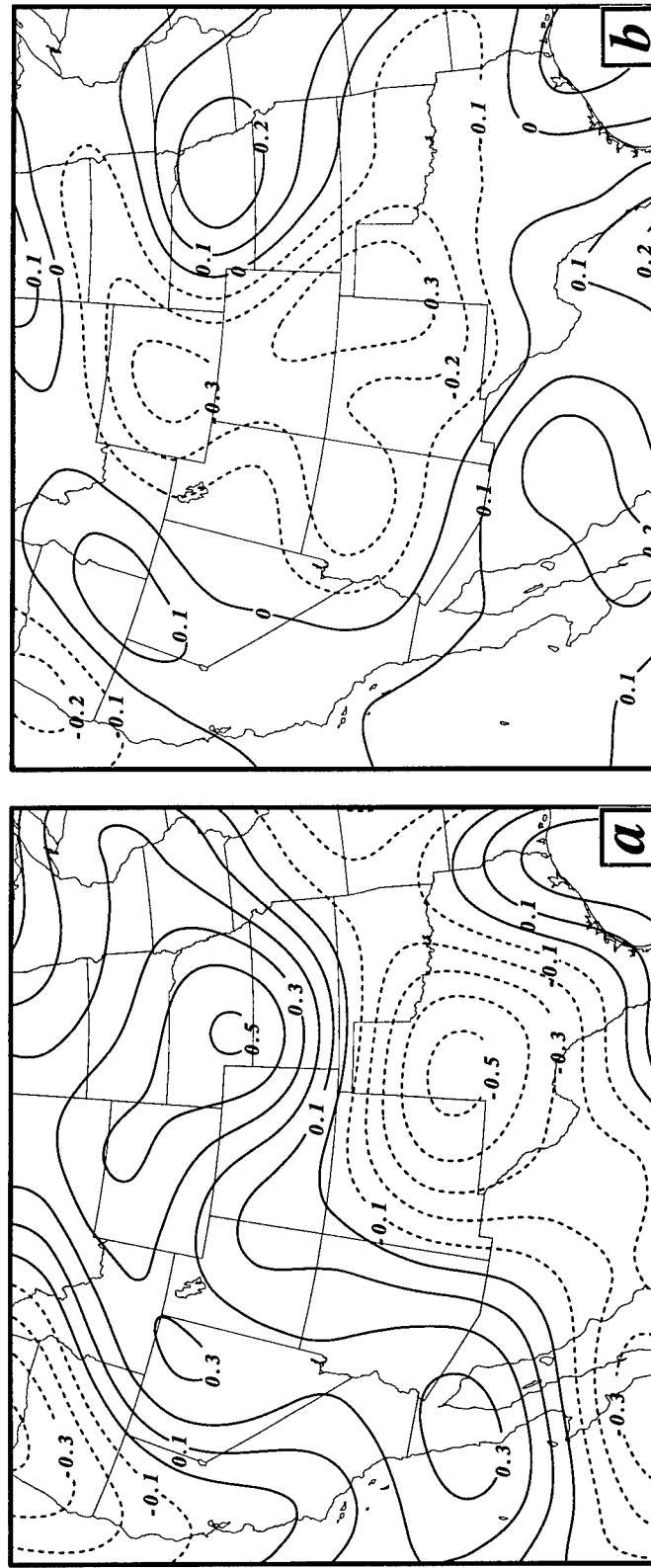


Figure 3.29. 0000 UTC 9 March 1992 160 km MASS model diagnostics. (a) 500 mb mass divergence calculations where divergence is depicted by solid lines and convergence by dashed lines ($\times 10^{-5} \text{ kg m}^{-3} \text{ s}^{-1}$). (b) Total 500 mb frontogenesis calculations based on Miller frontogenetic function. Solid lines depict frontogenesis, dashed lines frontolysis ($^{\circ}\text{K } 100 \text{ km}^{-1} \text{ 3 hrs}^{-1}$).

3.8.2 Mesoscale Environment

A 60 km full physics model run was conducted in order to diagnose the mesoscale development of the CFA. This simulation was generated using the full physics package (Table 3.0) along with a high resolution terrain data base consistent with the grid scale. Unlike the coarse run, the enhanced resolution captures the development of a CFA over the Texas panhandle by 09/00 UTC in response to the modified ageostrophic circulations downwind of the mountains.

This simulation produces stronger 500 mb gradients, both in the thermal and momentum fields than that observed in the coarse run, as the mesoscale influence of the terrain impact is detected. Three hours into the run, a significant 500 mb thermal gradient is observed over central New Mexico (Fig. 3.30a). A well-defined pool of cold air is situated over southern Arizona while a pronounced wedge of warm air is observed over the New Mexico/Texas boarder. An associated jet max of 35 ms^{-1} is observed in the vicinity of ELP. In response to the wedge of warm air a mesoscale ridge in the height field is observed over southeast New Mexico extending down towards Del Rio, Texas. As the nose of the jet encounters the warm air perturbation a divergent response is generated producing a thermally-direct circulation within the exit region of the jet (Fig 3.30a). This leftward-directed flow is indicative of acceleration as air parcels are directed towards lower heights and an increase in kinetic energy. The ageostrophic flow over northeast New Mexico is characterized by a leftward-directed flow ($>10 \text{ ms}^{-1}$) and a significant subgeostrophic flow ($>15 \text{ ms}^{-1}$) (Fig. 3.31). In response, a region of ascending air >10

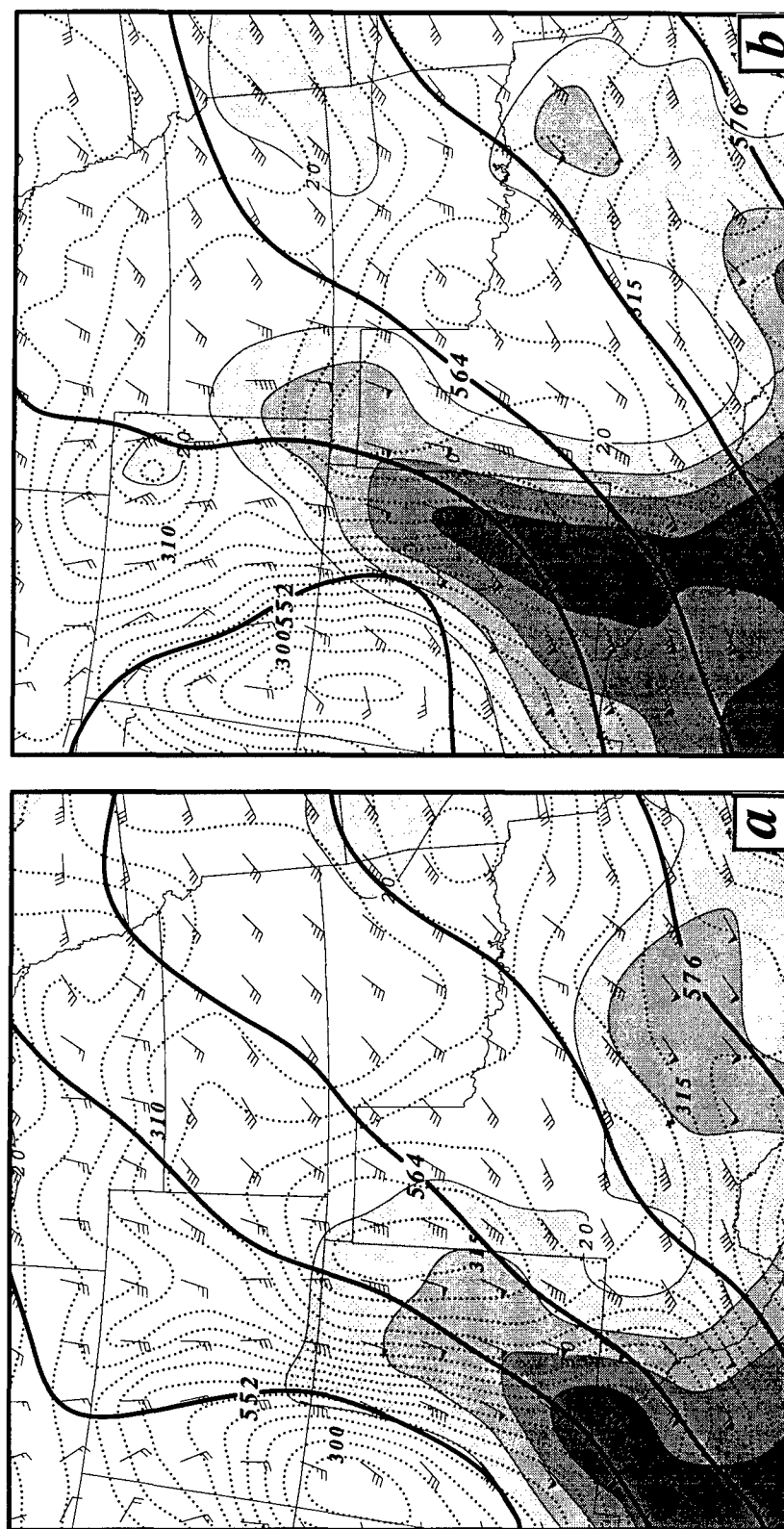


Figure 3.30. 60 km full physics 500 mb MASS model output valid at (a) 1500 UTC 8 March 1992, (b) 1800 UTC 8 March 1992. Parameters depicted: heights (solid - 6 dm interval), isotachs above 20 ms^{-1} (shading at a 5 ms^{-1} interval), theta (dotted - 1°K interval), and wind barbs (flag - 25 ms^{-1} , full staff - 5 ms^{-1} , half staff - 2.5 ms^{-1}).



Figure 3.31. 60 km full physics 500 mb MASS model output valid at 1500 UTC 8 March 1992. Parameters depicted: heights (solid - 6 dm interval), total wind isotachs above 20 ms^{-1} (shading at a 5 ms^{-1} interval), ageostrophic wind barbs (flag - 25 ms^{-1} , full staff - 5 ms^{-1} , half staff - 2.5 ms^{-1}), and kinematic omega where ascent is depicted by dashed line and descent is depicted by thin solid lines ($\mu\text{bar s}^{-1}$).

μbars^{-1} is observed along the New Mexico/Texas border. This region of ascent is found along the forward right flank of the accelerative jet exit region. The generation of a thermally-direct circulation is indicative of strong impact of the terrain-induced mesoscale forcing acting within the background synoptic scale flow.

Within three hours, the associated jet streak rapidly accelerates northward into southeast Colorado as a narrow ribbon of winds in excess of 35 ms^{-1} forms along the eastern slopes of New Mexico (Fig. 3.30b). The narrow concentration of warm air along the lee of the southern Rockies results in a juxtapositioning of the observed jet streak with the geostrophic jet max along the eastern slopes of New Mexico (Fig. 3.32a). This configuration allows the translation of momentum towards the northeast into north-central Texas by 08/21 UTC. The ageostrophic streamline analysis maintains a thermally-direct signal over western Texas as the flow accelerates toward the Texas panhandle (Fig. 3.32b). The acceleration of the jet exit region is marked by a tongue of high inertial Rossby numbers along the leading gradient in the difference between the geostrophic and total wind fields.

In concert with the accelerative flow, the associated ascent acts to tilt the vertical temperature gradient into the horizontal. This results in an along-stream temperature perturbation observed between MAF and Lubbock, Texas at 08/18 UTC. (Fig. 3.30b). The model does a good job in detecting this perturbation in the vicinity of the enhanced cumuliform cloud cover observed in the 1731 UTC satellite (Fig 3.3b). The trajectory analysis presented in Fig. 3.20 indicated the source of the cold air was not from the inner-mountain region but rather generated by the ascent observed over the eastern slopes of

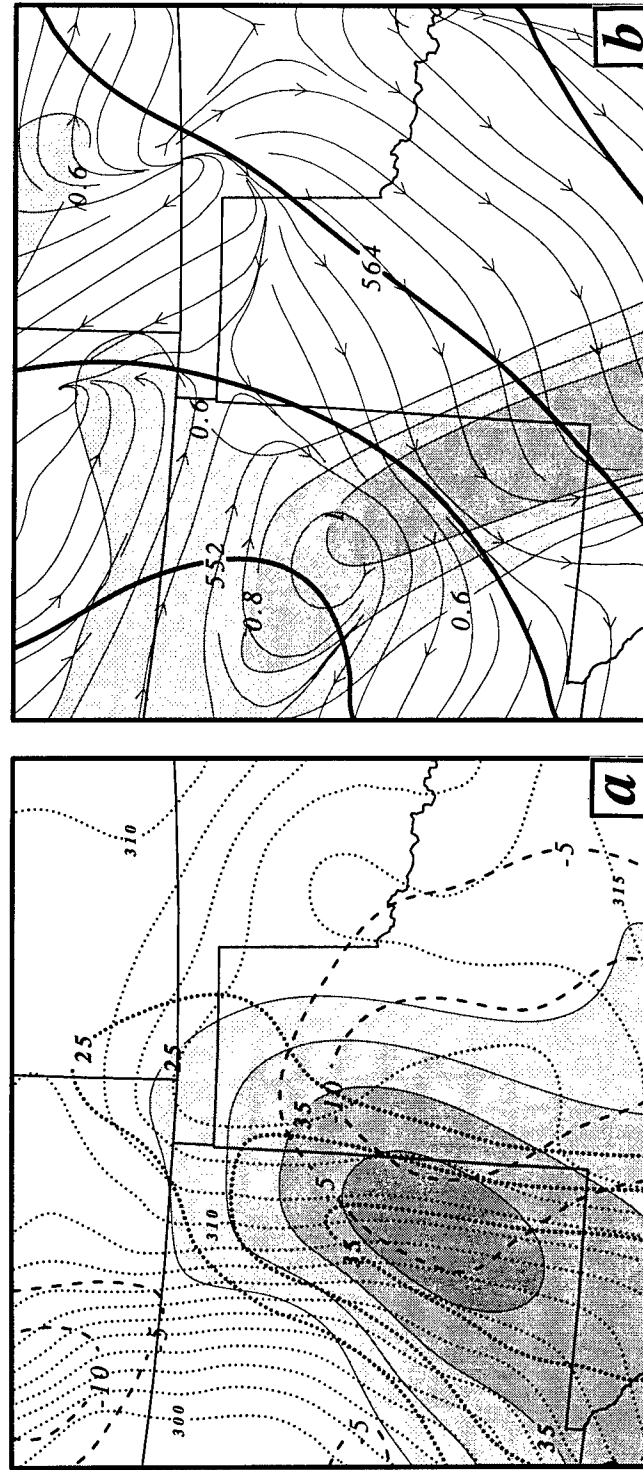


Figure 3.32. 1800 UTC 8 March 1992 60 km full physics 500 mb MASS model output of (a) Total wind isotachs (heavy dotted line/ ms^{-1}), geostrophic wind isotachs (shaded/ ms^{-1}), graphical subtraction of both fields (dashed line/ ms^{-1}), and theta (thin dotted line/ $^{\circ}\text{K}$). (b) height field (solid line - dm), ageostrophic streamlines (thin arrows), and inertial Rossby number (shaded).

New Mexico into Texas. As cold air aloft is generated, the jet exit region over the Oklahoma panhandle is shifted to the right of the flow and extended towards western Kansas. By 08/21 UTC, a new mesojets has formed over the Texas panhandle in response to the geostrophic adjustment process taking place.

The mutual adjustment between the mass and momentum field results in the formation of a 500 mb trough over central New Mexico by 08/18 UTC that extends from the primary low situated over the four corners region (Fig. 3.30b). The development of the 500 mb trough oriented towards the southeast acts to increase the westerly component of the wind field over the southern Rockies. By 08/21 UTC, winds over central New Mexico have become more westerly while the magnitude has increased in excess of 30 ms^{-1} (Fig. 3.33a). The increased westerly momentum over New Mexico and the ageostrophic circulation within the jet exit region provide an environment favorable for frontogenesis over the Texas panhandle (Fig. 3.34). A split in the frontogenesis forcing is observed as an increase in the confluence and tilting term contributions enhance the frontogenetic forcing downstream of the cold pool over the inner-mountain region. During the next three hours, the thermal perturbation over eastern New Mexico extends to the north phasing with the advancing cold air from the inner-mountain region. The resulting baroclinicity over the Texas panhandle at 09/00 UTC is much more pronounced than that observed in the coarse run (Fig 3.33b). Frontogenetic calculations at 09/00 UTC indicate frontogenesis rather than the strong frontolysis observed in the coarse run (Fig. 3.35). The increase in the divergent response to the mass perturbation acts to increase the meridional component of flow over the Texas panhandle while promoting ascent in the forward right quadrant of

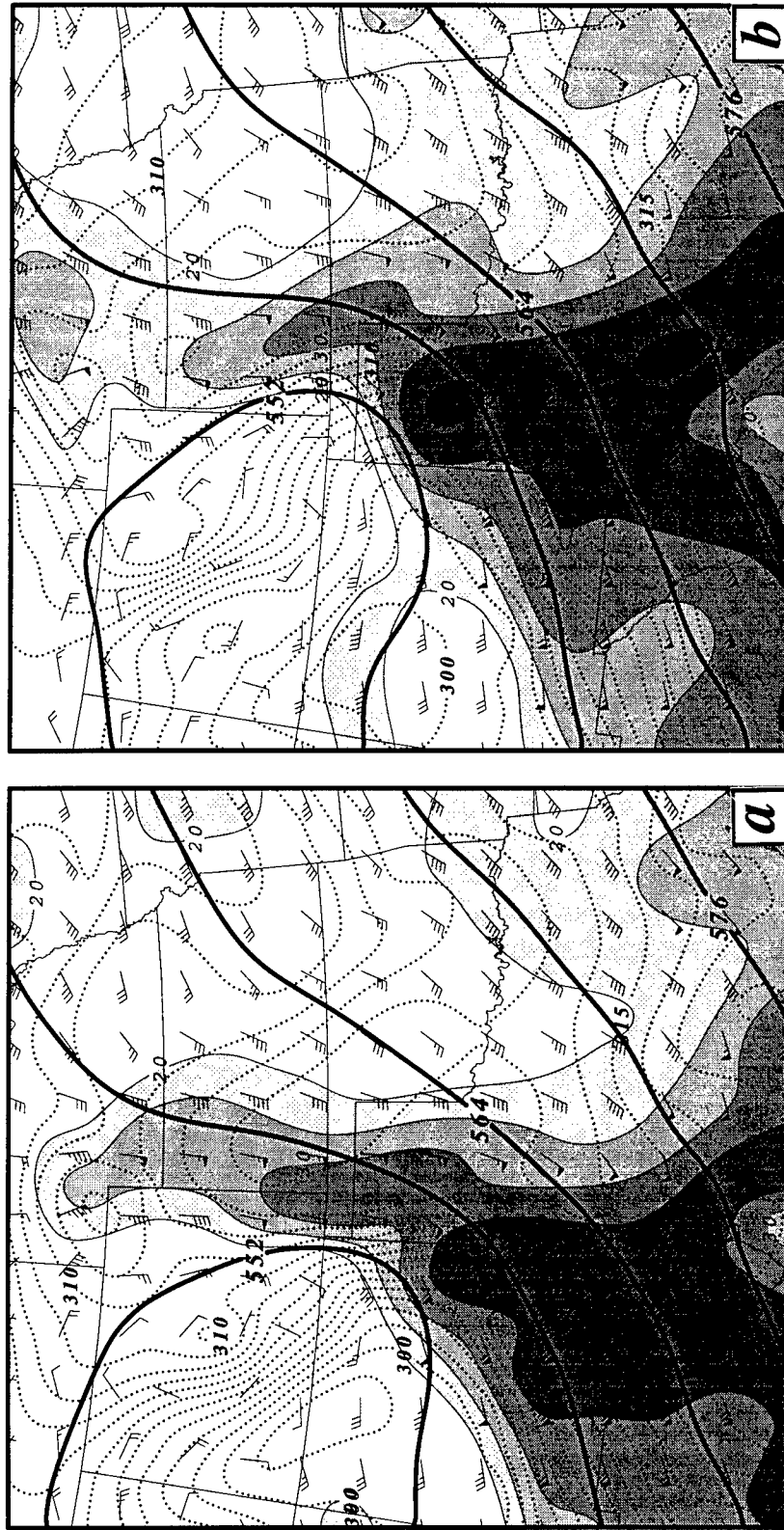


Figure 3.33. 60 km full physics 500 mb MASS model output valid at (a) 2100 UTC 8 March 1992, (b) 0000 UTC 9 March 1992. Parameters depicted: heights (solid - 6 dm interval), isotachs above 20 ms^{-1} (shading at a 5 ms^{-1} interval), theta (dotted - 1°K interval), and wind barbs (flag - 25 ms^{-1} , full staff - 5 ms^{-1} , half staff - 2.5 ms^{-1}).

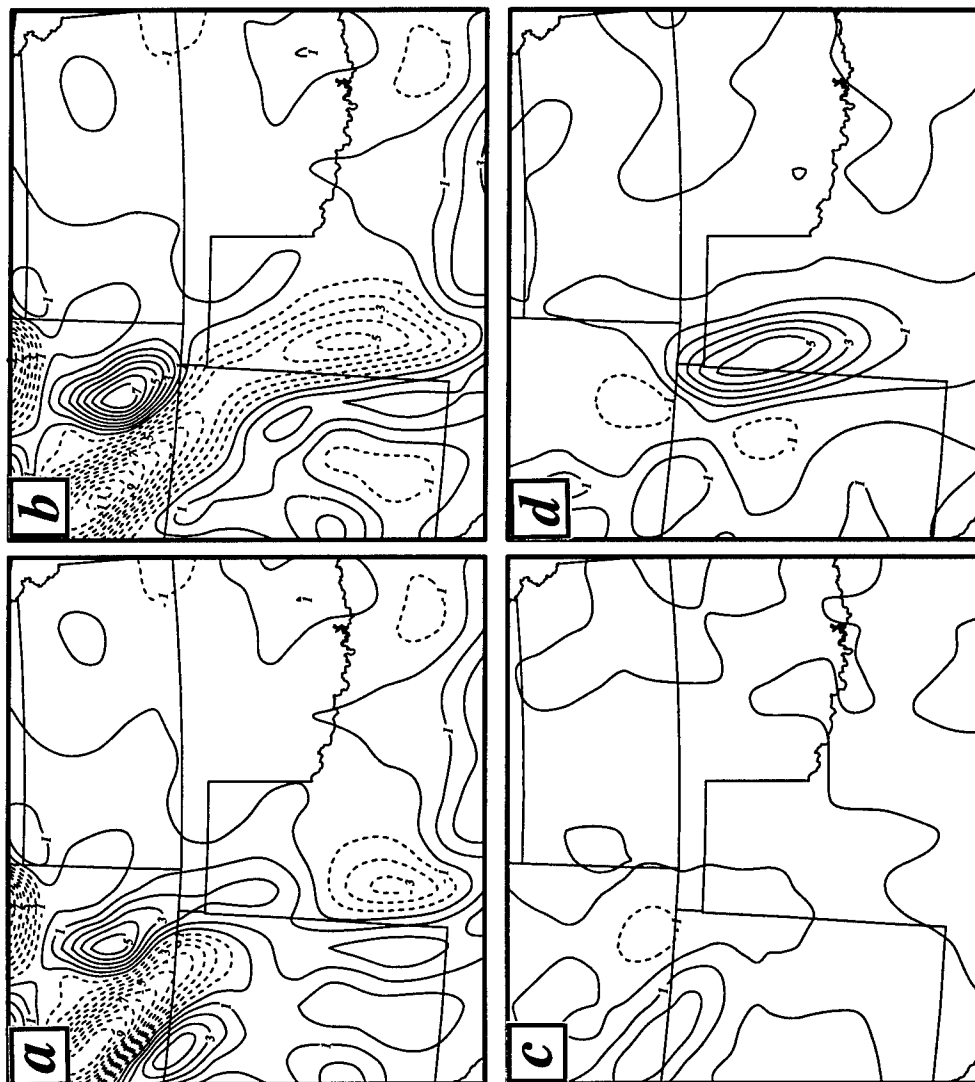


Figure 3.34. 2100 UTC 8 March 1992 500 mb frontogenesis calculations based on Miller Frontogenetic function derived from the 60 km MASS model simulation with high resolution terrain data base. (a) Total frontogenesis, (b) tilting term, (c) horizontal shear term, and (d) confluence term. Solid lines depict frontogenesis, dashed lines frontolysis ($^{\circ}\text{K } 100 \text{ km}^{-1} \text{ 3 hrs}^{-1}$).

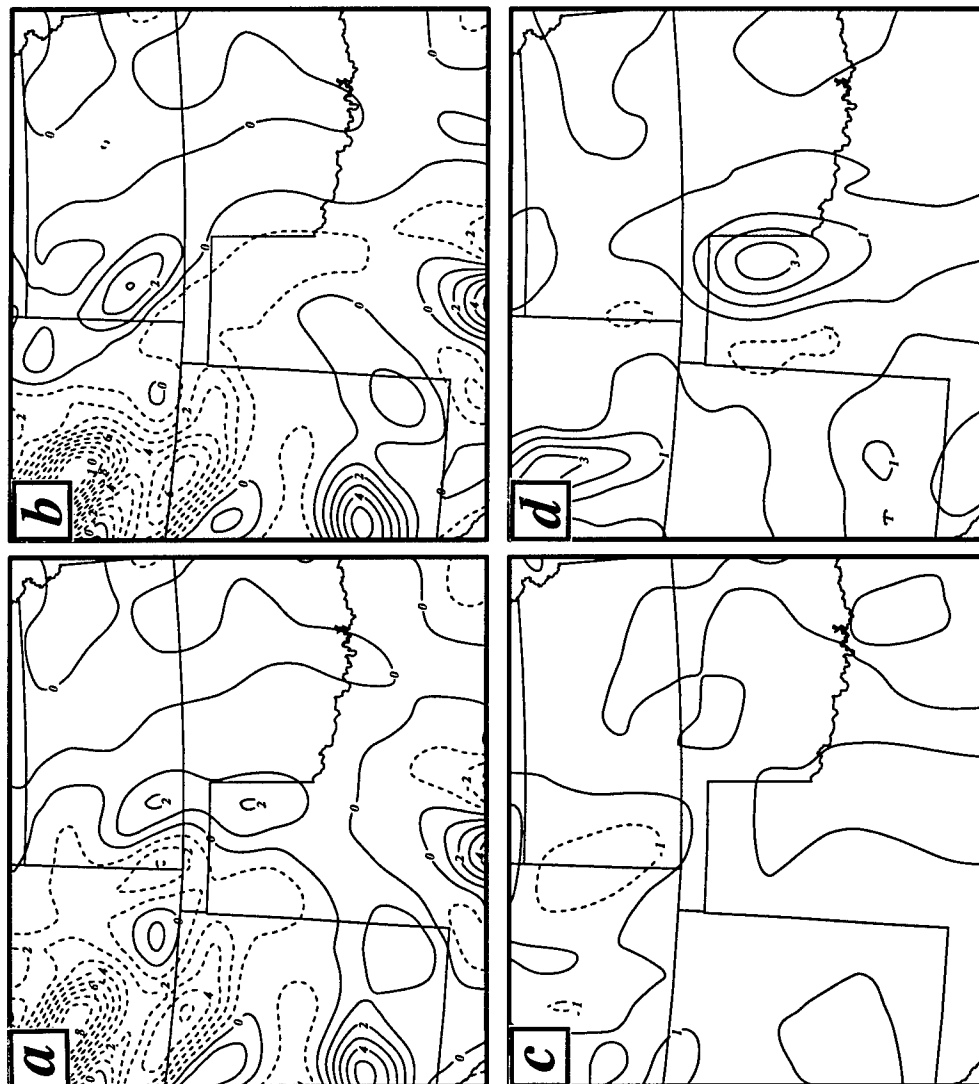


Figure 3.35. 0000 UTC 9 March 1992 500 mb frontogenesis calculations based on Miller Frontogenetic function derived from the 60 km MASS model simulation with high resolution terrain data base. (a) Total frontogenesis, (b) tilting term, (c) horizontal shear term, and (d) confluence term. Solid lines depict frontogenesis, dashed lines frontolysis ($^{\circ}\text{K } 100 \text{ km}^{-1} \text{ 3 hrs}^{-1}$).

the jet exit region. This leads to an enhanced signal of frontogenesis along the Texas/Oklahoma border in response to contributions by confluent deformation over the eastern portion of the Texas panhandle and tilting over south-west Kansas. The improved resolution of the 60 km model run provides a better depiction than the coarse resolution of the observed fields (Fig 3.25).

Construction of a series of east-west orientated cross sections through the Texas panhandle within the developing jet exit region show the developing jet and CFA structure (Fig. 3.36). At 08/15 UTC, the jet exit region is characterized by a deep layer of leftward-directed flow which extends from the surface up to the 400 mb level (Fig. 3.36a). The circulation vectors reveal a pronounced thermally-direct circulation within the jet exit region. As air parcels enter this region they accelerate in response to being driven towards lower heights by the terrain induced secondary circulation. By 08/21 UTC, the impact of the secondary circulation is observed in the concentrated zone of momentum extending down to the 700 mb level (Fig. 3.36b). A strong thermally-direct circulation persists within the exit region of the original jet streak while within the entrance region of a newly formed jet streak that extends into western Kansas/Oklahoma. Within the accelerative jet exit region an increase in the baroclinicity is observed.

The elevated thermal structure is similar to that seen in Hobbs *et al.* (1990) where the down-folding of the isentropes are positioned well ahead of the surface baroclinic zone. However, this is where the similarity ends in that the source of cold air is considerably different than Hobbs' conceptual model of CFA generation. Rather than the air simply being advected out of the mountains, cold air is generated in response to the

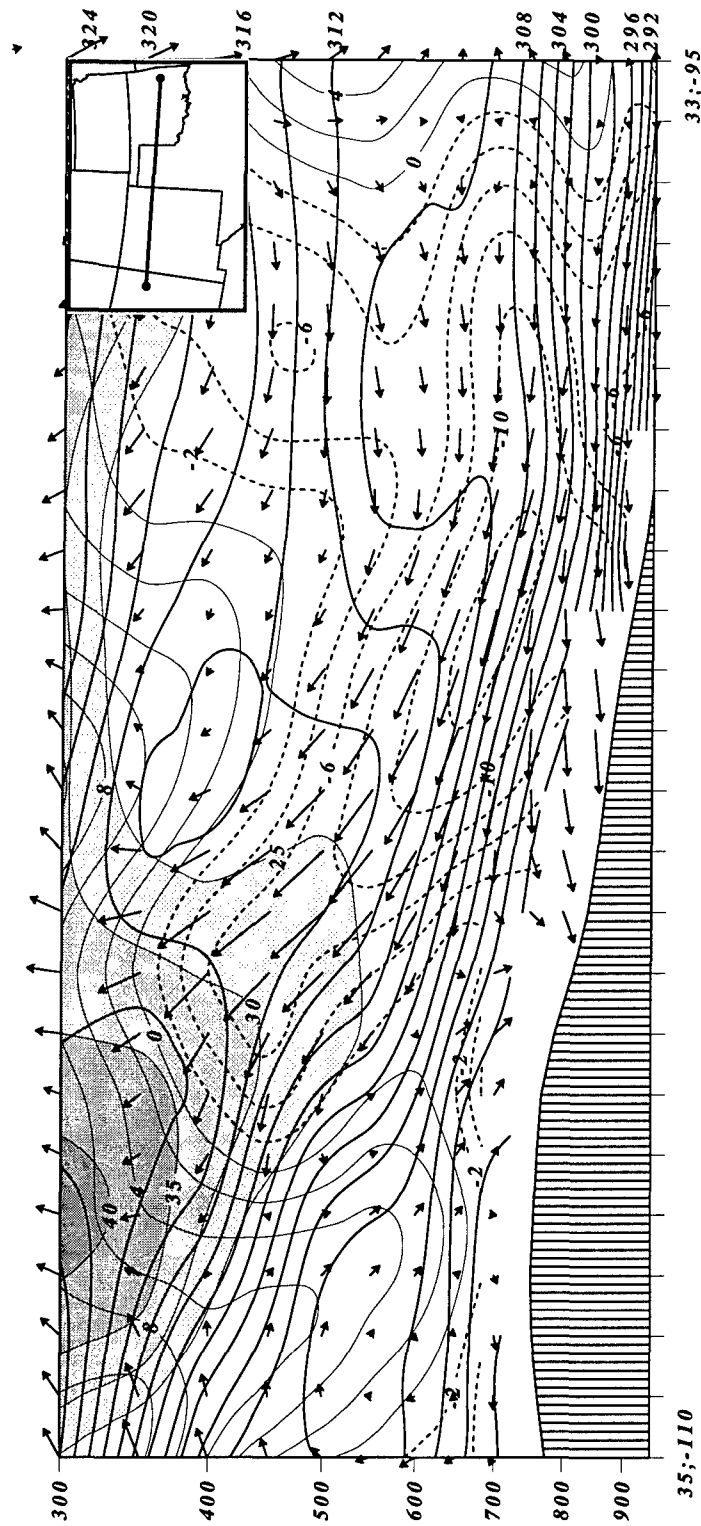


Figure 3.36a. 60 km full physics MASS model cross section valid at 1500 UTC 8 March 1992 extending from 35°N, 105°W to 35°N 95°W. The thin solid lines depict theta surfaces at a 2°K increment. The isotachs for the total wind speed are shaded above 25 ms⁻¹ at an increment of 5 ms⁻¹. The component of the wind directed left (dashed) or right (solid) of the geostrophic flow is displayed in 2 ms⁻¹ intervals. The circulation, derived from the ageostrophic wind and omega field, is depicted by the vectors.

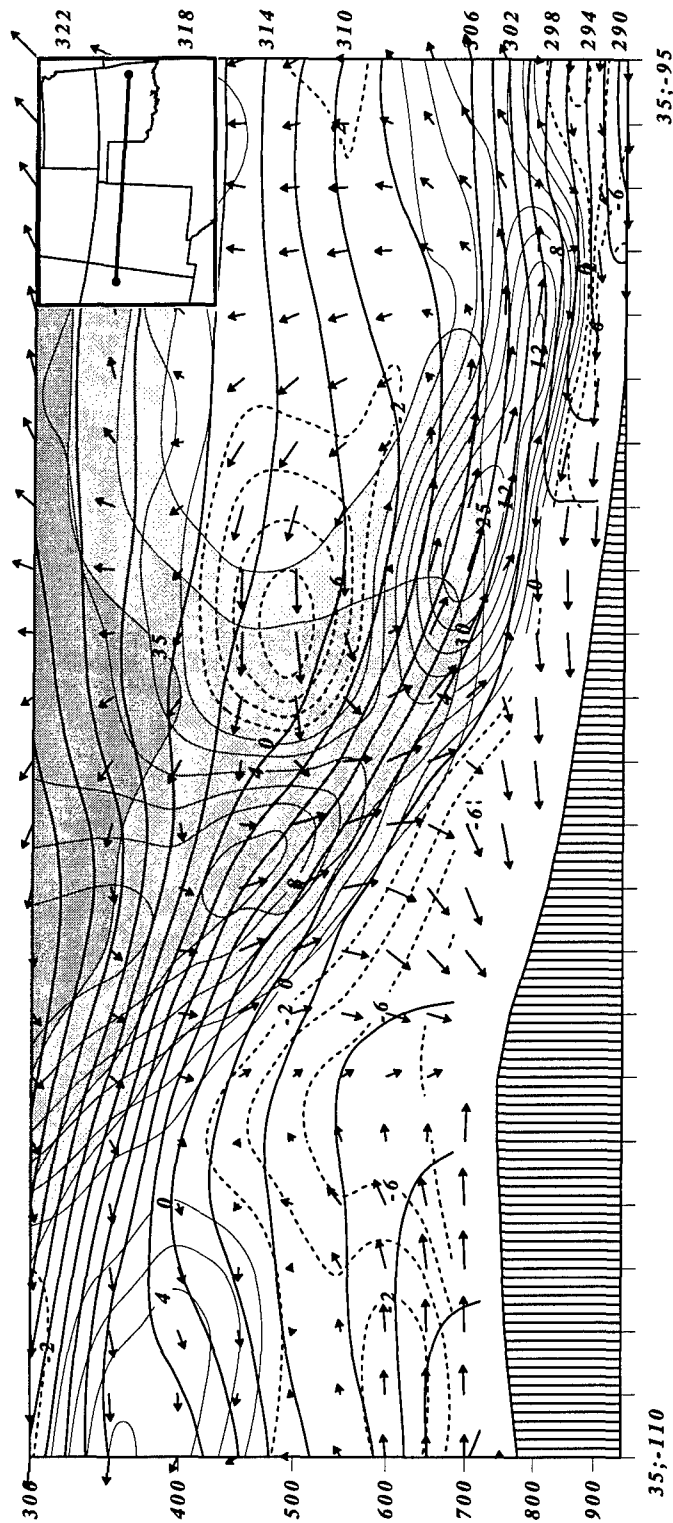


Figure 3.36b. 60 km full physics MASS model cross section valid at 2100 UTC 8 March 1992 extending from 35°N, 105°W to 35°N 95°W. The thin solid lines depict theta surfaces at a 2°K increment. The isotachs for the total wind speed are shaded above 25 ms⁻¹ at an increment of 5 ms⁻¹. The component of the wind directed left (dashed) or right (solid) of the geostrophic flow is displayed in 2 ms⁻¹ intervals. The circulation, derived from the ageostrophic wind and omega field, is depicted by the vectors.

development of complex secondary circulations set up by the mountains. In time, this elevated pool of cool dry air acts to enhance the destabilization over Oklahoma resulting in the generation of widespread convective activity well downstream of the mountains.

3.8.3 Adiabatic Sensitivity Study

The concentration of warm air in the lee of the mountains due to the downslope flow provides a very strong signal by 08/12 UTC. Sensitivity studies using a flat terrain model were attempted to diagnose the impact of the mountains in forming this mass perturbation. However, the persistent cross mountain flow had resulted in a well developed wedge of warm air at the 08/12 UTC period that could not be eliminated. In fact, a run initialized 24 hours prior at 07/12 UTC still contained a strong warm air signal. Consequently, a flat terrain simulation sensitivity study was abandoned.

A sensitivity study of another kind was developed to assess the impact of the strong warming of the boundary layer during the course of development. In order to address the impact of daytime surface sensible heating in amplifying the mass perturbation an adiabatic simulation was conducted. This run was performed by eliminating the vertical heat flux from the lowest sigma level to above levels and suppressing latent heat release generated by precipitation processes. Initialized moisture fields within the atmosphere acts as a tracer while being advected about the model domain during the course of the run.

During the first 12 hours of the adiabatic model run the evolution of the jet structure and cold air aloft provide subtle differences from that of the full physics run. The

lack of appreciable observed precipitation through the southern Plains during this period results in little impact from latent heat release. Consequently, differences are attributed to the boundary layer expansion as daytime heating increases the mean thickness of the lower troposphere. The cross-mountain flow provides a pronounced region of dry air over the south-western Plains as evident in the satellite image at 1731 UTC (Fig. 3.3b). The clear-dry conditions promote maximum sensible heating the lower troposphere. This increase acts to enhance the mass perturbation over the western Plains. In turn, a stronger adjustment develops producing an increase in cold air over the panhandle by 09/00 UTC.

Comparison between the 500 mb 60 km full physics and the adiabatic simulation at 08/21 UTC is shown in Fig. 3.37. The graphical subtraction of selected fields are provided in Fig. 3.38. The structure of the full physics run indicates a narrow zone of momentum extending northward along the western Plains. A split in the wind maximum with considerably tighter gradient of momentum in the cross stream direction than the adiabatic run is seen. The impact of the sensible heating is to raise the heights in the full physics run by as much as 20 m over New Mexico (Fig. 3.38b). In response, the axis of the cold pool over New Mexico is much more focused where as the adiabatic run has a broader pool of cold air that extends into northern Colorado. In the full physics run, the 500 mb temperatures are as much as 2.5°C colder over New Mexico and 5.5°C warmer over northern Colorado (Fig. 3.38a). The temperature decrease is quite significant, considering the increased destabilization brought on by an added 2.5°C cooling of the midtroposphere over the central Plains.

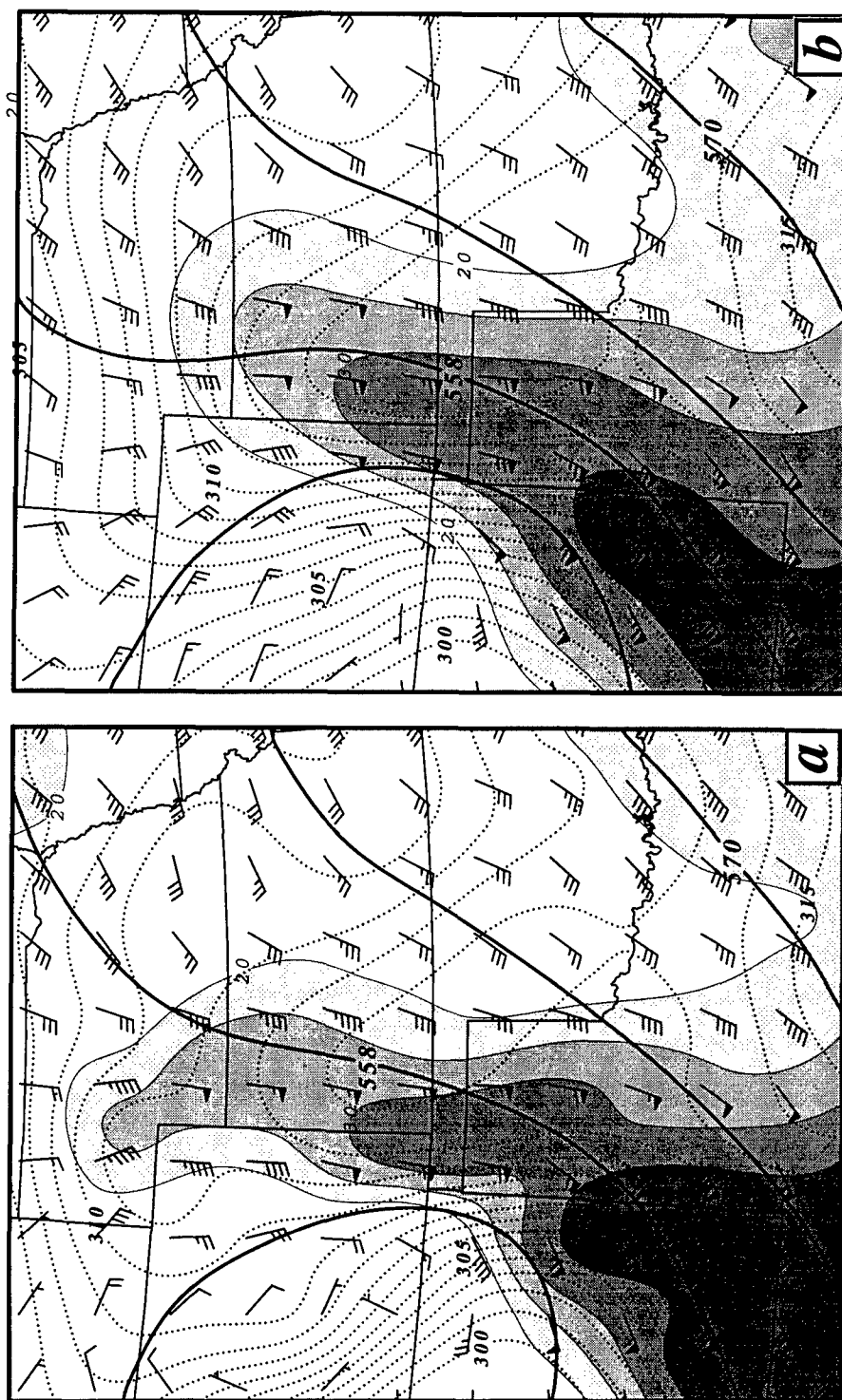


Figure 3.37. 2100 UTC 8 March 1992 60 km 500 mb MASS modeling study of (a) full physics output and (b) adiabatic model run. Parameters depicted: heights (solid - 6 dm interval), isotachs above 20 ms^{-1} (shading at a 5 ms^{-1} interval), theta (dotted - 1°K interval), and wind barbs (flag - 25 ms^{-1} , full staff - 5 ms^{-1} , half staff - 2.5 ms^{-1}).

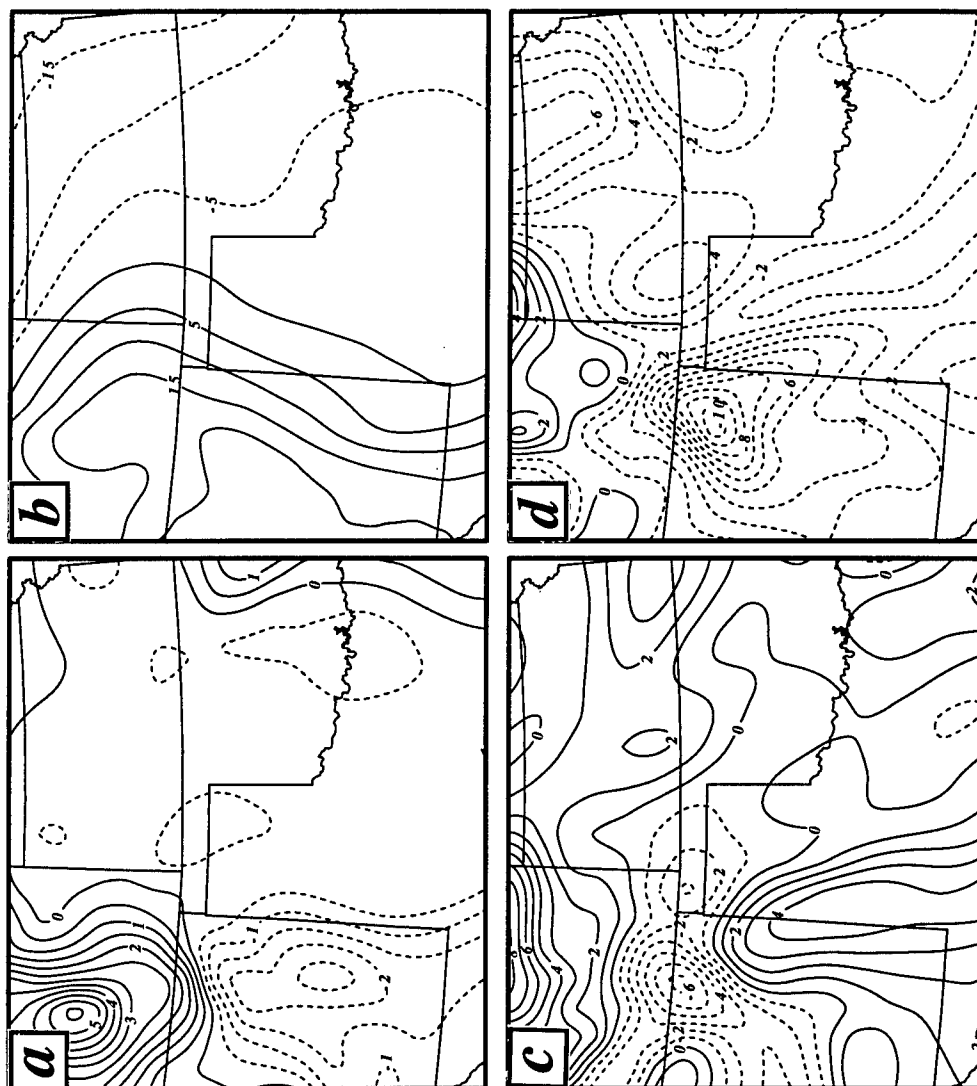


Figure 3.38. Graphical subtraction of the 2100 UTC 8 March 1992 60 km 500 mb full physics model output from the adiabatic model output files. Displayed fields are difference in (a) theta, (b) geopotential height, (c) u -wind component, (d) v -wind component. Solid line indicates full physics run has higher value and dashed indicates adiabatic run has higher value.

Inspection of the components of the wind field reveal some differences that impact the generation of the CFA. A stronger u-component in the wind field is found along the Texas/New Mexico border. Meanwhile, the v-component is generally larger in the adiabatic run than the full physic simulation (Fig. 3.38c and d). The increased v-component is consistent with the fact that the overall jet streak has a broader pattern extending further eastward than the full physics run. Inspection of the magnitudes of the v-component differences indicates a split in the pattern over the Texas panhandle. This split reflects an increase in the meridional component in the full physics run in response to the influence of the sensible heating in the lee of the mountains. This increase is carried well into western Nebraska where the full physics run has a v-component $>10 \text{ ms}^{-1}$.

The impact of the lower tropospheric heating is even more prevalent in the 700 mb pattern. Comparisons between the 08/21 UTC full physics and the adiabatic run reveal a significant pool of cold air developing over the Texas panhandle (Fig. 3.39). Significant differences are brought on by daytime sensible heating (Fig. 3.40). The heights at the 700 mb level are over 20 m higher in the full physics run along eastern New Mexico in response to the strong daytime sensible heating over the elevated terrain of the southeast Rockies. A stronger v-component over this region is seen while the u-component is significantly weaker. In response to the increased divergent response to the mass perturbation, a temperature anomaly of -2.5°C over the Texas panhandle is simulated in the full physics run.

The 08/21 UTC adiabatic simulation of frontogenesis indicate a pronounced split structure over eastern New Mexico in response to the wedge of warm air established

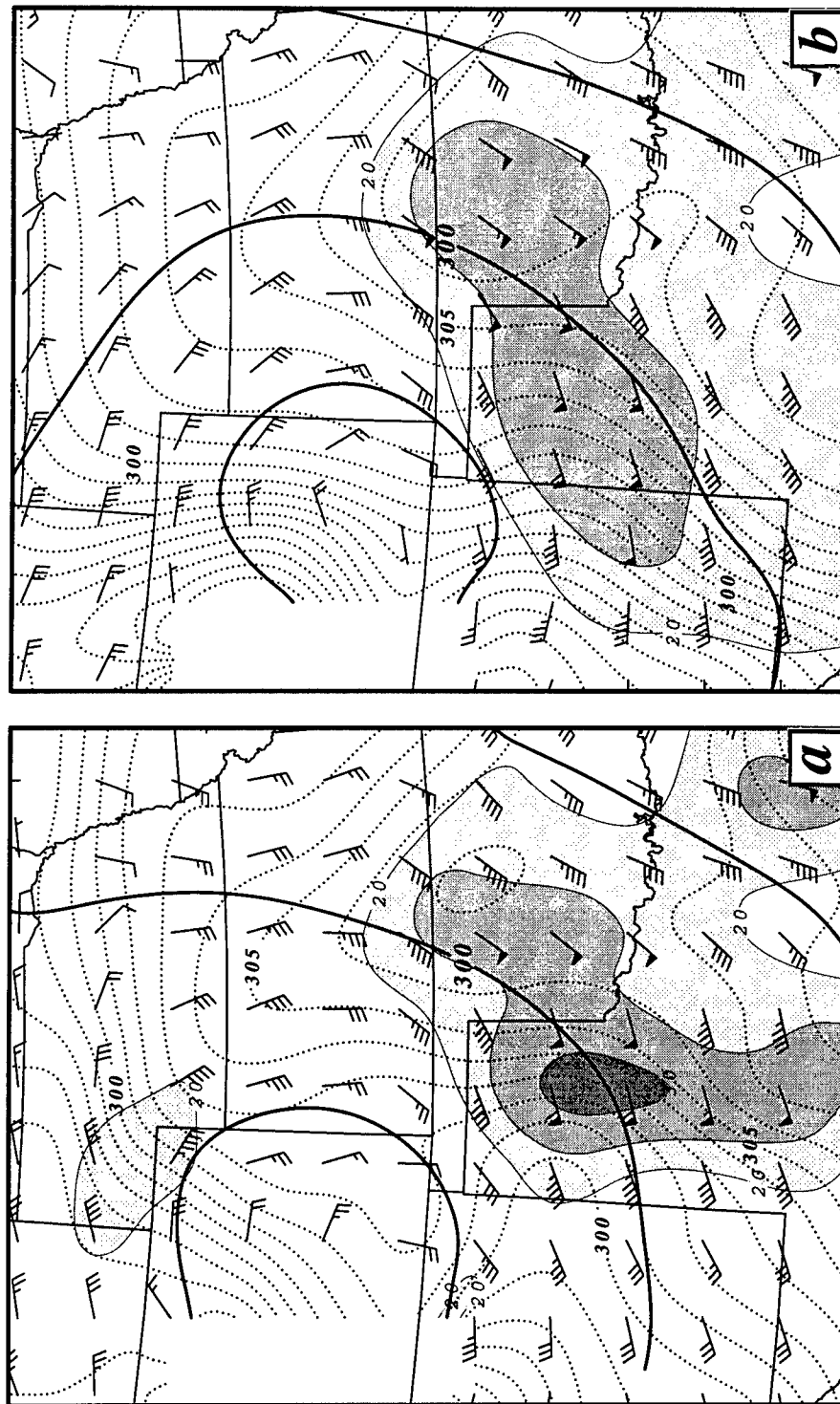


Figure 3.39. 2100 UTC 8 March 1992 60 km 700 mb MASS modeling study of (a) full physics output and (b) adiabatic model run. Parameters depicted: heights (solid - 6 dm interval), isotachs above 20 ms^{-1} (shading at a 5 ms^{-1} interval), theta (dotted - 1°K interval), and wind barbs (flag - 25 ms^{-1} , full staff - 5 ms^{-1} , half staff - 2.5 ms^{-1}).

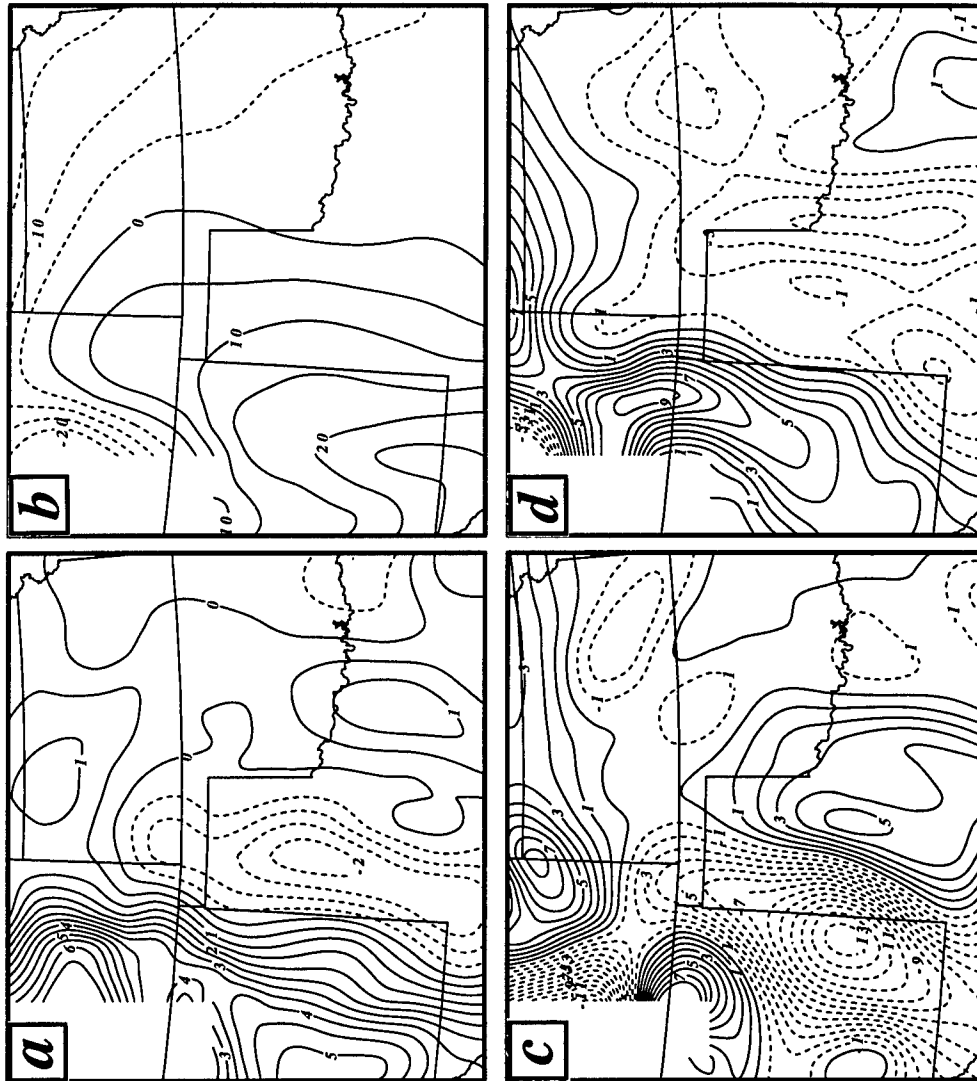


Figure 3.40. Graphical subtraction of the 2100 UTC 8 March 1992 60 km 700 mb full physics model output from the adiabatic model output files. Displayed fields are difference in (a) theta, (b) geopotential height, (c) u -wind component, (d) v -wind component. Solid line indicates full physics run has higher value and dashed indicates adiabatic run has higher value.

along the Front Range of the Rockies (Fig. 3.41). The impact of the confluence term is ~40% less than that of the full physics run while the negative impact of the tilting term in the adiabatic run is substantially less than that observed in the full physics run.

Since no significant precipitation was observed in the full physics run, model differences can be attributed to the impact of sensible heating. During the course of the morning, increased sensible heating develops over the southern Plains. This forcing acts to generate a stronger concentration of momentum along the western Plains while focusing the development of cold air aloft over northern New Mexico into the Texas panhandle.



Figure 3.41. 2100 UTC 8 March 1992 500 mb frontogenesis calculations based on Miller Frontogenetic function derived from the 60 km Adiabatic MASS model simulation. (a) Total frontogenesis, (b) tilting term, (c) horizontal shear term, and (d) confluence term. Solid lines depict frontogenesis, dashed lines frontolysis ($^{\circ}\text{K } 100 \text{ km}^{-1} \text{ 3 hrs}^{-1}$).

4. GEOSTROPHIC ADJUSTMENT AND CFA FORMATION IN RESPONSE TO A DEVELOPING COLD SURGE ALONG THE NORTHERN FRONT RANGE

4.1 Overview

The previous section provides evidence of an adjustment process taking place as the jet exit region encounters a mass perturbation established by a wedge of warm air in the lee of the southern Rockies. In response, an increase in the divergent wind field is observed as a thermally-direct circulation develops in order to regain a balance between the mass and momentum field. This adjustment stage encompassed a period of ~6 hours between 08/15 and 08/21 UTC. This stage of development was followed by a “balanced” thermally-indirect circulation within the jet exit region over the Texas panhandle. In response to the altered secondary circulations, the development of a CFA is observed downstream of the baroclinic zone over the inner-mountain region.

This portion of the research shifts the focus to a second set of adjustments that take place over the Kansas/Oklahoma region in response to a narrow surge of cold air down the Front Range of the northern Rockies. Shortly after 09/00 UTC cold air along the northern foothills begins to propagate southward into eastern Colorado. The confinement of an intense wedge of cold lower tropospheric air along a mountain barrier disrupts the mutual balance between the mass and momentum fields resulting in a geostrophic adjustment. The period of adjustment between 09/02-09/08 UTC acts to reinforce CFA development and allows for the formation of a significant jet streak over the central Plains.

4.2 Objectives

The focus of this part of the thesis will investigate the atmospheric response to a terrain-induced mass perturbation, brought on by an advancing cold surge, and its interaction with the southern branch of the polar jet stream. Section 4.3 will provide an overview of the environment leading up to the jet streak/CFA development. Section 4.4 will investigate the structure of the cold surge and the associated mass perturbation brought on by the terrain interaction with the low-level cold flow. Section 4.5 combines observational and model data to detail the structure of the CFA and identify the geostrophic adjustment process responsible for development. In addition, modeling sensitivity studies will be presented to quantify the terrain impact in CFA generation.

4.3 Observational Perspective

4.3.1 Evolution of the Low-Level Features

By 1800 UTC 8 March, an area of low pressure has organized over southeast Colorado (Fig. 3.6a). During the previous 24 hours a benign leeside trough was located over eastern New Mexico in response to adiabatic warming supplied by a persistent cross-mountain flow. This low is situated at the apex of a strong thermal ridge that extends along the foothills. The downslope flow provides an extended layer of dry air allowing a concentrated zone of intense sensible heating to develop. As the convective boundary

layer forms, the dryline advances into the Texas panhandle. The dryline is found along the leading edge of an air mass characterized by low θ_e . In contrast, a 25K increase in θ_e is found ahead of this boundary. Over the northern Plains, a surface front is found along the foothills of the northern Rockies associated with a short wave imbedded in the northern branch of the polar jet that had passed through the region several days earlier. The northeasterly return flow from a high pressure system over northern Alberta Canada forces the cold-dry Canadian air mass to damn up against the eastern slopes of the northern Rockies. In response, a stationary boundary is found along the barrier. Extending eastward along this boundary, frontolysis is observed as the low-level thermal gradient and convergence zone weakens along with the supporting northern branch of the polar jet stream. Meanwhile, frontogenesis is observed over southern Nebraska as the circulation about the developing surface low increases. Warm-moist high θ_e air is rapidly transported northward resulting in a zone of increased convergence and baroclinicity that is shifted southward over southern Nebraska.

By 09/00 UTC, the surface low has deepened by 5 mbs and the circulation dominates the central Plains (Fig 3.10a). The 994 mb low has pulled slightly eastward during the past six hours. The increased isallobaric forcing has generated a strong cross contour flow over southeastern Wyoming. In response, the winds have shifted from an upslope component to that of an along-barrier flow. Observations indicate a strengthening northerly wind in excess of 12 ms^{-1} over the area. The combined effects of a strong thermal ridge tied to the southern foothills along with an increased northerly wind over the northern Plains result in the strengthening of the baroclinic zone over northeast Colorado.

As the surface low slowly moves eastward, the thermal ridge is shifted away from the leeside allowing the cold surge to propagate down the Front Range.

During the next three hours the cold front has infiltrated eastern Colorado as it surges down the Front Range (Fig. 4.1a). The passage of the frontal zone is accompanied by a modest $10^{\circ}\text{C } 3 \text{ hr}^{-1}$ temperature drop, sustained winds of nearly 20 ms^{-1} , and heavy thundersnow storms. Meanwhile, the post frontal region is dominated by a strong upslope component of the wind producing an extensive area of precipitation. The associated dryline has propagated eastward towards central Oklahoma, providing a region of relatively dry air over the southern foothills of New Mexico. The generally clear skies and low humidity levels extending throughout the atmospheric column allow for maximum sensible heating to warm this region. This heating provides an important means of increasing the meridional temperature gradient along the Front Range.

During a span of seven hours, the surface low experienced a burst of rapid deepening of nearly 1 mb hr^{-1} over the period 08/15 - 08/22 UTC. Thereafter, the surface pressure showed little change in development as it slowly pulled away from the mountains. By 09/06 UTC the surface low has slowly moved eastward into western Kansas (Fig. 4.2a). In response, the cold air advances unimpeded towards the New Mexican border. In the wake of this boundary, winds in excess of 20 ms^{-1} are observed along the east slope of Colorado with temperatures falling some $10\text{-}15^{\circ}\text{C}$. Ahead of the developing low, a strong stationary boundary is established. The northern branch of the jet stream never phases in with the southern jet. Consequently, a strong dome of high pressure remains anchored

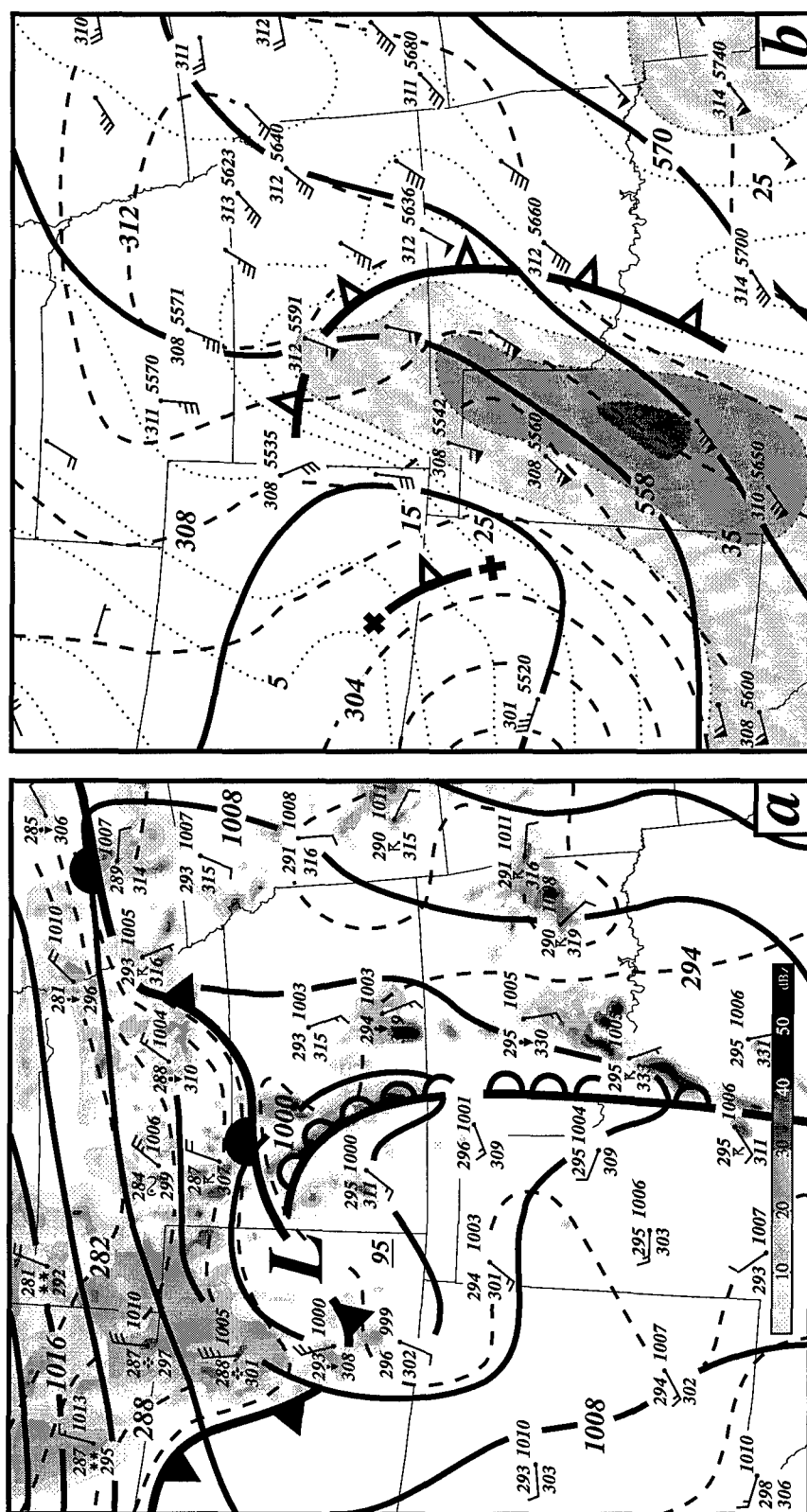


Figure 4.1. (a) 0300 UTC 09 March 1992 surface analysis: isobars (solid - mb), theta (dashed - °K), radar echo's (shading - interval of 10 dBz). Station plot: theta, theta-e, PMSL, observed weather, wind barb (full staff - 5 ms⁻¹, half staff - 2.5 ms⁻¹). Surface dry line depicted by line of open semicircles. (b) 0300 UTC 09 March 1992 500 mb analysis: heights (solid - dm), isotachs (dotted / shading - ms⁻¹), theta (dashed - °K). Station plot: theta, height, wind barb (flag - 25 ms⁻¹, full staff - 5 ms⁻¹, half staff - 2.5 ms⁻¹). Upper level cold front depicted by line of open triangles. Frontolysis depicted by broken line separated by a cross.

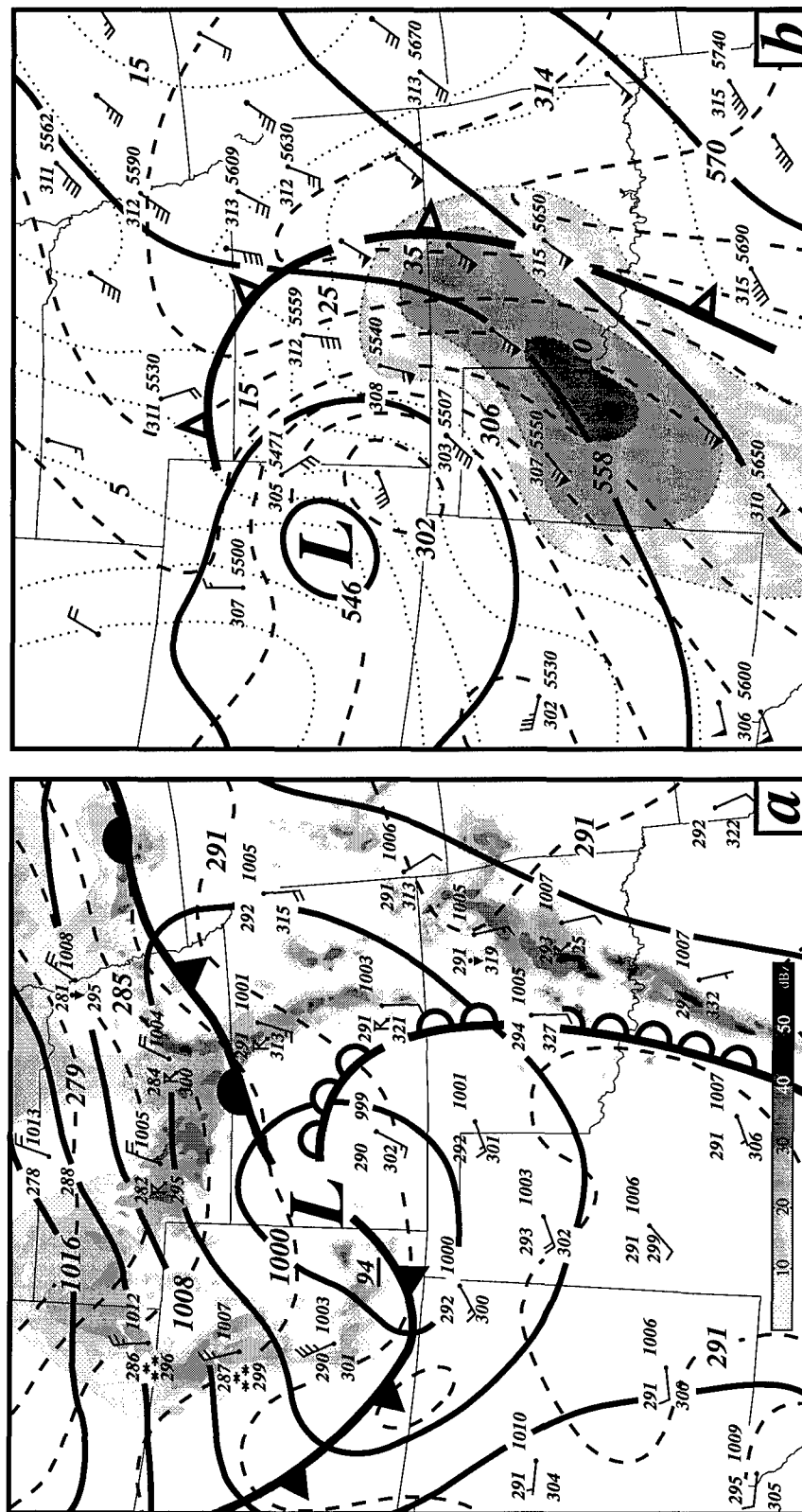


Figure 4.2. (a) 0600 UTC 09 March 1992 surface analysis: isobars (solid - mb), theta (dashed - $^{\circ}\text{K}$), radar echo's (shading - interval of 10 dBz). Station plot: theta, theta-e, PMSL, observed weather, wind barb (full staff - 5 ms^{-1} , half staff - 2.5 ms^{-1}). Surface dry line depicted by line of open semicircles. (b) 0600 UTC 09 March 1992 500 mb analysis: heights (solid - dm), isotachs (dotted / shading - ms^{-1}), theta (dashed - $^{\circ}\text{K}$). Station plot: theta, height, wind barb (flag - 25 ms^{-1} , full staff - 5 ms^{-1} , half staff - 2.5 ms^{-1}). Upper level cold front depicted by line of open triangles.

over central Canada. The position of the high pressure is to the north-northeast of the surface low. This configuration allows the cold Canadian continental air mass to act as a block to the northerly advancement of the warm frontal zone. In response, a strong baroclinic zone is found to the northeast of the surface low. Surface frontogenesis calculations for this portion of the boundary increase significantly during the course of the day. Early in the period, frontogenetic forcing of $1.1\text{K } 100 \text{ km}^{-1} \text{ } 3 \text{ hr}^{-1}$ is calculated over southern Nebraska. By 9/06 UTC, the forcing has increased significantly to $3.3\text{K } 100 \text{ km}^{-1} \text{ } 3 \text{ hr}^{-1}$ over the same region as confluence and shearing deformation increase. The strengthening boundary results in abundant over-running precipitation over the northern Plains. In response, persistent blizzard conditions were experienced over a wide region.

4.3.2 Evolution of the Midtropospheric Atmosphere

In the midst of the evolving surface pattern, the upper levels reveal the development of a potent CFA and bifurcation of the jet stream. The availability of 3-hourly sounding data over the Plains provides valuable information in discerning the evolution of the mid-troposphere. The 500 mb pattern at 08/18 UTC depicts a broad ridge over the central Plains with a narrowly focused ridge of warm air extending into northeastern Colorado (Fig. 3.6b). This thermal ridge is firmly entrenched along the Front Range which establishes a well-defined baroclinic zone over New Mexico. In response, an upper-level cold front is depicted in this region. A modest 35 ms^{-1} jet streak, in the vicinity of ELP represents the forward quadrant of an expansive jet stream that extends westward

through the northern Baja peninsula. The warm air in the lee of the Rockies provides an effective means of blocking the eastward progression of cold air as the jet streak propagates out across the mountain barrier. Consequently, the momentum field is in an environment that is no longer in geostrophic balance as the thermal field is disrupted by the interaction between the terrain and the flow.

By 09/00 UTC a mid-level pool of cold air has formed over the Texas panhandle resulting in the formation of a CFA (Fig. 3.10b). This feature has formed nearly 500 km downstream of the leading edge of cold air associated with the primary upper-level low. The jet streak has emerged over west-central Texas with 35 ms^{-1} winds extending from AMA to MAF. The strong signal of a bifurcation in the streak from the primary flow of the jet stream is observed in the weak wind field over central Oklahoma. The upper-level front over New Mexico begins to dissipate as the baroclinicity between the Front Range and the inner-mountain region is diminished as cold air develops over the Texas panhandle.

By 09/03 UTC temperatures over the Texas/Oklahoma panhandle have fallen 6°C as cold air overspreads the region (Fig. 4.1b). Significant height falls have developed along the eastern slopes with a negative anomaly of 45 m (3 hrs^{-1}) observed over Guymon, Oklahoma (GUY). The northern branch of the jet stream continues to remain a separate feature from the southern branch as it traverses the southern Canadian provinces. This acts to limit the ridge from building into the northern Plains maintaining the 500 mb ridge line through central Nebraska. As the CFA advances out ahead of the surface dryline, cool-dry air overrides the warm-moist air confined to the low levels. The reduction in static stability

results in the explosive development of convection along the advancing CFA (a process described by Martin *et al.* 1995). The rapid destabilization results in the formation of severe thunderstorms producing several F-0 tornadoes and numerous reports of golf ball size hail with some as large as 4" in diameter.

By 09/06 UTC, an intense upper-level low develops over eastern Colorado coincident with the surge of low-level cold air focused down the eastern slope of the Rockies (Fig 4.2b). An explosive 3-hour height fall of 64 m is observed over eastern Colorado at the Burlington CLASS site. During this period of rapid atmospheric changes, the 500 mb cold pool intensifies over southeastern Colorado with a pronounced thermal ridge over the eastern Plains. The increased baroclinicity is evident by the 3 hour temperature drop of 5° over Guymon, Oklahoma while increasing over 3°C at Norman, Oklahoma. The jet structure has undergone significant intensification as the core of the 40 ms⁻¹ 500 mb jet streak lies just east of Amarillo, Texas.

4.4 Cold Surge Structure

During IOP-17, strong static stability and the combined circulations of the developing low over eastern Colorado and return flow from high pressure situated over central Canada were effective in confining cold air along the northern slopes of the Rockies. The orientation and elevation of the mountains in relation to the stratified low-level flow provide an effective means of "damming" cold air on the windward (east) side of the mountains (Pierrehumbert 1984, Dunn 1987, Bell and Bosart 1988).

4.4.1 Flow Blockage Requirements

Under certain atmospheric conditions, nonlinear processes and large amplitude waves become important in defining the flow about a mountain range. The arrival of cold air at the foot of the mountain barrier requires a conversion of kinetic to potential energy in order to overcome the barrier. In order to cross the barrier, the nose of the boundary must acquire sufficient potential energy in the form g^*H_M , where the effective reduced gravitational force (g^*) equals $g\Delta\theta/\theta_0$, θ_0 is the temperature of the cold layer, $\Delta\theta$ is the temperature difference from the overlying warm layer, and H_M is the height of the barrier (Schumann 1987). The ratio of kinetic to potential energy takes on the form

$$N^* = U^2 / 2g^*H_M \quad (18)$$

where U is the wind component in the direction of the front. In the event that $N^* < 1$, the cold air will be prevented from crossing the barrier due to insufficient kinetic energy.

The calculation of the Froude number (F_R) provides a useful measure of the atmospheric response to the terrain. This non-dimensional parameter relates the inertial and buoyant forcing in relation to the barrier which is defined as

$$F_R = U / NH_M \quad (19)$$

were U is the mean wind component across the barrier within the layer beneath H_M , and N is the Brunt-Väisälä frequency. Flow blockage can occur when the inertial forcing is insufficient to counter the static stability of the air mass. In this case, insufficient kinetic energy exists to overcome the barrier resulting in an accumulation of mass on the windward (eastern) side of the mountain. Efforts by Pierrehumbert (1984) suggest flow blockage can be expected with a critical F_R value < 1.5 to 2.0 .

In time, this build up of mass on the windward side of the mountain can generate a component of flow parallel to the barrier resulting in the southerly surge of cold air. According to Kelvin wave theory, the oncoming flow of depth " h " is blocked by the topographical barrier. This blockage results in a buildup of mass in the vicinity of the barrier producing a mass perturbation of depth " h^* ". The buildup of energy is released isotropically in the form of gravity waves. As the energy propagates away from the center, the outward directed flow obtains a rightward directed component in response to the Coriolis force. In time, the flow becomes directed along and to the left (looking down the barrier) with the strongest component found near the barrier itself (Tilley 1990).

4.4.2 Application of Theory of Flow Blockage to Observations

Rawinsonde observations over the northern Plains indicate a strong signal of flow blockage and accumulation of cold air along the windward slopes of the northern Rockies. The 09/00 UTC 850 mb analysis indicates a substantial pool of cold-dry air confined by the mountains to the west extending eastward through the northern Plains (Fig. 4.3a).

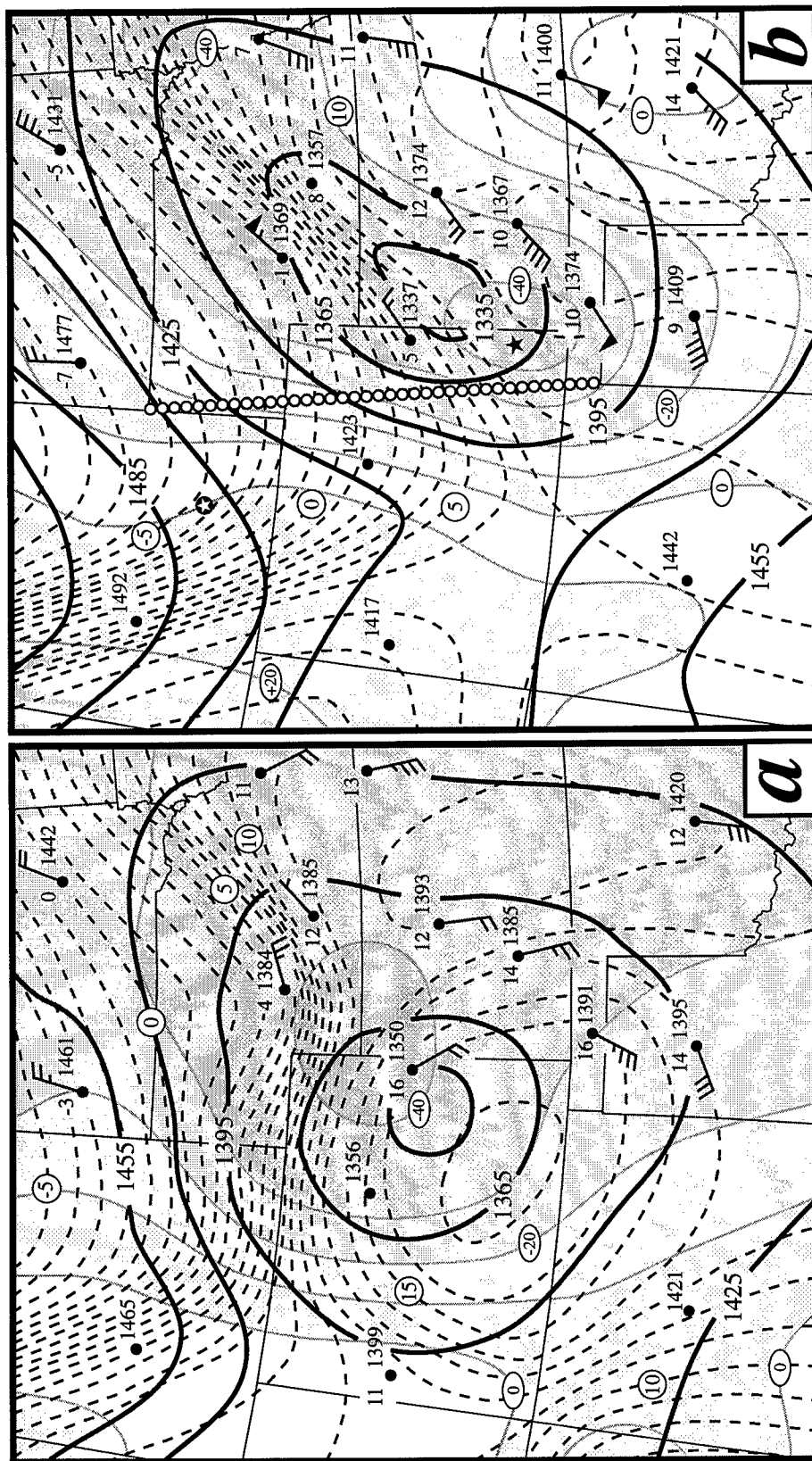


Figure 4.3. 850 mb analysis for 0000 UTC 9 March 1992 (a) and 0600 UTC 9 March 1992 (b). Solid lines depict heights (m), Dashed lines depict temperature ($^{\circ}\text{C}$). Station plot: temperature, height, wind barb (flag - 25 ms^{-1} , full staff - 5 ms^{-1} , half staff - 2.5 ms^{-1}). The 700 mb 6 hour height change is contoured and shaded at 10 m interval. Line of circles in (b) depicts cross-section location. Solid star in southeast Colorado is site of Granada, Colorado profiler site and open star in southeast Wyoming is the Medicine Bow, Wyoming profiler site.

Over western Wyoming/Colorado the average terrain is ~2500 m, with an orientation ~25° from north, which equates to a mean cross-barrier wind component of ~ 9 ms⁻¹ averaged over the depth H_M. Indicative of the strong static stability, the Brunt-Väisälä frequency is computed to be 0.014 s⁻¹, $\theta_0 = 288^\circ\text{K}$, and $\Delta\theta=10^\circ$ with $g^* = 0.34 \text{ ms}^{-2}$. Calculations indicate $F_R = .25$ and $N^* = .047$ which are less than the critical values described by Pierrehumbert (1984) and Schumann (1987). Such values are indicative of the favorable conditions for flow blockage and cold air damming in the eastern slopes of the northern Rockies.

This damming results in the concentration of cold air over the northern Plains observed in Fig. 4.3a. Temperatures below -5°C can be found over northeastern Wyoming into the Dakotas as a strong northerly ageostrophic flow supplies the region with cold Canadian air. To the south, a pool of warm, dry air develops in the lee of the mountains in response to the cross-mountain flow south of Denver, Colorado (DEN). Model trajectories of air parcels in this area indicates the parcels originate near the 800 mb level over central New Mexico and descend to the 850 mb level over western Texas (Fig. 3.11). During the descent the parcels undergo a 7°C increase in temperature in response to the downslope adiabatic warming. The combined affects of adiabatic warming and maximized sensible heating allow 850 mb temperatures to exceed +16°C over the region. This area of warm air is effective in retarding the southward extension of cold air down the Front Range. A significant 850 mb low is observed in the vicinity of this warm air resulting in a well- established cyclonic circulation over the Great Plains. The strong northerly ageostrophic flow over the northern Plains combined with the circulation associated with

the 850 mb low results in a strong convergent asymptote over southern Nebraska. In response, a strong east-west baroclinic zone of $\sim 4^{\circ}\text{C } 100 \text{ km}^{-1}$ extends eastward from the mountains into southern Nebraska.

As the low pressure area and the attendant warm pool slowly moves eastward, the 'flood gates' are opened allowing the cold surge to penetrate well southward (Fig 4.3b). In six hours, the pool of warm air over eastern Colorado is replaced by a wedge of cold-dry air. The apex of the cold air stream is found along and just downstream of the barrier. The cold surge has propagated southward down the Front Range at $\sim 17 \text{ ms}^{-1}$ as cold air infiltrates southeast Colorado. The wind profiler site located at Medicine Bow, Wyoming was unavailable prior to 08/23 UTC. However, after 09/00 UTC the profiler detects the development of a 22 ms^{-1} low-level jet located within the surging cold air. The core of this jet remains below 2 km as the wind profiles back with time (not shown).

The hourly observational trace from DEN clearly reflects the passage of the boundary at 08/23 UTC and the associated weather conditions (Fig. 4.4). Passage of the boundary was associated with rapidly decreasing cloud ceilings, increased precipitation, a sudden change from rain showers to heavy snow, plummeting temperatures, and an abrupt increase in surface winds approaching 20 ms^{-1} . The associated sounding profile between 09/00 and 09/06 UTC clearly reflects the dramatic cooling taking place in the low levels as the cold surge passes through the area (Fig. 4.5). The vertical depth of the cold air extends $\sim 2 \text{ km}$ AGL with the top of the frontal zone located at $\sim 650 \text{ mb}$. The development of the low-level jet is captured in the sounding data in which 22 ms^{-1} winds are detected near the 700 mb level. Construction of a cross section, valid at 09/03 UTC, along the axis of the

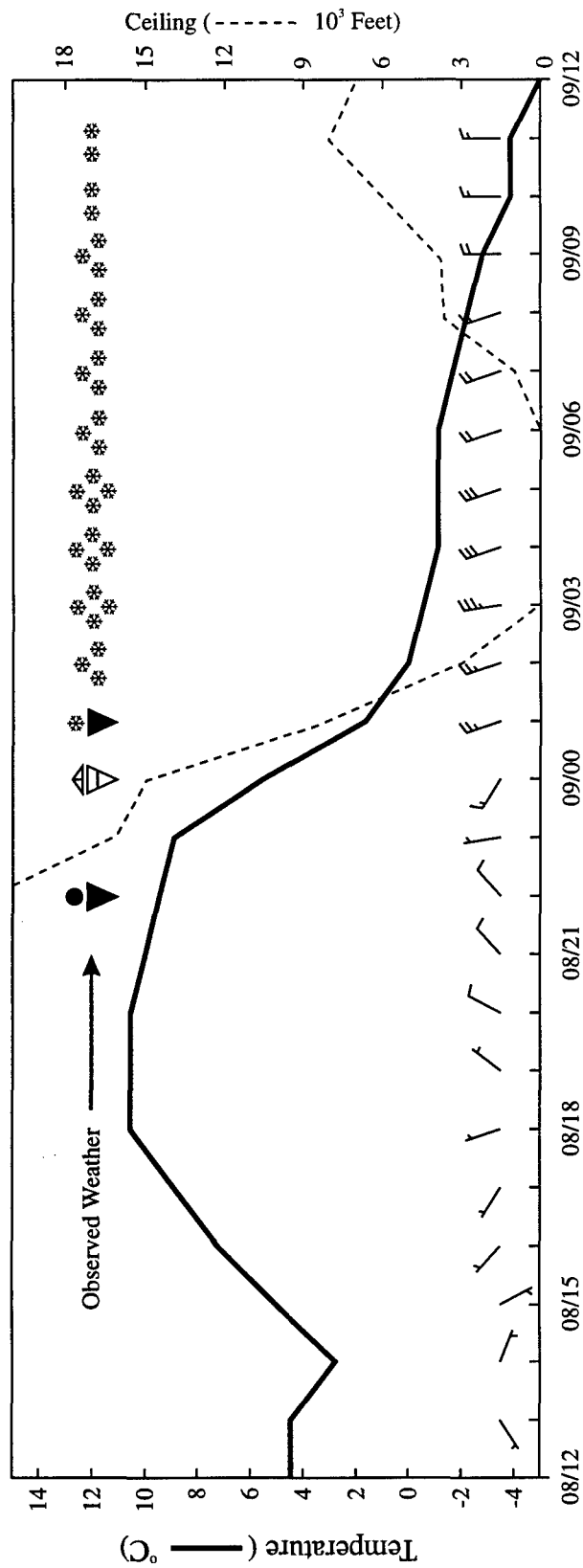


Figure 4.4. Observed weather conditions at Denver, Colorado for the 24 hour period 1200 UTC 8 March to 1200 UTC 9 March 1992. Observed temperature (solid line), ceiling height (dashed line), surface winds (full staff, 5 ms^{-1} and half staff, 2.5 ms^{-1}).

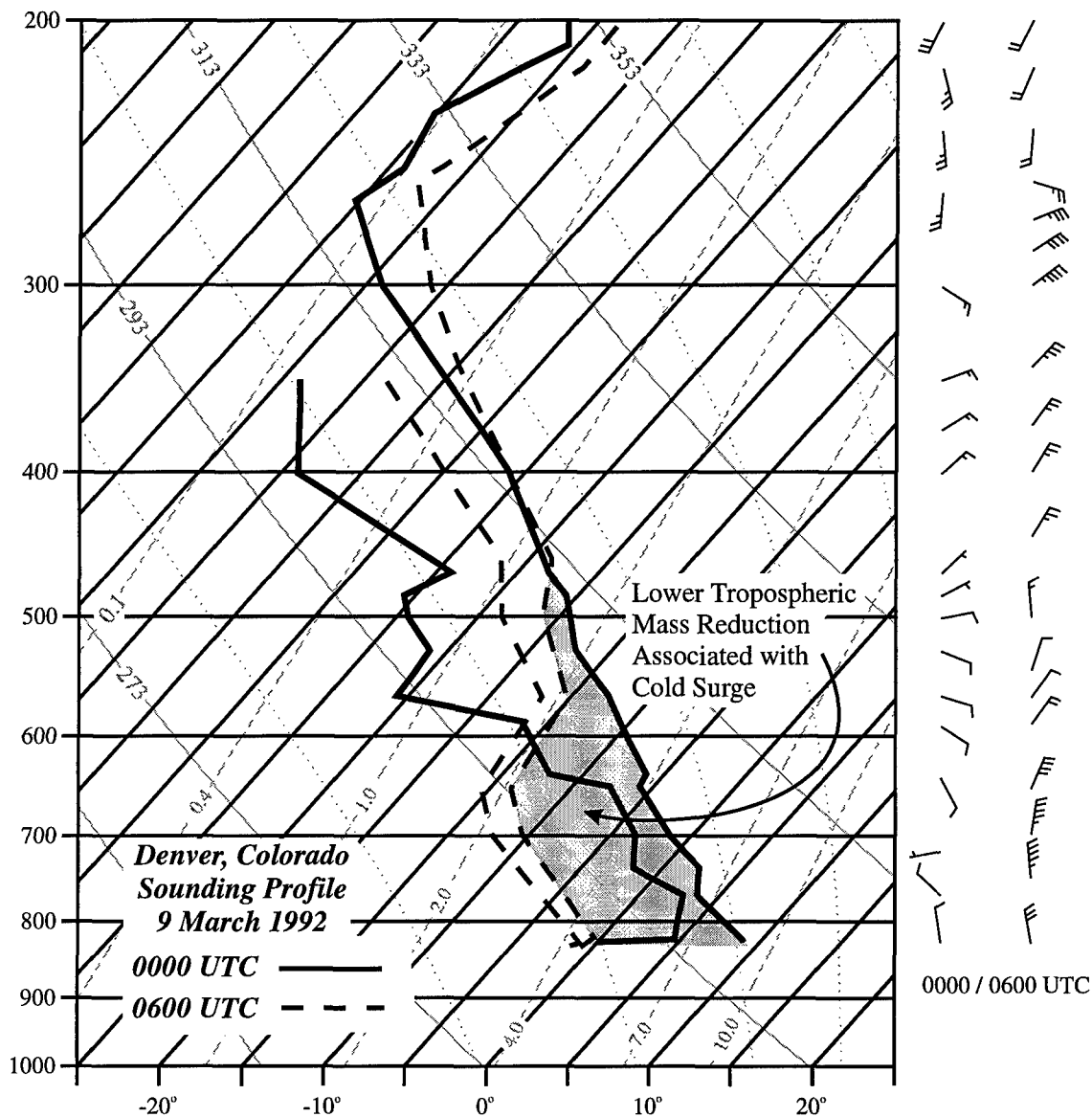


Figure 4.5. Denver, Colorado sounding profile for 0000 UTC (solid line) and 0600 UTC (dashed line) 9 March 1992. Isotherms - dark solid lines running from lower left to upper right, dry adiabats - light solid lines running from lower right to upper left, moist adiabats - light dotted lines running from lower right to upper left, mixing ratio - dashed lines running from lower left to upper right. Winds depicted at right (full staff - 5 ms^{-1} , half staff - 2.5 ms^{-1}).

cold surge is shown in Fig. 4.6. Despite the coarse resolution of the observational data in this region, the cold surge structure is depicted quite well. The strong signal of low-level cold air is detected below 650 mb in which a shallow frontal slope of 200:1 km is observed. Accompanying the cold surge is a marked increase in static stability as indicated by the strong isentropic gradient in the vertical. The component of the wind parallel to the plane of the cross-section reflects a 17 ms^{-1} jet orthogonal to the frontal zone. This is consistent with the rate of propagation of the cold surge and an indication that the propagation is primarily related to advective forcing. Above the frontal zone is an elevated maximum of vertical motion of $-12 \mu\text{bars}^{-1}$ which is in response to frontal lifting and development of the cyclonic circulation.

Trajectory plots constructed from a 14 km full physics MASS model run are shown in Fig. 4.7. The availability of 14 km model data provides a high resolution terrain data set to be used in assessing the impact on the low-level cold surge. Four parcel trajectories were generated upwind of the high terrain within the low-level cold layer. The parcels were initiated at 2300 UTC 8 March 1992 and ran out 7 hours. All four parcels indicate a deflection in their respective paths as the parcel approaches the barrier. As the large scale flow advects the parcels towards the mountain barrier significant cooling is observed as the sloping terrain results in an adiabatic lifting of the air parcels. Additionally, the air parcels experience a deceleration as they approach the barrier resulting in mass convergence and ascent. The combination of forced ascent by the surface topography and the convergence of mass result in an additional cooling of $3\text{-}5^{\circ}\text{C}$. Parcel #2 experiences the steepest terrain profile of the group. As the parcel approaches the barrier its kinetic

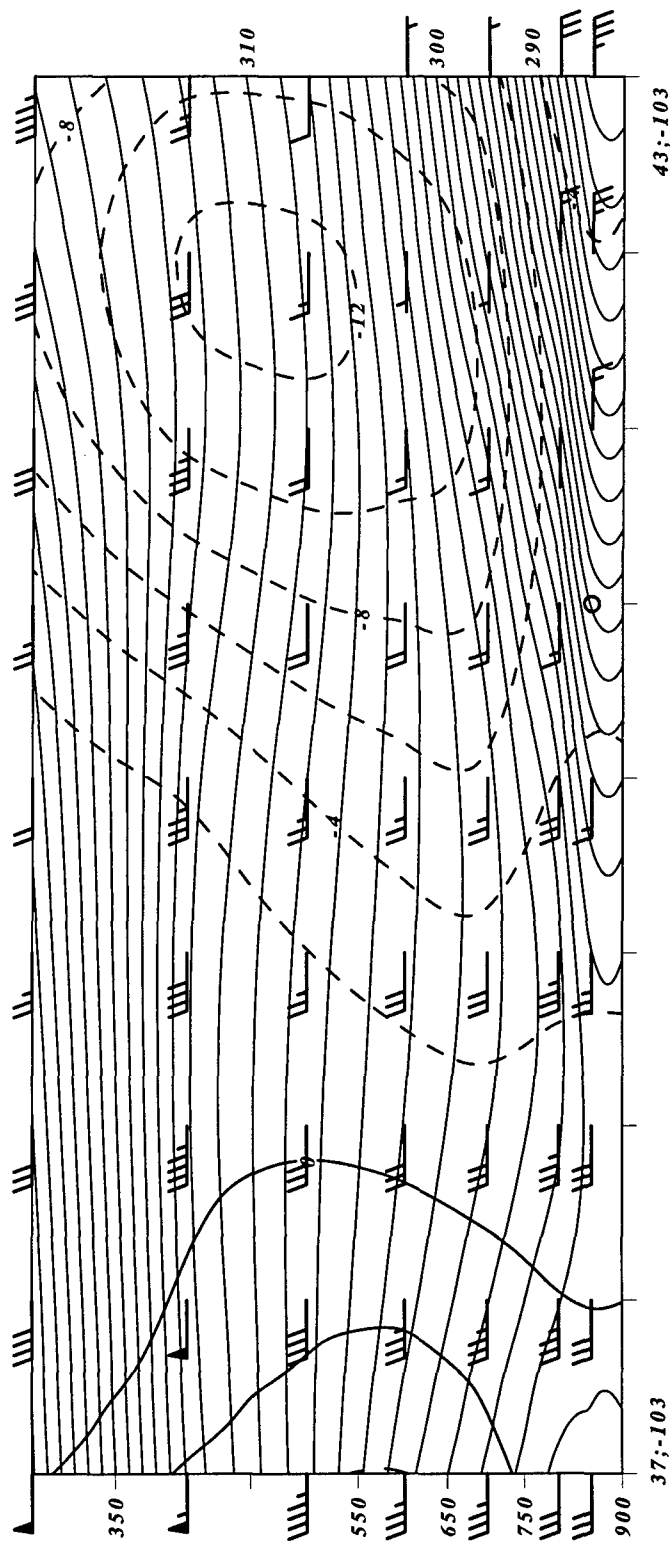


Figure 4.6. 0300 UTC 9 March 1992 objectively analyzed cross section derived from observed STORM-FEST data sets. Orientation of the cross section is found in Fig. 4.3b. The wind barbs represent the wind component orientated in the direction of the cross section (flag - 25 ms^{-1} , full staff - 5 ms^{-1} , half staff - 2.5 ms^{-1}). Solid lines are theta surfaces in 1°K increments. Kinematic omega field is displayed as dashed (ascent) and thin solid lines (descent) at an increment of $2 \mu\text{bars}^{-1}$.

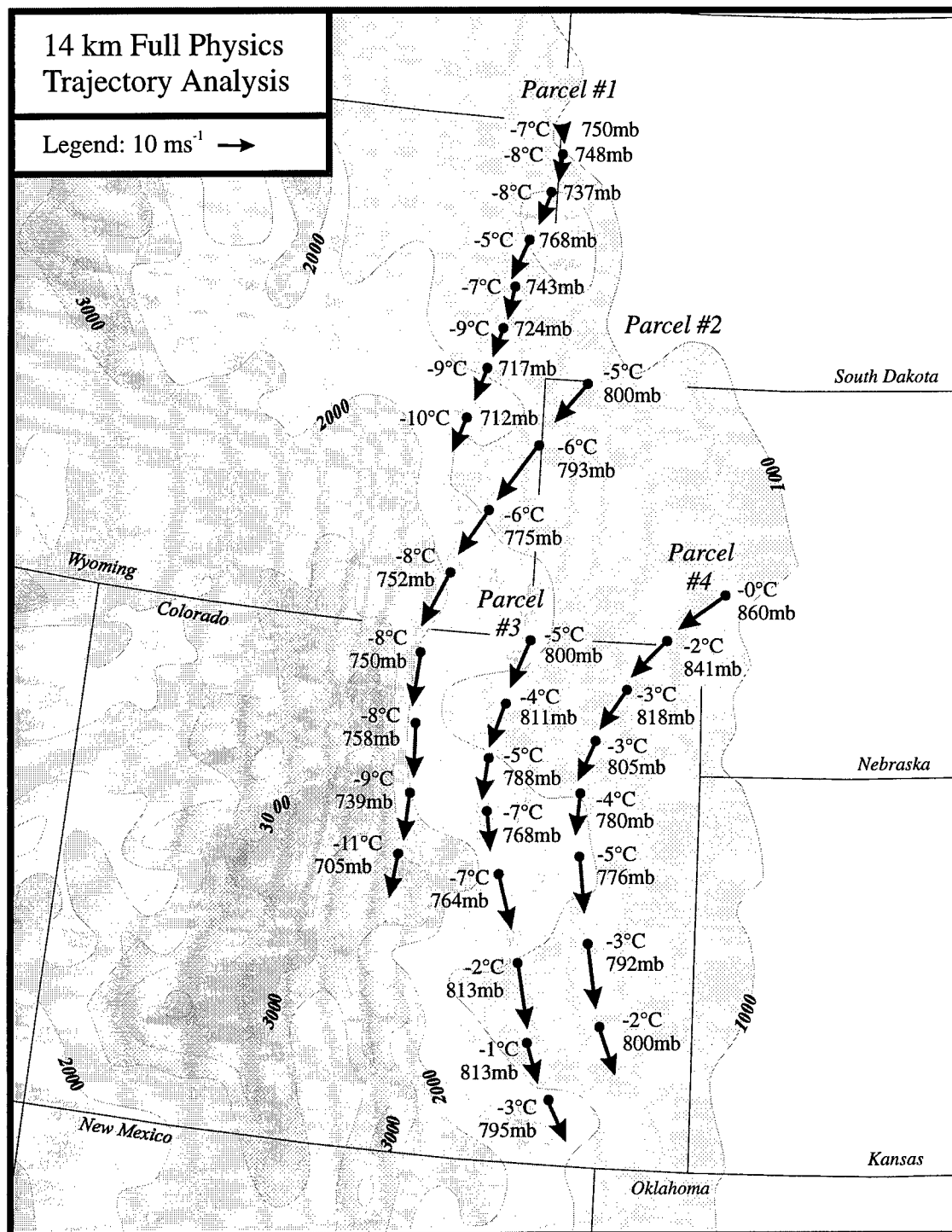


Figure 4.7. Forward trajectories based on 14 km resolution MASS full physics model simulation initialized at 1200 UTC 8 March 1992. Each of the four parcel positions are plotted every hour beginning at 2300 UTC 8 March 1992 and ending at 0600 UTC 9 March 1992. Each position displays the total wind vector (arrow), pressure level (mb), and the temperature (°C). Model resolution topography is contoured and shaded at a 500 m interval.

energy is insufficient to overcome the obstacle and is forced to flow alongside the barrier. As the parcel approaches higher terrain at the end of the trajectory we note the anticyclonic signature in the flow as negative vorticity is generated in order to conserve potential vorticity. The characteristics of parcel #4 are detailed in Table 5.0. The trajectory indicates a steady ascent of $\sim 4\text{-}6 \mu\text{bars}^{-1}$ through 09/03 UTC. The generation of cold air results in an increase in the vertical temperature gradient which acts to maintain the integrity of the cold surge. After 09/03 UTC the parcel experiences an acceleration as it descends down the slope of the Palmer Divide. This descent results in a brief increase in the kinetic energy of the parcel, though significantly insufficient to overcome the barrier. The ratio of kinetic to potential energy is $\ll 1.0$ throughout the path indicative of the inability of the air to overcome the barrier.

Table 5.0

Trajectory from 2300 UTC 8 March 1992 - 0600 UTC 9 March 1992. Trajectory data is derived from 14 km full physics MASS model run. The following abbreviations are defined: latitude (LAT), longitude (LON), pressure (PRES), above ground level (AGL), temperature (TMP), Brunt-Väisälä frequency (BVFQ), total kinetic energy (KE), and total potential energy (PE).

Time (UTC)	LAT (°N)	LON (°W)	PRES (mb)	AGL (m)	TMP (°C)	OMEGA ($\mu\text{bar/s}$)	D θ /DZ (°K/km)	BVFQ (s^{-1})	KE (J)	PE (J)
8/23	41.4	101.8	859.7	221	-0.44	+0.796	9.47	0.018	195.3	44359.7
9/00	41.1	102.4	840.6	326	-1.54	-6.626	5.75	0.014	138.1	50499.9
9/01	40.7	102.9	817.6	434	-3.00	-4.889	7.32	0.015	127.2	58058.0
9/02	40.2	103.2	805.4	442	-2.60	-6.540	8.93	0.017	102.6	61853.5
9/03	39.8	103.4	780.0	572	-4.29	-5.092	12.51	0.020	78.5	70219.2
9/04	39.4	103.3	775.6	541	-4.96	+2.380	15.16	0.022	160.5	71976.8
9/05	38.7	103.2	791.7	530	-3.15	+1.425	16.71	0.023	213.6	66152.0
9/06	38.1	103.0	800.0	657	-1.70	-13.251	9.69	0.018	127.7	63607.7

As the surge propagates down the Front Range a significant restructuring of the atmosphere is observed. The DEN sounding clearly reflects the dramatic cooling taking place in the low levels (Fig 4.5). As the depth of cooling increases down the Front Range a narrow ridge in the height field is observed to build east of the barrier (Fig 4.3). Hourly profiler data from Granada, Colorado provides additional insight into the evolving structure in the lee of the mountains (Fig. 4.8). Shortly after 09/00 UTC a strong 25 ms^{-1} lower tropospheric jet is observed as a predominantly southerly flow is observed throughout the atmospheric column. By 09/03 UTC a strong signal of the developing cyclonic circulation to the north of the station is detected as the flow veers westerly. The development of the cyclonic circulation rapidly extends from the surface at 09/03 UTC to nearly the 400 mb level by 09/06 UTC. The development of the circulation causes the mid-level momentum field to diminish over the site as the midtropospheric cold air and associated low pressure system shifts the jet structure out into the Texas panhandle. By 09/09 UTC the introduction of the cold surge is evident as the low-level flow becomes more northerly and increases to over 20 ms^{-1} .

4.5 Development of CFA and Bifurcated Jetstream

The surging lower tropospheric cold air to the north and the convectively-induced heating to the southeast act to strengthen a steepening northwesterly oriented pressure gradient force over the central Plains. The rapid restructuring of the atmosphere results in

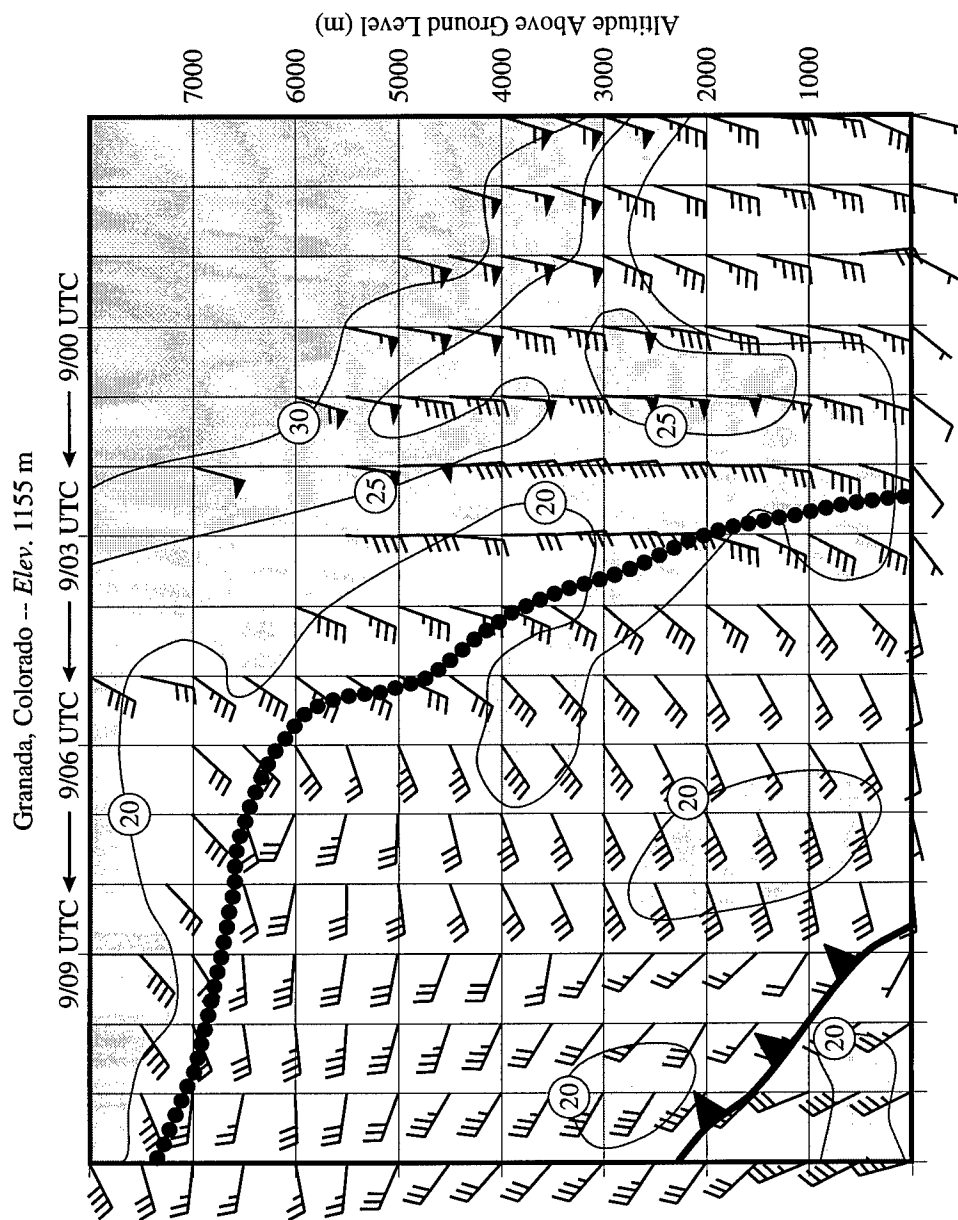


Figure 4.8. Observed hourly consensus averaged winds from the Granada, Colorado NOAA 403-MHz Profiler. Data displayed from 2100 UTC 8 March 1992 to 1200 UTC 9 March 1992. Wind bars: flag - 25 ms^{-1} , full staff - 5 ms^{-1} , half staff - 2.5 ms^{-1} . Isotherms are shaded at a 5 ms^{-1} interval above 20 ms^{-1} . Vertical axis is altitude above ground level in meters and time along the horizontal axis. Dotted line depicts cyclonic shear and cold surge depicted by solid line with pips.

an acceleration of the jet exit region which aids in CFA development and bifurcation of the jet stream over the region.

4.5.1 Cold Front Aloft Structure

By 09/00 UTC the formation of the CFA is evident in the vicinity of the Texas/Oklahoma panhandle (Fig. 3.10b). The sounding profile between 08/21 UTC and 09/00 UTC at the Guymon, Oklahoma CLASS site provides early indications of the developing CFA (Fig. 4.9). The thermodynamic structure over this area indicates modest cooling focused between 400-600 mb with a three hour temperature drop of $\sim 5^{\circ}\text{C}$ observed near the 550 mb level. Associated with this elevated cold pool is an increase in the moisture field as the destabilization and associated vertical motion of the CFA generate isolated convective showers in the region. Consistent with the developing CFA, a strong increase in the vertical wind shear is observed as the baroclinicity is increased over the site. During the 3-hour period, the lower troposphere experiences little change as a near-adiabatic layer extends from the surface to 600 mb. This increase in the depth of the adiabatic layer enhances the potential instability for future convection.

The 09/03 UTC horizontal depiction of the developing 500 mb cold pool indicates a strengthening baroclinic zone over west-central Oklahoma (Fig. 4.1b). Computation of the 09/03 UTC 500 mb adiabatic frontogenetic forcing (the horizontal confluence/shear and tilting contribution) is depicted in Fig. 4.10 (Eq. 17). Calculations indicate a well-defined zone of frontogenesis in excess of $1\text{K } 100\text{km}^{-1} \text{ } 3 \text{ hrs}^{-1}$ over central Texas

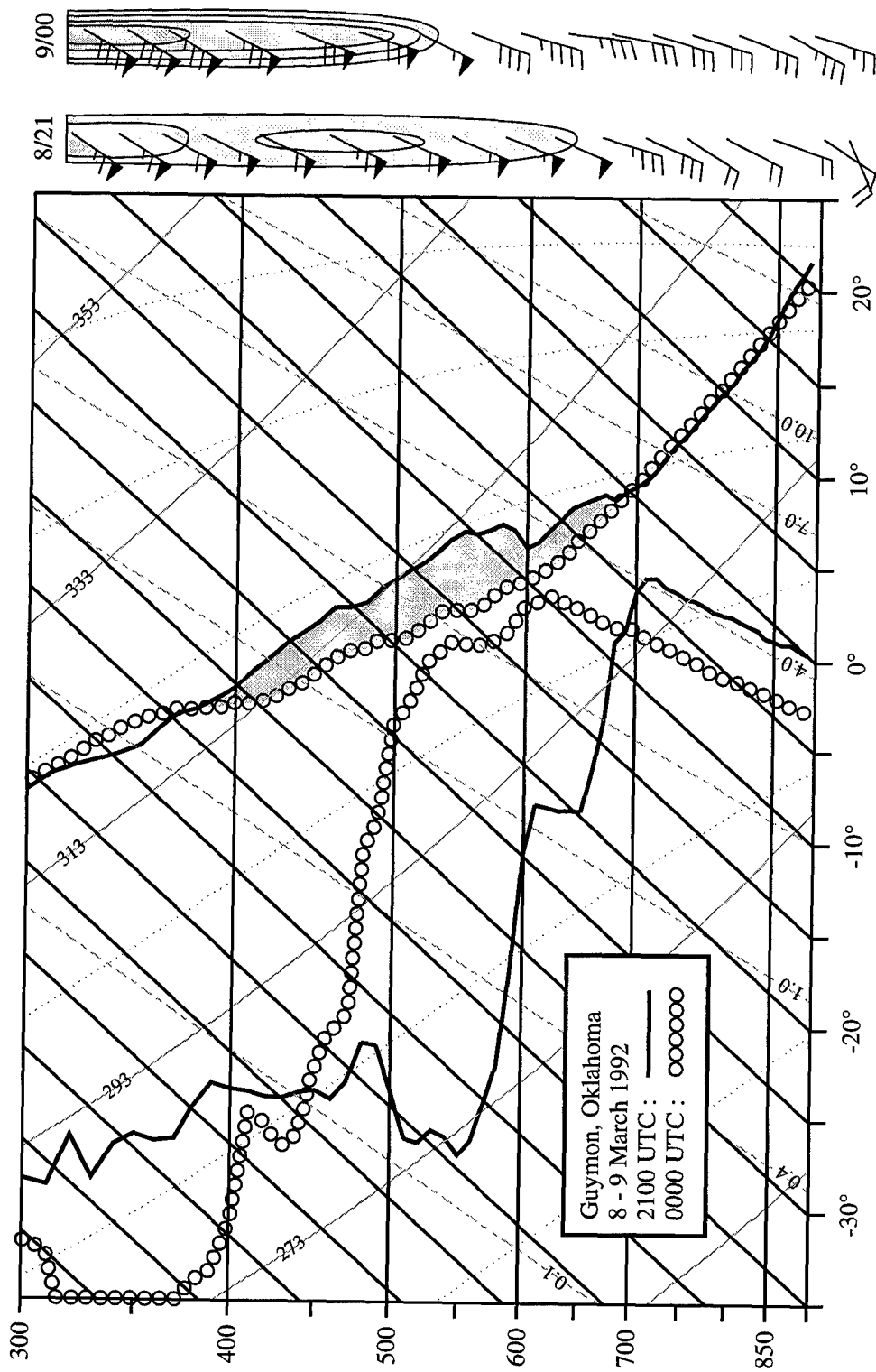


Figure 4.9. Guymon, Oklahoma sounding profile for 2100 UTC 8 March 1992 (solid line) and 0000 UTC 9 March 1992 (open dotted line). Isotherms - dark solid lines running from lower left to upper right, dry adiabats - light solid lines running from lower right to upper left, moist adiabats - light dotted lines running from lower right to upper left, mixing ratio - dashed lines running from lower left to upper right. Winds depicted to right (flag is 25 ms^{-1} , full staff - 5 ms^{-1} , half staff - 2.5 ms^{-1}).

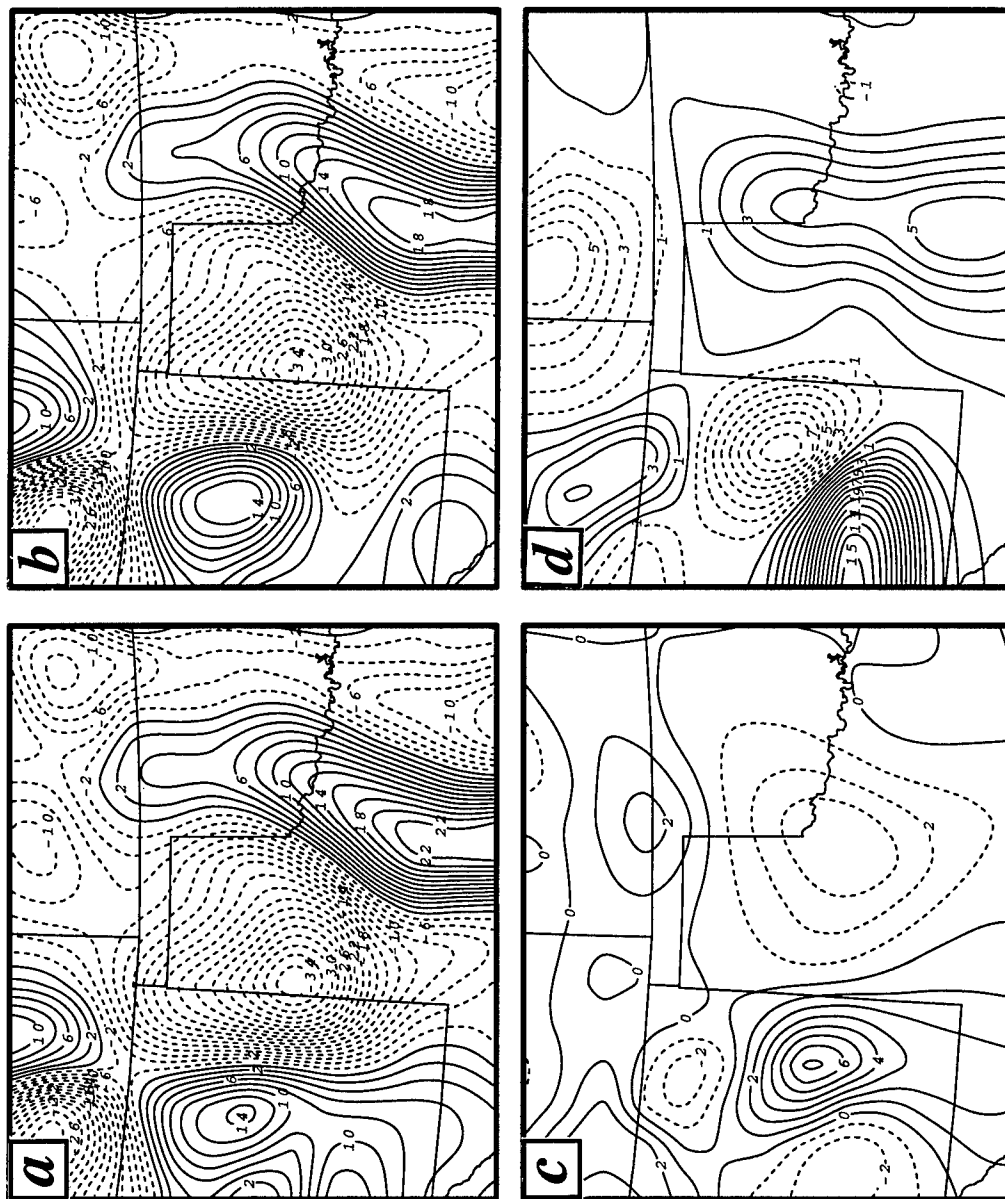


Figure 4.10. 0300 UTC 9 March 1992 observed 500 mb frontogenesis calculations based on Miller Frontogenetic function. (a) Total frontogenesis, (b) tilting term, (c) horizontal shear term, and (d) confluence term. Solid lines depict frontogenesis, dashed lines frontolysis ($\times 10^{-1} \sigma_K 100 \text{ km}^{-1} 3 \text{ hrs}^{-1}$).

northward into Oklahoma. The developing jet streak depicted in Fig. 4.1b is associated with a region of ascent along the forward right flank of the exit region. The development of a thermally-direct circulation within the exit region acts to alter the vertical motion pattern typically found within this region. In response, the vertical motion gradient acting on the thermal field results in a strong contribution by the tilting term in the frontogenetic process. The forcing provided by the shear and confluence terms provide a weaker signal in the generation of the CFA. Along the axis of frontogenesis the confluence term only contributes $0.4\text{K } 100 \text{ km}^{-1} \text{ 3 hrs}^{-1}$ while the shear term provides a negative contribution of $-0.2\text{K } 100 \text{ km}^{-1} \text{ 3 hrs}^{-1}$. An additional zone of frontogenesis is found over east-central New Mexico in relation to the cold air associated with the original baroclinic wave over the southern Rockies. A third frontogenetic zone is positioned over northern Nebraska in relation to the strong confluence associated with the accelerating jet streak from the south and the northwesterly flow of the northern branch of the jetstream over the upper midwest.

A cross section of θ_e is constructed for 09/03 UTC along the Texas/Oklahoma border parallel to the observed thermal gradient (Fig. 4.11). Inspection of the θ_e field is useful in locating the CFA since moisture provides a good tracer in delineating the transition zone between the advancing cool-dry air aloft and the warm-moist air ahead. The cross section indicates a well-defined pool of low θ_e air overriding a low-level dome of warm-moist air associated with high θ_e values. The surface dryline is located $\sim 100 \text{ km}$ to the west of the CFA. The CFA is located on the leading edge of the downward sloping isentropes indicative of the strengthening contrast between the two air masses. Trajectory

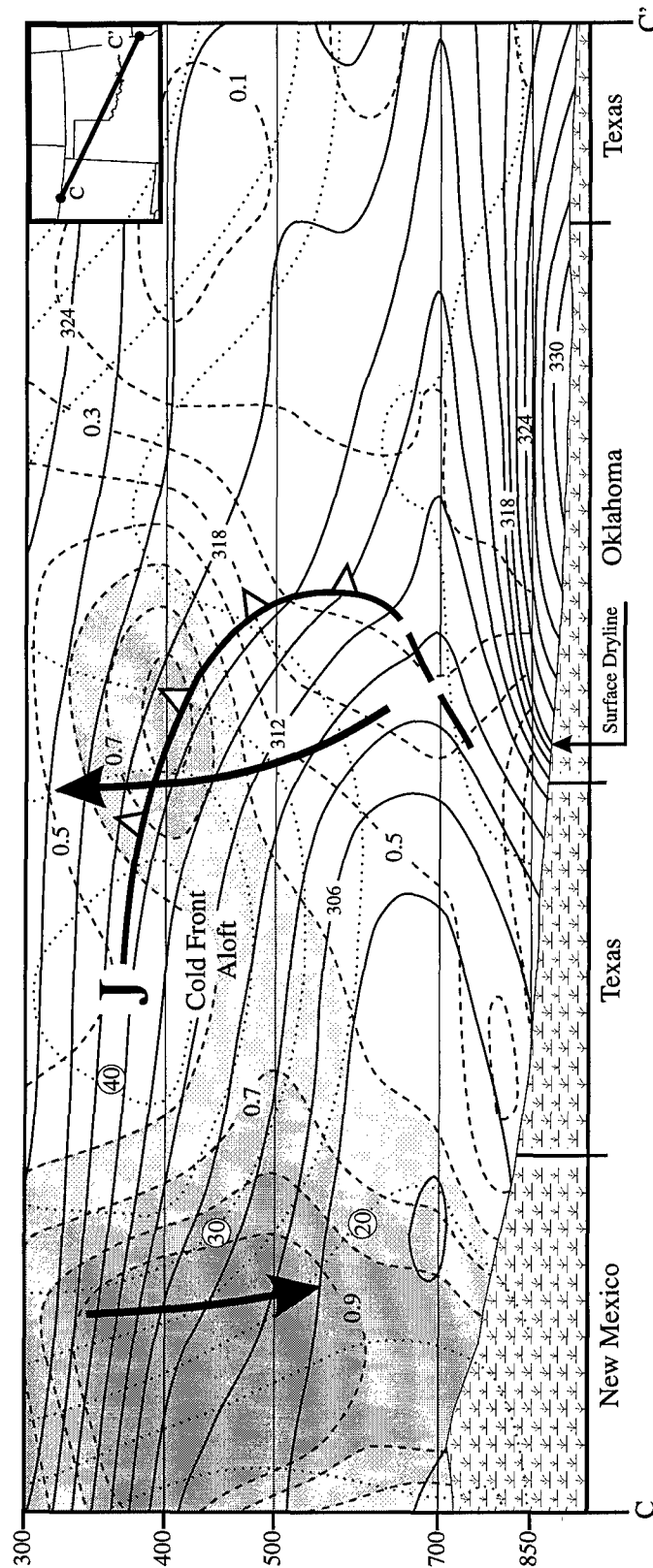


Figure 4.11. 0300 UTC 9 March 1992 vertical cross section through the nose of an accelerating jet exit region. Thin dashed lines depict inertial Rossby number (shaded area >0.6), derived isotachs (dotted lines $- \text{ms}^{-1}$). Thin solid lines depict equivalent potential temperature ($^{\circ}\text{K}$). Cold front aloft (CFA) depicted by heavy solid line with open triangles. Heavy arrows reflect vertical motion distribution. Jet streak core denoted by "J". Dashed portion of front depicts where front becomes diffuse. Insert depicts orientation of cross section.

analysis over this region indicates that the source of dry air to the west originated near the elevated terrain of northern Mexico (Fig. 3.11). This dry air mass provides a marked contrast to the warm-moist air over the eastern Plains. Low-level warm air advection is strengthened during the course of the day as the developing leeside low and associated dryline prime the eastern Plains with warm-moist air. The development of the lower tropospheric circulation described in the previous section results in an increased isallobaric component of the flow which is directed towards the west-northwest over the eastern Plains. By 08/21 UTC, an 850 mb isallobaric jet of 10 ms^{-1} develops over eastern Oklahoma. In response, warm-moist air is rapidly transported out of the Gulf region northward through the eastern Plains.

4.5.2 Cold Front Aloft Destabilization and Convective Initiation

As the CFA propagates across this region a marked decrease in the static stability is observed. A measure of the potential energy generated can be quantified by calculating the **Convective Available Potential Energy (CAPE)** from available sounding profiles (Houze 1993). The computation of CAPE is given by

$$\text{CAPE} \equiv g \int_{\text{LFC}}^{z_T} \frac{\theta(z) - \theta^*(z)}{\theta^*(z)} dz \quad (20)$$

where θ is the potential temperature of a parcel, θ^* is the potential temperature of the environment, g is gravity, z_T is the cloud top level, and LFC is the level of free convection.

During the period of CFA development, a rapid increase in the generation of CAPE is observed over Oklahoma. Early in the period, sounding profiles at Norman, Oklahoma (OUN) reflected no areas of positive buoyant energy. During the course of the day, CAPE values increase as the warm boundary layer moistens while warm dry air invades the mid-troposphere from the elevated terrain of northern Mexico. By 08/21 UTC, the generation of CAPE in the vicinity of OUN rapidly increased to a modest $1100 \text{ m}^2\text{s}^{-2}$.

Close inspection of radar (Fig. 3.10) and satellite imagery (Fig. 3.3d) at 09/00 UTC indicates two distinct areas of convective development in the vicinity of the Texas/Oklahoma panhandle. An area of weak convection is centered over the Oklahoma panhandle (Fig. 4.12a). This area is characterized by shallow convection, which extends vertically to 5-6 km, in response to the destabilization associated with the developing cold pool aloft. Despite the lack of appreciable moisture, the vertical motion in this area is vigorous enough to squeeze out an area of cumilform clouds and isolated showers. Along the dryline, an organized band of convection begins to take form from Abilene, Texas northward through Elk City, Oklahoma, into Dodge City, Kansas (DDC). The 09/00 UTC low-level flow clearly shows the strong convergence along the dryline. A second band of convection has organized along the leading edge of the CFA which has advanced out ahead of the dryline position. This band of convection extends from DDC southward to Vici, Oklahoma.

The advancing CFA over the dryline provides the necessary mechanism to ignite convection. The cross section in Fig. 4.11 depicts an elevated intrusion of low θ_e air ahead of the upper-level cold front of the inner-mountain region. Along the leading edge of this

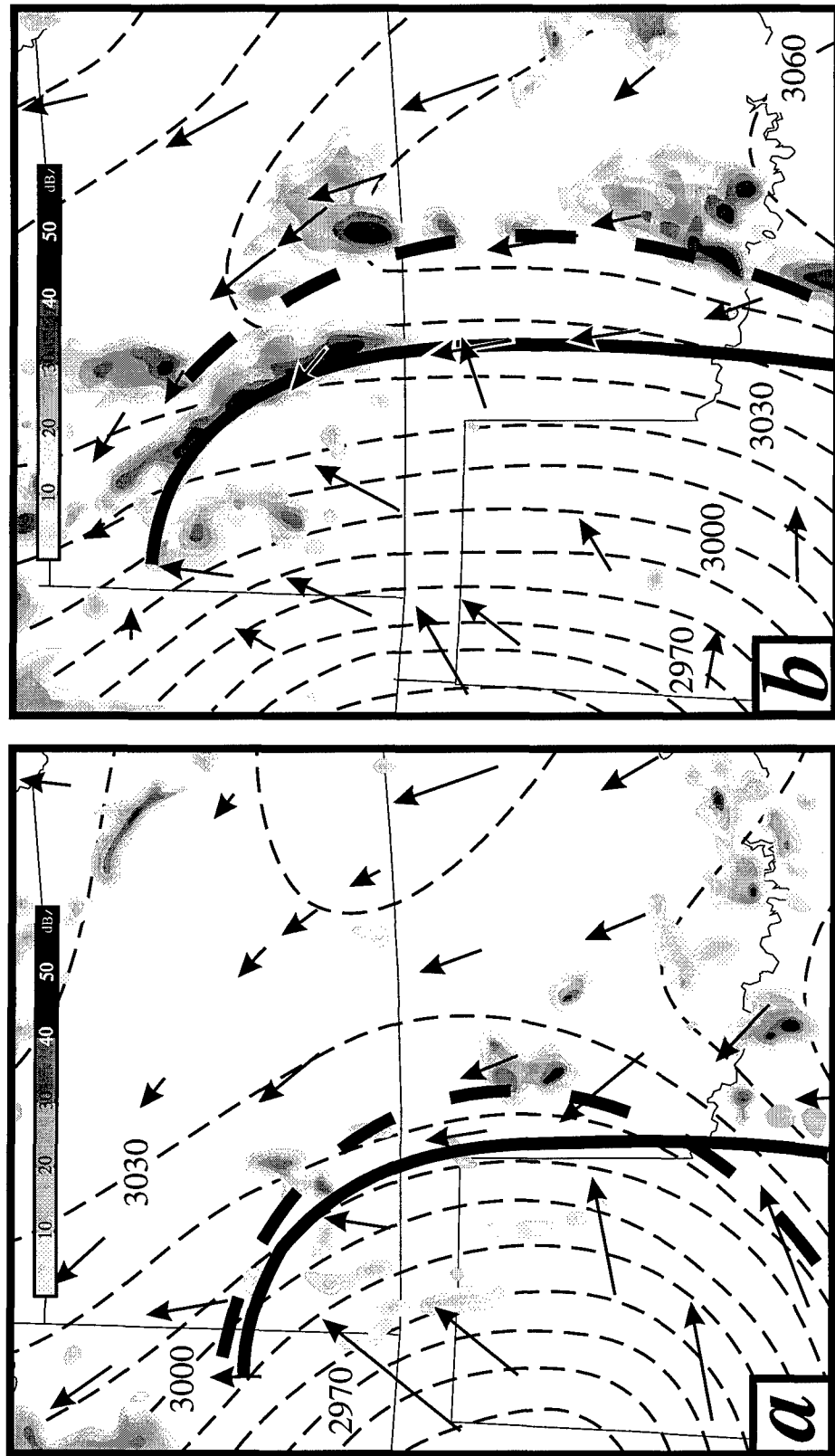


Figure 4.12. Depiction of the relationship between dryline (thick solid line), CFA (heavy dashed line), and developing convection (radar reflectivity at 10 dBz interval -- shaded). Arrows depict surface wind vectors from Portable Automated Mesonet (PAM) network (arrow length \longrightarrow is 10 m s^{-1}). Retrieved 600-400 mb thickness are thin dashed line - (m). (a) 0000 UTC 9 March 1992 and (b) 0300 UTC 9 March 1992.

air mass is the formation of the CFA. As the CFA moves across the dryline, the strong cross-stream advection of cold-dry air aloft overrides an enhanced zone of moisture-flux convergence resulting in a rapid destabilization of the environment. Inspection of the 600-400 mb thickness pattern reveals the midtropospheric cooling taking place (Fig 4.12a). To assess the destabilization associated with the advancing CFA, a sounding profile was constructed for the region just ahead of the dryline (not shown). The surface to 650mb sounding profile from OUN and the profile above 650 mbs at AMA were merged to provide a measure of the instability generated by the advancing CFA. Due to the lack of moisture over AMA, the 09/00 UTC Lifted Index is reduced to only a value of $+1.5^{\circ}\text{C}$. To the east, the potential for deep convection is evident as the Lifted Index decreases to -4.7°C . The combined profile reflects the strong destabilization associated with the CFA as the Lifted Index is reduced to -6.3°C and the generation of CAPE increases to $1364 \text{ m}^2\text{s}^{-2}$.

Within three hours widespread severe thunderstorms overspread the region. Several thunderstorms producing F-0 tornadoes and golfball to softball size hail were reported after the CFA crossed the low-level dryline. By 09/03 UTC, two distinct bands of thunderstorms have developed (Fig. 4.12b). Along the dryline, an intense line of convection extends from Oakley, Kansas southeastward towards Enid, Oklahoma. A second line is observed 60 km out ahead of the previous line in Oklahoma. The dryline has advanced eastward at 4.2 ms^{-1} while the CFA has raced across the region at 13.8 ms^{-1} . The strong surge of cold air directed across the stream in the exit region of the jet acts to advance the cold air downstream allowing the line of thunderstorms to break out from the

parent line. It is at the apex of the cold surge aloft that the convection advances ahead of the dryline activity and forms an organized convective line through central Oklahoma.

4.5.3 Observed CFA Generation and Geostrophic Adjustments

A significant restructuring of the deeper atmospheric circulation is observed as the cold surge propagates down the Front Range. The DEN sounder shows the dramatic cooling taking place in the low levels as cold air reduces the atmospheric column below 470 mb (Fig. 4.5). Between 09/00-06 UTC, the 700 mb height tendency pattern indicates a broad negative anomaly in excess of 30 m over the central Plains associated with the cold surge (Fig. 4.3a). The strongest falls are found to the northeast of the developing low-level circulation and extend eastward along the baroclinic zone. A large portion of the height falls are associated with the isentropic lift ahead of the developing trough. Between 00-0600 UTC a significant distortion in the height fall pattern is observed as the cold surge penetrates southern Colorado (Fig. 4.3b). The narrow wedge of cold air passing down the Front Range induces a 700 mb 6-hours height fall pattern of 40 m parallel to the mountains. To the southeast of this anomaly is a small pocket of height rises observed over central Oklahoma. The result is an increase in the isallobaric forcing acting upon the flow over this region which influences the characteristics of the secondary circulation of the jet exit region.

The quasi-geostrophic representation of the ageostrophic wind can be written

$$\mathbf{v}_a = f^{-1} \mathbf{k} \times [\partial \mathbf{V}_g / \partial t + (\mathbf{V}_g \cdot \nabla) \mathbf{V}_g] \quad (21)$$

The first term in the bracket represents the isallobaric component of the wind while the second term accounts for inertial advective forcing. The introduction of a diabatic heat source along the flow can significantly alter the jet structure as accelerating air parcels make quasi and semi-geostrophic approximations inappropriate (Kaplan and Karyampudi 1992a & b, Kaplan *et al.* 1996). The hydrostatic response is for the atmospheric depth on a surface of constant pressure to decrease toward cold air and increase towards the warm air. This results in an increased geopotential gradient which can disrupt the balance between the pressure gradient and the Coriolis force. If a perturbation introduced along the flow is sufficiently small, i.e. less than the Rossby radius of deformation, the divergent wind field rather than the rotational part dominates in adjusting to the perturbation. This imbalance leads to an adjustment of the atmosphere whereby the isallobaric acceleration acts towards the colder air. This results in the development of a subgeostrophic flow as the flow transforms from a thermally-indirect to a thermally-direct circulation in the exit region. In turn, ascent and cooling is enhanced on the forward right flank in order to regain a balance between the fields. This cooling prompts development of the CFA downstream and to the right of the flow.

The mesoscale distribution of the height tendency field over western Kansas results in an increase in the isallobaric forcing exerted upon air parcels passing through the

jet exit region (Fig 4.13). The 500 mb height fall pattern centered at 09/03 UTC provides a strong signal of the impact of the combined effects of the surging cold air down the Front Range and the development of convection on the dryline over central Texas as observed in the radar depiction in Fig. 4.1a. The perturbation in the mass field has a length scale of ~425 km which lies within the Rossby radius of deformation making the region susceptible to strong irrotational ageostrophic adjustments. As air parcels enter this mesoscale region of strong isallobaric forcing, the perturbation is small enough that there is insufficient time for the rotational part of the wind to respond. However, in response to the perturbation, rapid adjustments are provided by the divergent part of the ageostrophic wind. The strong gradient in the height tendency field lies directly within the nose of the jet exit region extending out of western Texas. As the jet streak enters this region it is exposed to a strong isallobaric acceleration directed towards the northwest at 15 ms^{-1} . The increased forcing acts to produce a subgeostrophic response as the divergent part of the ageostrophic wind responds to the perturbation. In turn, the parcels accelerate as the flow attempts to regain a geostrophic balance. This acceleration is found in a region, according to semi-geostrophic theory, typically characterized by a rightward, thermally-indirect circulation in which the flow decelerates.

The lower tropospheric impact on the transverse circulation within the jet exit region is evident through a series of cross sections through the nose of the jet streak between 09/00-09/06 UTC. The horizontal analyses of the jet streak indicates the core of the jet stream remains over the Texas panhandle through the period (Fig. 3.10b, 4.1b and 4.2b). The cross sections were constructed from southeast Colorado to southwest

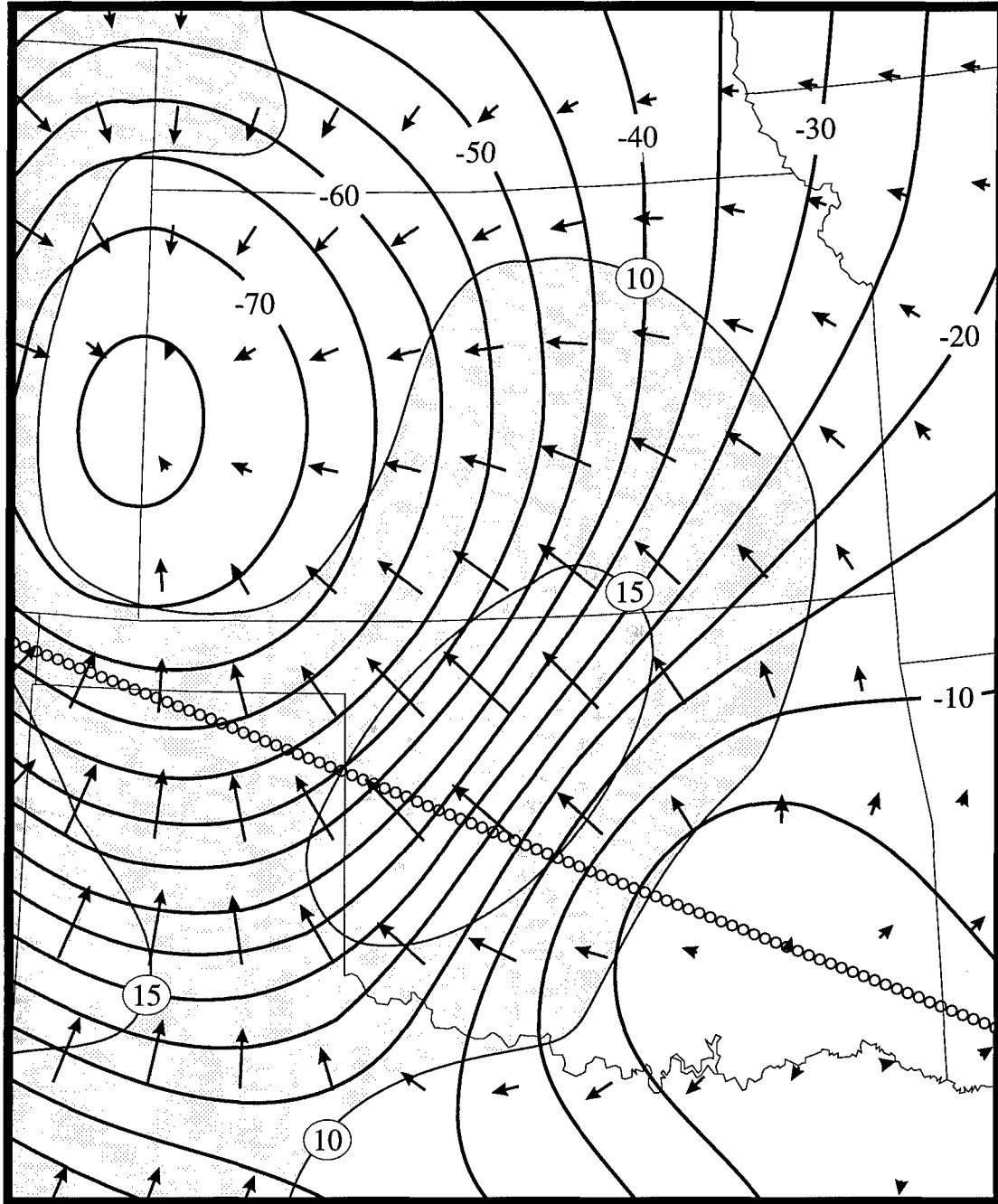


Figure 4.13. 0000-0600 UTC 9 March 1992 500 mb height fall (m) pattern (solid line) and isallobaric wind vector. Isallobaric wind isotach is shaded in 5 ms^{-1} increments. Line of circles depict location of cross section displayed in next figure.

Arkansas aligned within the jet exit region nearly orthogonal to the developing flow and baroclinic zone. The 09/00 UTC cross section indicates a modest jet streak in excess of 35 ms^{-1} above 450 mb (Fig. 4.14a). Consistent with jet streak dynamics, the circulation within the jet exit region is thermally indirect. A significant rightward-directed flow in excess of 18 ms^{-1} is found near 400 mb with a compensating leftward-directed flow below. However, just to the right of the jet core between the 600-700 mb level, a signal of a developing thermally-direct circulation is captured. This secondary circulation within the jet exit region provides a means of enhanced cooling and acceleration of the momentum field. By 09/03 UTC, the low-level cold surge had begun driving southward along the Front Range. As the cold surge propagates down the Front Range the vertical extent of the mass perturbation increases as evident by the growth of the cyclonic circulation in the Granada, Colorado profiler data (Fig. 4.8). As the vertical extent of low-level cold surge builds, the mass perturbation builds through the atmosphere. In response to the mass perturbation brought on by the surging cold air a strong thermally-direct circulation develops in the lower troposphere (Fig. 4.14b). The elevated leftward-directed flow between the 500-600 mb level coincides with the concentration of a momentum descending along the developing baroclinic zone of the CFA. The development of the thermally-direct circulation coincides with an acceleration of the air parcels passing through the region. This acceleration is evident in the computation of the inertial Rossby number (Eq. 15). Regions in which the nonlinear-advective accelerations dominate over the Coriolis accelerations, i.e. >0.5 , are areas in which the quasi- and semi-geostrophic approximations brake down and are an indication of the imbalance between the mass and

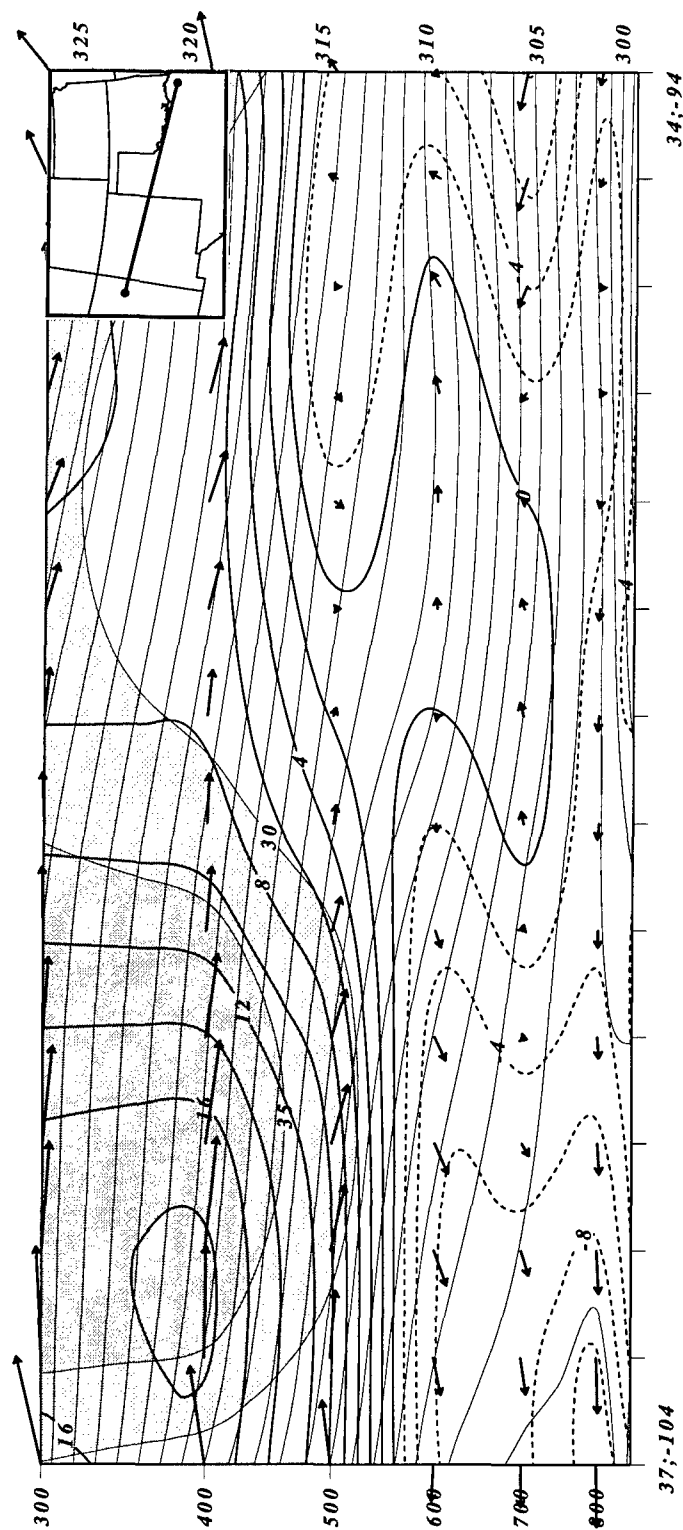


Figure 4.14a. Vertical cross section valid at 0000 UTC 9 March 1992 extending from 37°N, 104°W to 34°N 94°W. The thin solid lines depict theta surfaces at a 1°K increment. The isotachs for the total wind speed are shaded above 30 ms⁻¹ at an increment of 5 ms⁻¹. The component of the wind directed left (dashed) or right (solid) of the geostrophic flow is displayed in 2 ms⁻¹ intervals. The circulation, derived from the ageostrophic wind and omega field, is depicted by the vectors. Cross section location depicted in Fig. 4.13.

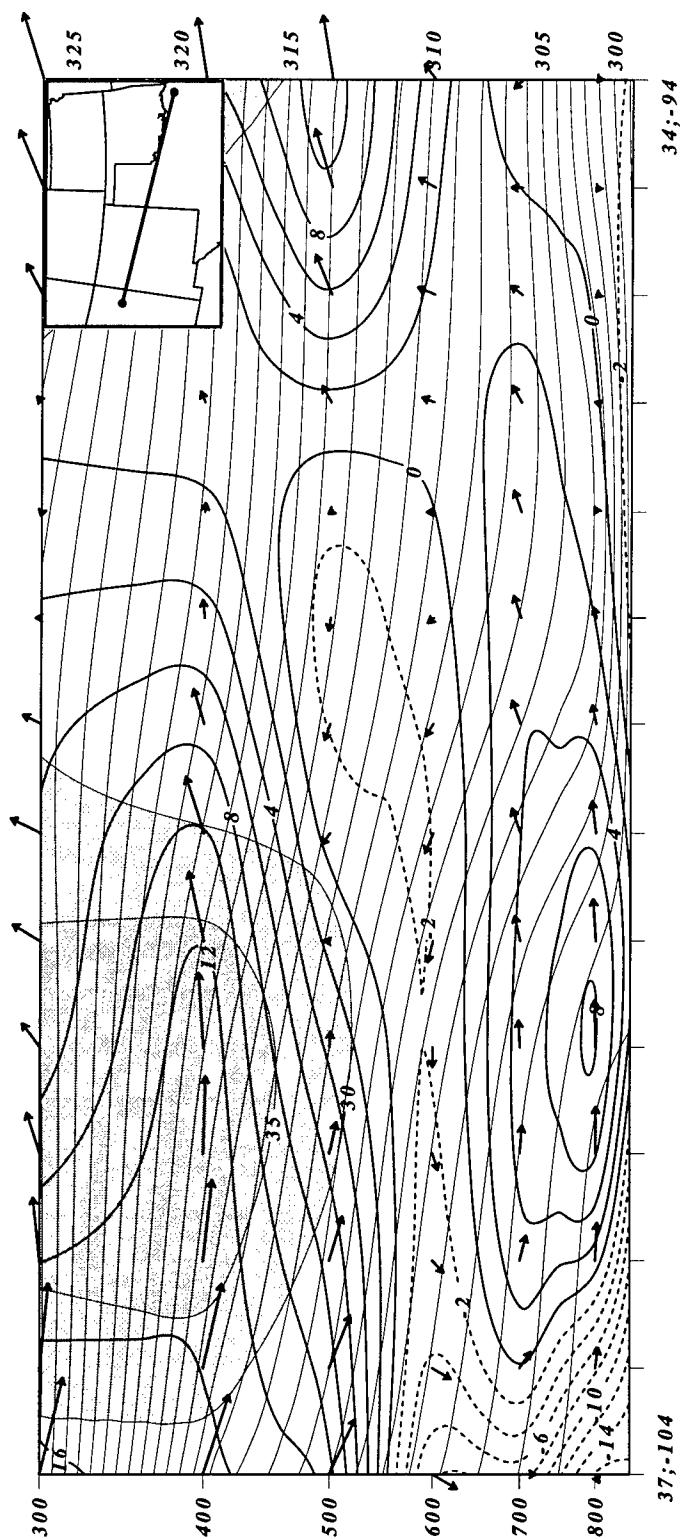


Figure 4.14b. Vertical cross section valid at 0300 UTC 9 March 1992 extending from 37°N, 104°W to 34°N 94°W. The thin solid lines depict theta surfaces at a 1°K increment. The isotachs for the total wind speed are shaded above 30 ms⁻¹ at an increment of 5 ms⁻¹. The component of the wind directed left (dashed) or right (solid) of the geostrophic flow is displayed in 2 ms⁻¹ intervals. The circulation, derived from the ageostrophic wind and omega field, is depicted by the vectors. Cross section location depicted in Fig. 4.13.

momentum field (Koch and Dorian 1988). The cross section in Fig. 4.11 indicates an elevated region of R_o in excess of 0.5 within the developing thermally-direct circulation. As the nose of the jet exit region comes under the influence of the mass perturbation a net mass flux divergence and ascent develops in response to the accelerating air parcels. The axis of maximum ascent, depicted by the heavy arrow, provides an effective means of cooling the atmosphere downstream of the mountains allowing the CFA to strengthen. By 09/06 UTC, a strong thermally-direct circulation is evident extending well into the 400 mb level (Fig. 4.14c). This elevated thermally-direct circulation coincides with the strongest observed surge of cold air down the Front Range. In response to the strong isallobaric forcing, a well-established elevated leftward-directed flow is found through a broad region. As the air parcels are directed towards lower heights, the increased kinetic energy results in the transport of momentum down to the 600 mb level while increasing the baroclinicity.

During the six-hour period between 09/00 and 09/06 UTC the thermally-direct circulation grows from the 600 mb level to 400 mb as the cold surge drives down the Front Range. The 600 mb horizontal analysis of the emerging circulation at 9/00 and 9/03 UTC is depicted in Fig. 4.15. The ageostrophic streamline analysis indicates the development of a leftward-directed flow through the Texas/Oklahoma panhandle region into eastern Colorado. The accelerative nature of this flow coincides with the rapid increase in the momentum field over the Texas panhandle by 09/03 UTC. The temperature gradient has increased significantly within the developing thermally-direct circulation. The formation of a cold pool is observed over the Texas panhandle at 09/00 UTC. Within just three hours, a strong baroclinic zone is established on the Texas/Oklahoma border while a

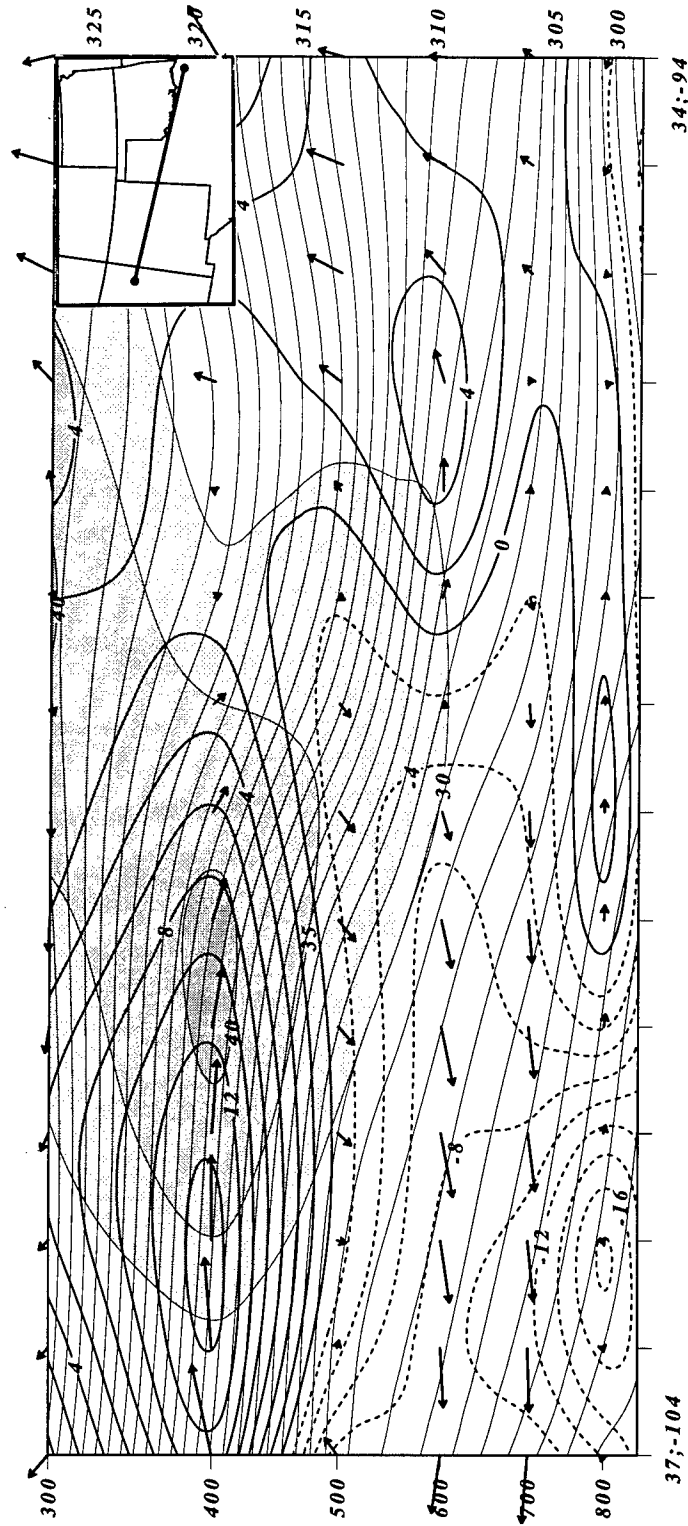


Figure 4.14c. Vertical cross section valid at 0600 UTC 9 March 1992 extending from 37°N, 104°W to 34°N 94°W. The thin solid lines depict theta surfaces at a 1°K increment. The isotachs for the total wind speed are shaded above 30 ms^{-1} at an increment of 5 ms^{-1} . The component of the wind directed left (dashed) or right (solid) of the geostrophic flow is displayed in 2 ms^{-1} intervals. The circulation, derived from the ageostrophic wind and omega field, is depicted by the vectors. Cross section location depicted in Fig. 4.13.

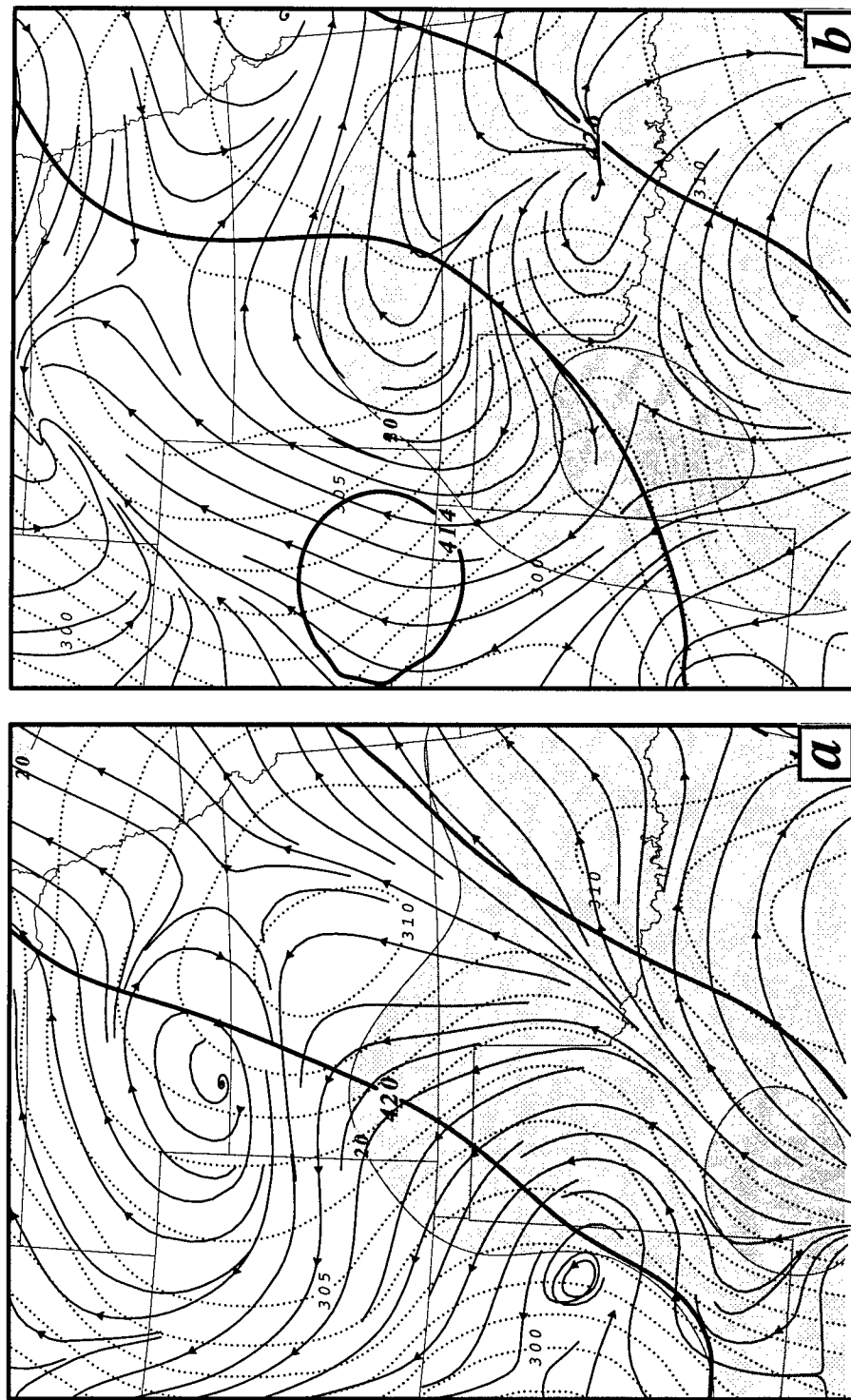


Figure 4.15. 600 mb objective analysis for (a) 0000 UTC and (b) 0300 UTC 9 March 1992. Solid heavy lines depict the height field (dm), isotachs are shaded above 20 ms^{-1} at a 5 ms^{-1} interval, theta depicted as dotted lines at 1°K interval, and the ageostrophic streamline analysis is represented by thin arrows.

temperature decrease of $\sim 3^{\circ}\text{C}$ is observed over the Texas panhandle. By 09/06 UTC the secondary circulation has reached the mid-upper troposphere. The 500 mb pattern for 09/06 and 09/09 UTC indicates the transformation of the secondary circulation from an 'unbalanced' thermally-direct circulation at 0600 UTC to a 'balanced' thermally-indirect circulation by 0900 UTC (Fig. 4.16). By 0600 UTC the low-level cold surge has moved into southern Colorado and begins to pull away from the Front Range as the cold air extends eastward under the influence of the circulation of the propagating low pressure system. This acts to diminish the mass perturbation and a strong thermally-indirect circulation develops in the jet exit region of a newly-formed jet streak over the central Plains indicating a return to a more balanced state.

The increase of the divergent part of the wind field is evaluated by making use of the two-dimensional divergence equation (Eq. 4). Application of the NLB equation over the STORM-FEST domain reveals divergence growth over the central Plains (Fig. 4.17). Strong divergence is captured over the southern Front Range at 9/00 UTC (Fig. 4.17a). The Jacobian term accounts for the strongest contribution in response to the developing trough over eastern New Mexico. By 09/06 UTC a strong increase in divergence is evident between DEN and OUN (Fig. 4.17b). The terrain-induced mass perturbation manifests itself in the form of enhanced divergence in the accelerating jet exit region. *The divergent component of the wind field dominates in the adjustment process since the response of the rotational part of the wind reacts on a time scale that is too large in relation to the size of the mass perturbation.* The increase in the inertial Rossby number depicted in Fig. 4.17a and b indicates a significant increase in the imbalance over the west-

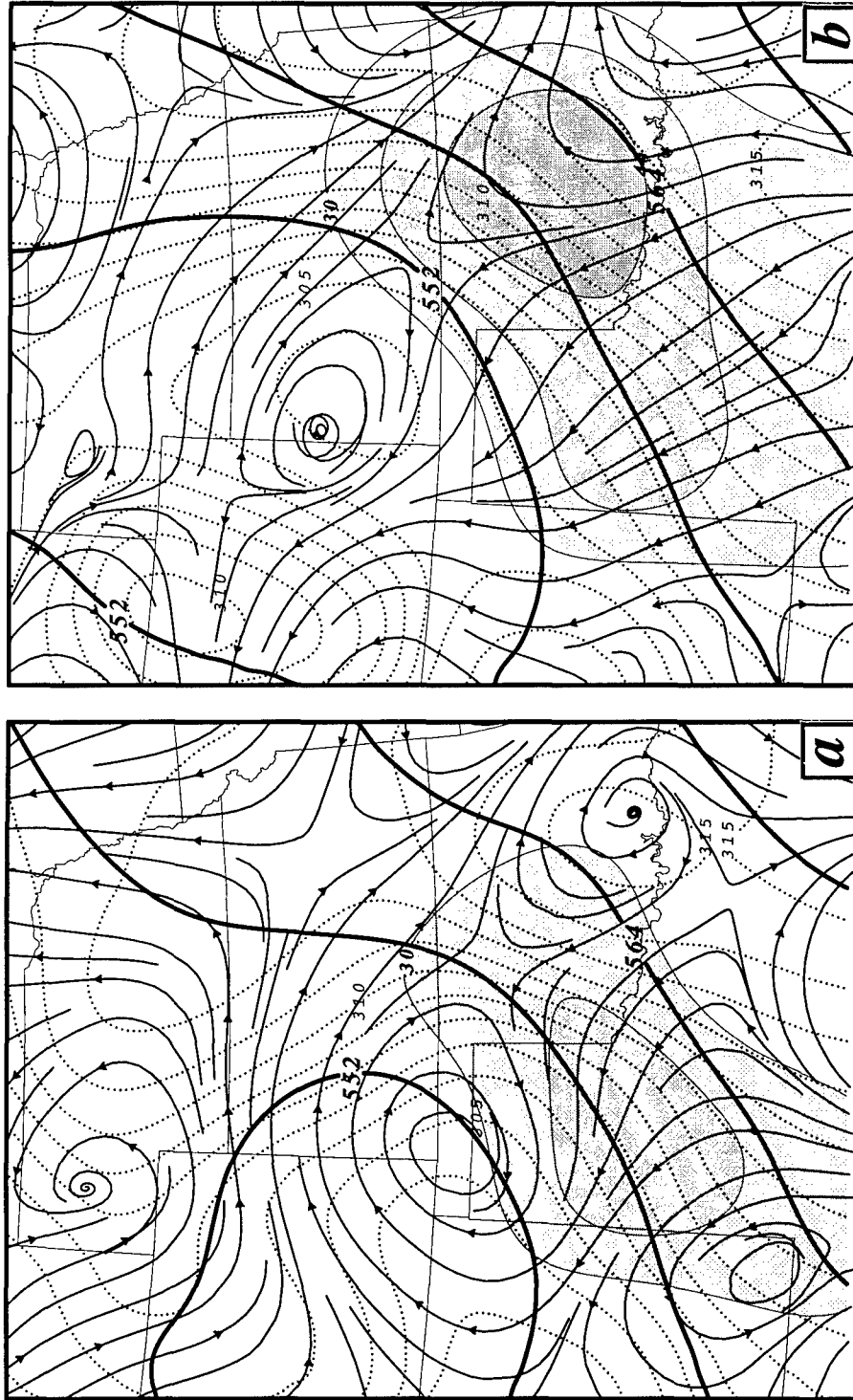


Figure 4.16. 500 mb objective analysis for (a) 0600 UTC and (b) 0900 UTC 9 March 1992. Solid heavy lines depict the height field (dm), isotachs are shaded above 20 ms^{-1} at a 5 ms^{-1} interval, theta depicted as dotted lines at 1°K interval, and the geostrophic streamline analysis is represented by thin arrows.

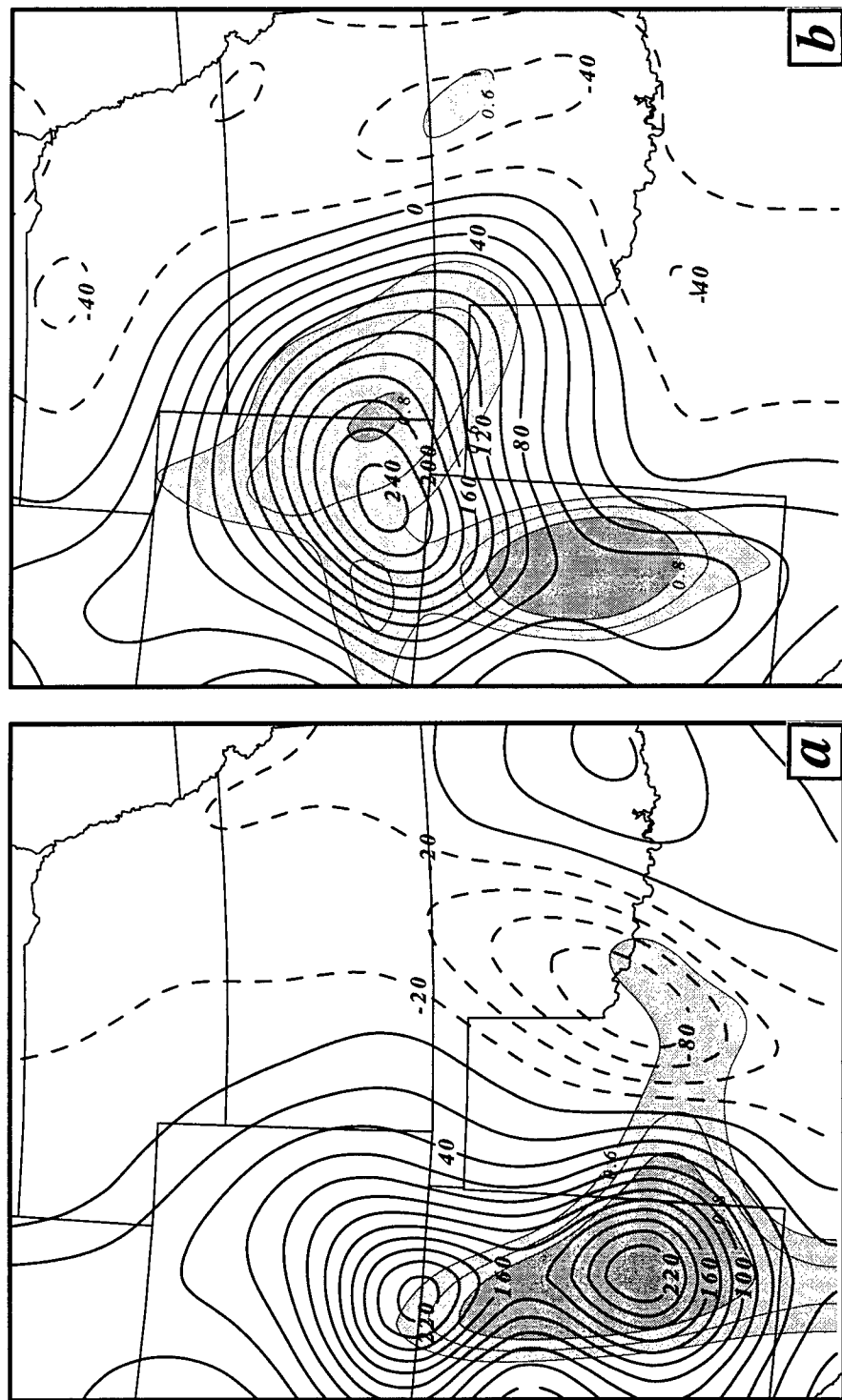


Figure 4.17. 500 mb objective analysis of the summation of four terms that make up the non-linear balance equation ($f\zeta$, $+2I(u,v)$, $-\nabla^2\phi$, $-\beta u$) for (a) 0000 UTC and (b) 0600 UTC 9 March 1992. Solid lines depict positive divergence values and the dashed lines depict negative divergence values ($\times 10^{-10} \text{ s}^{-2}$). Inertial Rossby number shaded above 0.6, at an interval of 0.1.

central Plains and correlates to the increase in divergent growth seen from the NLB equation calculations.

4.5.4 MASS Model Trajectory Analysis.

A parcel trajectory was constructed from the 60 km full physics MASS model run. The path is depicted in Fig. 4.18 and the corresponding diagnostic data sets are listed in Table 6.0. The parcel positions are based on a timestep of 0.5 hours with 20 iterations per timestep which was initiated at 2100 UTC 8 March and run out through 0900 UTC 9 March 1992. The parcel position coincides with the right exit region of the emerging jet streak over the Texas panhandle. During the first 3-hours the parcel exhibits a balanced state. The parcel trajectory is directed to the right of the geostrophic flow as a strong rightward directed ageostrophic vectors acts upon the parcel motion. During this period the parcel experiences a loss of nearly half its kinetic energy as the parcel is driven towards the anticyclonic side of the flow. Consistent with quasi-geostrophic theory a substantial deceleration is observed as the parcel speed decreases from 34 ms^{-1} at 09/00 UTC to 24 ms^{-1} at 09/03 UTC. The parcel experiences a descent of $\sim 570 \text{ m}$ resulting in a local temperature increase of $\sim 5.5^\circ\text{C}$.

Shortly after 09/00 UTC, the parcel enters south-central Kansas where the mesoscale mass perturbation is located. This mass perturbation primarily results from the thickness decrease caused by the leeside cold surge. Consequently, according to classical adjustment theory, the divergent component of the wind responds to the mesoscale mass

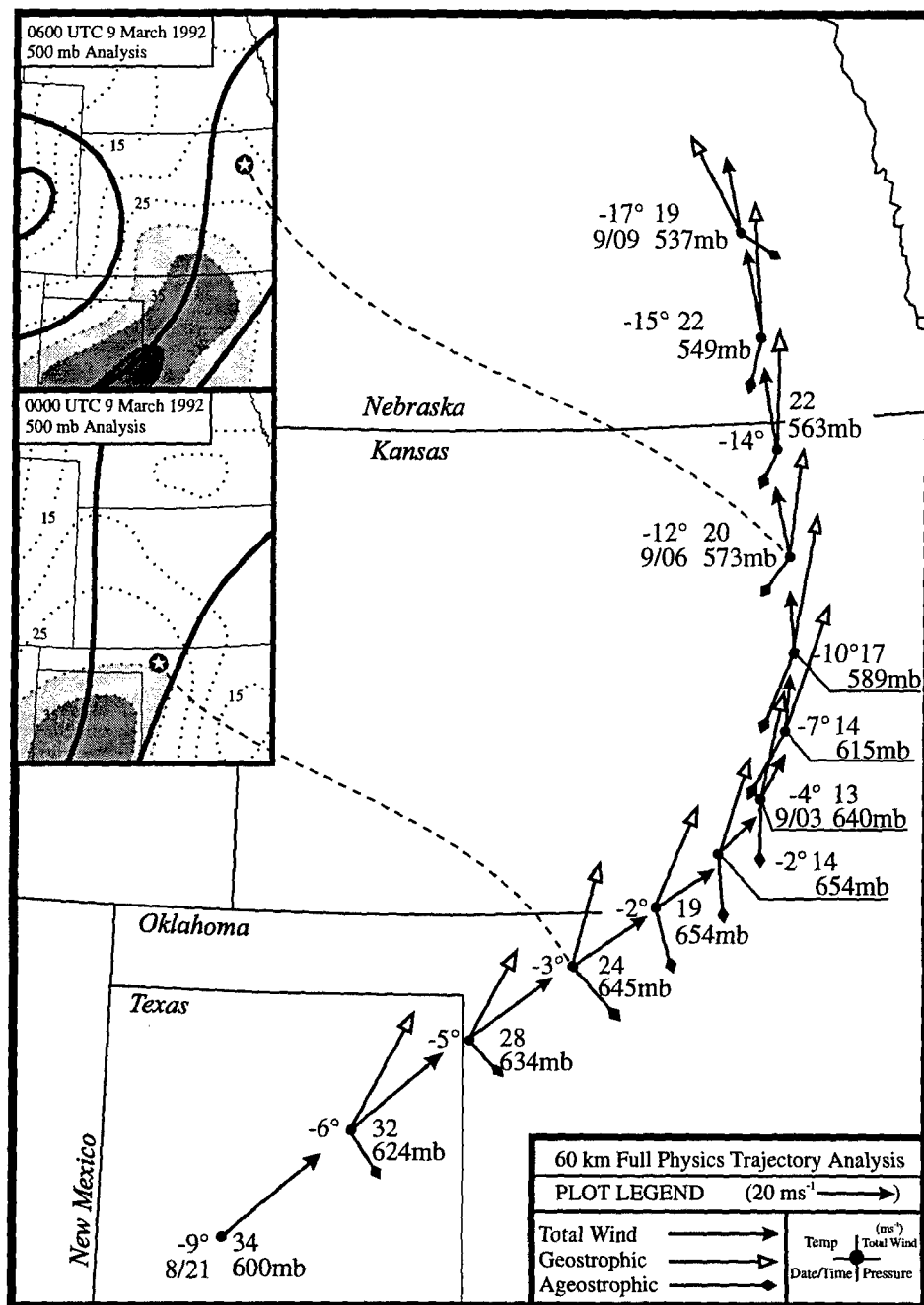


Figure 4.18. Forward trajectory constructed from 60 km full physics MASS model output. Trajectory started at 2100 UTC 8 March 1992 and ran to 0900 UTC 9 March 1992. Station plot contains parcel pressure level (mb), temperature (°C), total wind speed (ms⁻¹) and time of parcel location. Displayed wind vectors depict total wind vector (solid head), geostrophic component (open head), ageostrophic component (diamond head). 500 mb map insert displays associated height field at 60 m interval (solid) and isotachs at 5 ms⁻¹ interval (dotted).

Table 6.0

Forward trajectory initiated at 2100 UTC 8 March 1992 from 35°N, 102°W at the 600 mb level. Trajectory data is derived from 60 km full physics MASS model run. The following abbreviations (not previously defined) are: height above mean sea level (Z-MSL), Lagrangian Rossby number (R_{Lag}), modified Rossby number (R_c), and divergence computed on a theta surface (DIV).

TIME (UTC)	LAT (°N)	LON (°W)	PRES (mb)	Z-MSL (m)	TEMP (°C)	OMEGA ($\mu\text{bar s}^{-1}$)	R_{Lag} ($DV/Dt/V$)	R_c (Ce/fV)	K.E. (J)	DIV ($\times 10^{-5} \text{ s}^{-1}$)
8/21	35.0	102.0	600	4189	-8.94	+9.53	0.21	****	583	-3.773
9/00	36.7	99.1	645	3620	-3.48	+4.10	0.76	0.16	280	-5.473
9/03	37.6	97.4	640	3682	-3.77	-6.58	1.07	0.99	89	+0.603
9/06	39.2	97.0	573	4516	-12.32	-2.82	0.50	0.33	201	+0.821
9/09	41.2	97.4	537	4953	-16.98	-2.63	0.51	0.34	185	-3.270

perturbation in order to regain a balance between the mass and momentum fields since the rotational part of the wind reacts at a much larger time scale. Between 09/00 and 09/03 UTC, the parcel decelerates as the flow becomes increasingly subgeostrophic. The parcel maintains a thermally-indirect circulation as the parcel path remains $\sim 25^\circ$ to the right of the geostrophic flow. By 09/03 UTC the parcel develops a thermally-direct circulation as the cold surge drives down the Front Range. During the period 03-0800 UTC the parcel is directed left of the geostrophic wind while accelerating from 13 ms^{-1} to 22 ms^{-1} . This acceleration is significant considering it is located well within a region that should be experiencing a deceleration under quasi- and semi-geostrophic theory. The accelerating parcel's kinetic energy increases from 88 Joules at 09/03 UTC to a maximum of 243 Joules by 09/08 UTC. As the parcel is driven to the left of the flow, the parcel accelerates and an increase in the divergence field is observed as the parcel acquires an increase divergence of $0.8 \times 10^{-5} \text{ s}^{-1}$ by 09/06 UTC. In response to the divergent flow, ascent $> 8 \mu\text{bars}^{-1}$ is observed shortly after 09/04 UTC. The ascent results in a parcel temperature

drop of -12°C by 09/06 UTC. During the course of the trajectory the parcel remains within 0.5K of the 306K theta surface indicating that the temperature changes are driven by adiabatic rather than diabatic processes.

A measure of the imbalance is obtained through the calculation of the Lagrangian Rossby number (R_{Lag}). The total 'instantaneous' acceleration vector of the parcel was computed by calculating the parcel location over a period of $2\delta t$, where $t = 1/20$ the time step. The ratio of this nearly instantaneous acceleration to the Coriolis acceleration provides the Lagrangian Rossby number. Calculation of R_{Lag} give values below 0.5 through 08/23 UTC. These values are consistent with a balanced thermally-indirect circulation observed during this period. By 09/00 UTC, the value increases to 0.76 as the flow becomes more subgeostrophic. The R_{Lag} values peak during the period of 09/02-0500 UTC as the thermally-direct circulation increases. In order to assess the impact of centripetal accelerations on the emerging signal, a modified Rossby number (R_c) was calculated whereby the ratio of the centripetal acceleration to the Coriolis acceleration is evaluated. Calculations of R_{Lag} values indicate an increase above 0.5 after 09/00 UTC whereas the R_c values remain at ~ 0.15 through 09/02 UTC. As the cyclonic circulation increases the centripetal acceleration increases through the period of 09/03-09/05 UTC. After 09/05 UTC the centripetal acceleration drops off as the radius of curvature of the trajectory path increases whereas the R_{Lag} values remain near the critical value of 0.5. These results indicate that the impact of centripetal accelerations on the calculation of R_{Lag} and the derived ageostrophic flow only affects a small portion of the period of the adjustment process. The trajectory indicates a balanced structure prior to 09/00 UTC,

whereas an unbalanced adjustment process is observed between 09/02 UTC through 09/0800 UTC. During this period the centripetal acceleration dominates only for a short period as high R_c values are calculated between 09/03 UTC to 09/05 UTC.

4.5.5 MASS Model Derived Fields

The strongest adjustment process occurs between 09/03 and 09/06 UTC when the southward surge in the Front Range cold surge sets up a strong mass reduction over eastern Colorado. Output from the full physics 60 km MASS model run provides insight into the adjustment process taking place (Fig. 4.19). The secondary circulations are significantly altered as the forward quadrant of the emerging jet streak enters the corridor between OUN and DEN. In response to the mass perturbation, the 09/03 UTC geostrophic jet max is located ~400 km downstream of the observed jet max (Fig. 4.19a). The downstream positioning of the geostrophic jet streak results in a momentum anomaly in excess of 20 ms^{-1} located over south-central Kansas. The increased disparity of $\mathbf{V} \bullet \nabla \mathbf{V}$ and $\mathbf{V} \bullet \nabla \mathbf{V}_g$ is an indication of the imbalance present. This configuration of the jet streaks results in the positioning of the observed exit region within the geostrophic entrance region. In response, air parcels in the observed exit region are accelerating towards the momentum anomaly in order to regain a geostrophic balance between the mass and momentum fields.

By 09/06 UTC the geostrophic jet streak has expanded into central Oklahoma while the observed jet streak has rapidly accelerated into west-central Oklahoma where

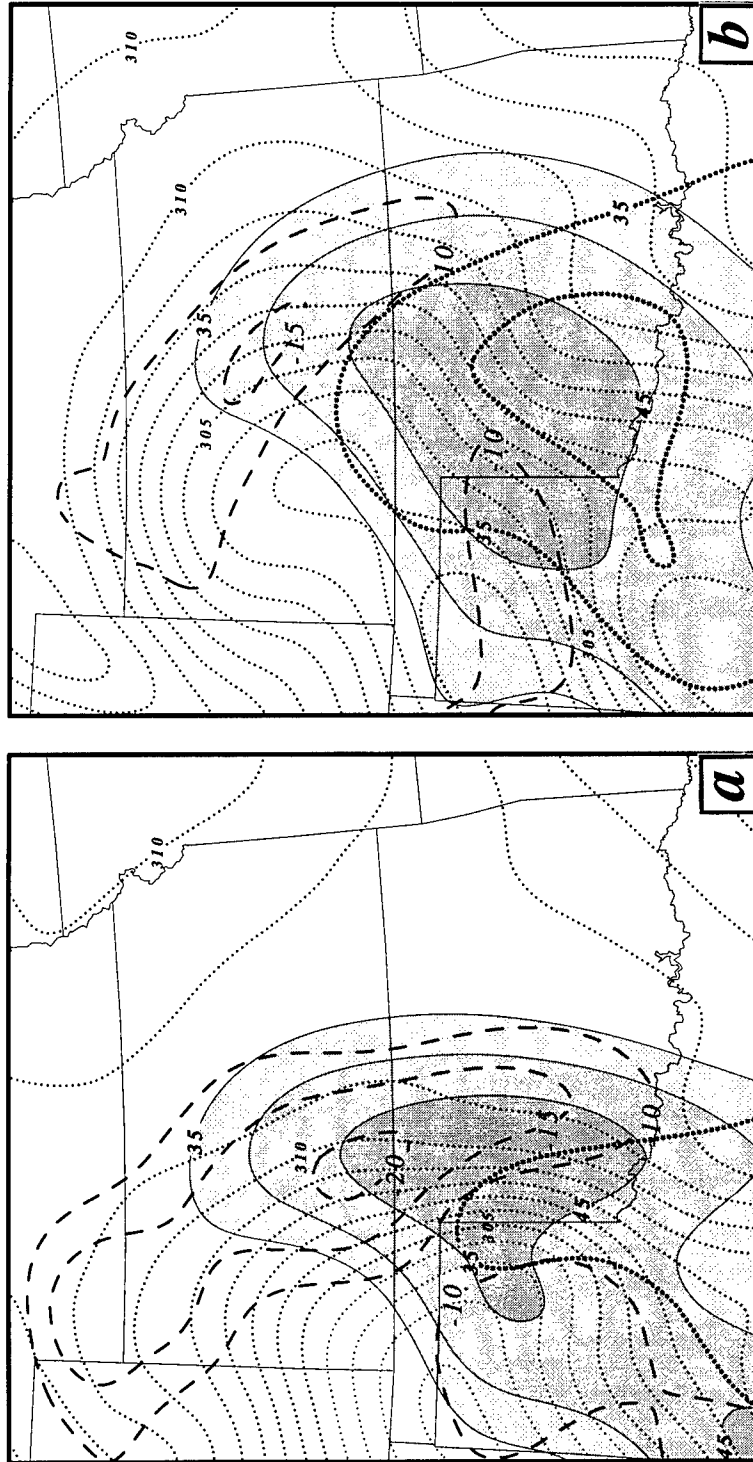


Figure 4.19. 500 mb MASS model 60 km output from (a) 0300 UTC 9 March 1992 and (b) 0600 UTC 9 March 1992. The derived theta field is displayed by the thin dotted line at a 1°K interval. The geostrophic isotachs are shaded above 35 ms^{-1} at an interval of 5 ms^{-1} . The observed wind isotachs above 35 ms^{-1} are displayed by the heavy dotted line at a interval of 5 ms^{-1} . The difference between the geostrophic and observed wind speed is displayed by a dashed line at a 5 ms^{-1} interval.

the wind speed has increased to over 40 ms^{-1} (Fig. 4.19b). Consistent with the accelerative nature of the jet exit region, high R_o values > 0.6 are found along the forward edge of the developing jet exit region (Fig 4.20a). In response to the accelerating jet exit region, a net mass flux divergence is observed within the exit region of the expanding jet streak (Fig. 4.20b). To coincide with the depth of maximum observed cooling, layer averaged mass divergence calculations were conducted through the 600-400 mb layer. A maximum divergence tendency $> 60 \times 10^{-7} \text{ kg m}^{-2} \text{ Pa s}^{-1}$ is observed at 09/03 UTC within the accelerating jet exit region over the Texas panhandle (Fig. 4.20b). As the air parcels accelerate away from this region towards central Kansas, the parcels converge with the slower moving parcels out ahead. It is along this gradient of maximum convergence that the upward vertical velocity is greatest resulting in a region of dry ascent over Kansas.

Inspection of the thermal field between 0300 and 0600 UTC reveals a region of substantial cooling downstream and to the right of the flow (Fig 4.19a,b). This pattern reflects the downwind generation of cold air allowing for the eastward development of the CFA/jet streak system as the atmosphere works to regain a balance between the mass and momentum fields. This cooling is occurring within the accelerating jet exit region characterized by the subgeostrophic, leftward-directed ageostrophic circulation. In response, a 6°C area of cooling is generated over central Kansas by 09/06 UTC (Fig 4.20b). The generation of cold air is located in a region substantially different from that provided by advection alone. Advection of the thermal field by the total wind provides a 3 hour temperature decrease of $\sim 18^\circ\text{C}$ over the Texas/Oklahoma border while temperatures over Kansas reflect little change (Fig. 4.20a). The disparity between the advective

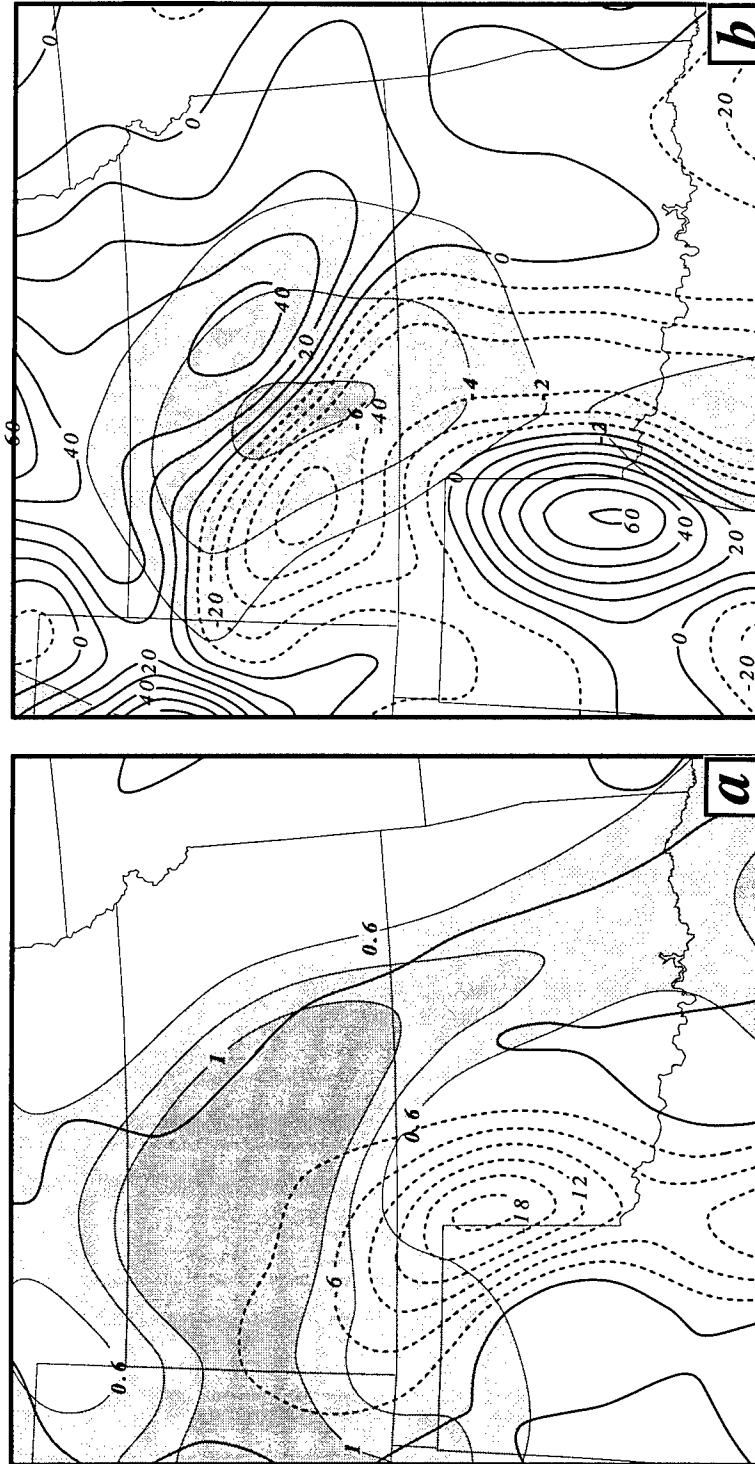


Figure 4.20. (a) MASS model 60 km output displaying the 500 mb inertial Rossby number at 0600 UTC 9 March 1992 (shaded above 0.6 at an interval of 0.1) and the 500 mb temperature advection by the total wind at 09/03 UTC. (b) MASS model 60 km output displaying the 500 mb layer averaged mass divergence ($10^{-7} \text{ kg m}^{-2} \text{ Pa s}^{-1}$) for 0300 UTC 9 March 1992 (thin solid - divergence, thin dashed convergence) and the derived change in the theta field between 09/03 and 09/0600 UTC (shaded at 2°K).

temperature anomalies to the actual changes are an indication of the significant impact of the complex secondary circulations established by the terrain forced mass perturbation.

4.6 Terrain Impact in CFA Formation and Jet Stream Bifurcation

The topography has been implicated in playing a dominate role in altering the secondary circulations downstream of the mountain barrier. A modeling study was conducted in order to assess the impact of the terrain in generating a CFA and bifurcation of the jet stream. This study involved running the MASS model with the same initial conditions as the original 60 km full physics run with the exception that a uniform terrain of 1200 m replaced the complex surface terrain file. The model run was initialized at 1200 UTC 8 March 1992 and contained all the structure induced by topography prior to this time, i.e. strong pool of warm air tied to the southern Front Range and damming of cold air along the northern slopes of the Canadian Rockies. The influence of these terrain induced features is minimized since the period of adjustment investigated is ~12 to 18 hours into the run.

The evolution of the flat model run results in a simulation that does not generate a well-defined CFA over the central Plains. In the absence of the western barrier, the low-level cold surge never materializes as cold air is allowed to spread westward rather than being forced down the Front Range. In response, the mid tropospheric heights do not fall as rapidly over eastern Colorado. Rather, the 500 mb low initialized over the inner-mountain region slowly propagates eastward during the course of the run. The associated

cold pool is allowed to overspread the region and weak baroclinicity is obtained in the flat model results.

By 09/03 UTC the 15 hour full physics results displayed in Fig. 4.21a show an intensifying upper-level low over eastern Colorado in concert with the surging low-level cold air down the Front Range. The 500 mb pattern shows an amplified wave with a circulation center, <546 dm, located over southeast Colorado. The associated amplifying ridge ahead of the system has built back into northwestern Nebraska as warm air is drawn into the circulation. The intensifying baroclinic zone over the Texas/Oklahoma border is evident as the axis of cold air pushes across the Texas panhandle. In response to the adjustment process taking place in the lee of the mountains, a developing jet streak over eastern Kansas forms downstream and to the right of the primary jet streak over the Texas panhandle.

The 15 hour forecast from the flat terrain model run indicates marked differences in the evolution of the atmosphere (Fig. 4.21b). In the absence of lower tropospheric cooling, the strong dynamics are no longer focused over western Oklahoma/Kansas. Consequently, the 500 mb low lags ~ 350 km to the northwest of the observed position. The intensity of the upper air features are dampened as heights over the Oklahoma panhandle are ~ 50 m higher than the full physics run. The amplified trough in the terrain run allows for a much stronger meridional flow to develop. This acts to enhance the baroclinicity over the central Plains as a thermally-direct secondary circulation develops within the emerging jet exit region. The wind field is characterized by a narrow concentration of momentum evident by an axis of winds in excess of 12 ms^{-1} stronger than

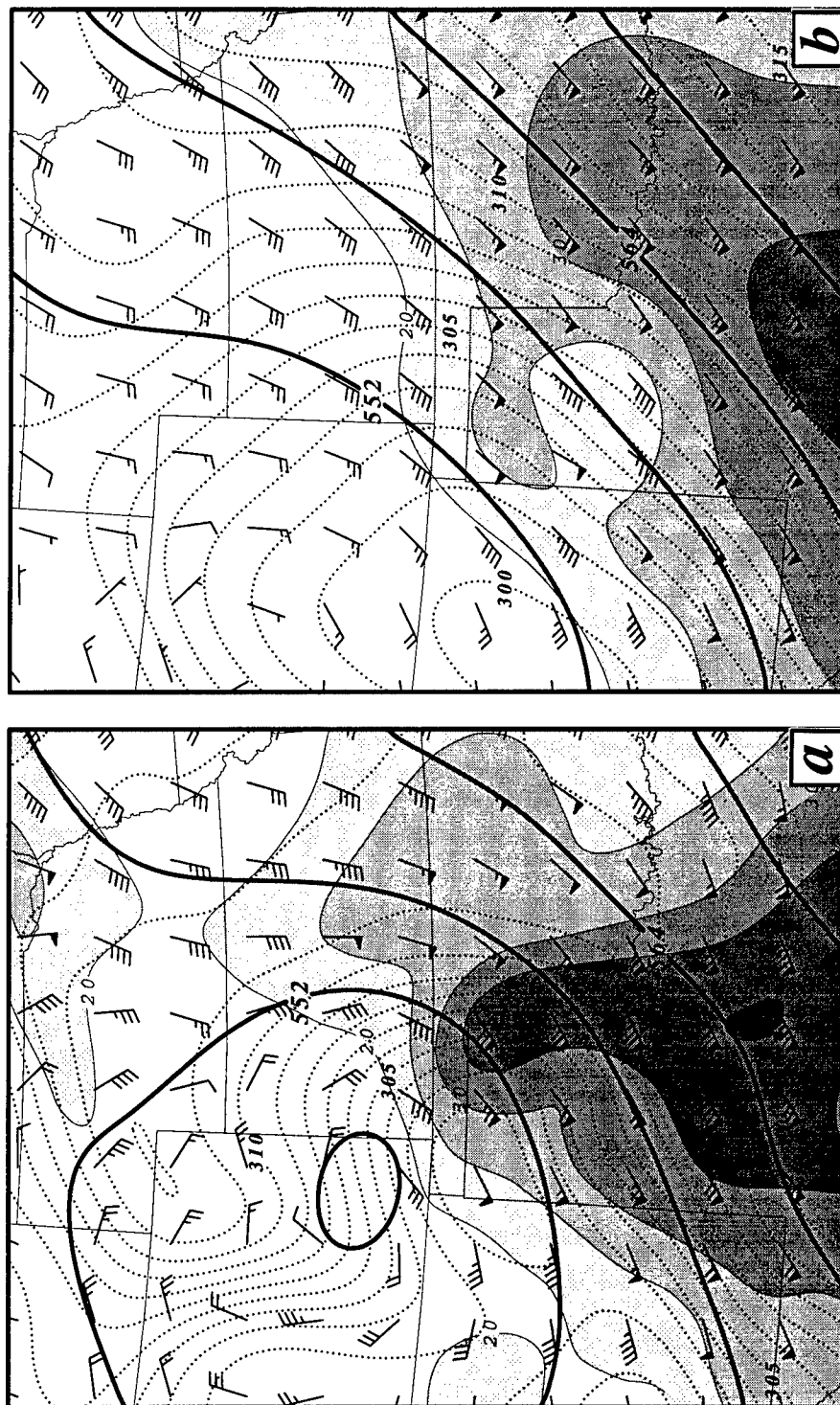


Figure 4.21. (a) 60 km MASS model output with high resolution surface terrain data base. (b) 60 km MASS model output with flat 1200 m surface elevation. 500 mb model generated fields are from the 15 hour forecast valid at 0300 UTC 9 March 1992. Displayed fields are: gridded wind vectors (flag - 25 ms^{-1} , full staff - 5 ms^{-1} , half staff - 2.5 ms^{-1}), theta (dotted lines at a 1°K interval), geopotential heights (solid lines at an interval of 6 dm), isotachs (shading - above 20 ms^{-1} at an interval of 5 ms^{-1}),

that of the flat run extending from Abilene, Texas into Dodge City, Kansas. In the flat terrain simulation, the winds over the eastern Plains have a greater zonal component limiting the warm advection into the downstream ridge. In response, the amplitude of the ridge is reduced ~ 25 m over central Nebraska. The divergence tendency is significantly diminished as a broad jet streak extends into the eastern Plains. Throughout Kansas and Oklahoma the total wind is within 5 ms^{-1} of the geostrophic wind indicative of the balanced, decelerative nature of the jet exit region. The thermal field simply advects out of the inner-mountain region resulting in minimal baroclinicity over the central Plains.

Frontogenetic calculations for both model runs reflect the impact of the terrain in the generation of a CFA (Fig. 4.22 and 4.23). The impact of the terrain and the adjustment process described in section 4.5.3 results in an area of marked frontogenesis on the Texas/Oklahoma border at 09/03 UTC (Fig. 4.22a). Frontogenesis on the order of $8\text{K } 100\text{km}^{-1} \text{ } 3 \text{ hrs}^{-1}$ is calculated in this area which agrees well with observed placement and calculations depicted in Fig. 4.1 and 4.10. The development of an increased divergent ageostrophic flow, as a thermally-direct circulation forms within the exit region, results in a zone of enhanced convergence over western Oklahoma. The ageostrophic convergent zone provides a positive contribution in the generation of the CFA as the flow becomes more meridional (Fig. 4.22d) while the modest cross-stream shear provides an additional contribution (Fig. 4.22c). However, the dominant forcing is found with the tilting contribution associated with the vertical motion distribution acting upon the vertical temperature gradient (Fig. 4.22b). The signal of ascent in the exit region of the jet provides a strong contribution in the generation of cold air and increased baroclinicity in

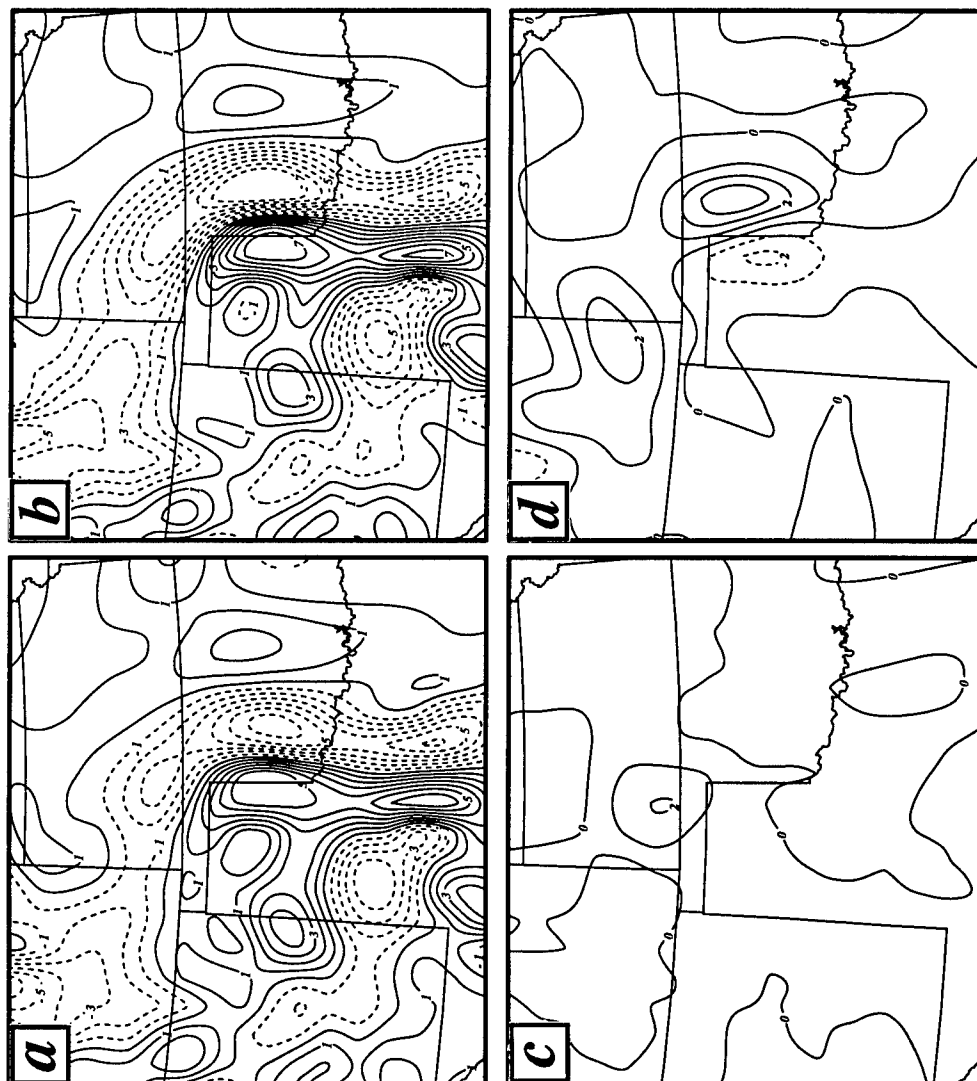


Figure 4.22. 0300 UTC 9 March 1992 500 mb frontogenesis calculations based on Miller Frontogenetic function derived from the 60 km MASS model simulation with high resolution terrain data base. (a) Total frontogenesis, (b) tilting term, (c) horizontal shear term, and (d) confluence term. Solid lines depict frontogenesis, dashed lines frontolysis ($^{\circ}\text{K } 100 \text{ km}^{-1} \text{ 3 hrs}^{-1}$).



Figure 4.23. 0300 UTC 9 March 1992 500 mb frontogenesis calculations based on Miller Frontogenetic function derived from the 60 km MASS model simulation with flat terrain data base. (a) Total frontogenesis, (b) tilting term, (c) horizontal shear term, and (d) confluence term. Solid lines depict frontogenesis, dashed lines frontolysis ($^{\circ}\text{K } 100 \text{ km}^{-1} \text{ 3 hrs}^{-1}$).

response to the developing thermally-direct circulation. In marked contrast, the total frontogenesis calculations for the flat terrain run indicates a very nondescript pattern over the Great Plains (Fig. 4.23). Both the shear and confluence contributions act negatively over the Texas panhandle while generating only an area of weak positive forcing over central Oklahoma in response to the broad thermally-indirect circulation of the jet exit region. Meanwhile the generation of isolated convection and the associated vertical motion distribution over the Texas panhandle result in a positive contribution by the tilting term.

5. SUMMARY AND CONCLUSIONS

The effect of *two distinct episodes* of terrain-induced mass perturbations on the development of a midtropospheric jet streak and cold front aloft (CFA) have been analyzed using STORM-FEST data sets for the 8-9 March 1992 period. This study indicates the Rocky Mountains act as an important source region for the generation of CFA and influencing the bifurcation of the polar jet stream. Previous studies have emphasized the role of geostrophic deformation processes in CFA development and maintenance. The role of the mountains has been thought of in terms of a barrier preventing the lower tropospheric cold air from progressing eastward over the central Plains. These studies suggest the blocking of the lower tropospheric cold front results in a surge of midtropospheric cold air which extends some 200-300 km ahead of the surface feature. This study also recognizes the strong terrain influence in the generation of the CFA. However, unlike previous work, the mountains are credited with disrupting the balance between the mass and momentum field which disrupts the classical straight-line jet streak dynamics. This results in an acceleration of the jet exit region and cooling downstream of the mountains. In response, a positive velocity divergence tendency produces a net mass flux divergence. In turn, ascent and midtropospheric cooling is observed downstream of the large scale baroclinic zone over the inner-mountain region producing a CFA and bifurcating the jet stream as a northward directed jet streak forms over the central Plains.

Diagnostic analyses were conducted using the extensive data sets made available during the STORM-FEST field experiment. This project provided an excellent opportunity in which to review and refine a method, based on application of the divergence equation, to extract geopotential height and thermal structure from observed wind data. At rawinsonde sites, the retrieved heights compared very well with observed heights (Table 2.0). When comparisons were made at a number of times and at various levels in the troposphere, the average standard deviation was only ~ 10 m, well within the accuracy of the rawinsonde instrumentation (± 24 meters). Results of the comparison of retrieved and observed temperatures show comparable accuracy to that of the heights, with an average standard deviation of $\sim 1.5^{\circ}\text{C}$. The retrieved temperature profile was within 1°C of the observed temperature sounding over GUY, as the CFA passed over the area. For both retrieved fields (temperature and height) the greatest accuracy was obtained at lower atmospheric levels (700 and 500 mb) and the accuracy decreased at higher levels.

The derived mass and momentum fields combined with numerical modeling studies identify two distinct periods of adjustment leading to the CFA formation. Each period of adjustment occurs within a sub-inertial time scale of ~ 6 hours. The first period of adjustment occurs as the mountains act to increase the leeside baroclinic zone along the southern foothills. The persistent cross mountain flow has a direct effect in concentrating lower tropospheric heating along the lee of the Rockies. The downwind structure is influenced by the formation of downslope adiabatic warming, enhanced surface sensible heating. In turn, the restructuring of the mass field forces a geostrophic adjustment between the mass and momentum fields downstream of the barrier. Low-level trajectory

calculations reveal parcels warming nearly 7°C as they descend down the eastern slopes of New Mexico. This flow not only induces an adiabatic warming but also acts to dry the atmosphere. Shortly after sunrise, the extensive dry layer limits the amount of absorption and scattering of short wave radiation thus enhancing its penetration to the surface. This allows maximum sensible heating of the boundary layer over a confined region along the southwestern Plains. In response to the increased heating, the boundary layer rapidly expands during the course of the day. By 2100 UTC, boundary layer expansion is evident as the MAF sounding shows the inversion base lifting from 870 mb to the 650 mb level.

Inspection of the synoptic scale height change pattern reflects the quasi-geostrophic signal of the slow approaching 500 mb low from the inner-mountain region and the building ridge associated with warm advection over the Mississippi Valley. However, in response to the wedge of warm air focused along the Front Range, a mesoscale perturbation in the mass field in the form of height rises split the height fall pattern observed over the Great Plains. The resultant mass perturbation induces an increase in the geostrophic wind max along the eastern slopes of New Mexico. By 08/18 UTC the observed jet max of 35 ms^{-1} is positioned over ELP while a geostrophic jet max of 45 ms^{-1} is located 300-400 km downstream in the vicinity of CVS. The disparity of the two centers results in the observed jet exit region lying within the thermally-direct circulation of the geostrophic jet entrance region. As the jet exit extends across the mountain barrier it becomes superimposed with the wedge of warm air in the lee of the mountains. An atmospheric response in the form of a thermally-direct circulation develops within the jet exit region in order to compensate for the lack of lower tropospheric cold

air. The role of the developing ageostrophic motion is to regain thermal wind balance. In response, the vertical motion over southeast Colorado is accentuated as evident by the rapid deepening of the surface low in which pressure falls exceed 1 mb hr^{-1} . This produces a cooling of the mid-levels downstream and to the right of the flow as the atmosphere works to regain a balanced state. This leads to an increase in a divergent response by the flow producing a thermally-direct circulation within the exit region of the jet. This leftward-directed flow is not consistent with quasi-geostrophic jet streak dynamics and is indicative of an accelerating flow in the exit region. This results in the conversion of excess potential energy, generated by the mass perturbation, into kinetic energy in the form of accelerating air parcels. This response occurs over a sub-inertial time period of 5-7 hours.

During the period 08/15-08/21 UTC a number of signals exist indicating imbalance over the southwestern Plains. Inspection of the disparity between the 700-500 mb vertical shear vector for the observed winds and the geostrophic wind indicates the thermal wind imbalance over the region. Over southeast New Mexico, the vector difference indicates the development of a flow directed left of the flow within the exit region of the observed jet exit region. Meanwhile, over eastern New Mexico the alignment of the vectors indicates the increased alongstream inertial advective forcing acting to achieve a balance. During this period, the trajectories show a fairly straight path which indicates that centripetal acceleration do not play a significant role in the acceleration of the parcel. Consequently the generation of subgeostrophic tendencies can be attributed to the along- and cross-stream accelerations taking place rather than the effects of curvature.

Frontogenetic calculations from both observed and model data both indicate that tilting process followed by confluent deformation dominate in CFA development.

A second set of terrain-induced adjustments are observed in relation to a narrow corridor of intense cooling accompanying a surge of cold air focused along the western Plains. The terrain provides a ridged western barrier concentrating cold air along the Front Range of the Rockies. In order for the cold air to overcome the barrier a conversion of kinetic to potential energy is required. Flow blockage occurs when the inertial forcing is insufficient to counter the static stability of the air mass. In this case, insufficient potential energy exists to overcome the barrier resulting in an accumulation of mass on the windward side of the mountain. By 09/00 UTC a Froude number of 0.25 was calculated indicative of the favorable conditions for flow blockage and cold air damming along the eastern slopes of the northern Rockies. Between 09/00 and 09/09 UTC, the accumulation of cold air eventually develops into a cold surge which rapidly propagates southward through eastern Colorado at $\sim 17 \text{ ms}^{-1}$. The vertical depth of the cold air extended $\sim 2 \text{ km}$ AGL with the top of the frontal zone located at $\sim 650 \text{ mb}$ level. Passage of the boundary was associated with decreasing ceilings, increased precipitation, plummeting temperatures and an abrupt increase in surface winds approaching 20 ms^{-1} .

The southward surge of cold air concentrated along a narrow axis along the lee of the Rockies results in a rapid restructuring of the lower troposphere. The 500 mb height fall pattern centered at 09/03 UTC provides a strong signal of the impact of the combined effects of the surging cold air down the Front Range and the development of convection along the dry line over central Texas. The perturbation in the mass field has a length scale

of ~425 km which lies within the Rossby radius of deformation making the region susceptible to strong irrotational ageostrophic adjustments. As air parcels enter this region of strong isallobaric forcing, the perturbation is sufficiently small that there is not enough time for the rotational part of the wind to respond resulting in rapid adjustment by the divergent part of the wind. In response, the “classical jet streak” configuration is distorted as the jet exit region accelerates downstream. This acceleration is found in a region, according to semi-geostrophic theory, typically characterized by a rightward, thermally-indirect circulation in which the flow decelerates. As the jet streak enters this region it is exposed to increased isallobaric forcing directed towards the northwest at 15 ms^{-1} . The increased forcing acts to direct the air parcels left of the flow as the divergent part of the ageostrophic wind responds to the perturbation resulting in a thermally-direct circulation. In response, the parcels accelerate as the flow is directed towards lower heights converting potential into kinetic energy. Trajectory analyses indicate that parcels originating within the “warm sector” of the jet exit region result in a three hour adiabatic cooling of $\sim 9^\circ\text{C}$ as the parcel acquires an increase in divergence of $0.821 \times 10^{-5} \text{ s}^{-1}$. Such values are considered significant in that they are observed in an environment typically associated with strong deceleration, mass convergence, and warming. As the accelerating jet exit region attempts to regain the balance between the mass and momentum field the vertical motion gradients and convergence associated with the increased thermally-direct ageostrophic flow result in the formation of a CFA downstream and to the right of the flow. By 09/03 UTC, calculation from both observed and model data indicate the CFA is associated with frontogenesis on the order of $8^\circ\text{C } 100 \text{ km}^{-1} \text{ } 3 \text{ hrs}^{-1}$.

A conceptual model illustrating the development of the CFA in response to the terrain-induced mass perturbations is depicted in Fig. 5.1. This model reflects the terrain enhanced adiabatic and diabatic forcing which act to perturb the mass field producing an acceleration in the momentum field. In response, the "classical jet streak" configuration is distorted as the jet exit region accelerates downstream. The positive velocity divergence tendency produces a net mass flux divergence throughout the column. In turn, ascent and midtropospheric cooling is observed downstream of the large scale baroclinic zone over the inner-mountain region.

The formation of the CFA and powerful jet streak are remarkable in that the forcing is not dominated by the upper-level synoptic scale dynamics. Rather, lower tropospheric processes act in controlling the observed mid-upper tropospheric geostrophic adjustment processes resulting in increased ageostrophic motion leading to frontogenesis and jet streak formation.

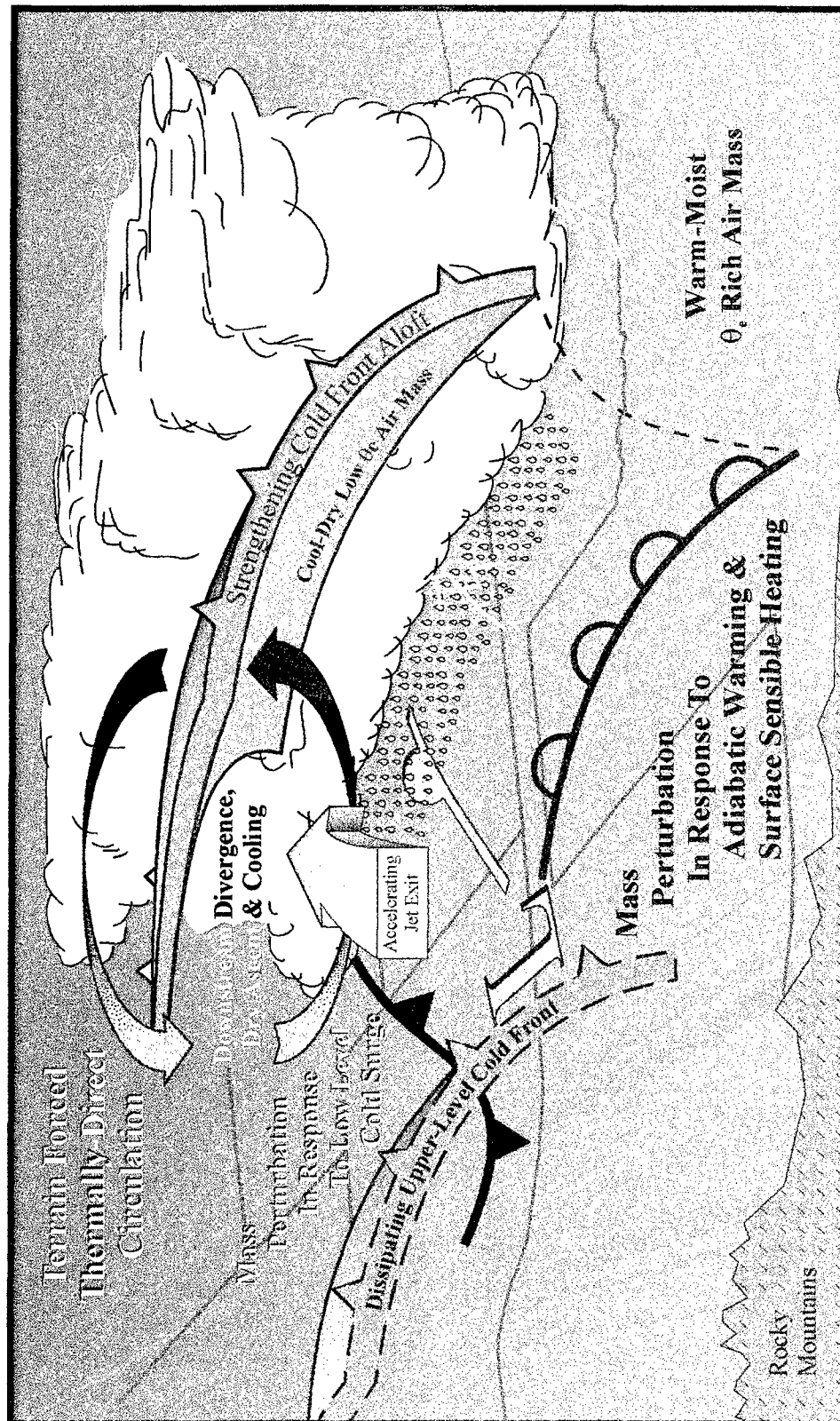


Figure 5.1. Conceptual model depicting structure of terrain induced Cold Front Aloft and developing midtropospheric jet streak over the central Plains in response to terrain induced secondary circulation downstream of the mountains.

6. LIST OF REFERENCES

- Adams, M. E., 1989: Anatomy of a "Bomb" - Diagnostic Investigation of Explosive Cyclogenesis Over the Mid-West United States, Masters Thesis, North Carolina State University, 102 pp.
- Anderson, J. R., E. E. Hardy, J. T. Roach, and R. E. Witmer, 1976: A land use and land cover classification system for use with remote sensor data. *U.S. Geological Survey Professional Paper 964*. U.S. Government Printing Office, Washington 28 pp.
- Barnes, S.L., 1964: A technique for maximizing details in numerical weather map analysis. *J. Appl. Meteor.*, **3** 396-409.
- Bauman, W. H., III, 1995: Synoptic and mesoscale forcing of convective activity over Cape Canaveral during easterly flow and nowcasting for space shuttle landing facility at Kennedy Space Center. Ph. D. Thesis. North Carolina State University, 140 pp.
- Bell, G. D., and L. F. Bosart, 1988: Appalachian cold-air damming. *Mon Wea. Rev.*, **116**, 137-161.
- Bergeron, T., 1937: On the physics of fronts. *Bull Amer. Meteor. Soc.*, **18**, 265-275.
- Bleck, R., R. Brummer, and M. A. Shapiro, 1984: Enhancement of remotely sensed temperature fields by wind observations from VHF radar network. *Mon. Wea. Rev.*, **112**, 1795-1803.
- Bluestein, H. B., 1993: *Synoptic-Dynamic Meteorology in Midlatitudes; Observations and Theory of Weather Systems*. Vol. 2, Oxford University Press, 594 pp.
- Blumen W., 1972: Geostrophic adjustment. *Rev. Geophys. Space Phys.*, **10**, 485-528.
- Bosart, L. F., 1970: Mid-tropospheric frontogenesis. *Quart. J. Roy. Meteor. Soc.*, **96**, 442-471.
- Businger, S., W. H. Bauman III, and G. F. Watson, 1991: The development of the Piedmont front and associated outbreak of severe weather on 13 March 1986. *Mon. Wea. Rev.*, **119**, 2224-2251.
- Campistron, B., A. W. Huggins, and A. B. Long, 1991: Investigations of a winter mountain storm in Utah. Part III: Single Doppler radar measurements of turbulence. *J. Atmos. Sci.*, **48**, 1306-1318.

- Carlson, T. N. and F. H. Ludlam, 1968: Conditions for the occurrence of severe local storms. *Tellus*, **20**, 203-226.
- Chang, C., J. Millard, and G. Chen, 1983; Gravitational characteristics of cold surges during winter MONEX. *Mon Wea. Rev.*, **111**, 293-307.
- Colle, B. A., and C. F. Mass, 1995: The structure and evolution of cold surges east of the Rocky mountains. *Mon Wea. Rev.*, **123**, 2577-2610.
- Cram, J. M., M. L. Kaplan, C. A. Mattocks, and J W. Zack, 1991: The use and analysis of Profiler winds to derive mesoscale height and temperature fields: Simulation and real data experiments, *Mon. Wea. Rev.*, **119**, 1040-1056.
- Daley, R., 1991: Atmospheric Data Analysis, Cambridge University Press, 457 pp.
- Danielsen, E. F., 1968: Stratospheric-tropospheric exchange based upon radioactivity, ozone, and potential vorticity, *J. Atmos. Sci.*, **25**, 502-518.
- DesJardins, M. L., K. F. Brill, S. Jacobs, S. S. Schotz, and P. Bruehl, 1992: GEMPAK5 Users manual Version 5.1, NASA/GSFC, National Meteorological Center, and Unidata Program Center/UCAR. 267 pp.
- Dunn, L., 1987: Cold air damming by the Front Range of the Colorado Rockies and its relationship to locally heavy snows. *Wea and Forecasting*, **2**, 177-189.
- Durran, D. R. and L. W. Snellman, 1987: The diagnosis of synoptic-scale motion in an operational environment. *Wea and Forecasting*, **1**, 17-31.
- _____, 1986: *Mesoscale Meteorology and Forecasting*. Chpt 20: Mountain Waves, Amer. Met. Soc., 472-492.
- Fankhauser, J.C., 1974: The derivation of consistent fields of wind and geopotential height from mesoscale rawinsonde data. *J. Appl. Meteor.*, **13**, 637-646.
- Feren, G., 1995: The 'stratified delta' cloud system - A satellite imagery precursor to major cyclogenesis in the eastern Australian - western Tasman sea region. *Wea and Forecasting*, **10**, 286-309.
- Fortune, M. and V. Kousky, 1983: Two severe freezes in Brazil: Precursors and synoptic evolution. *Mon Wea. Rev.*, **111**, 181-196.
- Gill, A. E., 1982: Atmospheric-Ocean Dynamics. New York: Academic Press, 662 pp.

- Haltiner, G.J., and R.T. Williams, 1980: *Numerical Weather Prediction and Dynamic Meteorology*, John Wiley and Sons, Inc., 477 pp.
- Hobbs, P. V., J. D. Locatelli, and J. E. Martin, 1990: Cold front aloft and the forecasting of precipitation and severe weather east of the Rocky Mountains. *Wea. and Forecasting*, **5**, 613-626.
- _____, 1994. "STORM - Structurally Transformed by Orography Model, for winter storms in the central United States. Video developed by the Atmospheric Sciences Department of the University of Washington.
- _____, J. D. Locatelli, and J. E. Martin, 1996. A new conceptual model for cyclones generated in the lee of the Rocky mountains. *Bull. Amer. Meteor. Soc.*, **77**, 1169-1178.
- Hoehne, W.E., 1980: Precision of National Weather Service upper air measurements. NOAA Tech. Memo. NWS T&ED-16, National Weather Service (NTIS#PB81-108136, 23 pp.
- Holton, J. R., 1979: *An Introduction to Dynamic Meteorology*, Academic Press, Inc., 391 pp.
- Houze, R. A., Jr., 1993, *Cloud Dynamics*, Academic Press, Inc., 573 pp.
- Kalnay, E., M. Kanamistu, R. Kistler, W. Collins, D. Deaven, L. Gandin, M. Iredell, S. Saha, G. White, J. Woollen, Y. Zhu, M. Chelliah, W. Ebisuzaki, W. Higgins, J. Janowiak, K. C. Mo, C. Ropelewski, J. Wang, A. Leetmaa, R. Reynolds, R. Jenne, and D. Joseph, 1996: The NMC/NCAR 40-year reanalysis project. *Bull. Amer. Meteor. Soc.*, **77**, No. 3, 437-471.
- Kaplan, M. L. and D. A. Paine, 1977: The observed divergence of the horizontal velocity field and pressure gradient force at the mesoscale. Its implications for the parameterization of three-dimensional momentum transport in synoptic-scale numerical models. *Beitr. Phys. Atmos.*, **50** 321-330.
- _____, and V. M. Karyampudi, 1992a: Meso-beta scale numerical simulations of terrain drag-induced along-stream circulations. Part I: Midtropospheric frontogenesis. *Meteorol. Atmos. Phys.* **49**, 133-156.
- _____, _____, 1992b: Meso-beta scale numerical simulations of terrain-induced along-stream circulations. Part II: Concentration of potential vorticity within dryline bulges. *Meteorol. Atmos. Phys.* **49**, 157-185.

- _____, S. E. Koch, Y-L. Lin, R. P. Weglarz, and Rozumalski, R. A., 1996: Numerical simulation of gravity wave event over CCOPE. Part I: The role of geostrophic adjustment in mesoscale jet streak and gravity wave generation. *Mon. Wea. Rev.* (in press).
- Karyampudi, V. M., M. L. Kaplan, S. E. Koch, and R. J. Zamora, 1995: The influence of the Rocky Mountains in the 13-14 April 1986 severe weather outbreak. Part I: Mesoscale lee cyclogenesis and its relationship to severe weather and dust storms. *Mon. Wea. Rev.*, **123**, 1394-1422.
- Keyser, D., and M. A. Shapiro, 1986: A review of the structure and dynamics of upper-level frontal zones. *Mon. Wea. Rev.*, **114**, 452-499.
- Klemp, J. B., and D. K. Lilly, 1975: The dynamics of wave-induced downslope winds. *J. Atmos. Sci.*, **32**, 320-339.
- Koch, S. E., and J. McCarthey, 1982: The evolution of an Oklahoma Dryline. Part I: A meso- and subsynoptic-scale analysis. *J. Atmos. Sci.*, **39**, 225-236.
- _____, M. DesJardins, and P. J. Kocin, 1983: An interactive Barnes objective map analysis scheme for use with satellite and conventional data. *J. Clim. and Appl. Met.*, **22**, 1487-1503.
- _____, and P. B. Dorian, 1988: A mesoscale gravity wave event observed over CCOPE. Part III: Wave environment and possible source mechanisms. *Mon. Wea. Rev.*, **116**, 2570 - 2592.
- Kuo, Y.-H., and R.A. Anthes, 1985: Calculation of geopotential and temperature fields from an array of nearly continuous wind observations. *J. Atmos. Oceanic Tech.*, **2**, 22-34.
- _____, E. G. Donald, and M.A. Shapiro, 1987a: Feasibility of short range numerical weather prediction using observations from a network of profilers. *Mon. Wea. Rev.*, **115**, 2402-2427.
- _____, D.O. Gill and L. Cheng 1987b: Retrieving temperature and geopotential fields from a network of wind profiler observations. *Mon. Wea. Rev.*, **115**, 3146-3165.
- Lichtblau, S., 1936: Upper cold fronts in North America. *Mon. Wea. Rev.*, **64**, 414-425.
- Lin, Y-L., and T-A. Wang, 1996: Flow regimes and transient dynamics of two-dimensional stratified flow over an isolated mountain ridge. *J. Atmos. Sci.*, **53**, 139-158.

- Lindzen, R. S., and K-K. Tung, 1976: Banded convective activity and ducted gravity waves. *Mon. Wea. Rev.*, **104**, 1602-1617.
- Lloyd, J. R., 1942: The development and trajectories of tornadoes. *Mon. Wea. Rev.*, **70**, 65-75.
- Locatelli, J. D., J. M. Sienkiewicz, and P. V. Hobbs, 1989: Organization and structure of clouds and precipitation on the mid-Atlantic coast of the United States. Part I: Synoptic evolution of a frontal system from the Rockies to the Atlantic coast. *J. Atmos. Sci.*, **46**, 1327-1348.
- _____, J. E. Martin, J. A. Castle, and P. V. Hobbs, 1995: Structure and evolution of winter cyclones in the central United States and their effects on distribution of precipitation. Part III: The development of a squall line associated with weak cold frontogenesis aloft. *Mon. Wea. Rev.*, **123**, 2641-2662.
- _____, and P. V. Hobbs, 1995: A world record rainfall rate at Holt, Missouri: was it due to cold frontogenesis aloft ?. *Wea and Forecasting*, **10**, 779-785.
- Mahrt L., and H. Pan, 1984: A two-layer model of soil hydrology. *Boundary-Layer Meteorol.*, **29**, 1-20.
- Manibianco, J., L. W. Uccellini, K. F. Brill, and P. J. Kocin, 1991: Contrasting the impact of dynamic data assimilation on the numerical simulation of cyclogenesis during GALE IOP-10 and IOP-1. *Meteor. Atmos. Phys.*, **45**, 41-63.
- Martin, J. E., J. D. Locatelli, and P. V. Hobbs, 1990: Organization and structure of clouds and precipitation on the mid-Atlantic coast of the United States. Part III: The evolution of a middle-tropospheric cold front. *Mon. Wea. Rev.*, **118**, 195-217.
- _____, P. Wang, and J. A. Castle, 1995: Structure and evolution of winter cyclones in the central United States and their effects on the distribution of precipitation. Part I: A synoptic-scale rainband associated with a dryline and lee trough. *Mon. Wea. Rev.*, **123**, 241-264.
- Mattocks, C. and R. Bleck, 1986: Jet streak dynamics and geostrophic adjustment processes during the initial stages of lee cyclogenesis. *Mon. Wea. Rev.*, **114**, 2033-2056.
- May, P.T., and R.G. Strauch, 1989: An examination of wind profiler signal processing algorithms. *J. Atmos. Oceanic Tech.* **6**, 731-735.

- Mecikalski, J., and J. Tilley, 1992: Cold surges along the Front Range of the Rocky mountains: Development of a classification scheme. *Meteorol. Atmos. Phys.*, **48**, 249-271.
- MESO, 1995: MASS Version 5.8 Reference Manual, MESO, Inc., Troy, NY, 119 pp.
- Miller, J. E., 1948: On the concept of frontogenesis. *J. Meteor.*, **5**, 169-171.
- Modica, G.M., and T.T. Warner, 1987: The error associated with various forms of the divergence equation to diagnose geopotential and temperatures. *Mon. Wea. Rev.*, **115**, 455-462.
- Moore, J. T. and W. A. Abeling, 1988: Adjustments of unbalanced flow in upper levels during the AVE-SESAME I period, *Mon. Wea. Rev.*, **116**, 2425-2436.
- Murray, R. and S. M. Daniels, 1953: Transverse flow at entrance and exit to jet streams. *Quart. J. Roy. Meteor. Soc.*, **79**, 236-241.
- Newton, C. W., 1958: Variations in frontal structure of upper level troughs. *Geophysica*, **6**, 357-375.
- Nieman, S. J., J. Schmetz, and W. P. Menzel, 1993: A comparison of several techniques to assign heights to cloud tracers. *J. Appl. Meteor.*, **32**, 1559-1568.
- Noilhan, J. and S. Planton, 1989: A simple parameterization of land surface processes for meteorological models. *Mon. Wea. Rev.*, **117**, 536-549.
- Orlanski, I., 1975: A rational subdivision of scales for atmospheric process. *Bull. Amer. Meteor. Soc.*, **56**, 527-530.
- O'Brien, J. J., 1970: Alternative solutions to the classical vertical velocity problem. *J. Appl. Meteo.*, **9**, 197-203.
- Pierrehumbert, R. T., 1984: Linear results on the barrier effects of mesoscale mountains. *J. Atmos. Sci.*, **41**, 1356-1367.
- Ralph, F. M., P. J. Neiman, D. W. Van de Kamp, and D. C. Law, 1995: Using spectral moment data from NOAA's 404-MHz radar wind profilers to observe precipitation. *Bull. Amer. Meteor. Soc.*, **76**, 1717-1739.
- Reed, R. J., 1955: A study of a characteristic type of upper-level frontogenesis, *J. Meteo.*, **12**, 226-237.
- Reiter, E. R., 1967: *Jet Streams*, Doubleday & Company, Inc., 189 pp.

- Rossby, C.-G., 1938: On the mutual adjustment of pressure and velocity distributions in certain simple current systems, II. *J. Mar. Res.*, **1**, 239-263.
- Rozumalski, R. A., 1996: Role of diabatic geostrophic adjustments in preconditioning the environment for explosive cyclogenesis. Ph. D. Thesis., North Carolina State University, 250 pp. (draft)
- Sawyer, J. S., 1956: The vertical circulation at meteorological fronts and its relation to frontogenesis. *Proc. Roy. Soc. London.*, **A234**, 346-362.
- Schumann, U., 1987: Influence of mesoscale orography on idealized cold fronts. *J. Atmos. Sci.*, **44**, 3423-3441.
- Scorer, R., 1949: Theory of waves in the lee of the mountains. *Quart. J. Roy. Meteor. Soc.*, **75**, 41-56.
- Shapiro, M. A., 1981: Frontogenesis and geostrophically forced secondary circulations in the vicinity of jet-frontal zone systems. *J. Atmos. Sci.*, **38**, 954-973.
- _____, 1982: Mesoscale weather systems of the Central United States, CIRES/NOAA Report.
- _____, 1983: Mesoscale weather systems of the central United States. The National STORMS Program: Scientific and Technological Bases and Major Objectives (R. A. Anthes, Ed.), University Cooperation for Atmospheric Research., P. O. Box 3000, Boulder, Co 80307, 3.1-3.77.
- STORM-FEST Operations Summary and Data Inventory: 1993, NOAA/U.S. Weather Research Program Office, 389 pp.
- Strauch, R.G, B.C. Weber, A.S. Frisch, C.G. Little, D.A. Merritt, K.P. Moran and P.C. Welsh, 1987: The precision and relative accuracy of profile wind measurements, *J. Atmos. Oceanic Tech.* **4**, 563-571.
- Stull, R. B., 1993, *An introduction to boundary layer meteorology*, Kluwer Academic Publishers, 666 pp.
- Tilley, J., 1990: On the application of edgewave theory to terrain-bounded cold surges: A numerical study. NCAR/Coop. Thes. 130, pp. 1-353.
- Uccellini L. W. and D. Johnson 1979: The coupling of upper and lower tropospheric jet streaks and implication for the development of severe convective storms. *Mon. Wea. Rev.*, **107**, 682-703.

- _____, D. Keyser, K. F. Brill, and C. H. Wash, 1985: The Presidents' Day cyclone of 18-19 February 1979: Influence of a tropopause fold on rapid cyclogenesis. *Mon. Wea. Rev.*, **113**, 962-988.
- Weber, B.L., and D.B. Wuertz, 1990: Comparison of rawinsonde and wind profile radar measurements, *J. Atmos. Oceanic Tech.* **7**, 157-174.
- Williams, M., 1981: Inter-Hemispheric interactions during Winter MONEX, *Proceedings, International Conference on early results of FGGE and large-scale aspects of its monsoon experiment, World Meteorological Organization*, **10**, 12-16.
- Zack, J. W., and M. L. Kaplan 1987: Numerical simulations of the subsynoptic features associated with the AVE-SESAME I case. Part I: The preconvective environment. *Mon. Wea. Rev.*, **115**, 2367-2393.
- Zamora, R. J., M. A. Shapiro, and C. A. Doswell III, 1987: The diagnosis of upper tropospheric divergence and ageostrophic wind using profiler wind observations. *Mon. Wea. Rev.*, **115**, 871-884.
- Zang, D.-L., and R. A. Anthes, 1982: A high resolution model of the planetary boundary layer-sensitivity tests and comparisons with SESAME-79 data. *J. Appl. Meteor.*, **21**, 1594-1609.